MONTANUNIVERSITÄT LEOBEN

PhD Thesis

Reliability assessment of microelectronic systems: from single crystals to ceramic boards

Manuel GRUBER

This work was financially supported by the Styrian and the Tyrolean Provincial Government, represented by Steirische Wirtschaftsförderungsgesellschaft mbH and Standortagentur Tirol, within the framework of the COMET Funding Programme.

Institut für Struktur- und Funktionskeramik

Montanuniversität Leoben

Peter-Tunner-Straße 5

8700 Leoben, Austria

Affidavit

I declare in lieu of oath, that I wrote this thesis and performed the associated research myself, using only literature cited in this volume.

Leoben, März 2018 Manuel GRUBER

Danksagung

Zu Beginn möchte ich mich herzlich bei allen Mitarbeitern des Instituts für Struktur- und Funktionskeramik und des Erich Schmid Instituts bedanken. Allen voran sei meinem Doktorvater assoz.Prof. Dr. Daniel Kiener, Priv.-Doz. Dr. Raul Bermejo und Ao.Univ.-Prof. Dr. Peter Supancic für ihr stets offenes Ohr, hilfsbereites Wesen und vor allem für die bereitwillige Teilung ihrer großen fachlichen Kompetenz gedankt.

O.Univ.-Prof. Dr. Robert Danzer danke ich für die Möglichkeit der Verfassung dieser Arbeit auf seinem Institut und die vielen hilfreichen Diskussionen und Ratschläge.

Ein besonderer Dank gilt meiner Familie, allen voran meinen Eltern, für den bedingungslosen Rückhalt, die ständige Zuversicht und Unterstützung. Meiner Freundin Tanja danke ich für ihre jahrelange Treue, Loyalität und Liebe, die mir auch in schwierigen Momenten stets Kraft und Motivation gab.

Darüber hinaus danke ich all meinen Freunden für die vielen schönen und unterhaltsamen Momente im Laufe der letzten Jahre und hoffentlich noch weit darüber hinaus.

Des Weiteren möchte ich mich bei den Projektpartnern EPCOS OHG, Continental und dem Materials Center Leoben für die gute Zusammenarbeit bedanken. Der österreichischen Bundesregierung (insbesondere dem Bundesministerium für Verkehr, Innovation und Technologie und dem Bundesministerium für Wissenschaft, Forschung und Wirtschaft) vertreten durch die Österreichische Forschungsforderungsgesellschaft mbH (FFG), und den Ländern Steiermark und Tirol, vertreten durch die Steirische Wirtschaftsförderungsgesellschaft mbH (SFG) sowie die Standortagentur Tirol, sei für die Förderung im Rahmen des COMET Förderprogramms ebenfalls herzlich gedankt.

Kurzfassung

Um der Nachfrage nach immer höheren Übertragungsraten in modernen Smartphones gerecht werden zu können, erweitern Mobilfunkanbieter die genutzten Frequenzbänder für jede neue Generation von Mobilfunkstandards. Das breitere Portfolio an verwendeten Frequenzbändern bedingt dabei eine signifikante Erhöhung der Anzahl an Frequenzfiltern in aktuellen Geräten für die mobile Kommunikation. Dies, zusammen mit der weltweit starken Nachfrage nach z. B. Smartphones, führt zu einem erhöhten Bedarf an präzisen, effizienten und preiswerten Filterkomponenten. In diesem Zusammenhang sind akustische Oberflächenwellen (AOW) - Filter heute eine der führenden Technologien.

Eine große Herausforderung bei diesen hochentwickelten mikroelektronischen Bauteilen stellt die große Vielfalt an verwendeten Materialklassen und die damit verbundenen Unterschiede in den thermo-mechanischen Eigenschaften dar. Als Konsequenz können hohe mechanische Spannungen beim Abkühlen nach der Produktion, beim Thermozyklieren während der Qualifizierung oder später im Einsatz auftreten. Bei den verwendeten spröden Materialien besteht immer eine gewisse Versagenswahrscheinlichkeit, sobald mechanische Belastungen auftreten. Ziel der vorliegenden Arbeit ist es, ein vertieftes Verständnis für die Versagens- und Verformungsmechanismen für die in modernen AOW-Frequenzfiltern integrierten spröden Bauelemente zu gewinnen. Die mechanischen Eigenschaften stark anisotroper, piezoelektrischer Einkristalle sowie mehrschichtiger Keramik-/Metall-Schichtsysteme, welche komplexe elektrische 3D-Verbindungen zwischen funktionellen Komponenten bilden, wurden eingehend untersucht. Es wurden biaxiale und uniaxiale Festigkeitsmessungen in Kombination mit fraktographischen Untersuchungen durchgeführt, um beobachtete Unterschiede mit dem jeweiligen Bruchausgang verknüpfen zu können. Nanoindentationsexperimente und In-situ-Zähigkeitsmessungen lieferten bedeutende Erkenntnisse über den Ursprung von irreversiblen Deformationen bzw. des daraus resultierenden Bruchverhaltens.

Das gewonnene Wissen kann verwendet werden, um die Kristallorientierungen gezielt zu variieren und die Ausrichtung der notwendigen Oberflächenrauheit in Bezug auf die identifizierten Spaltebenen maßzuschneidern. Folglich konnte die mechanische Festigkeit der einkristallinen Materialien für spezifische Orientierungen signifikant verbessert werden. Für die untersuchten Mehrschichtkeramiksubstrate konnte die Wirkung einzelner, gezielt eingebrachter Merkmale, z. B. Vias oder Elektroden, zusammen mit Umgebungseinflüssen untersucht und zur Entwicklung verbesserter Konstruktionsrichtlinien für mikroelektronische Systeme angewandt werden. Um die Bedeutung dieser scheinbar kleinen Details zu unterstreichen, konnte für ein echtes Vielschicht-Bauteil gezeigt werden, dass eine kleine Änderung des Elektroden-Designs die mechanische Festigkeit des Bauteils beinahe verdoppeln kann, was die für eine zuverlässige und kosteneffiziente Produktion erforderliche Stabilität liefert. Dieser Punkt ist für Unternehmen unverzichtbar, um sich im hart umkämpften Bereich der mikroelektronischen Zuliefererindustrie behaupten zu können.

Abstract

To satisfy the demand for ever higher up -and download rates in modern smartphones, the mobile communication providers expand the utilized frequency bands for every new generation of mobile communication standards. The wider portfolio of used frequency bands leads to a significantly increased number of frequency filters in modern devices for mobile communications. This, together with the worldwide increased request for e.g. smartphones, led to an excessive demand for precise, efficient and cheap filter components. In this context, Surface Acoustic Wave (SAW) filters are one of today's leading technologies.

A serious challenge going along with these advanced microelectronic parts is the wide range of used material classes and their corresponding differences in thermo-mechanical properties. As a consequence, high stresses may arise after cooling down from production or thermo-cycling during qualification and service. Especially for the used brittle materials always a certain chance for failure exists once a mechanical stress is applied. In this context, the goal of the present work is to gain a deep understanding on the failure and deformation mechanisms occurring in the brittle parts integrated in modern SAW frequency filters. The mechanical properties of strongly anisotropic, piezoelectric single crystals, as well as multilayer ceramic/metal compounds forming the complex 3D electrical connections between functional components, were investigated in depth. Therefore biaxial and uniaxial strength measurements together with fractography are employed to link differences in mechanical strength with their fracture origins. Nanoindentation experiments and in-situ toughness measurements revealed the origins of irreversible deformations and the obtained fracture behaviour, respectively.

The gained knowledge was further used to selectively vary crystal orientation and to tailor the orientation of inevitable surface roughness with respect to identified cleavage planes. As a consequence, the mechanical strength of the single crystalline materials could be significantly improved for specific orientations. For the multilayer ceramic substrates of interest the effect of individual features, e.g. vias or electrodes, together with environmental effects were studied and can be utilized for developing new design rules for microelectronic systems. To substantiate the importance of these apparently small details, it is shown for a real multilayer component that a simple change of the electrode's design can double the mechanical strength of the component delivering the structural integrity required for reliable and cost-efficient production. This point is indispensable for companies to participate in the shark-tank of microelectronic suppliers.

Content

Abbreviations

3PB	*Three-point-bending*
4PB	*Four-point-bending*
a	*Spacing between electrodes*
a_c	*Defect size*
b	*Specimen width*
B3B	*Ball-on-three-balls*
BAW	*Bulk Acoustic Wave*
Conf.1	*Configuration 1*
Conf.2	*Configuration 2*
CTE	*Coefficient of thermal expansion*
DFT	*Density Functional Theory*
E	*Young's modulus*
E^*	*Reduced modulus*
f	*Dimensionless factor*
FEA	*Finite element analysis*
FIB	*Focused-ion-beam*
GG	*Grinding groove*
h	*Width of electrodes*
IDT	*Interdigital transducers*
k	*Electromechanical coupling factor*
K_c	*Fracture toughness*
l	*Inner span between loading rolls*
L	*Span between supporting rolls*
$LiNbO_3$	*Lithium Niobate*
$LiTaO_3$	*Lithium Tantalate*
LTCC	*Low temperature co-fired ceramic*
m	*Weibull modulus*
PCB	*Printed Circuit Board*
P_{max}	*Maximum load*
R	*Radius of the shperical indenter tip*
RF	*Radio frequency*
SAW	*Surface Acoustic Wave*
SCCG	*Sub-critical crack-growth*
SEM	*Scanning electron microscope*
t	*Specimen thickness*
TCD	*Temperature coefficient of delay*
TCF	*Temperature coefficient of frequency*
TCV	*Temperature coefficient of velocity*
V_0	*Normalization volume*
V_{eff}	*Effective volume*
Y	*Dimensionless factor*
ZnO	*Zinc Oxide*
λ	*Wavelength*
σ_0	*Characteristic strength*
σ_c	*Fracture stress*
τ_{max}	*Maximum shear-stress*

1. Introduction and motivation

Over the last millenniums, ceramics have proved as ideal structural materials wherever compressive loading conditions are applied. Nevertheless, due to their exceptional properties such as corrosion resistance, high-temperature stability, high strengths at low densities, high hardness and corresponding wear resistance, the demand for brittle materials such as ceramics or glasses for applications, where also tensile stresses occur, has emerged. Due to the lack of plasticity, these brittle materials can easily fail under the combination of tensile stresses and pre-existing defects like pores, agglomerates or surface defects such as scratches. Since for almost all technical applications tensile stresses act on the corresponding parts, the mechanical behaviour of respective brittle materials are of great interest in terms of mechanical reliability and structural integrity.

Lesser known to the general public, ceramics have further emerged as essential parts of microelectronic systems over the last decades due to their unique electrical, magnetic and optical properties [1]. In this context, the non-linear dependence of electrical resistance with electric field or temperature is used in e.g. varistors and thermistors, respectively. Furthermore, the partly extraordinary high piezo-electric coefficients of these materials (often in single crystalline form) are used for sensors and actuators and consequently have become indispensable for the constantly growing mobile communication market. One example is thereby the application as frequency filter, where multilayer ceramic substrates and functional brittle single crystalline components are connected. Again considerable tensile stresses are present due to thermo-mechanical mismatches. Since functional performance of advanced microelectronic devices increase rapidly, a short insight into evolution and targets of the mobile communications market, where ceramic components play a decisive role, will be given in the next paragraphs before challenges concerning their mechanical behaviour are discussed.

Since the first digital mobile communication standard, the 2G Global System for Mobile Communications (GSM), was introduced in 1991 an exponential growth of data traffic volume has been observed and is also predicted for the future [2, 3]. To satisfy the need for faster up- and download rates of more and more connected mobile devices, around every 10 years a new standard of mobile communication has been introduced. Data rates increased from 64 kilobit per second for the GSM network to 2 megabit per second (Mbps) for the 3G Universal Mobile Telecommunication System (UMTS), launched in 2001. Today's leading technology is the 4G Long Term Evolution (LTE) standards, providing data rates up to 100 Mbps [4].

New developments such as the internet of things with the corresponding massive machine-to-machine, person-to-machine or vehicle-to-vehicle communication in combination with home sensor networks and integrated sensor systems lead to a huge automatically communicating system [4-6]. Together with the constantly growing person-to-person communication satisfying our urge to interact with anyone all over the world, a total of 50 billion connected devices is predicted by 2020 [7], leading to a total mobile data and internet traffic of over 34 Exabytes per month [3]. In other words: Due to the expected 1000-fold of data traffic increase for 2020 and beyond, the limits of 4G will be reached shortly and a new 5G standard needs to be introduced [8, 9]. The most effective method to process the required data demand is a wide bandwidth which could be provided in the mm Wave bands far above 3 GHz, where e.g. most of today's 2G, 3G and 4G spectrums operate [2, 10, 11].

In this context, the increased counts of frequency bands and request for ever faster down- and upload rates makes efficient and precise filtering of frequencies substantial for achieving the required high data rates in mobile devices. Especially for frequencies below 2 GHz [12], Surface Acoustic Wave (SAW) filters, where brittle single crystalline components are connected to ceramic circuit boards, dominate the smartphone market due to their cost-efficient mass production, where lithographic techniques originating from the semiconductor industry are employed [13]. For higher frequencies the usually more expensive Bulk Acoustic Wave (BAW) filters need to be used, though rarely any information can be found on filter techniques for the expected mm Wave bands employed for the 5G communication standard. However, it can be assumed that SAW filters, whose mechanical reliability and structural integrity is the main focus of this work, will play a substantial role for already existing frequency bands below 2 GHz together with new ones emerging in the new 600-700 MHz regime [14].

Due to thermo-mechanical loading during fabrication, qualification and/or in-service, the functionality of SAW devices strongly relies on the structural integrity of the single crystals as well as multilayer ceramic/metal substrates. Their brittle character and stochastic (Weibullian) mechanical strength imposes a limitation on lifetime of the devices. A certain failure probability exists during such thermo-mechanical loading, becoming extremely critical considering that about a hundred filters are integrated into every single next generation smartphone. In this context, a schematic of a SAW module consisting of a polymer circuit board, a ceramic circuit board and the single functional SAW filters on top is given in Figure 1a together with possible failure scenarios for the circuit board (Figure 1b) and SAW-filter (Figure 1c), respectively.

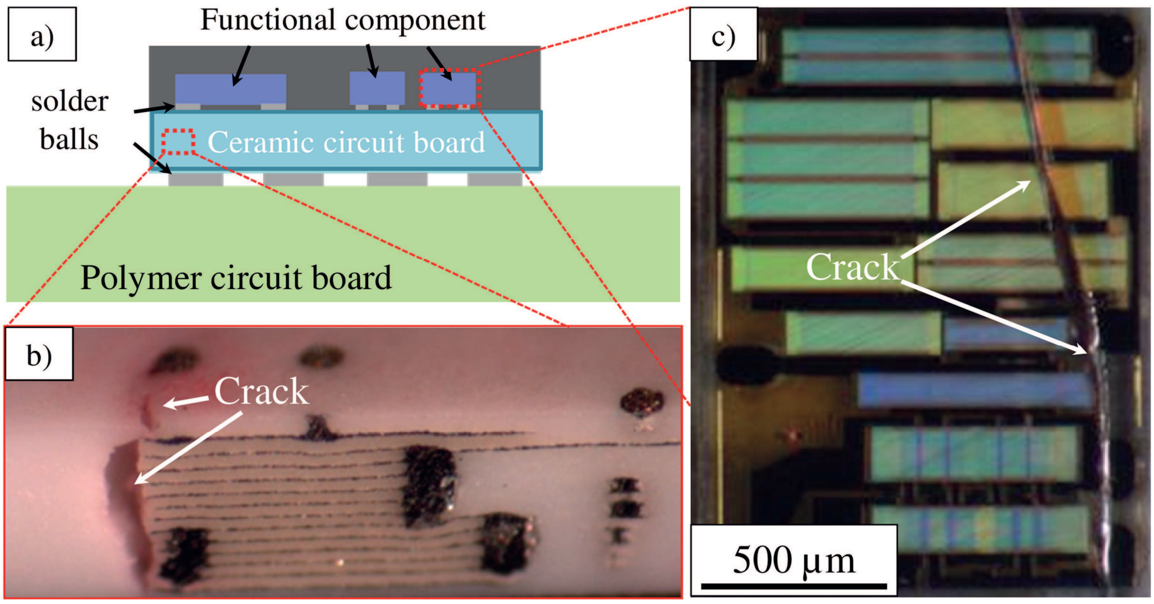

Figure 1: Schematic representation of SAW filter module (a) together with possibly occurring mechanical collapses due to cracks in the ceramic circuit board (b) or the SAW-filter component (c).

Since residual tensile stresses, which may lead to initiation and propagation of cracks from e.g. surface defects like scratches, are unavoidable in the process route, enhanced material properties in terms of mechanical strength of the corresponding brittle functional materials are still required. Therefore extended investigations regarding fracture behaviour, deformation mechanisms, orientation dependencies and design effects were performed in the framework of this thesis to gain a deeper insight into the mechanical performance of the respective materials and components. The progress of knowledge allows providing concepts to improve the structural integrity and reliability of the ceramic circuit board as well as the functional single crystalline components concerned, which design and functionality will be shortly described in the next chapters.

2. The use of single crystals and ceramics in microelectronics

Due to their outstanding functional properties, some brittle materials are indispensable in microelectronic systems. In this context, especially single crystalline silicon is widely used in the semiconductor industry as well as for Micro Electro Mechanical Systems (MEMS). For optoelectronics, actuators, sensors, detectors or filter technologies further single crystalline materials like e.g. $LiTaO_3$, $LiNbO_3$ or Sapphire are of great importance.

The corresponding functional components are usually joined on a Printed Circuit Board (PCB) which provides the electrical connection. Therefore, polymer as well as ceramic PCBs can be used. For applications in harsh environments or systems operating at high frequencies the latter one is usually preferable.

An example for microelectronic systems where both, single crystalline functional components and ceramic circuit boards are assembled together, is the Surface Acoustic Wave (SAW) frequency filter.

2.1. Surface Acoustic Wave frequency filters

The aim of a frequency filter is to filter out one frequency within a certain bandwidth and simultaneously suppress all other possibly occurring frequencies, leading to a bandpass-filter characteristic as exemplarily shown in Figure 2. Possible bandpass filter technologies for radio frequencies that lie in a range between 3 kHz and 300 GHz, are Surface Acoustic Wave (SAW), Bulk Acoustic Wave (BAW) and Film Bulk Acoustic Wave Resonator (FBAR) devices [12]. The focus of this work lies on filters for mobile devices, where the SAW technologies are leading due to their efficient production process and applicability for low-frequency applications (below 2 GHz) [12, 15, 16].

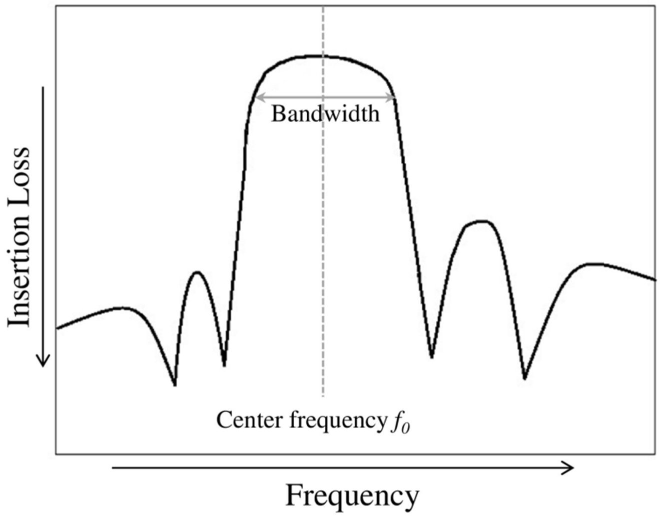

Figure 2: Schematic representation of a bandpass filter characteristic provided by a SAW-filter device.

2.1.1 Acoustic (elastic) waves in solid materials

The SAW was discovered in 1885 by Lord Rayleigh [17] and is an acoustic (or elastic) wave propagating along the surface of a solid material. In an isotropic material the atoms move in the plane containing the surface normal and propagation direction. Its amplitude is thereby decaying exponentially with the distance from the surface. Figure 3a shows the equilibrium state of the atoms (dots) and the displacements due to a Rayleigh wave (arrows) [18].

Mathematically, SAWs are the sum of a longitudinal and a transversal wave which are also depicted in Figure 3b and c for comparative purposes. Figure 3b corresponds thereby to a longitudinal wave, where the displacement is parallel to the propagation direction and Figure 3c to a transversal wave, with the displacement normal to the propagation direction. All three described waves are non-dispersive, which means that the velocity of the wave is independent of its frequency. Besides of frequency filters, which are described in the next section, several functional microelectronic devices like transducers, sensors or detectors work on the basis of SAWs.

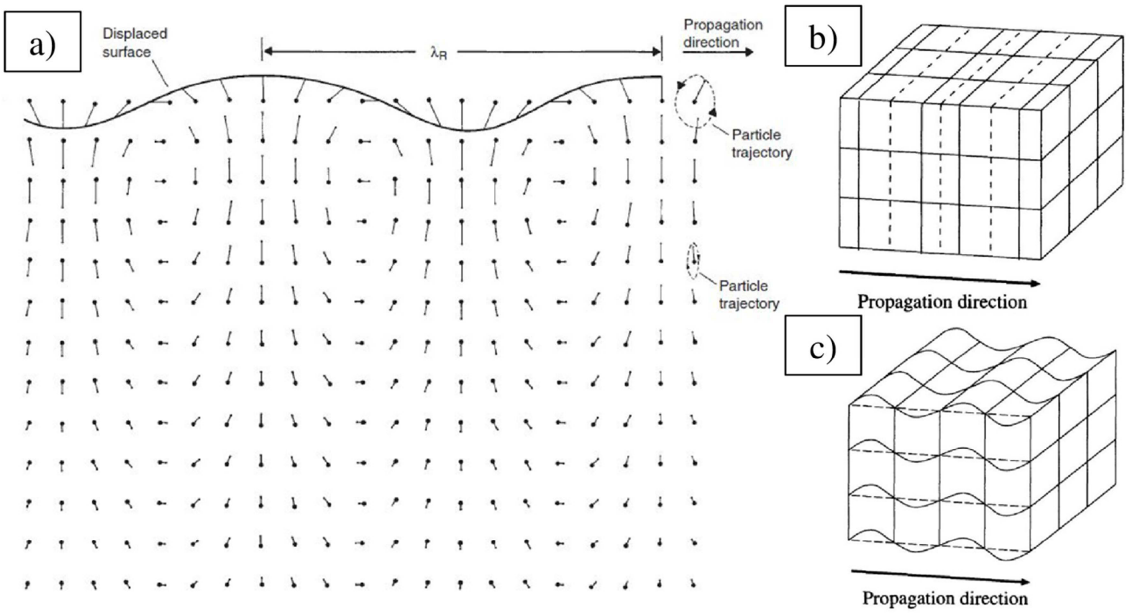

Figure 3: (a) 2D representation of a SAW taken from [18], (b) displacement of a cubic grid due to wave propagation of a longitudinal and (c) transversal wave, both taken from [15].

2.1.2 Functionality of SAW-filter devices

A basic SAW device consists of two interleaved thin-film metal electrodes (interdigital transducers, IDTs) deposited on a piezoelectric substrate which is schematically shown in Figure 4a. The IDTs, which are shown in Figure 4b in more detail, convert electrical signals into acoustic waves (and vice versa) using the piezoelectricity (coupling of the electric and mechanic field) of the substrate material. When an alternating current is applied to the input IDT, it causes periodic displacement of the surface and thus SAWs between the fingers. These waves reinforce each other if the wavelength (λ) equals the transducers pitch. For other frequencies (and therefore different wavelengths) the waves are not in phase, which leads to a decrease in amplitude. So the wavelength of the generated SAW corresponds to the electrode's width (h) and the spacing between electrodes (a). If they are identical, the wavelength of the centre-frequency equals four times the width of the electrode and thus the resonance frequency is given by:

$$f_0 = \frac{v_s}{\lambda} = \frac{v_s}{2(a+h)} = \frac{v_s}{4h} \qquad \textbf{Equation (1)}$$

with f_0 being the centre frequency and v_s the wave’s velocity with values of typically around 3000 m/s. For some crystal cuts extraordinarily high velocities can be reached. For example, for the 128° Y-X-$LiNbO_3$ cut, which was of great interest in this work, velocities of ~4000 m/s are reached [19, 20]. To reach an operating frequency of 2 GHz, accordingly a minimum width of 0.5 µm between electrodes is required. Nevertheless, special techniques can enable an extension up to 5 GHz [18].

Due to the strongest response at a certain frequency the device exhibits the desired bandpass characteristic shown in Figure 2. At the output IDT the incident SAW is then converted back into an electrical output signal [21].

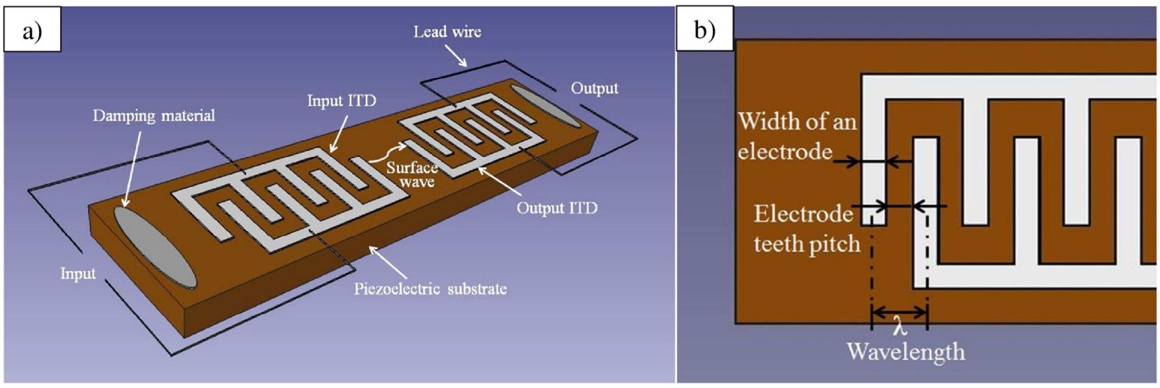

Figure 4: (a) Schematic representation of a basic SAW-filter device with (b) a detailed view on the IDTs responsible for the input/output signals. Depending on geometrical conditions of the electrodes and the wave’s velocity, a certain frequency within a bandwidth is converted back into an electrical signal at the output IDT.

From the basic bandpass filter in Figure 4 different requirements can be fulfilled by modifying the component’s design. The main types are transversal filters (high losses, narrow passbands, precisely controlled amplitudes and phases), low or medium loss intermediate frequency filters (e.g. for television receivers) and many types of radio frequency (RF) filters which are essential for mobile phones. These RF filters demand low losses for wide bandwidths, high suppression outside the passband, ability for mass production and very small sizes. The above points are discussed into detail in [20, 22].

2.1.3 Demands on substrate materials and designs

The most important property required for transduction is piezoelectricity of the substrate material. The name piezoelectricity comes thereby from the Greek word "*Piezo*", which means pressure, and was discovered by Pierre and Jacques Curie in 1880 [23]. It is the electrical response of a material to mechanical loads which is described in [24] in detail and shortly summarised in this section. The direct piezoelectric effect is shown in Figure 5a, where a load is applied and the material becomes electrically polarized. When the load is released also the induced electric field vanishes. The reverse process (Figure 5b) appears, when an electric field is applied on a piezoelectric material, leading to mechanical strains. In order to explain this phenomenon, a deeper look into the ionic microstructure is required. For the undeformed sample gravity centres of positive and negative ions coincide for each part of the microstructure. The charge distribution under a load leads to polarization due to separation of positive and negative gravity centres which generates electric dipoles and thus a measurable electric field. On the other hand, placing of an unloaded piezoelectric material in an electric field leads to displacement of charges and thus specific strains. The described internal arrangement of charges responsible for the piezo-effect can only arise in an anisotropic material [24, 25]. The coupling between electrical and mechanical field can be described by the electromechanical coupling factor, *k*, where for SAW-filters a high value is favourable [15, 26].

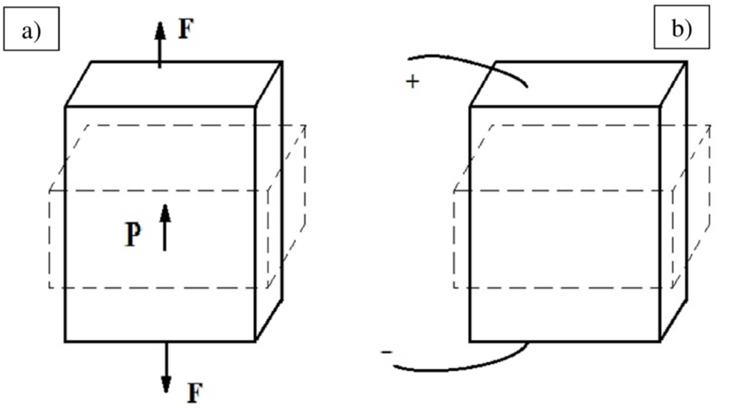

Figure 5: (a) Direct piezoelectric effect leading to an electric polarization in presence of a mechanical load and (b) reverse piezoelectric effect causing mechanical strains in presence of an electric field [24].

Another crucial issue is the temperature stability of the functional properties due to the possible exposure of a device to temperature variation. Depending on the application, SAW devices may be used in a wide temperature range, e.g. from -40 °C to +80 °C, in which the device shall meet the electrical specifications. Resonance frequency, SAW velocity and delay are all temperature dependent, which is described by the temperature coefficient of frequency (TCF), the temperature coefficient of velocity (TCV) and the temperature coefficient of delay (TCD). Unfortunately, materials with preferable lower temperature dependences usually occupy an undesirable low coupling factor. E.g. for Quartz with a low *k*, crystallographic cuts with a TCF of zero are known [27] and used where accurate frequency generation is needed (e.g. wristwatches). Important parameters responsible for temperature dependences are the coefficient of thermal expansion (CTE) and wave velocity, both strongly related to the elastic properties of the corresponding material. The piezoelectric crystals are anisotropic and so are CTE and wave velocities. Therefore properties can be tailored by using the well-defined direction dependent properties of the single crystalline materials through different cuts of the crystal under certain angels to meet the required properties for the application the material have been conceived for [19]. Besides coupling factor and temperature dependences also other properties (e.g. insertion loss, Q-factor, beam steering, propagation loss, radiation of bulk acoustic waves, low cost growth and wafer scale device production) have to be taken into account for the choice of the substrate materials, as detailed in relevant literature [15, 22, 28].

Further considerations, less depending on the substrate material, are regarding to wave deviations which trace back on reflection, absorption, interference and diffraction of the SAW. Triple-transit-interference, electromagnetic feedthrough, electrode finger reflections, circuit factor loading, impedance mismatches, diffraction and especially bulk-wave-interferences need to be mentioned as well [15, 20]. In order to minimize these effects, several techniques must be implemented. Adhesive, soft and conducting coatings, which absorb incident waves, can be attached to the bottom surface. Another method is thinning of the substrate which reduces the available volume for the bulk waves. In most cases, however, the bottom surface of the substrate is additionally roughened in order to scatter away the bulk waves from the output IDT [20]. This technique may increase the functionality but certainly compromises the structural integrity of the brittle substrate. More details on this are given in *Publication B* and Chapter 4.1.5. Nevertheless, all issues need to be taken into account for designing an up-to-date SAW-frequency-filter satisfying the harsh requirements implemented by the mobile communication market. In this context, Figure 6 shows the design of a sophisticated design used for mobile phones in the 1 GHz frequency range. Due to the wide range of used frequency bands, several filters as the one shown in Figure 6 are integrated in a modern device for mobile communication. To electrically connect the microelectronic components, a complex 3D network of conductive metal paths within a non-conductive matrix must be realized. For high frequency applications, Low Temperature Co-Fired Ceramics (LTCCs) are usually chosen [29].

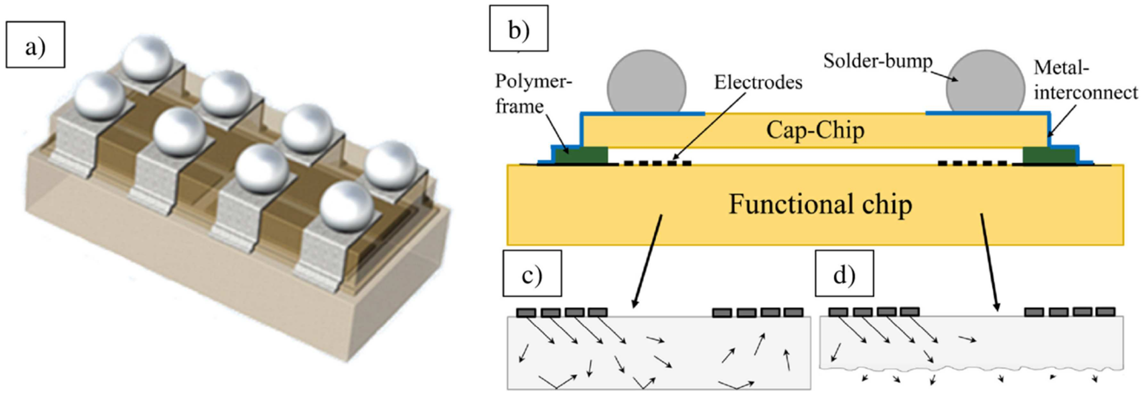

Figure 6: (a) SAW filter for the 1 GHz range integrated in modern mobile phones taken from [30] [31] together with (b) a cross-section showing main parts and materials and (c), (d) a schematic representation of the effect of surface roughening on undesired bulk waves.

The SAW filter components are soldered onto the LTCC board which is itself soldered onto a polymer PCB. Due to the different materials and their corresponding differences in thermo-mechanical properties, significant stresses are expected to arise. LTCCs as well as $LiTaO_3$ and $LiNbO_3$ are of brittle character and thus a certain probability of failure exists once a mechanical stress is applied. For illustrative purposes , the results of a representative Finite Element Analysis (FEA) performed on the microelectronic system shown in Figure 7a is provided in Figure 7b to gain a perception of the stress distributions on the single crystalline parts of a chosen SAW-component. It can be seen that the maximum stresses occur on the bottom surface of the single crystal, in vicinity of the solder balls (red). Depending on the design and the chosen materials, stresses of several hundred MPa in the single crystalline as well as in the LTCC parts are possible.

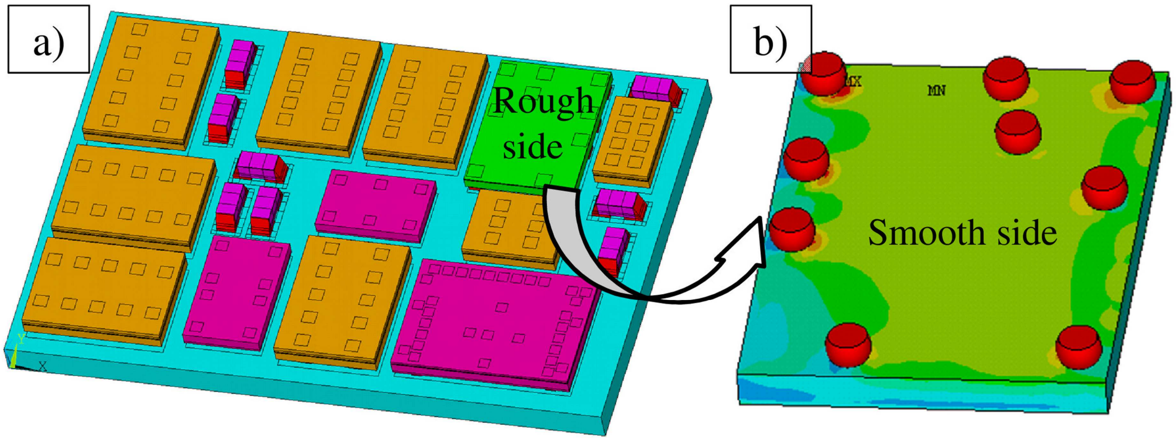

Figure 7: (a) Schematic of a functional system consisting of a ceramic board (turquois) and functional components. (b) Selected single crystalline component showing the highest stresses in vicinity of solder balls (red), scale bar is intentionally skipped. Depending on the actual design and chosen materials/orientations, stresses of several hundred MPa can occur.

2.1.4 Lithium Tantalate and Lithium Niobate

The two materials which seem to meet the specifications best for many SAW-filter substrates are Lithium Tantalate ($LiTaO_3$) and Lithium Niobate ($LiNbO_3$) single crystals. Their properties strongly depend on the crystallographic directions, making a detailed knowledge on crystallographic conditions inevitable. In this context, both show a trigonal crystal structure and belong to the 3*m* point group and the R3c space group (No. 161) [32-34]. The trigonal crystal structure is rather difficult to handle, making it common to transform it into a hexagonal unit cell ($a_h=b_h \neq c_h$ and $\alpha=\beta=90°$, $\gamma=120°$) which is shown in Figure 8a. It consists of 30 atoms, three times more than the corresponding trigonal version. Accordingly also its volume is tripled. Convenient ways to illustrate crystallographic planes in 2D are pole-figures, where stereographic projections of corresponding surface normals are constructed. In this context, the alignment of low indexed crystallographic planes is illustrated in the pole-figure in Figure 8b for $LiNbO_3$ where the (0001) plane was chosen as equator. Required lattice parameters of the unit cell were taken from X-Ray studies performed by Hsu et.al. [35]. The three-fold rotation symmetry around the c_h-axis for this crystal structure [36] leads to the obtained regular arrangement, where planes of interest are highlighted by larger, coloured dots.

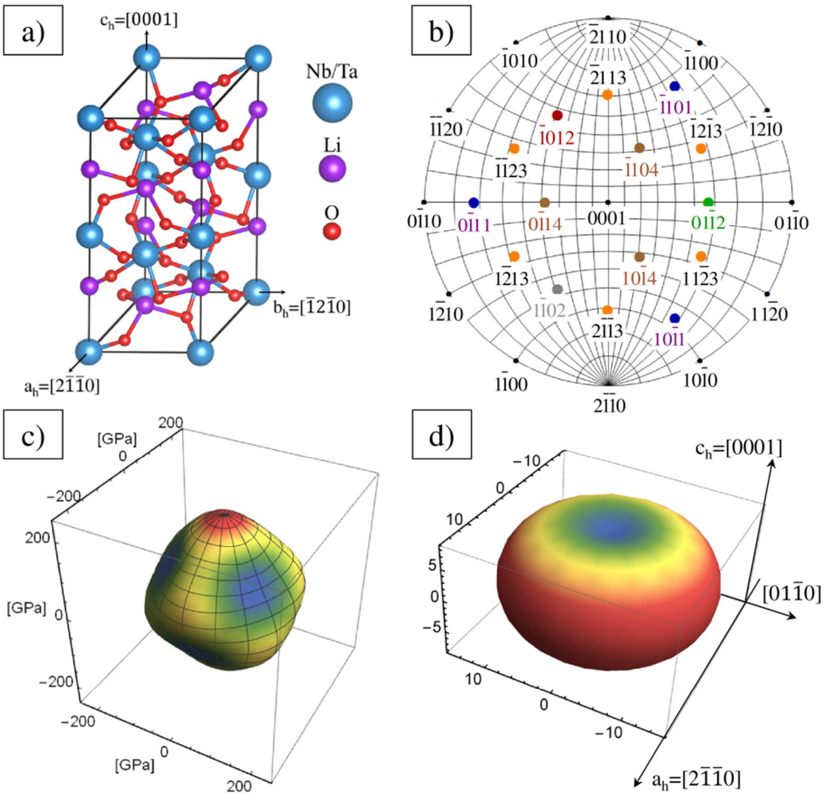

Figure 8: (a) Hexagonal unit cell of $LiTaO_3$ and $LiNbO_3$ consisting of 30 atoms, (b) corresponding pole-figure providing the alignment of low indexed crystallographic planes, (c) and (d) evaluation of Young's modulus and CTE in space for $LiNbO_3$, respectively, constructed using values at room temperature and constant electric field obtained from Smith et.al [37].

This 120° symmetry manifests also in Figure 8c, where the direction dependent variation of Young's modulus is plotted exemplarily for $LiNbO_3$ according to the anisotropic stiffness values measured by Smith et.al. [37]. Details on the construction of the plot can be found in *Publication C*, which also contains corresponding figures for $LiTaO_3$. To complete the visualisation of the direction dependent thermo-mechanical properties also the CTE of $LiNbO_3$ is provided in Figure 8d, constructed using values from [37]. It can be concluded that the strongest atomic bonds are along the c_h-axis, manifesting in the highest stiffness and lowest CTE in this direction.

While extended data is available regarding functionality [19, 38, 39], only few information can be found on the materials' response to mechanical loading [40-42]. Furthermore, information is mainly restricted to loading along the [0001] or $[01\bar{1}0]$ direction for both materials, which are often not relevant for real applications, where rather complicated crystal cuts are manufactured. Nevertheless, the following rudimentary findings regarding fracture and plastic deformation are available:

- Both materials naturally cleave along the $\{01\bar{1}2\}$ family of planes [34, 42]
- Twinning along the same set of planes is documented for $LiTaO_3$ [43] as well as $LiNbO_3$ [44, 45] and even at elevated temperatures favourable over dislocation glide [46, 47]
- Cracks can develop in the intersection of twins in $LiNbO_3$ [48]

Gained extensions on this knowledge within the framework of this thesis will be discussed in Chapter 4.1 and *Publications A-D.*

2.2. Ceramic based printed circuit boards

For microelectronic applications where either harsh operation conditions occur or high frequencies are applied, ceramic circuit boards are favourable over their polymer counterparts. In this context, LTCCs provide better performance at elevated temperatures and aggressive environments [49] together with excellent damping properties at higher operation frequencies in e.g. mobile communications [29]. For some applications the use of ZnO, which acts as varistor material [50], can be advantageous in terms of higher integration densities since further assembly of functional components for over-voltage protection is no longer required. Possible further applications of ceramic/metal multilayer components are piezoelectric actuators, multilayer ceramic capacitors, LTCCs, multilayer, planar solid oxide fuel cells or semiconducting devices. Corresponding functional substrates are usually fabricated combining ceramic layers with external and internal metallization. The different metal layers are thereby printed and fired onto the ceramic part to provide the component with the requested functionality. Ceramic multilayer substrates for microelectronic applications will be in the main focus of the present work.

2.2.1 Multilayer technology

For all above highlighted components a combination of a ceramic based substrate with internal and external electrodes as well as surface features has to be realised. In this context, LTCCs are preferred due to their low sinter temperatures (below 900°C) to allow a decent combination of substrate and metal paths. Commonly used materials are e.g. alumina-glass composites or ZnO, which enable the co-sintering of glass ceramics with highly conductive metals (e.g. silver, gold, galvanized nickel) [51].

The complex 3D networks of real components are implemented by a tape-casting process which features a high degree of dimensional accuracy and can therefore deliver the required low allowable tolerances [52, 53]. Thereby thin ceramic foils are manufactured and printed with metal paste. Through vias to electrically connect the final substrate are fabricated by punching of holes into the ceramic layers, which are then also filled with metal paste. The individual layers with filled vias and printed conductive parts are subsequently stacked and finally sintered.

2.2.2 Demands on substrate materials and architectures

The functionality of the multilayer ceramic substrates is twofold: On the one hand electrical conductivity along the metal paths needs to be provided to connect functional components and on the other hand adequate electrical insulation should be provided from the ceramic parts to prevent short circuits. In this context, the mechanical reliability of the present substrate needs to be guaranteed since the presence of cracks may trim the conductive paths. Moreover, also small cracks in the ceramic parts between metal layers can compromise the functionality since they may be filled with metal through diffusion or electro-migration which would lead to short circuits. In this context, thermomechanical stresses caused by differences in CTE and elastic properties can lead to residual distortions in the material. Especially residual tensile stresses may compromise the structural integrity of the later microelectronic component [54, 55], since brittle materials tend to fail due to the highest normal tensile stresses. These residual stresses may be superimposed by further stresses coming from external loading. Particularly material junctions, where stress concentrations can occur, are therefore expected to be prone for initiating and propagating cracks.

In this context, mechanical properties of corresponding LTCC bulk materials have been widely investigated in [49, 56, 57] and can be summarized as follows:

- The characteristic strength strongly relies on the loading rate, temperature as well as the environment and lies for room temperatures in the range of ~220 MPa for low stress rates in water and ~420 MPa for high loading rates in water free environments (oil or argon atmosphere). At elevated temperatures (125 °C) in air a slight reduction in strength compared to room temperature measurements is noticed.

- Fracture toughness values between 1.3 MPam$^{1/2}$ and 2.3 MPam$^{1/2}$ are documented with lower values corresponding to measurements in water and higher values to Argon (inert) environment, respectively.
- While mechanical properties of “bulk” multilayer materials are well investigated in different environments, the complexity of real designs makes a detailed analysis very complex. This is exemplarily shown in the cross-section of a ceramic circuit board (with a functional component on top) in Figure 9a together with a close-up of the LTCC’s microstructure. The crack initiation may be a combination of residual tensile stresses, stress concentrations, surface defects together with environmental influences and cannot be ascribed to one single contribution. To make a step forward, selected samples with different features (see Chapter 3.1.2) of various complexities were manufactured and tested in the framework of this thesis. Results could be applied and complement the understanding of the fracture behaviour of more complex and real functional ZnO-based microelectronic components (see Chapter 4.2.2).

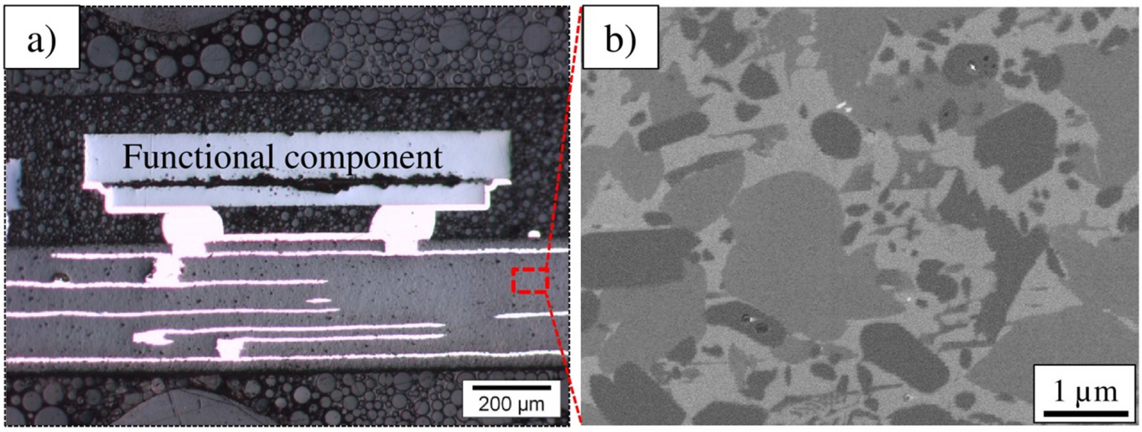

Figure 9: (a) Cross-section of a LTCC circuit board together with a functional component on top and (b) close-up of the LTCCs microstructure where the dark constituents are the ceramic particles.

3. Mechanical characterization of brittle substrate materials: Materials and methods

In ductile materials such as many metals it is energetically favourable to realize plastic deformation by nucleation and movement of dislocations once the respective yield strength is reached. In ceramics, dislocation plasticity would require higher shear stresses and the materials usually fail in brittle manner well before reaching this yield strength. Due to the lack of plastic deformation, which would dissimilate a large amount of energy, the corresponding fracture energies for ceramic materials are consequently low. Therefore, the fracture behaviour is triggered by pre-existing flaws such as agglomerates, pores or surface defects like scratches [58]. Fracture initiates thereby at the most critical defect and cracks usually grow in an unexpected and catastrophic manner [59]. The corresponding relationship between fracture stress σ_c, fracture toughness K_c and defect size a_c is given according to the Griffith/Irwin criterion [60]:

$$\sigma_c = \frac{K_c}{Y \cdot \sqrt{\pi \cdot a_c}}$$ **Equation (2)**

with Y being a dimensionless factor depending on the defects geometry. While in conventional sintered ceramics volume defects (pores, agglomerates) or surface defects play a role, the latter one is the main reason for failures in brittle single crystals, where intrinsic defects are usually negligibly small (in the range of several atoms due to e.g. lattice defects or contamination). Thus pre-existing flaws coming from the harsh cutting, grinding or polishing processes, as well as sub-surface cracks which are a result of contact loading during assembly procedures determine their bearable stresses [61-64].

Since the size of the most critical defect can vary from specimen to specimen [65, 66], the strength of the respective material cannot be described by one single value but a statistical analysis of a sufficient large number of specimens needs to be performed [67, 68]. Nevertheless, it can be concluded that for conventional as well as single crystalline brittle materials the underlying defect population determines the fracture stress distribution [69]. As a direct consequence, the strength of a sample also depends on tested (effective) volumes of the corresponding specimens since in large effective volumes the chance for finding a larger defect is higher. The corresponding statistical theory was published by Waloddi Weibull [70, 71] and manifested as excellent method for the description of strength distributions in ceramic materials [72].

Once a mechanical stress σ is applied onto a brittle material, a certain probability of failure, P, exists. Considering the effect of the effective volume V_{eff} this probability of failure can be described by the Weibull distribution:

$$P(\sigma,V)=1-\exp\left[-\frac{V_{eff}}{V_0}\cdot\left(\frac{\sigma}{\sigma_0}\right)^m\right] \qquad \textbf{Equation (3)}$$

where m is the Weibull modulus, σ the characteristic strength and V_0 the corresponding normalization volume. σ_0 is thereby the stress where a probability of failure of ~ 63 % exists. The Weibull modulus describes the scatter in strength values; accordingly a low value corresponds to a broad strength distribution and vice versa. Both values are to be determined by the Maximum Likelihood method according to the EN-843-5 standard [68]. In the respective norm the lower limit for statistical relevance is set to 30 specimens. Due to statistical uncertainties, σ_0 as well as m are to be given in 80 %, 90 % or 95 % confidence intervals. For illustrative purposes, strength values can be plotted in a Weibull diagram, where the probability of failure is plotted versus failure stress. To be more precise, a double logarithmic scaling is thereby chosen, e.g. $LnLn\left(\frac{1}{1-P}\right)$ is plotted versus $Ln(\sigma)$. For Weibull distributed data a linear relationship between them can be obtained, where m corresponds to the slope of the corresponding line.

Another crucial issue comes from the sensitivity of some brittle materials to humid environments [49, 73]. Especially for glasses [74] it is known that water molecules can dissolve the silicon-oxide bonds at a crack front through hydrolysing [75], leading to Sub-Critical Crack-Growth (SCCG). Accordingly, cracks can grow sub-critically under stresses far below the fracture stress. As the fracture stress σ depends on the defect size a according to Equation (2), a larger crack consequently reduces the bearable load of a material. Thus materials sensitive to SCCG show lower strength values when tested in water or humid environments. As a diffusion controlled process this effect depends on the loading speed of the respective material. Even for rather fast loading rates a significant reduction of strength has to be taken into account when lifetime or reliability of a certain microelectronic component in harsh environments needs to be guaranteed.

Before a statistical analysis can be made, strength values of corresponding materials need to be determined. In contrast to metals, tensile tests are inconvenient in ceramics due to the difficult and expensive specimen preparation. In this context, uniaxial as well as biaxial bending methods are usually favoured. Since strength values can strongly depend on the tested volume and the underlying defect distribution, a more intrinsic property, namely fracture toughness, is sometimes more meaningful and can be utilized to correlate obtained defects and strength values. Thereby no volume effects are assumed once the specimen dimensions are sufficiently large compared to the size of the plastic zone [76]. Furthermore hardness and stiffness are of great relevance to classify the susceptibility of a material to penetration of a foreign body and elastic response to mechanical loading, respectively. Correspondingly, scratch resistance and compatibility to other materials in microelectronic systems in terms of thermo-mechanical properties are often required.

The following sections will briefly summarize the materials of interest and the conducted methods for strength, toughness and nanoindentation experiments in the framework of this thesis and related publications.

3.1. Materials and samples investigated

3.1.1 Selected crystallographic orientations of Lithium Tantalate and Lithium Niobate single crystals

Depending on the intended functionality, a special rotation of the used single crystals needs to be provided for optimizing functional properties in the respective microelectronic application. For SAW-filters two different cuts provide an excellent compromise in desired properties mentioned in Chapter 2.1.3. In this context, the c_h-axis is rotated counter clockwise (-48°) for $LiTaO_3$ and clockwise (+38°) for $LiNbO_3$ around the a_h-axis as schematically illustrated in Figure 10a and b.

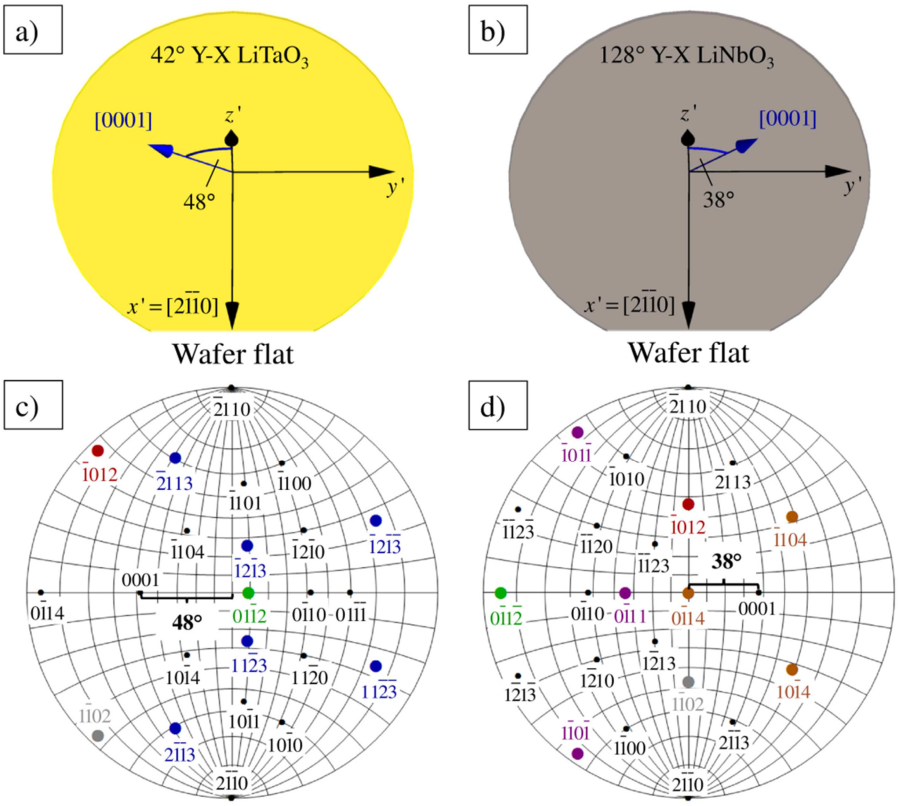

Figure 10: Schematic representation of wafer orientation for 42° Y-X-$LiTaO_3$ (a) and 128° Y-X-$LiNbO_3$ (b), respectively, together with corresponding alignment of low indexed planes in pole-figures (c, d).

In dependence on the angle between the wafer surface and the c_h-axis these cuts are referred to as 42° Y-X-$LiTaO_3$ and 128° Y-X-$LiNbO_3$, where the latter one is already known since 1976 for its extraordinarily large electromechanical coupling coefficient and relatively high wave velocity [19]. As a consequence of the respective rotations, all crystallographic planes and directions are rotated in a similar way. The corresponding alignment of low indexed planes for both cuts is available in the pole-figure in Figure 10c and d for $LiTaO_3$ and $LiNbO_3$, respectively. Planes of later importance in this thesis are highlighted with larger, coloured dots.

The investigated $LiNbO_3$ and $LiTaO_3$ single crystal samples were diced and grinded by the company EPCOS OHG, Deutschlandsberg, Austria (a TDK group company). Plate-like specimens with dimensions of $2 \times 2 \times 0.13\ mm^3$ and $12 \times 12 \times 0.35\ mm^3$ were prepared from wafers for the respective mechanical tests described in Chapters 3.2 - 3.4. It is worth pointing out that both materials had the same surface finish, i.e. a mirror-like polished surface on the one side and a roughened backside to enhance the functional properties. Due to the fabrication process residual stresses, which were not elaborated in this work, could be present at the surface and may influence the obtained mechanical results. Further information on testing procedures, specimen preparation together with a schematically representation of respective planes may be found in *Publications A-D.*

3.1.2 Ceramic based architectures with metallization: "building blocks"

The ceramic circuit board carries and electrically connects the functional components on top. In the case of fracture, the complex 3D network consisting of several metal layers and vias makes it difficult to ascribe the failure event to only one structural part. In this context, simplified LTCC samples, referred to as "building blocks", were manufactured in order to investigate the contribution of individual features to changes in strength distributions. Gained knowledge was then applied to a more complex realistic ZnO multilayer substrate, where it was demonstrated how a small change in design could almost double the mechanical strength (see details in *Publication E*).

The corresponding designs tested in this work are exemplarily shown in Figure 11. LTCC with empty via (Ø ~ 100 µm) (a, b), LTCC with filled via (Ø ~ 80 µm) (c, d), LTCC with metal electrode (~ 500 × 500 µm) underneath the surface (e, f), LTCC with a filled via (Ø ~ 80 µm) and an electrode (~ 500 × 500 µm) underneath (g, h), LTCC with a trough top-metal layer (thickness: ~ 25 µm) (i) and LTCC with a through top-glass layer (thickness: ~15 µm) (j) were therefore chosen. Length, width and thickness of specimens are 25 mm, 2 mm and ~0.4 mm, respectively. Outer and inner span of the four-point-bending (4PB, described in Chapter 3.2.2) testing jig are 20 mm and 10 mm, respectively.

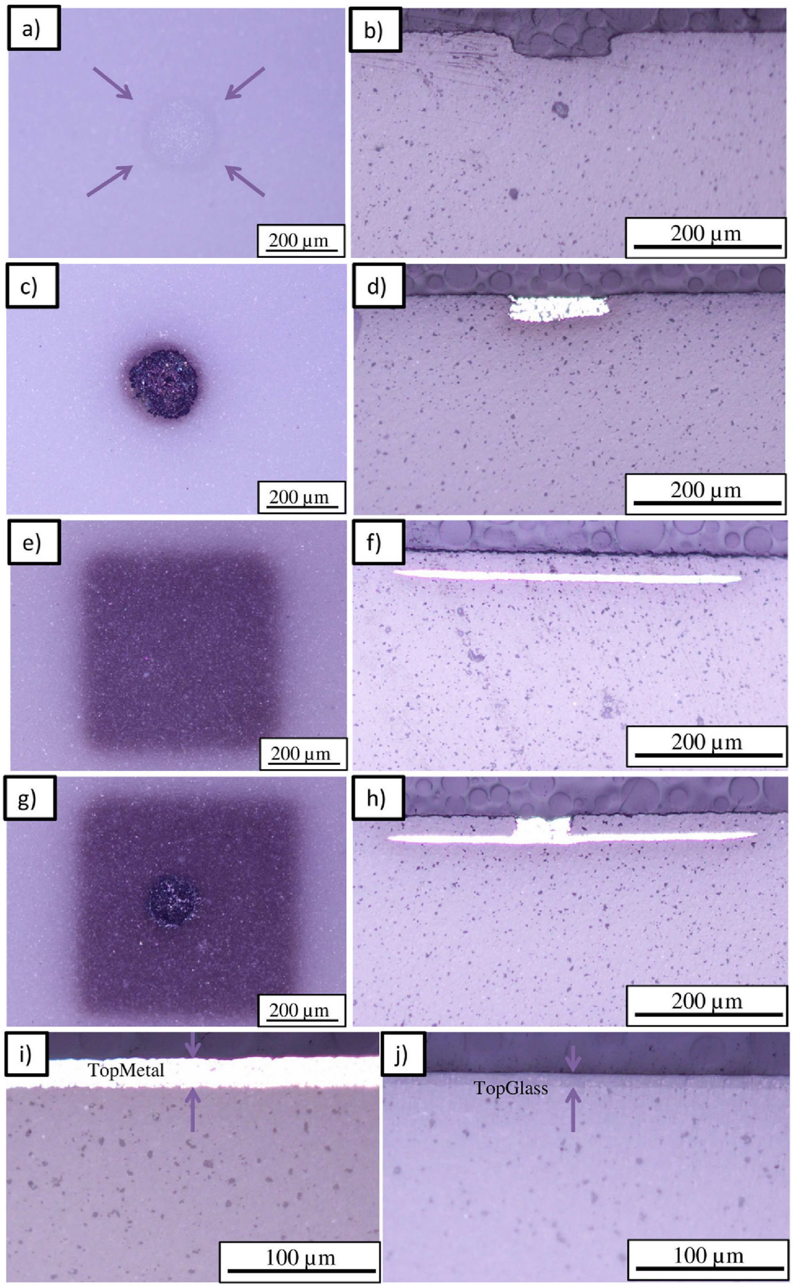

Figure 11: LTCC building blocks with empty via (Ø ~ 100 µm) (a, b), LTCC with filled via (Ø ~ 80 µm) (c, d), LTCC with metal electrode (~ 500 × 500 µm) underneath the surface (e, f), LTCC with a filled via (Ø ~ 80 µm) and an electrode (~ 500 × 500 µm) underneath (g, h), LTCC with a through top-metal layer (thickness: ~ 25 µm) (i) and LTCC with a through top-glass layer (thickness: ~15 µm) (j).

To increase the level of complexity, a real but still rather simple multilayer component consisting of inner electrodes, vias, glass layers and top metal layers was mechanically tested under three-point-bending (3PB, see Chapter 3.2.2). Two slightly different configurations, referred to as Configuration 1 (Conf.1) and Configuration 2 (Conf.2), were manufactured and are shown in Figure 12. The main difference between the two configurations is the ratio of the top electrodes

(Compare M1/M2 in Figure 12c and d). Up to the final components several process steps are applied and shown in detail in *Publication E.*

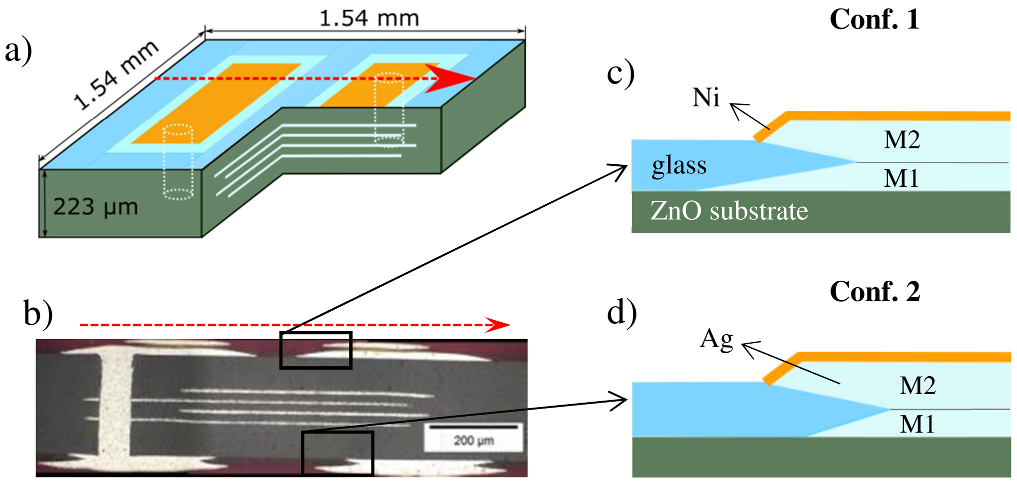

Figure 12: (a) 3D schematic of a real multilayer component with (b) corresponding cross-section showing its top and bottom architecture magnified in (c) for metallization configuration 1 (Conf. 1), and (d) metallization configuration 2 (Conf. 2). The only difference lies in the size ratio of the top electrodes M1 and M2.

3.2. Strength measurements

3.2.1 Biaxial bending: Ball-on-three-balls (B3B) testing

Biaxial strength testing methods are suitable for circular or rectangular brittle specimens of sufficient thickness to guarantee ideal elastic behaviour. They can be supported by a ring or balls and loaded through a smaller ring or punch on the opposite side, leading to a biaxial stress field. In this context, the ring-on-ring as well as punch-on-three-balls test are standardized [77, 78]. Another method, namely the ball-on-three-balls (B3B) has proven to be an excellent test for strength evaluation of brittle materials, as for instance used in microelectronic applications [54, 79-81]. This method holds high testing accuracy and can be utilized in different environments [82], The circular or rectangular specimen is thereby supported by three balls on one side and axially loaded through a fourth ball in the centre of the opposite side as schematically shown in Figure 13. This delivers a well-defined biaxial stress field comparable to the loading scenario in real components, where stress field maxima usually occur in small areas or volumes (e.g. at edges of electrodes or in the vicinity of solder balls). The corresponding fracture stress σ_c is calculated by:

$$\sigma_c = f \cdot \frac{P_{\max}}{t^2}$$ **Equation (4)**

with P_{max} being the maximum load, t the specimens thickness and f a dimensionless factor depending on the geometry of testing set-up and specimen together with the Poisson’s ratio of the tested material. Since no analytical solutions are available, FEA has to be performed for receiving accurate values for *f* [79-81]. Details on respective dimensions and testing conditions may be obtained from *Publications A* and *B*.

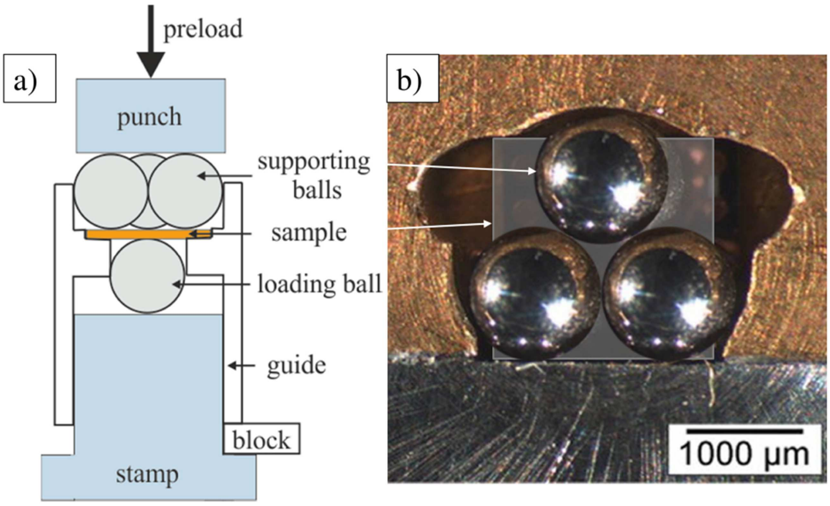

Figure 13: (a) Schematic side view and (b) top view of the B3B testing configuration. The specimen is thereby supported by three balls on one side and loaded through a fourth ball from the centre of the opposite side.

3.2.2 *Uniaxial bending: three- and four point bending (3PB and 4PB)*

For strength evaluation of brittle materials also uniaxial strength measurements can be performed by either three-point-bending (3PB) or four-point-bending (4PB) experiments, where the latter one is usually favoured due to the larger sampled effective volume and therefore schematically shown in Figure 14.

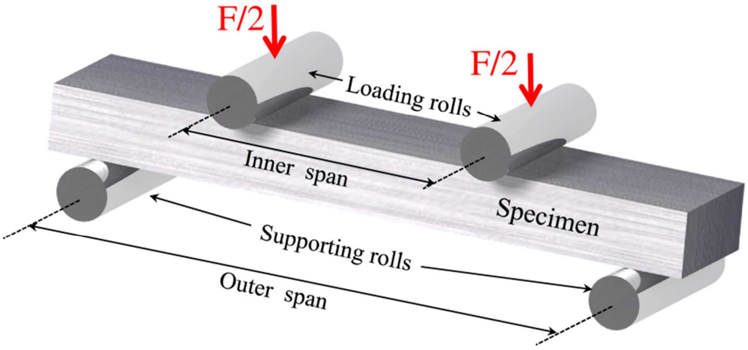

Figure 14: Schematic representation of a 4PB test set-up.

The applied uniaxial stresses for both methods are inhomogeneous, with the highest tensile stresses responsible for failure acting on the specimen's surface. The failure stress σ_{max} can be calculated by dividing the maximum bending moment by the modulus of resistance. By introducing the corresponding geometrical conditions the following equations are received:

$$\sigma_{\max,3PB} = \frac{3P_{\max}L}{2bt^2}$$ **Equation (5)** $$\sigma_{\max,4PB} = \frac{3P_{\max}(L-l)}{2bt^2}$$ **Equation 6**

with P_{max} being the maximum load, b and t the specimen's width and thickness, L and l the outer and inner span between the supporting and loading rolls (see Figure 14). According dimensions and requirements for testing jigs are standardized [83, 84]. For materials in microelectronic applications not all possible uncertainties (listed in [85]) are expected to arise due to the required precise manufacturing of corresponding components. Also regarding specimen dimensions usually smaller geometries than the standardized ones are used since strength measurements should be performed at the desired length scale of a real component. Even though smaller specimen geometries are possible, larger systematic uncertainties are to be expected [85-87].

3.3. Toughness measurements

By introducing an artificial defect (notch) into a specimen and loading it to failure, toughness values can be estimated by transforming Equation (2). Several uniaxial as well as biaxial testing techniques such as Single Edge V-Notched Beam (SEVNB) [88], Chevron Notched Beam (CNB) [89] or Ball-on-three-Balls with indentation crack (B3B-K_{Ic}) method [90] have thereby been developed and found to deliver reasonable values for different materials and environments [56]. Due to small available specimen geometries in this work and usually complex alignment of cleavage planes for the tested single crystalline materials, the specified testing geometries could not be realised. For similar problems, several small scale toughness experiments of specimens prepared through Focused-Ion-Beam (FIB) milling have thereby been developed and are summarized in [91]. These methods are usually restricted to brittle materials since the plastic zone size can become relatively large compared to the specimen dimensions which would lead to higher toughness values compared to macroscopic experiments. In this context, certain minimum values for the specimen dimensions need to be ensured [76]. Due to the high yield strength and low toughness this condition could easily be fulfilled for $LiTaO_3$ and $LiNbO_3$ specimens in the µm-regime (see *Publication C*), where similar preparation techniques and dimensions compared to references [92, 93] where applied. Nevertheless, damage through FIB milling [94] and relatively large notch radii may compromise the obtained toughness values. Therefore atomistic modelling using a Density Functional Theory (DFT) approach was conducted where all additional possibilities of absorbing fracture energies are neglected and thus theoretical minimum toughness values for the corresponding materials could be obtained. Work of separation, W_{sep}, was calculated as follows:

$$W_{sep} = (U_{slab} - U_{bulk}) / A$$ **Equation (7)**

where U_{slab} is the total energy of a supercell containing a slab of $LiNbO_3$ or $LiTaO_3$ and a thick layer of vacuum, U_{bulk} is the total energy of the bulk, and A is the area of the cleavage plane. Corresponding computational details may be obtained from *Publication C*.

3.4. Nanoindentation based hardness, stiffness and scratch tests

Since the strength of brittle materials and especially single crystals is often determined by surface defects, the resistance of the respective materials against penetration of harder bodies and corresponding irreversible deformation can provide a deeper understanding of the fracture behaviour. In this context, the materials hardness adequately samples its sensitivity against surface damages, which can occur during grinding, polishing and assembly procedures. By following the procedure suggested by Oliver & Pharr [95], instrumented nanoindentation can thereby not only deliver hardness of the corresponding material but also its elastic response, which can be of importance for simulation approaches. The used Berkovich tip is expected to cause deformation in preferred crystallographic directions due to the applied anisotropic stress field. However, this may not adequately sample the onset of plastic deformation which was of interest to gain a deeper insight into deformation mechanisms of the corresponding single crystalline materials.

Therefore, spherical nanoindentation is the better choice to investigate the impact of crystallographic orientation or testing speed on the deformation behaviour [96, 97]. It may also replicate possible contact damage scenarios that could occur during pick-and-place of a final device, where high stresses are expected due to the small contact area between single crystal and used needle. Thereby, gradual as well as abrupt losses in strength are documented for multigrain ceramics, depending on the actual deformation mechanisms (quasi plastic deformation or cone cracking, respectively) [98-101]. The influences on $LiTaO_3$ and $LiNbO_3$ single crystals were examined in the framework of this thesis and are further explained in Chapter 4.1.3 and *Publication D*, which also contains all experimental details.

The low toughness of single crystals with rather broad defect size distributions are expected to often yield large scatter and corresponding low Weibull moduli for strength values. In this context, another possible application of the nanoindenter was used in order to apply artificial surface scratches under well-defined and reproducible conditions for the respective single crystalline materials. The orientation dependent effects of those scratches on the biaxial strength and scatter of data are discussed in Chapter 4.1.1 and *Publication B.*

3.5. Fractographic analyses

Fractography is an indispensable tool for understanding fracture in brittle materials. By finding the fracture origin and its size a direct correlation between failure stress and fracture toughness can be drawn according to Equation (2). In the present thesis it was further used to identify cleavage planes in single crystals, assess the influence of different surface conditions and evaluate different crack paths in multilayer components. Throughout all publications related to this work, extensive investigations on fractured or pre-loaded specimens were carried out using optical, stereo-optical, Scanning Electron Microscope (SEM) and FIB techniques to substantiate observations from strength, toughness and nanoindentation experiments. In this context, the work of Roger Morrell [102] and George Quinn [103] can be recommended as an excellent guideline for required pattern recognition and understanding of fundamental relationships.

4. Extended summary of publications

A brief overview of mechanically tested single crystalline as well as multilayer ceramic materials for the application as SAW-filter devices together with corresponding results obtained in the framework of this thesis will be given in the next chapters. Suggestions on how to improve mechanical reliability will be discussed. Nevertheless, it should be mentioned that functionality of the investigated functional materials determines their applicability and consequently possible improvements need to be considered carefully.

4.1. Characterization of single crystals for filter applications

4.1.1 Biaxial strength and anisotropic fracture behaviour

B3B strength measurements on mirror-polished 2 × 2 × 0.13 mm³ specimens at three different testing speeds in air and water revealed no (significant) susceptibility of both materials to SCCG. Thus data pooling of corresponding strength values could be performed and all 240 data points per materials are shown in the Weibull plot in Figure 15. A large scatter, similar to other brittle single crystalline materials [54, 63], can be noticed. Further, large deviations from Weibull behaviour are observable for the $LiNbO_3$ material. In this context, strength results of larger (12 × 12 × 0.35 mm³) samples are also shown in Figure 15 and reveal a missing effect regarding different effective volumes/surfaces on the strength substantiating the lacking Weibull character of the corresponding materials. Nevertheless, it can be concluded that with an overall characteristic strength of ~1800 MPa $LiTaO_3$ is around 2.5 times stronger than $LiNbO_3$. This large difference in strength is rather unexpected as both materials exhibit the same crystal structure [32-35] and Ta as well as Nb belong to the same group of the periodic table, implying similar chemical properties. According to Equation (2), differences in strength between two brittle materials would originate in either different toughness or critical defect sizes. For single crystals the toughness can thereby strongly depend on the respective crystallographic plane and even on the crack propagation direction [104-107]. To qualitatively sample the anisotropic fracture behaviour of the differently oriented single crystalline materials, fractographic analyses were performed.

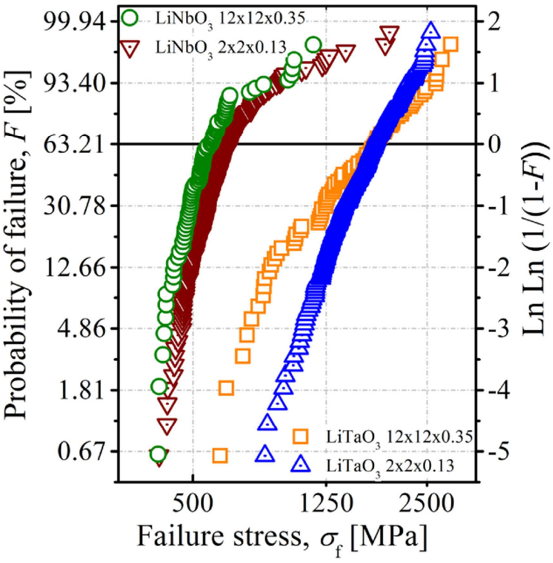

Figure 15: Weibull plot of LiNbO$_3$ and LiTaO$_3$ samples with different specimen sizes of (2 × 2 × 0.133 mm³ and 12 × 12 × 0.35 mm³).

Figure 16 provides representative post mortem top-views on biaxially tested specimens. Independent of the specimen size, similar fracture patterns are observable. By calculating inclination angles of planes with respect to surface and edges, cracks can be ascribed to specific crystallographic planes. Especially planes aligned almost perpendicular to the surface are exposed to the highest tensile normal stresses responsible for failure of the corresponding atomic bonds. In this context, for both materials cracks along the steepest $\{01\bar{1}2\}$ planes to the surface could be obtained in specimens failing at low fracture forces. Accordingly, they are suspected to be the most critical ones for both materials, being in good agreement with literature [34, 42, 48]. As fracture forces are increasing, further planes, e.g. $\{1\bar{2}13\}$ for LiTaO$_3$ and $\{10\bar{1}1\}$ for LiNbO$_3$ (see Figure 16), are activated due to the release of more elastically stored energy [108]. In some cases also cracks along the $(2\bar{1}\bar{1}0)$ plane, being perpendicular to the surface, could be discerned.

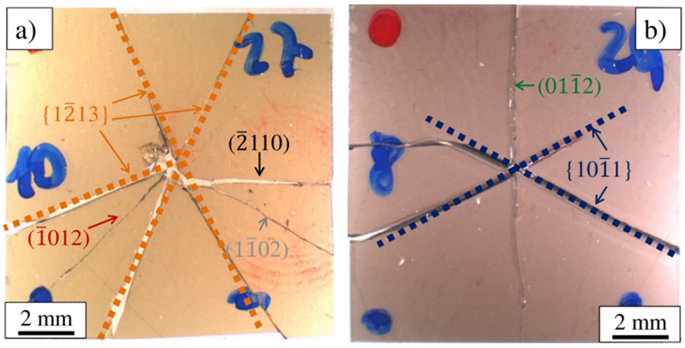

Figure 16: Observed cracks on B3B 12 × 12 mm2 tested specimens from (a) LiTaO$_3$ and (b) LiNbO$_3$ samples. Additionally to the typical $\{01\bar{1}2\}$ cleavage planes, further planes could be identified and indexed as $\{1\bar{2}13\}$ for LiTaO$_3$ and $\{10\bar{1}1\}$ for LiNbO$_3$ (see dashed lines).

To reveal the origin of fracture, further examinations on fracture surfaces were employed. Figure 17 provides the fracture surface of a $LiNbO_3$ specimen which has failed under low applied stress. A pronounced surface scratch with a depth of ~1-2 µm (marked with white arrows) parallel to the most critical $\{01\bar{1}2\}$ plane is observable in the centre of the specimen, where the highest loads are applied during B3B testing. The smooth fracture surface, where only small cleavage steps are observable (highlighted with black arrows), indicate a low fracture energy of the corresponding crystallographic plane. Altogether it can be concluded that low fracture loads are to be expected when defects are aligned parallel to highly loaded planes of low fracture energies which comparable to other brittle single crystalline materials [93].

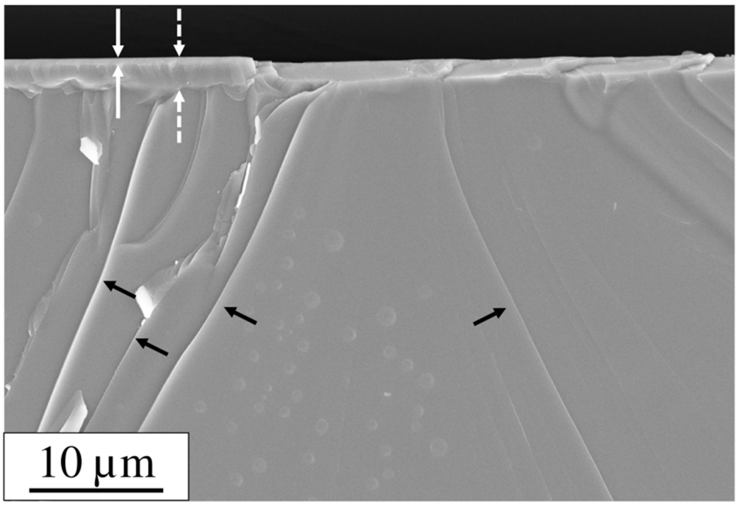

Figure 17: Fracture surface of a $LiNbO_3$ specimen that has failed at a low fracture force

To identify the influence of surface defect orientation on the strength, well-defined artificial scratches were introduced onto mirror-polished surfaces of both single crystalline materials by a nanoindentation scratch method. Figure 18a-d shows thereby artificial scratches in $LiTaO_3$ and $LiNbO_3$ in the centre of the respective specimens introduced by a Berkovich indenter tip, for which alignment and scratch direction are schematically shown. Additionally to the scratches also cracks and pitting can be discerned for selected orientations. Details on experimental procedure and sub-surface damages can be found in *Publication B*. The corresponding strength distributions, obtained utilizing the B3B method, are available in Figure 18. For both materials a similar characteristic strength of ~280 MPa is obtained for specimens with a scratch parallel to the most critical cleavage plane. Scratches oriented along a tough direction lead to significantly higher strength values for both materials: 87% and 55% increase in strength are thereby discerned for $LiTaO_3$ and $LiNbO_3$, respectively. Nevertheless, the corresponding characteristic strength values of 521 MPa and 430 MPa are still significantly lower compared to the mirror polished counterparts (see Figure 15).

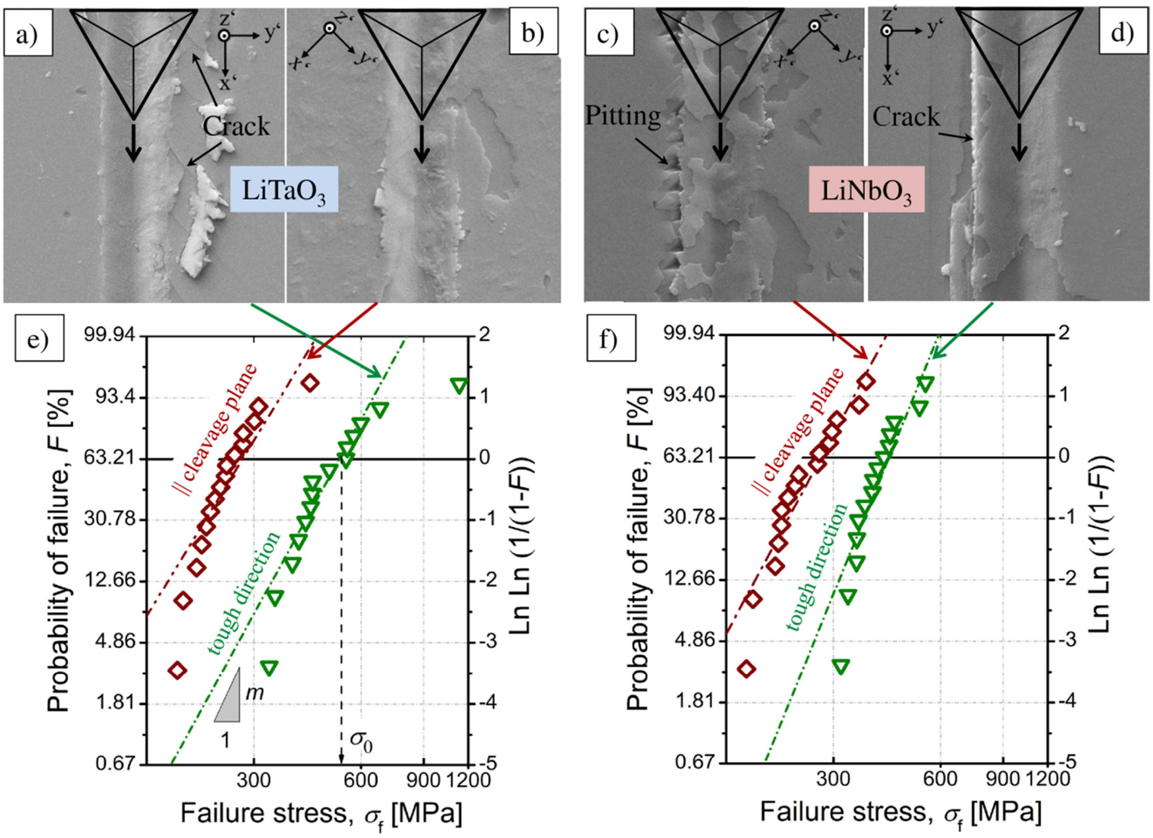

Figure 18: Top views on nano-scratched specimens of $LiTaO_3$ (a and b) and $LiNbO_3$ (c and d). Scratches are crossed to the most critical cleavage plane for a) and d) and parallel to it for (b) and (c). Corresponding strength distributions show strong orientation dependencies for both materials (e and f).

Paying attention to the distribution of strength data reveals that even for scratches introduced under well-defined and reproducible conditions, a large scatter of data is observable. Interestingly, the corresponding Weibull moduli of ~5 do not exceed documented values for mirror-polished (Figure 15), etched or ground single crystalline materials [54, 62, 63, 109]. This clearly shows that due to the combination of flaw type, orientation with respect to critical cleavage planes and depth of defects a high scatter of strength values is unpreventable for this material class.

The origins for the scratch-orientation dependent strength values can be explained by the fractographic analyses shown in Figure 17. Whenever a surface defect is orientated with a large inclination angle to the most critical cleavage plane, the crack needs to start along a tough direction (Figure 19a, c, e, and g), which requires a higher load for the same defect size. After initiation, cracks turn into planes of lower fracture toughness which consumes further energy. For scratches oriented parallel to a highly loaded plane with low fracture energy, a crack can initiate under lower stresses and directly follow the corresponding plane as shown in Figure 19b, d, f and h). Comparing the fracture surfaces of specimens with scratches parallel to the most critical cleavage plane (Figure 19f and h) with the mirror-polished ones in Figure 16, a similar pattern is observable. Thus it is expected that after mirror-polishing small surface defects are still present and responsible for fracture, especially in $LiNbO_3$. In this context, either a higher sensitivity of $LiNbO_3$ to surface scratches or significant differences in toughness could explain the large difference in strength between the two investigated materials. Since fractography of all specimens is impossible due to the large number of fracture pieces (see Figure 16), evaluation of fracture toughness was employed to reveal the origins of the observed phenomenon.

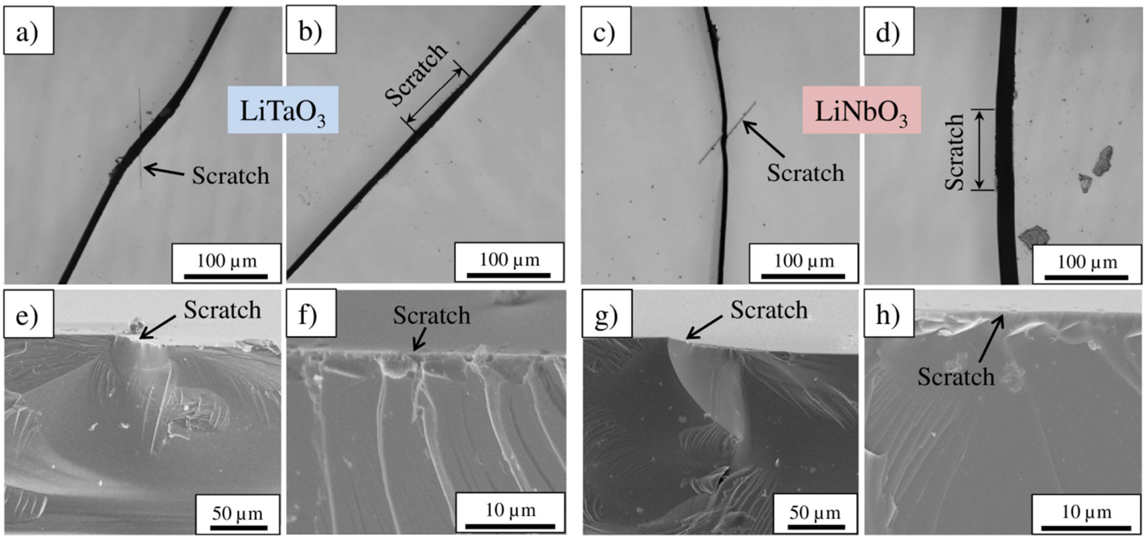

Figure 19: Top view on post-mortem specimens (a-d) together with corresponding fracture surface (e-h). Scratches are crossed to the most critical cleavage plane for (a), (c), (e), and (g), and parallel to it for (b), (d), (f) and (h).

4.1.2 Fracture toughness and origins of fracture anisotropy

Visualization of Young's modulus in Figure 8c indicates that bonding forces depend on crystallographic directions. For toughness values an even stronger direction dependence is expected for brittle single crystalline materials [103, 104]. This leads to fracture along certain cleavage planes depending on the actual loading conditions as observable in Figure 16. Since also the crack propagation direction can influence the result [105-107], a well-defined toughness testing condition needs to be ensured. In this context, the complex alignment of the weak $\{01\bar{1}2\}$ cleavage planes (Figure 10c and d) together with only small available specimens makes standard measurements insufficient [76]. However, high yield strength and expected low toughness of the corresponding materials yields small plastic zone sizes for $LiTaO_3$ and $LiNbO_3$, respectively, which allows testing of specimens the µm-regime. In this context, specimens were prepared through FIB milling and measured in-situ in an SEM, a method known to deliver adequate toughness values for comparable brittle single crystalline materials like Si, silicon oxide/nitride and even semi-brittle materials like W or NiAl [93, 110-112]. Notched beams with rectangular cross-sections, as exemplarily shown in the insert in Figure 20a, were fabricated and loaded through an indenter wedge similar to the experiments performed by Wurster et.al [92].

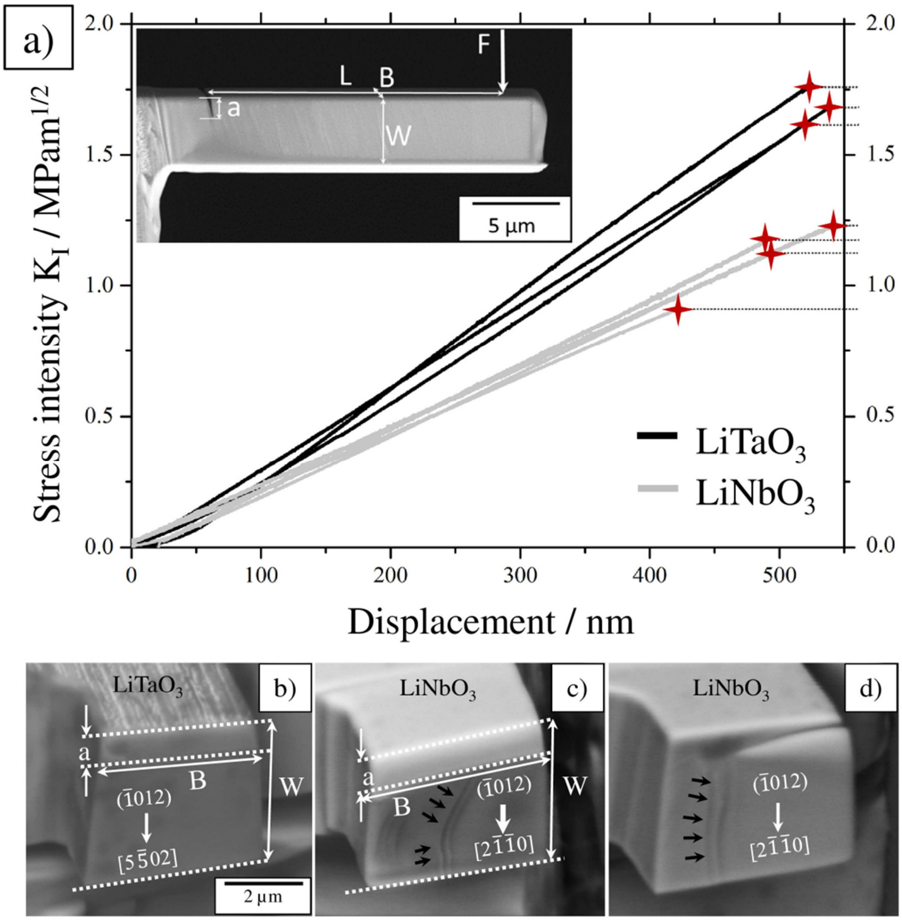

Figure 20: **(a)** Stress intensity factor K_I vs. displacement for all tested LiTaO$_3$ and LiNbO$_3$ cantilevers. The inserted side view shows a representative cantilever and provides schematically important geometrical dimensions. (b-d) Fracture surfaces of a LiTaO$_3$ (b) and two LiNbO$_3$ cantilvers (c, d). Observed cleavage steps for the latter ones are highlighted with black arrows.

Respective stress intensity versus displacement curves for all tested LiTaO$_3$ and LiNbO$_3$ specimens are also accessible in Figure 20a. Toughness values for $\{01\bar{1}2\}$ planes of 1.7 ± 0.1 MPam$^{1/2}$ for LiTaO$_3$ and 1.1 ± 0.1 MPam$^{1/2}$ for LiNbO$_3$, respectively, are obtained. These values fit into the documented ranges of comparable single crystalline materials like Sapphire [113], Quartz [114] or Si [115]. Linearity of the corresponding curves (Figure 20a) together with smooth fracture surfaces (Figure 20b-d) substantiate the brittle character of both materials. Detailed information on specimen geometry, crystallographic information and testing setup may be found in *Publication C*. Since the determination of toughness values for all low indexed planes (see Figure 10c and d) of both materials would be of extensive work, a simulation of fracture energies was performed using a DFT approach in the framework of *Publication C*. Respective values are presented in Figure 21a. A good qualitative agreement to the experiment is thereby observable since for $LiTaO_3$ as well as $LiNbO_3$ the lowest fracture energies are calculated for the $\{01\bar{1}2\}$ planes. Further, significantly higher direction dependent fracture energies could be obtained for $LiTaO_3$ compared to $LiNbO_3$, which partly explains the differences in biaxial mechanical strength (see Figure 15). DFT calculations also revealed the atomistic origins for this phenomenon: In $LiNbO_3$ a weaker and more anisotropic chemical bond between the six O atoms surrounding Nb could be discerned. The minimum electron density, indicating the respective bond strength, is thereby more than 50% lower than for $LiTaO_3$. The more rigid and isotropic TaO_6 polyhedra network for $LiTaO_3$ could thereby further explain a higher melting point and hardness [116].

Nevertheless, transformation into toughness values (see Figure 21b) using elastic constants of the corresponding materials shows that absolute values of ~0.7 $MPam^{1/2}$ for $LiTaO_3$ and ~0.4 $MPam^{1/2}$ for $LiNbO_3$, respectively, are significantly lower than their experimental counterparts. This could be explained by the testing setup (generation of sound waves, deformation of the material underneath the indenter wedge, no perfectly stiff/elastic testing jig, relatively blunt notch, etc.) on the one hand and further dissipation of fracture energy in the plastic zone (e.g. through twinning, plastic displacive deformation, piezo-elastic domain switching [117]) on the other hand.

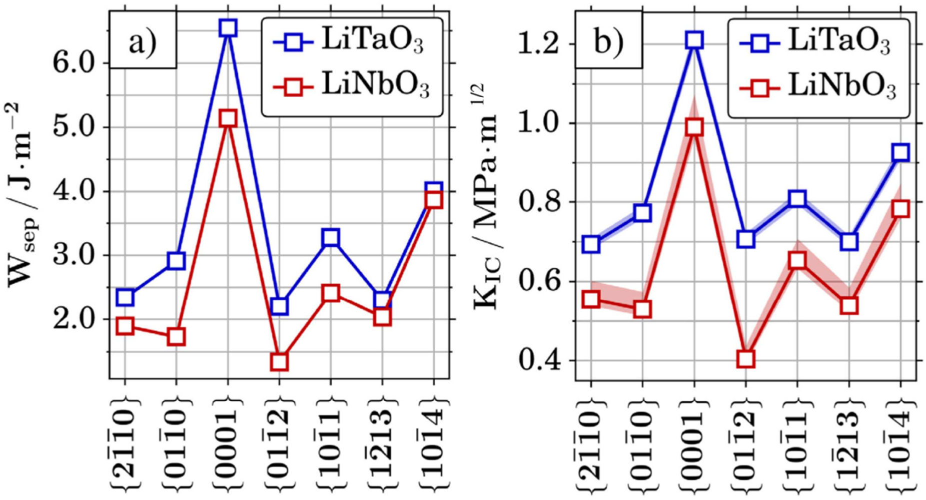

Figure 21: Calculated work of separation (a) and fracture toughness K_{IC} (b) of $LiTaO_3$ and $LiNbO_3$ for several low-indexed crystallographic planes at 0 K. The solid lines connecting the data points are drawn to guide the eye. Shaded areas indicate the uncertainties (see computational details in *Publication C*).

It can be concluded that, indeed, a difference in toughness between $LiTaO_3$ and $LiNbO_3$ by a factor of ~1.6 could be evaluated by experiments as well as DFT calculations for the most critical $\{01\bar{1}2\}$ cleavage planes. Nevertheless, to fully explain the difference in characteristic strength of ~2.5, also a higher sensitivity of $LiNbO_3$ to the initiation of surface defects is expected. This may be attributed to its rather soft (see Chapter 4.1.3) but brittle character, which would make surface conditioning very challenging. Further, not only polishing itself but also contact damage during the harsh cutting, grinding and polishing process may be responsible for surface flaws. In this context, nanoindentation techniques were employed for a better understanding of contact and surface damage in $LiTaO_3$ and $LiNbO_3$.

4.1.3 Nanoindentation experiments for unveiling the origins of surface defects

To emulate contact damage in in $LiTaO_3$ and $LiNbO_3$, nanoindentation was employed for the two respective materials. A spherical indenter tip (radius R=4.5 µm) was chosen for applying a symmetrical stress field to receive the response of the anisotropic materials concerned optimally. Corresponding load (P) versus displacement (h) curves are thereby to see in Figure 22. Up to the pop-in events (highlighted with red arrows in the inserts), where the first irreversible deformation occurs, curves indicate purely elastic Hertzian contact behaviour according to [118]:

$$P = \frac{4}{3} E^{*} h^{\frac{3}{2}} \sqrt{R}$$ **Equation (8)**

$E^*$is thereby the reduced modulus, which was calculated for isotropic materials according to [119] since only negligible deviations coming from a small anisotropy factor of 1.3 and 1.4 for $LiTaO_3$ and $LiNbO_3$ [37], respectively, are expected according to Vlassak and Nix [120, 121]. Corresponding experimental Young's moduli values are 254 GPa and 195 GPa for $LiTaO_3$ and $LiNbO_3$, respectively. Remaining required values were taken from literature [122].

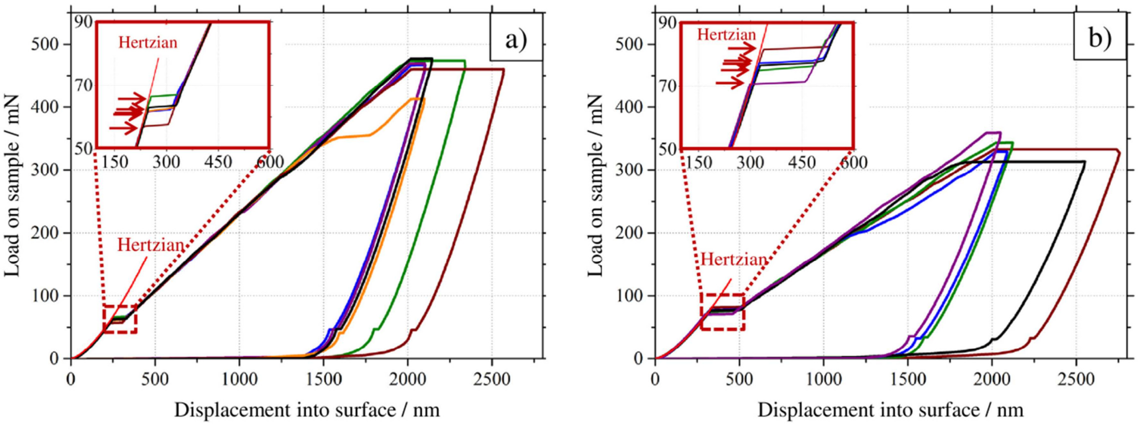

Figure 22: Load-displacement curves for spherical indents (R =4.5 µm) into a) $LiTaO_3$ and b) $LiNbO_3$. Pop-ins are clearly visible and marked with arrows in the magnified inserts.

Surface damage caused by indentation in Figure 22 is shown in Figure 23, where the first row belongs to $LiTaO_3$ and the second row to $LiNbO_3$ surfaces. Schematic representations in Figure23 c and f show that similar planes compared to the biaxial B3B strength measurements (see Figure

16) are activated. For comparative purposes, the same colour code as in the pole-figures (Figure 10c and d) is chosen. In this context, all three $\{01\bar{1}2\}$ and the four out of six $\{11\bar{2}3\}$ planes with a steeper angle to the surface were activated in $LiTaO_3$. The $(01\bar{1}2)$ plane, which is almost parallel to the surface, is thereby responsible for the observable chipping in vicinity of the indents.

For $LiNbO_3$ the most pronounced cracks are along the $(01\bar{1}2)$ plane. Also the $(\bar{1}101)$ and $(10\bar{1}1)$ plane are usually activated. These three planes are all almost perpendicular to the surface. In some specimens cracks following the $(1\bar{1}04)$ and $(10\bar{1}4)$ planes are also observable (compare Figure 23e and f). In contrast to performed biaxial measurements, cracks along these two planes, both with an angle of 64° to the surface, were only visible for the spherical nanoindentation experiments.

Nevertheless, the almost identical fracture patterns for both kinds of experiments, where significantly different stress conditions are applied, substantiate the brittleness of certain planes in both materials. This is in contrast to e.g. polycrystalline ceramics, where usually ring cracks are observable in the vicinity of a spherical indent [98, 123, 124].

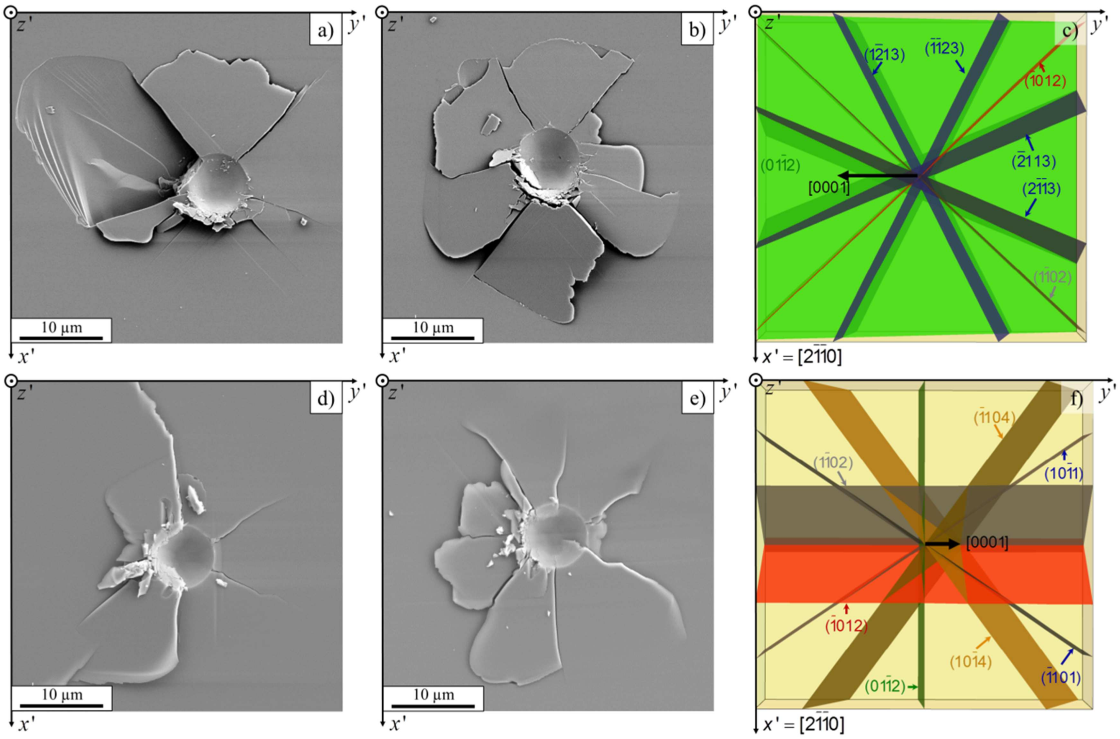

Figure 23: Representative SEM images after spherical indentation (R = 4.5 µm) with a depth of ~2 µm in $LiTaO_3$ (a,b) and $LiNbO_3$ (d,e). Schematics of frequently activated low indexed planes for $LiTaO_3$ (c) and $LiNbO_3$ (f).

To evaluate incipient (sub-) surface damage and plastic deformation, further experiments were performed to loads where the first pop-in occurs. Figure 24a shows thereby a surface after this very first irreversible deformation. Traces of plastic deformation are visible along the $\{01\bar{1}4\}$ as well as the $\{01\bar{1}2\}$ planes (compare with Figure 23f). Together with them, already the first cracks occur, following the $(01\bar{1}2)$ cleavage plane. A FIB-cut perpendicular to the surface as indicated in Figure 24a is shown in Figure 24b. It can be seen that the crack follows the $(01\bar{1}2)$ plane close to the surface and bends into other directions in greater depths. Opening of the $(01\bar{1}2)$ plane (see Figure 24a) is thereby supported by the corresponding plastic deformation along the same direction. In this regard, twinning of the $\{01\bar{1}2\}$ planes is known to be the preferred deformation mechanism for both materials [43-45], and even at elevated temperatures preferable over dislocation glide [46, 47].

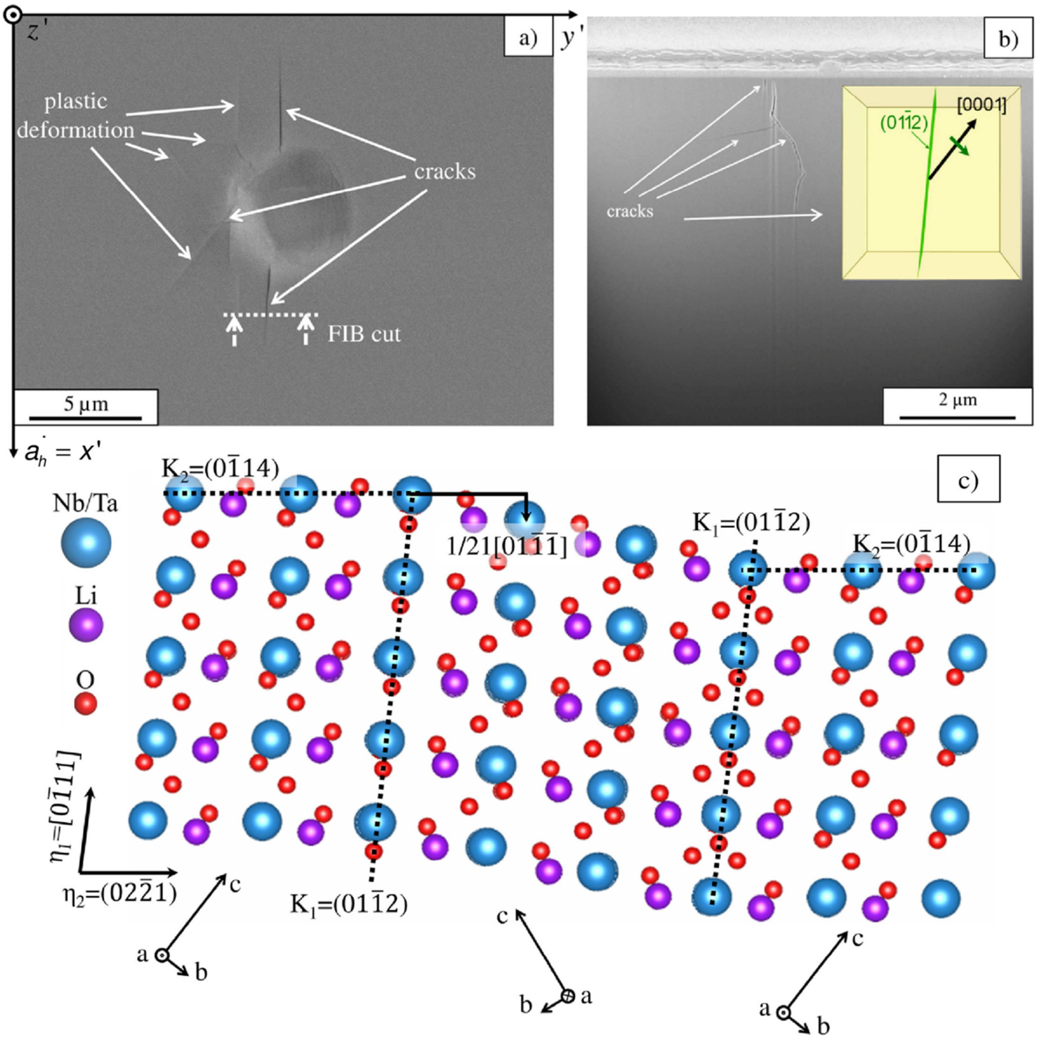

Figure 24: a) SEM image of the surface of a 128° Y-X $LiNbO_3$ specimen after spherical indentation (R = 4.5 µm) up to the first pop-in load and b) FIB cross-section according to the white, dashed line in a) with inserted alignment of the activated $(01\bar{1}2)$ cleavage plane. c) Schematic representation of a twin domain mirrored onto the $(01\bar{1}2)$ plane as observed in $LiNbO_3$ single crystals after spherical indentation.

The corresponding atom alignment for the $(01\bar{1}2)$ plane is shown in Figure 24c, with indicated details regarding the twinning system as summarized in [125]. Due to the head-to-head and tail-to-tail alignment of the polar c-axis, repulsive electrostatic forces are expected perpendicular to this plane. Together with tensile residual stresses after unloading [126, 127] this would promote activation of this weak cleavage plane (see Figure 21). This could explain why twinning of the $\{01\bar{1}2\}$ plane is documented to occur often together with cracks along the same set of planes [48]. To provide the space for the residual spherical imprint, twinning along $(\bar{1}012)$ and $(1\bar{1}02)$ need to occur for the required shortening of the lattice perpendicular to the surface, since $(01\bar{1}2)$ twins would only provide shear strains and almost no shortening in this direction. In this regard, for $LiTaO_3$ also twinning together with cracking along the $\{01\bar{1}2\}$ planes could be discerned, which is shown and described in *Publication D* more in detail.

For both materials plastic deformation occurs together with cracks at the very first deviation from the purely elastic contact. Since these defects are located along the most critical cleavage plane, a severe reduction in strength is expected after contact damage for both materials [98, 100]. To evaluate if these flaws coming from contact damage could be responsible for the large difference in strength between $LiTaO_3$ and $LiNbO_3$ (see Figure 15), a statistical analysis of pop-in stresses needs to be performed. Maximum shear-stresses, τ_{max}, responsible for plastic deformation underneath the indenter were thereby evaluated according to Hertzian contact theory [128]:

$$\tau_{\max} = 0.31 \times \left(\frac{6 P_{pop-in} E^{*2}}{\pi^3 R^2} \right)^{1/3} \qquad \textbf{Equation (9)}$$

with P_{pop-in} being the pop-in load, E* the reduced modulus according to [119] and R the indenter radius (4.5 µm). τ_{max} for 35 spherical indents in both $LiTaO_3$ and $LiNbO_3$, to guarantee statistical significance [68], are plotted in a Weibull diagram in Figure 25 together with the characteristic shear stress τ_0 and Weibull modulus m within their 90% confidence intervals. Slightly higher τ_0 and m values for $LiTaO_3$ are thereby obtainable. While the maximum τ_{max} data points are similar for both materials, $LiNbO_3$ shows some extraordinarily low values, which cause the evaluated small statistical differences. Nevertheless, with ~Young's modulus (E)/27 for $LiTaO_3$ and ~E/22 for $LiNbO_3$ both τ_0 values are close to the theoretical strength of ~E/8 - E/15 [108].

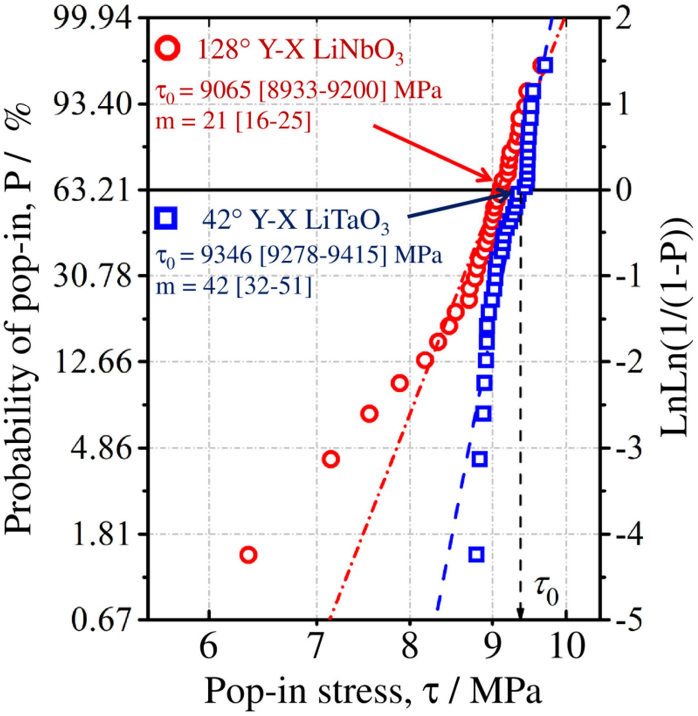

Figure 25: Weibull diagram showing the probability of pop-in event versus the measured (pop-in) shear stresses for spherical indents (R = 4.5 µm) in LiTaO$_3$ and LiNbO$_3$. Corresponding τ_0 and *m* values are inserted.

Nevertheless, the averaged bearable loads for the same indenter geometry are higher for LiNbO$_3$ (79 ± 16 mN versus 57 ± 5 mN) which can be seen in Figure 22. This can be explained by its lower Young's modulus and corresponding *E** value. Since also the observable damage after a pop-in event is more severe in LiTaO$_3$ (see *Publication D*) and occurs at lower loads, contact damage may be excluded as origin of pre-existing flaws causing the large differences in strength between the two investigated materials (see Figure 15). In this context, again surface scratches may be suspected to cause this phenomenon, which cannot sufficiently be explained by the evaluated differences in toughness (see Chapter 21). Therefore, Berkovich nanoindentation tests were performed to gain accurate hardness values, a property defining the resistance of a material against penetration of a harder body, which may therefore also indicate the scratch resistance. Hardness values of 9.7 ± 0.1 GPa and 6.6 ± 0.2 GPa were measured for LiTaO$_3$ and LiNbO$_3$, respectively, substantiating the assumption that the latter is more sensitive to surface scratches. Since hardness also depends on the crystal orientation [129, 130], a harder surface may prevent the material from those scratches which could cause an increase in strength.

4.1.4 *Tailoring of wafer orientation for enhanced mechanical properties in $LiNbO_3$*

Up to this point the 128° Y-X $LiNbO_3$ orientation shown in Figure 10b was investigated. Thereby the $(0\bar{1}14)$ plane is parallel to the surface (Figure 10d), which is known to be relatively soft according to the work of Bhagavat and Kao [130]. In this context, Figure 8c shows that the strongest atomic bonds are aligned along the c_h-axis, perpendicular to the (0001) plane. Rotating these strong bonds into the surface plane was expected to impede fracture of atom layers and therefore increase hardness and scratch resistance. The corresponding wafer orientation of 0° Y-X $LiNbO_3$ is shown Figure 26a together with alignment of low-indexed planes schematically illustrated in the pole figure (Figure 26b). It can be seen that for this orientation the $(01\bar{1}0)$ plane becomes parallel to the surface.

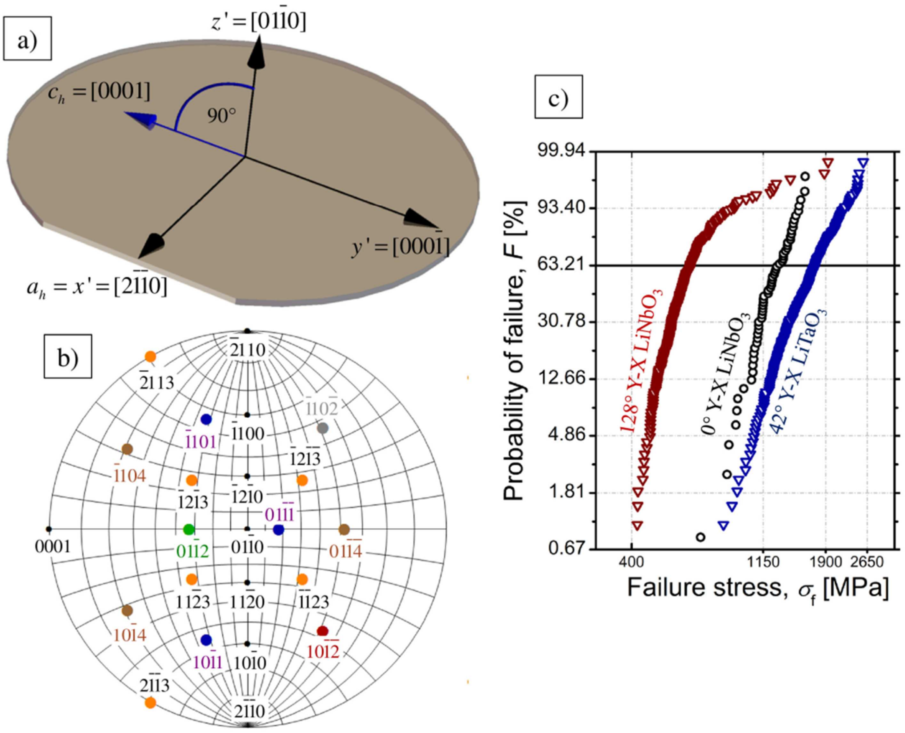

Figure 26: (a) Schematic representation of the relationship between crystallographic directions and wafer for the 0° Y-X $LiNbO_3$ orientation, (b) corresponding pole-figure and (c) Weibull diagram showing failure stresses of 0° Y-X $LiNbO_3$ together with similar 2 × 2 × 0.13 mm³ samples from Figure 15.

Nanoindentation tests with a Berkovich tip under similar conditions as described in the last chapter revealed indeed an increase in hardness of ~20%, from 6.6 ± 0.2 GPa to 8.0 ±0.3 GPa. Corresponding B3B strength measurements on similarly mirror-polished samples (all with dimensions of 2 × 2 × 0.13 mm³) are shown in Figure 26c for both $LiNbO_3$ orientations together with values for the $LiTaO_3$ specimens as shown in Chapter 4.1.1. For $LiNbO_3$ the characteristic strength almost doubled up from 694 [671 – 718] MPa to 1314 [1272 – 1357] MPa for the harder 0° Y-X $LiNbO_3$ orientation. Further, no strong deviations from Weibullian behaviour could be discerned with data points lying acceptable on a straight line with a slope of m ~ 7. Nevertheless, the strength is still below the $LiTaO_3$ material. This is not unexpected due to the higher toughness for the latter, leading to higher strength values for similar defect sizes according to Equation (2). Assuming same defect sizes would nevertheless lead to a larger difference between 0° Y-X $LiNbO_3$ and $LiTaO_3$. In this context, investigating the pole-figure in Figure 26b reveals that the most critical $\{01\bar{1}2\}$ cleavage planes of the latter have a shallower angle to the surface of 65° compared to 87° for $LiTaO_3$. Thus, the tensile stresses acting perpendicular to these planes, responsible for fracture, are smaller which would further increase the measured biaxial strength. Overall it could be proved that surface defects caused by the relatively soft surface of 128° Y-X $LiNbO_3$ are responsible for the obtained low biaxial strength values. Accordingly, it can be concluded that all kind of defects are to be avoided for advantageous mechanical properties. In this context, a well mirror-polished surface without scratches, contact damage induced cracks or plastic deformation is favourable. However, for selected applications, a certain surface conditioning/roughening is required in order to meet demanded functional properties (see Chapter 2.1.3).

4.1.5 *Tailoring of surface roughness orientation*

Up to now it could be shown that in order to receive high strength values any kind of defect should be avoided. Whenever a rough surface roughness is required (see Chapter 2.1.3), knowledge of the alignment of critical cleavage planes in respect to the defect orientation may be used in order to tailor the orientation of surface damages. In this context, different orientations of grinding grooves were tested and are schematically shown in Figure 27, where the first row belongs to $LiTaO_3$ and the second to $LiNbO_3$. The average roughness is thereby 38 ± 2 nm and 49 ± 2 nm for $LiTaO_3$ and $LiNbO_3$, respectively. Maxima and minima do not differ by more than 200 nm for both materials, independent on the grinding groove (GG) orientation.

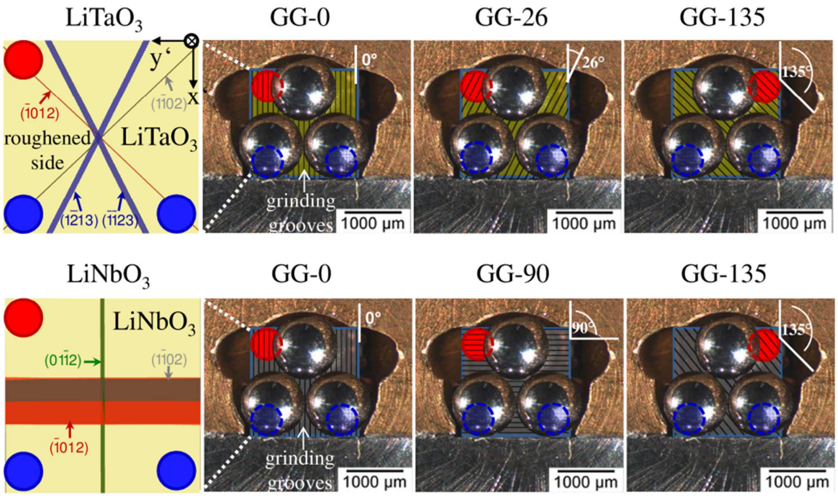

Figure 27: Alignment of critical cleavage planes and orientation of surface features introduced by grinding for $LiTaO_3$ (first row) and $LiNbO_3$ (second row). Coloured dots indicate the testing configuration of the respective samples.

Strength results for the respective testing configuration are provided in Figure 28 together with their mirror polished counterparts for the same testing conditions.

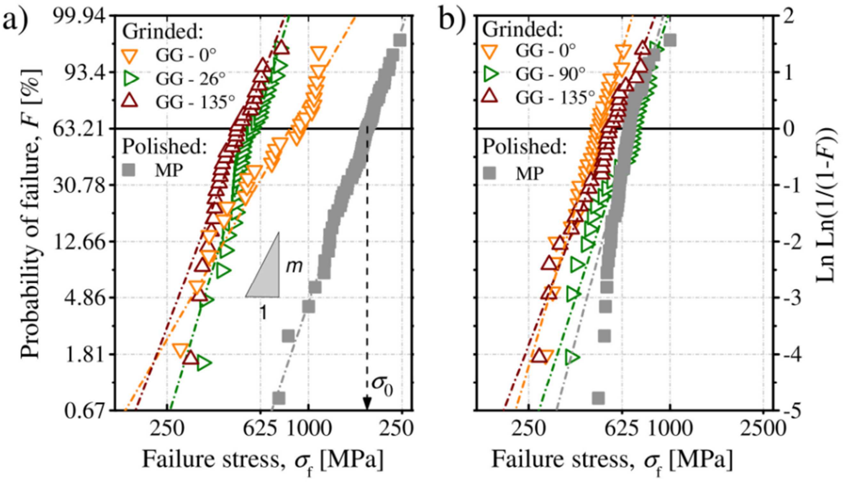

Figure 28: Strength results of ground samples with different orientations of grinding grooves (GG) together with mirror-polished data from Figure 15: Weibull plot of $LiTaO_3$ and $LiNbO_3$ samples with different specimen sizes of (2 × 2 × 0.133 mm³ and 12 × 12 × 0.35 mm³) for (a) $LiTaO_3$ and (b) $LiNbO_3$, respectively.

Corresponding σ_0 and m values within their 90% confidence intervals are also provided in Table 1. Similar conclusions compared to the scratch tests in Chapter 4.1.1 can be drawn: Whenever the grinding grooves are parallel to a cleavage plane with a steep angle to the surface, relatively low strength values are measured. In this context, similar effects were already documented for single crystalline Si [109, 131, 132]. This phenomenon can again be explained by the different crack initiation and propagation. Whenever grinding grooves are oriented parallel to a plane with a steep angle to the surface and low fracture energy, cracks initiate from the surface scratch under low stresses according to Equation (2) and directly follow the corresponding plane as illustrated in Figure 19b, c, f and g.

Table 1: Characteristic strength σ_0 and Weibull modulus m within their 90% confidence interval in square brackets for testing configurations shown in Figure 27.

$LiTaO_3$	**Grinding grooves 0°**	**Grinding grooves 26°**	**Grinding grooves 135°**	**Mirror polished**
σ_0 [MPa]	835 [740-943]	593 [561-626]	523 [487-561]	1789 [1714-1867]
m	3.1 [2.2-3.8]	6.0 [4.5-7.2]	4.8 [3.6-5.8]	4.9 [4.5-5.4]
$LiNbO_3$	**Grinding grooves 0°**	**Grinding grooves 90°**	**Grinding grooves 135°**	**Mirror polished**
σ_0 [MPa]	499 [472-529]	685 [644-729]	566 [526-609]	694 [671-718]
m	6.1 [4.5-7.5]	5.5 [4.1-6.7]	4.7 [3.5-5.7]	6.7 [5.5-7.7]

Similar fracture patterns compared to Figure 16 could be obtained for ground specimens and may be considered in *Publication B*. It should be noted that orientation dependencies of strength values with respect to grinding grooves can also originate in differently severe damages along diverging crystallographic directions as shown in [132], a behaviour which could not be evidenced for the $LiTaO_3$ and $LiNbO_3$ specimens.

Comparison of Figure 28a and b reveals that while roughened $LiTaO_3$ specimens show a significantly reduced strength compared to their mirror-polished counterparts, almost no difference is observable for $LiNbO_3$, where only few specimens with extraordinarily high strength values could be documented. According to Equation (2) this can only be explained by similar defect size distributions for ground as well as mirror-polished specimens, since the direction dependent toughness values are the same for all $LiNbO_3$ samples. This supports the assumption that $LiNbO_3$ is more sensitive to surface defects than $LiTaO_3$, since even mirror-polished specimens contain unfavourable scratches. Altogether, a deep insight into the anisotropic mechanical properties of $LiTaO_3$ and $LiNbO_3$ single crystals together with possibilities for improvements was given over the previous chapters and in *Publications A - D.* Nevertheless, failure due to mechanical loading does not only affect the single crystalline parts of a SAW-filter but also the ceramic circuit board, which will be in the focus of the next chapters.

4.2. Characterization of ceramic based substrates for circuit boards

4.2.1 Strength and fracture behaviour of LTCC building blocks

Weibull plots of the designs shown in Figure 11 together with bulk specimens are displayed in Figure 29a and b for tests performed in air and in water, respectively. The corresponding Weibull parameters σ_0 and m are summarized in Table 2 together with their 90% confidence intervals in square brackets. It can be seen that the strength values of building blocks with internal features (vias, metallization) show significantly lower strength values together with lower scatter of strength values compared to bulk specimens. Specimens with a top layer (e.g. glass/metal) withstand higher loads compared to the bulk material. These observations apply for testing in air as well as testing in water. However, it can be observed that testing in water reduces the strength, which can be ascribed to SCCG [49, 73, 74]. Nevertheless, different designs seem to react differently to the presence of water. While for bulk specimens a reduction in strength of 19% was observed, the specimens with vias failed at stress values lower by 26%. Specimens with vias and internal electrode, inner electrode only as well as those with a top layer revealed similar strength losses compared to the bulk material. All in all a significant trend to lower strength values for testing in water can be observed for all configurations, where specimens which only contain vias were more sensitive to humid environment.

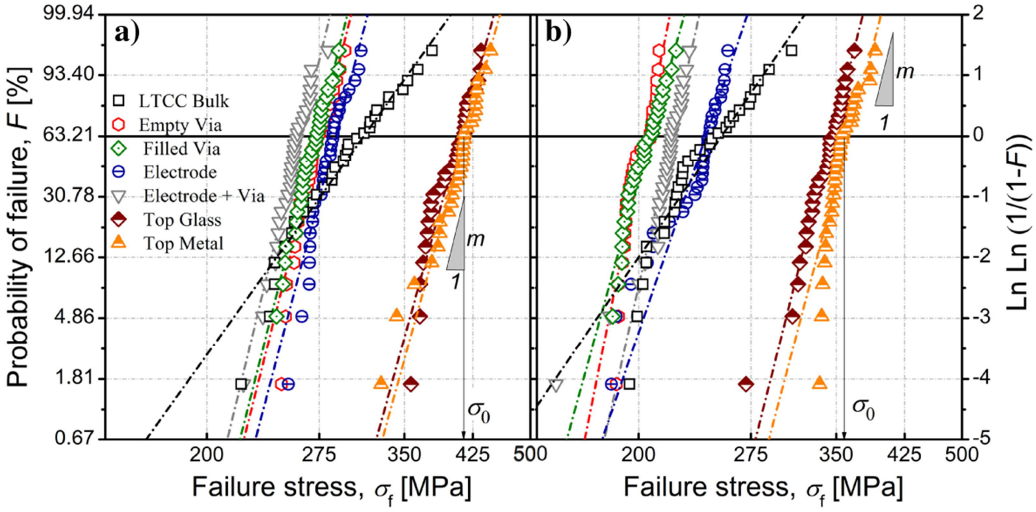

Figure 29: Weibull diagrams representing strength distribution of tested designs (a) in air and (b) in water

Table 2: Characteristic strength σ_0 and Weibull modulus m within their 90% confidence intervals for tested designs in water an air.

	Testing in **air** at a crosshead displacement speed of 5 mm/min						
	LTCC Bulk	Empty via	Filled via	Electrode	Electrode + via	Top glass	Top metal
σ_0 [MPa]	**312** [300-326]	**276** [273-281]	**273** [269-277]	**288** [284-293]	**261** [257-264]	**410** [403-417]	**417** [410-424]
m	**8.1** [6.1-9.9]	**23** [17-28]	**23** [17-27]	**22** [16-27]	**24** [18-29]	**21** [15-25]	**21** [16-25]
	Testing in **water** at a crosshead displacement speed of 5 mm/min						
σ_0 [MPa]	**253** [243-263]	**204** [202-207]	**207** [268-275]	**242** [237-247]	**220** [217-223]	**346** [341-352]	**363** [357-368]
m	**8.5** [6.3-10.4]	**29** [22-35]	**21** [16-26]	**17** [13-21]	**26** [19-32]	23 [17-28]	**22** [17-27]

For all investigated designs it could be shown that the origin of fracture for most specimens is located at the implemented features. This introduction of a relatively large artificial defect can thereby explain the significant reduction of strength compared to the LTCC bulk material. Also the lower scatter and thus higher *m* can be explained by acting of the vias/electrodes as defects, which all have similar sizes. In this context, typical fracture behaviour of building blocks is exemplarily shown in Figure 30 on the example of a specimen with an inner electrode and via (Figure 11g, h), which failed along the electrodes edge. Fractography of further designs revealed preferred fracture along the introduced features. It can be concluded that while bulk specimens with small defects in the whole stressed volume reach high strength values, the specimens with features fail at the introduced artificial defects at lower strengths even though the surrounding LTCC bulk may contain only small defects.

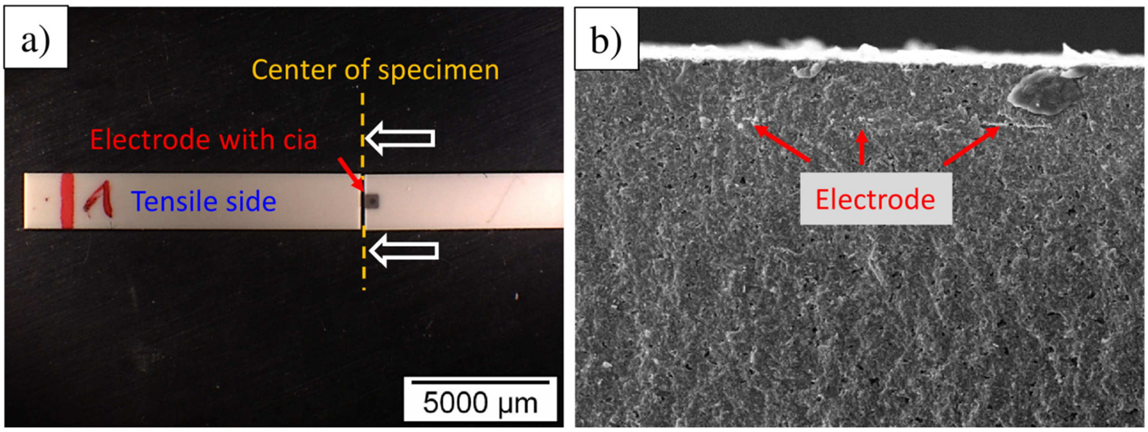

Figure 30: Fractographic analyses of a LTCC building block specimen with inner electrode and via.

4.2.2 *Strength of a real multilayer component*

For the more complex components shown in Figure 12, 3PB strength measurements were performed after each process step. Corresponding results are illustrated in Figure 31, where characteristic strength values within their 90% confidence intervals are plotted and compared with ZnO bulk material.

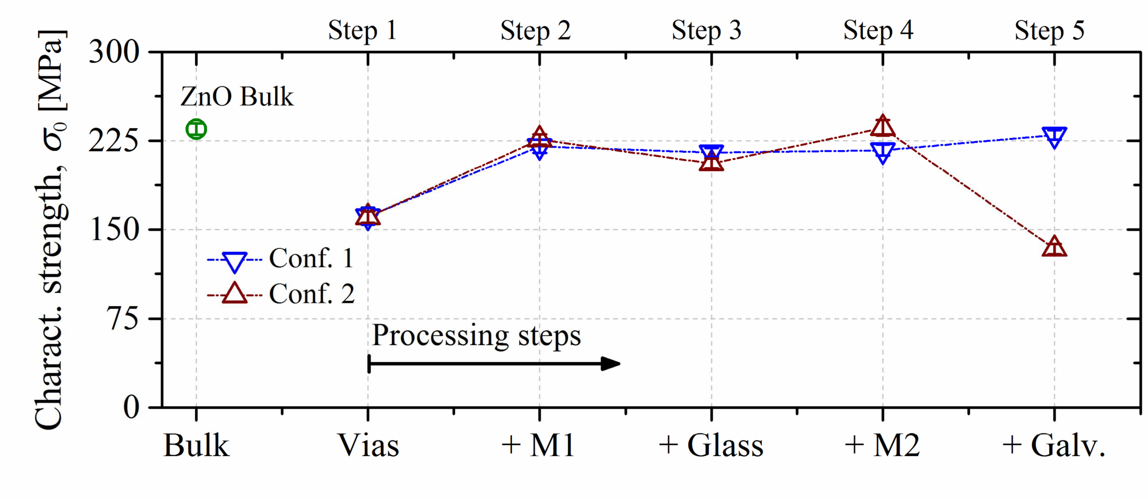

Figure 31: Comparison of characteristic strength for ZnO-bulk material and a real multilayer component after different process steps. Error bars represent the 90 % confidence intervals.

Similar to the behaviour of LTCC building blocks, vias lead to a significant reduction of the mechanical strength. This effect is diminishes after a metal electrode is applied and fully covers the respective via. Accordingly, similar strength compared to ZnO bulk material is observed for the following process steps. Nevertheless, after the final galvanization process, where a thin Ni and Au layers are deposited, a large discrepancy in strength between the two different designs is observable: While for Conf.1, where the smaller metallization layer is closer to the component's surface no significant changes compared to previous process steps are observable, a severe profound of Conf.2, with the larger metal layer on top, occurred. FIB cuts perpendicular to the surface metallization layers (Figure 32) show that after the final galvanisation step delamination between glass and M2 is observable.

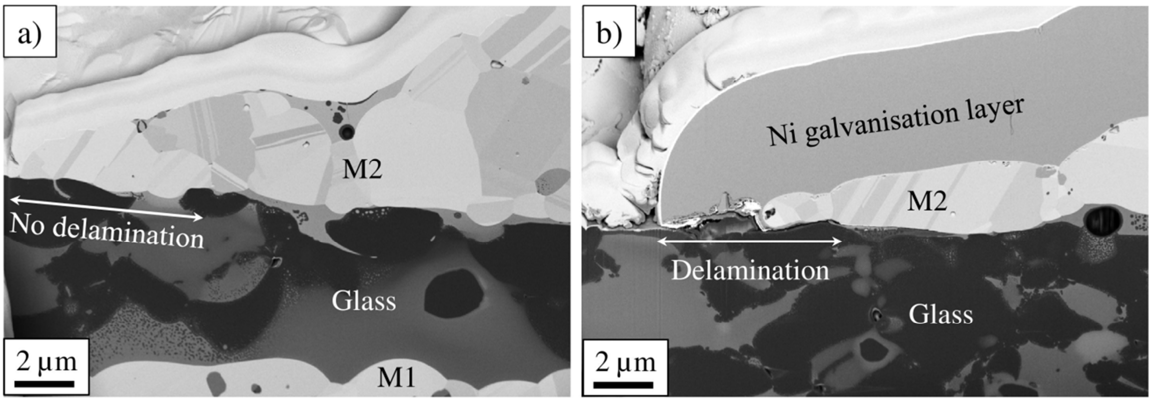

Figure 32: FIB cut perpendicular to surface metallization before (a) and after (b) the final galvanisation step showing the occurring delamination between metal and glass.

This could provide a preferred spot for initiation and propagation of cracks under mechanical loading. Since this phenomenon could be evidenced for both configurations, it does not explain the significant decrease in strength for Conf.2. Conf.1 specimens were pre-loaded up to a point where every Conf.2 specimen would already have failed and afterwards examined utilizing FIB preparation (see Figure 33). It can be seen that indeed cracks propagate from the initial delamination crack caused by the galvanisation process. Nevertheless, for Conf.1, cracks can arrest in the longer M1 layer below the surface, comparable to ceramic designs with tailored compressive stresses [133]. For Conf.2 specimens no similar behaviour could be obtained. Cracks grow in an instable manner once the stresses are high enough to activate the initial defect coming from delamination. Accordingly, no successful pre-loading experiment could be performed. A detailed analysis of fracture behaviour over all process steps together with further pre-loading experiments are provided in *Publication E*.

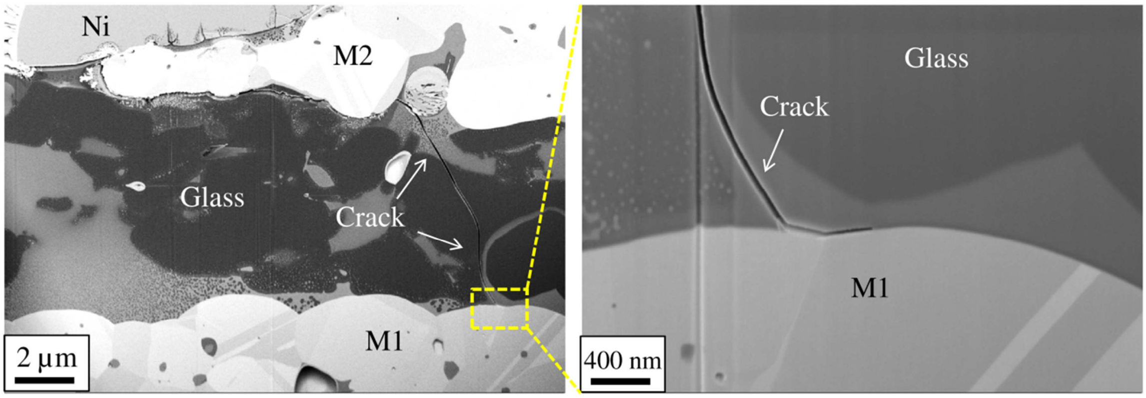

Figure 33: FIB-cut in preloaded sample with an applied equivalent stress of ~80 % of σ_0,Conf.1.

Overall, it could be shown that even small differences in design can significantly influence the mechanical strength of a given ceramic substrate. In this context, understanding of individual effects coming from small internal/external features in these complex 3D structures are essential, justifying further experiments on simpler building blocks, as those performed during this thesis.

5. Conclusions and outlook

A thorough mechanical characterization of single crystalline materials for SAW-filter components and ceramic printed circuit boards was performed using a combination of biaxial as well as uniaxial testing methods, in-situ toughness tests and nanoindentation experiments.

For the case of single crystals,

- biaxial strength measurements on $LiTaO_3$ and $LiNbO_3$ revealed large differences in strength. The ~2.5 times higher characteristic strength values of $LiTaO_3$ compared to $LiNbO_3$ could thereby be ascribed to a combination of differences in defect sizes on the one hand and toughness values on the other hand. Corresponding fractographic analysis revealed anisotropic fracture behaviour of both materials with crack following preferential cleavage planes. In this context, extraordinarily low strength values were obtained in samples previously scratched with a nano-indenter, where the surface defect was aligned parallel to a critical cleavage plane.
- In-situ toughness experiments supported by atomistic modelling revealed that the anisotropic fracture toughness of $LiNbO_3$ was lower compared to its $LiTaO_3$ counterpart. Nevertheless, the differences could not entirely explain the observed difference in strength. Accordingly, a different sensitivity of both materials to the development of surface defects was expected. In this context, nanoindentation measurements could not only reveal the onset of irreversible deformation through twinning and cracking but also evidence significant differences in hardness values, with $LiTaO_3$ being harder and stiffer than $LiNbO_3$. Considering the hardness anisotropy in single crystalline $LiNbO_3$, an orientation with a significantly harder surface can be provided. Corresponding samples showed an almost doubled characteristic strength values, only slightly below those of $LiTaO_3$.
- Further improvement can be gained for the roughened backside of both single crystals: Knowledge on alignment of weak crystallographic planes can be used to change the orientation of grinding grooves along tougher directions which lead to significantly higher strength values compared to specimens with grinding grooves parallel to the most critical cleavage planes.

In case of ceramic boards,

- simplified building blocks were designed and mechanically tested to assess individual influences contributing to the mechanical strength of ceramic circuit boards. Impacts of single features like vias, electrodes or glass layers were investigated. Furthermore, influences of environment regarding SCCG were determined und found to differ for distinct features.

- Protective top layers and dry environments were noticed to enhance the mechanical strength, whereas single metal electrodes and vias affected the strength distribution of ceramic multilayer samples. It was demonstrated that even small changes in design can significantly improve the mechanical behaviour of brittle components in microelectronic systems.
- It could be demonstrated on a real multilayer component that by changing the size-ratio of the two top electrodes, the strength values can double-up due to a favourable design and improve the mechanical reliability. Thereby it could be shown that if the lower electrode is designed larger than the top electrode, cracks can arrest in this metal layer below, while mechanical properties are still similar to those of the bulk material.

Overall, fundamentals on the structural integrity of brittle systems, ranging from single crystals to ceramic boards, could be far extended. The effect of design, environment and material internal structure on the reliability of the entire system was carefully examined. The constantly increasing complexity of microelectronic systems will be considered in ongoing work by modifying used specimens to decently meet the currently used component designs in future.

6. List of Publications

6.1. Contributions as first author

Publication A:

Strength distribution and fracture analyses of $LiNbO_3$ and $LiTaO_3$ single crystals under biaxial loading

M. Gruber, I. Kraleva, P. Supancic, J. Bielen, D. Kiener and R. Bermejo
in Journal of the European Ceramic Society 2017, 37, 4397.
doi:https://doi.org/10.1016/j.jeurceramsoc.2017.02.002
Biaxial strength measuremtens were perforemed onto mirror-polished $LiTaO_3$ and $LiNbO_3$ single crystalline samples using the ball-on-three-balls test. Different sizes of specimens were tested in water and air at various testing speeds to investigate influences of effectiv volumes/surfaces and sub-critical crack growth on the strength of both materials. While a large difference in strength with $LiTaO_3$ showing ~2.5 times higher charactersitic strength values than $LiNbO_3$ could be discerned, no significant influences regarding specimen size or environmental influences could be obtained. Fractography revealed critical cleavage planes for both materials and showed that scratches parallel to the most critical cleavage plane are responsible for the lower strength values in respective samples. Also more pronounced surface damages in $LiNbO_3$ compared to $LiTaO_3$ could be discerned which could explain the large differences in strength between the two investigated materials.

Publication B:

Understanding the effect of surface flaws on the strength distribution of single crystals

M. Gruber, A. Leitner, I. Kraleva, D. Kiener, P. Supancic and R. Bermejo.
Under review

B3B tests were performed on single crystalline $LiTaO_3$ and $LiNbO_3$ specimens with grinded as well as nano-scratched surfaces. In general, a significant reduction in strength compared to mirror-polished specimens could be discerned. Further, not only the surface conditioning itself but also its orientation with respect to critical cleavage planes turned out to strongly influence the obtained strength distribution of the two materials concerned. In this context, the weakest samples corresponded to specimens with the artificial defects parallel to the most critical cleavage plane for both materials. Fractography revealed that for other defect orientations cracks need to initiate along tougher planes requiring higher loads and then turn into the closest cleavage plane, which again disseminates further fracture energy. Consequently, tailoring of surface roughness orientation can significantly improve the mechanical reliability of single crystalline components for which a certain surface roughness is inevitable for maintaining the desired functional properties.

Publication C:

Atomistic origins of the differences in anisotropic fracture behaviour of $LiTaO_3$ and $LiNbO_3$ single crystals

M. Gruber, R. Konetschnik, M. Popov, J. Spitaler, P. Supancic, D. Kiener and R. Bermejo
in Acta Materialia 2018, doi:https://doi.org/10.1016/j.actamat.2018.03.020

In this work the fracture energies/toughness of $LiTaO_3$ and $LiNbO_3$ single crystals have been assessed by a combined approach using in-situ micro-mechanical tests together with Density Functional Theory (DFT) analysis. For respective calculations the $\{01\bar{1}2\}$ family of crystallographic planes emerged as most critical one for both materials were accordingly investigated experimentally. Overall, higher direction dependent fracture energies for $LiTaO_3$ compared to $LiNbO_3$ could be discerned for both experimental and computational analysis, which could partly explain the observed differences in mechanical strength in previous work.

Publication D:

Incipient plasticity and surface damage in $LiTaO_3$ and $LiNbO_3$ single crystals

M. Gruber, A. Leitner, D. Kiener, P. Supancic and R. Bermejo.
under revision

Nanoindentation experiments were performed on $LiTaO_3$ and $LiNbO_3$ single crystalline materials in order to sample the onset of irreversible deformation caused by contact damage. It could be shown that twinning is the dominant deformation mechanism and occurs under similar applied shear stresses for both materials. Already after the first twins occur due to incipient plastic deformation, cracks following the same planes are observable, which would significantly reduce the bearable strength of a respective functional component. It could be shown that the overall fracture and deformation behaviour is triggered by alignment of certain crystallographic planes, hardness and elastic properties of the single crystalline material, which all of has to be taken into account for designing of functional components in terms of mechanical reliability.

Publication E:

Effect of metallization on the strength and fracture behaviour of functional co-fired multilayer ceramics

M. Gruber, P. Supancic, F. Aldrian and R. Bermejo
in Journal of the European Ceramic Society 2017, 37, 4389.
doi:https://doi.org/10.1016/j.jeurceramsoc.2017.02.018

In this work, the effect of metallization design on the three-point-bending strength of a ZnO-based multilayer functional substrate was evaluated. Strength distributions and fracture behaviour over all process steps were investigated. It could be shown that, depending on the size ratio of the two top metallization layers, significant differences in strength can be obtained after the final galvanization process. If the lower top electrode is significantly larger than the upper one, cracks can arrest in the metal layer below leading to almost doubled characteristic strength values of the final functional substrate.

6.2. Contributions as co-author

Mechanical testing and fracture analyses of miniaturized ZnO-based multilayer components

K. Macurova, M. Gruber, M. Pletz, P. Supancic, R. Danzer, F. Aldrian and R. Bermejo in International Symposium on Microelectronics 2015(1), 163-168.

6.3. Contributions to the publications as first author

Publication A

Manuscript preparation, definition of specimen geometries and marking of specimens, mechanical testing, calculation of fracture stresses, statistical analysis of strength distributions, parts of fractographic analyses, correlation between fracture patterns and crystallography

Publication B

Manuscript preparation, calculation of the required alignment of introduced artificial defects, parts of mechanical testing, calculation of fracture stresses, statistical analysis of strength distributions, parts of fractographic analyses

Publication C

Manuscript preparation, calculation of the required alignment of micro-cantilevers, evaluation of experiments, statistical analysis and error calculations, illustration of elastic properties, parts of fractographic analyses

Publication D

Manuscript preparation, calculation of pole-figures, fractography, correlation between fracture/deformation patterns and crystallography, statistical evaluation of pop-in shear stresses

Publication E

Manuscript preparation, mechanical testing, calculation of fracture stresses, statistical analysis of strength distributions, main parts of fractographic analyses

7. References

[1] Wachtman JB, Cannon WR, Matthewson MJ. Mechanical properties of ceramics. New York, Chicester: John Wiley, 2009.

[2] Rappaport TS, Sun S, Mayzus R, Zhao H, Azar Y, Wang K, Wong GN, Schulz JK, Samimi M, Gutierrez F. Millimeter wave mobile communications for 5G cellular: It will work! IEEE access 1 (2013) 335-349.

[3] Cisco. Cisco visual networking index: Global mobile data traffic forecast update, 2015–2020. 2016.

[4] Mitra RN, Agrawal DP. 5G mobile technology: A survey. ICT Express 1 (2015) 132–137.

[5] Zhang S, Xu X, Wu Y, Lu L. 5G: Towards energy-efficient, low-latency and high-reliable communications networks. Communication Systems (ICCS), 2014 IEEE International Conference on: IEEE, 2014. p.197-201.

[6] Agarwal A, Misra G, Agarwal K. The 5th generation mobile wireless networks- key concepts, network architecture and challenges. Am. J. Electr. Electron. Eng. 3 (2015) 22–28.

[7] Ericsson L. More than 50 billion connected devices—taking connected devices to mass market and profitability. Tech. Rep., 2011, http://vdna.be/publications/Wp-50-Billions. Pdf, 2011.

[8] Networking Index CV. Forecast and methodology, 2016-2021, White paper. San Jose, CA, USA 1 (2016).

[9] Li QC, Niu H, Papathanassiou AT, Wu G. 5G network capacity: Key elements and technologies. IEEE Vehicular Technology Magazine 9 (2014) 71-78.

[10] Chen S, Zhao J. The requirements, challenges, and technologies for 5G of terrestrial mobile telecommunication. IEEE Communications Magazine 52 (2014) 36-43.

[11] Roh W, Seol JY, Park J, Lee B, Lee J, Kim Y, Cho J, Cheun K, Aryanfar F. Millimeter-wave beamforming as an enabling technology for 5G cellular communications: Theoretical feasibility and prototype results. IEEE Communications Magazine 52 (2014) 106-113.

[12] Hashimoto K-Y. RF bulk acoustic wave filters for communications: Artech House, 2009.

[13] Ruppel CCW, Fjeldly TA. Advances in surface acoustic wave technology, systems and applications: World Scientific Publishing Group, 2000.

[14] Mahon S. The 5G effect on RF filter technologies. IEEE Transactions on Semiconductor Manufacturing 30 (2017) 494-499.

[15] Hashimoto K-Y. Surface acoustic wave devices in telecommunications: Modelling and simulation: Springer-Verlag Berlin Heidelberg GmbH, 2000.

[16] Matsuda T, Uchishiba H, Ikata O, Nishihara T, Satoh V. L and S band low-loss filters using SAW resonators. Ultrasonics Symposium, 1994. Proceedings., 1994 IEEE, vol. 1: IEEE, 1994. p.163-167.

[17] Rayleigh L. On waves propagated along the plane surface of an elastic solid. Proceedings of the London Mathematical Society 1 (1885) 4-11.

[18] Morgan D. Surface acoustic wave filters: Academic Press, 2007.

[19] Shibayama K, Yamanouchi K, Sato H, Meguro T. Optimum cut for rotated Y-cut $LiNbO_3$ crystal used as the substrate of acoustic-surface wave filters. Proceedings of the IEEE, vol. 64, 1976. p.595–597.

[20] Campbell C. Surface acoustic wave devices and their signal processing applications. Academic Press, 1989. pp. 427–458.

[21] White R, Voltmer F. Direct piezoelectric coupling to surface elastic waves. Appl. Phys. Lett. 7 (1965) 314-316.

[22] Ruppel CC, Fjeldly TA. Advances in surface acoustic wave technology, systems and applications: World scientific, 2001.

[23] Curie J. Développement par compression de l'électricité polaire dans les cristaux hémièdres à faces inclinées. Bull. Soc. Fr. Mineral. 3 (1880) 90.

[24] Yang J. An introduction to the theory of piezoelectricity: Springer Science & Business Media, 2004.

[25] Vives AA. Piezoelectric transducers and applications: Springer Science & Business Media, 2008.

[26] Slobodnik AJ. Surface acoustic waves and saw materials. Proceedings of the IEEE 64 (1976) 581–595.

[27] Schulz MB, Matsinger BJ, Holland MG. Temperature dependence of surface acoustic wave velocity on α Quartz. J. Appl. Phys. 41 (1970) 2755–2765.

[28] Lewis M. Surface skimming bulk wave, SSBW. 1977 Ultrasonics Symposium, 1977. p.744–752.

[29] Imanaka Y. Multilayered low temperature cofired ceramics (LTCC) technology. In: Springer Science-Business Media I (Eds.). New York, NY 10013, USA, 2005. pp. 260.

[30] Heuser T, Bauer C, Dragoi V, Mittendorfer G. Adhesive wafer bonding applied for fabrication of true-chip-size packages for SAW devices. ECS Transactions 50 (2013) 363-370.

[31] Bauer T, Eggs C, Wagner K, Hagn P. A bright outlook for acoustic filtering: A new generation of very low-profile SAW, TC SAW, and BAW devices for module integration. IEEE Microwave Magazine 16 (2015) 73-81.

[32] Abrahams SC, Reddy JM, Bernstein JL. Ferroelectric Lithium Niobate. 3. Single crystal X-Ray diffraction study at 24°C. J. Phy. Chem. Solids 27 (1966) 997–1012.

[33] Vainshtein BK, Cardona M, Fulde P, Queisser HJ. Modern crystallography I, symmetry of crystals. Methods of structural crystallography. Crystal Research and Technology 17 (1982) 352-352.

[34] Weis RS, Gaylord TK. Lithium Niobate: Summary of physical properties and crystal structure. Appl. Phys. A 37 (1985) 191–203.

[35] Hsu R, Maslen EN, Du Boulay D, Ishizawa N. Synchroton X-Ray studies of $LiNbO_3$ and $LiTaO_3$. Acta Crystallographica Section B 53 (1997) 420 - 428.

[36] Nye JF. Physical properties of crystals. Oxford: Clarendon Press, 1985.

[37] Smith RT, Welsh FS. Temperature dependence of the elastic, piezoelectric, and dielectric constants of Lithium Tantalate and Lithium Niobate. J. Appl. Phys. 42 (1971) 2219–2230.

[38] Slobodnik AJ. The temperature coefficients of acoustic surface wave velocity and delay on Lithium Niobate, Lithium Tantalate, Quartz, and Tellurium Dioxide. Physical Sciences Research Papers 477 (1971) 1-115.

[39] Kuz'minov YS. Lithium Niobate crystals: Physico-chemical aspects of technology: Cambridge International Science Publishing, 1999.

[40] Miyazaki N, Hattori A, Uchida H. Thermal shock cracking of Lithium Niobate single crystal. Journal of Materials Science: Materials in Electronics 8 (1997) 133–138.

[41] Miyazaki N, Koizumi N. Analysis of cracking of Lithium Tantalate ($LiTaO_3$) single crystals due to thermal stress. J. Mater. Sci. 41 (2006) 6313–6321.

[42] Hang W, Zhou L, Shimizu J, Yuan J, Yamamoto T. Study on the mechanical properties of Lithium Tantalate and the influence on its machinability. Fuji Technology Press LTD. 7 (2013) 644–653.

[43] Anasori B, Sickafus KE, Usov IO, Barsoum MW. Spherical nanoindentation study of the deformation micromechanisms of $LiTaO_3$ single crystals. J. Appl. Phys. 110 (2011) 023516.

[44] Basu S, Zhou A, Barsoum MW. Reversible dislocation motion under contact loading in $LiNbO_3$ single crystal. Journal of Materials Research 23 (2008) 1334-1338.

[45] Zhang Z, Yang S, Xu C, Wang B, Duan N. Deformation and stress at pop-in of Lithium Niobate induced by nanoindentation. Scripta Mater. 77 (2014) 56–59.

[46] Vere A. Mechanical twinning and crack nucleation in Lithium Niobate. J. Mater. Sci. 3 (1968) 617-621.

[47] Cordier P, Boulogne B, Dotikiian N, Doukhan J. Lattice defects in Lithium Tantalate. physica status solidi (a) 112 (1989) 493-510.

[48] Park BM, Kitamura K, Furukawa Y, Ji Y. Relation between mechanical twinning and cracking in stoichiometric Lithium Niobate single crystals. J. Am. Ceram. Soc. 80 (1997) 2689–2692.

[49] Bermejo R, Supancic P, Krautgasser C, Morrell R, Danzer R. Subcritical crack growth in low temperature co-fired ceramics under biaxial loading. Eng. Fract. Mech. 100 (2013) 108–121.

[50] Clarke DR. Varistor ceramics. J. Am. Ceram. Soc. 82 (1999).

[51] Bermejo R, Supancic P, Kraleva I, Morrell R, Danzer R. Strength reliability of 3D low temperature co-fired multilayer ceramics under biaxial loading. J. Eur. Ceram. Soc. 31 (2011) 745–753.

[52] Roosen A. Tape casting of ceramic green tapes for multilayer device processing. In: Jean HJ, Gupta TK, Nair KM, Niwa K (Eds.). Ceramic transactions, vol. 97. Columbus, Ohio: The American Ceramics Society, 1999. pp.

[53] Bermejo R, Daniel R, Schuecker C, Paris O, Danzer R, Mitterer C. Hierarchical architectures to enhance structural and functional properties of brittle materials Adv. Eng. Mat. 19 (2017) 1600683.

[54] Deluca M, Bermejo R, Pletz M, Supancic P, Danzer R. Strength and fracture analysis of Silicon-based components for embedding. J. Eur. Ceram. Soc. 31 (2011) 549–558.

[55] Hsueh CH, Evans AG. Residual stresses and cracking in metal/ceramic systems for microelectronics packaging. J. Am. Ceram. Soc. 68 (1985) 120–127.

[56] Krautgasser C, Chlup Z, Supancic P, Danzer R, Bermejo R. Influence of subcritical crack growth on the determination of fracture toughness in brittle materials. J. Eur. Ceram. Soc. 36 (2016) 1307-1312.

[57] Leguillon D, Li J, Martin E. Multi-cracking in brittle thin layers and coatings using a FFM model. Eur. J. Mech. A-Solid 63 (2017) 14-21.

[58] Bermejo R, Danzer R. Mechanical characterization of ceramics: Designing with brittle materials. In: Sarin VK (Eds.). Comprehensive hard materials. Oxford: Elsevier, 2014. pp. 285–298.

[59] Danzer R. A general strength distribution function for brittle materials. J. Eur. Ceram. Soc. 10 (1992) 461–472.

[60] Griffith AA. The phenomenon of rupture and flow in solids. Phil. Trans. Roy. Soc. London A221 (1920) 163–198.

[61] Tsai YL, Mecholsky Jr JJ. Fracture mechanics description of fracture mirror formation in single crystals. Int. J. Fract. 57 (1992) 167–182.

[62] Chen K-S, Ayon A, Spearing SM. Controlling and testing the fracture strength of Silicon on the mesoscale. J. Am. Ceram. Soc. 83 (2000) 1476–1484.

[63] Wereszczak AA, Barnes AS, Breder K, Binapal S. Probabilistic strength of {1 1 1} n-type Silicon. J. Mater. Sci. 11 (2000) 291–303.

[64] C. Funke EK, M. Kuna, H.J. Möller,. Biaxial fracture test of Silicon wafers. Adv. Eng. Mat. 6 (2004) 594–598.

[65] Danzer R. Ceramics: Mechanical performance and lifetime prediction. In: Cahn RW, Brook R (Eds.). Encyclopedia of advanced materials, vol. 1. Oxford: Pergamon Press, 1994. pp. 385–398.

[66] Davidge RW. Mechanical behaviour of ceramics. Cambridge: Cambridge University Press, 1979.

[67] Roosen A. New lamination technique to join ceramic green tapes for the manufacturing of multilayer devices. J. Eur. Ceram. Soc. 21 (2001) 1993-1996.

[68] EN 843-5. Advanced technical ceramics - monolithic ceramics - mechanical tests at room temperature - part 5: Statistical analysis. EN 843-5, 1997. p.40.

[69] Danzer R, Lube T, Supancic P. Monte-carlo simulations of strength distributions of brittle materials - type of distribution, specimen- and sample size. Zeitschrift für Metallkunde 92 (2001) 773–783.

[70] Weibull W. A statistical theory of the strength of materials. Stockholm: Generalstabens Litografiska Anstalts Förlag, 1939.

[71] Weibull W. A statistical distribution function of wide applicability. J. Appl. Mech. 18 (1951) 293–297.

[72] Lu C, Danzer R, Fischer FD. Fracture statistics of brittle materials: Weibull or normal distribution. Physical Review E 65 (2002) 067102.

[73] Wiederhorn SM. Subcritical crack growth in ceramics. In: Bradt RC, Hasselman DPH, Lange FF (Eds.). Fracture mechanics of ceramics. New York: Plenum, 1974. pp. 613-646.

[74] Wiederhorn SM. Influence of water vapour on crack propagation in soda-lime glass. J. Am. Ceram. Soc. 50 (1967) 407–414.

[75] Michalske TA, Freiman SW. A molecular mechanism for stress corrosion in vitreous Silica. J. Am. Ceram. Soc. 66 (1983) 284–288.

[76] ASTM-E399-09. Standard test method for linear-elastic plane-strain fracture toughness Kic of metallic materials. ASTM International, West Conshohocken, PA, (2009).

[77] ASTM-C-1499-01. Determination of monotonic biaxial flexural strength advanced ceramics. In: Materials ASfTa, editor. West Conshohocken, Pennsylvania, 2001. p.779–788.

[78] ISO 6872. Dentistry — ceramic materials. 2015.

[79] Börger A, Supancic P. Fracture of brittle discs under biaxial loading. In: Neimitz A, Rokach IV, Kocanda D, Golos K (Eds.). Fracture mechanics beyond 2000, vol. I. Sheffield: EMAS Publications, 2002. pp. 345–352.

[80] Börger A, Supancic P, Danzer R. The ball on three balls test for strength testing of brittle discs: Part II: Analysis of possible errors in the strength determination. J. Eur. Ceram. Soc. 24 (2004) 2917–2928.

[81] Danzer R, Supancic P, Harrer W. Biaxial tensile strength test for brittle rectangular plates. J. Ceram. Soc. Jpn. 114 (2006) 1054–1060.

[82] Bermejo R, Supancic P, Krautgasser C, Danzer R. Evaluation of subcritical crack growth in low temperature co-fired ceramics American Ceramic Society (2013).

[83] EN 843-1. Advanced technical ceramics, monolithic ceramics, mechanical properties at room temperature, part 1: Determination of flexural strength. EN 843-1, 1995.

[84] ASTM C 1161-02c. Standard test methods for flexural strength of advanced ceramics at ambient temperature. American Society for Testing and Materials, 2002.

[85] Baratta FI, Matthews WT, Quinn GD. Errors associated with flexure testing of brittle materials. Watertown: U.S. Army Materials Technology Laboratory, 1987. p.43.

[86] Quinn GD, Morrell R. Design data for engineering ceramics: A review of the flexure test. J. Am. Ceram. Soc. 74 (1991) 2037–2066.

[87] Lube T, Manner M, Danzer R. The miniaturisation of the 4-point bend-test. Fatigue and Fracture of Engineering Matererial Structures 20 (1997) 1605–1616.

[88] ISO 23146. Fine ceramics (advanced ceramics, advanced technical ceramics) -- test methods for fracture toughness of monolithic ceramics -- single-edge v-notch beam (SEVNB) method. 2008.

[89] ISO 24370. Fine ceramics (advanced ceramics, advanced technical ceramics) - test method for fracture toughness of monolithic ceramics at room temperature by chevron-notched beam (CNB) method. 2005.

[90] Strobl S, Rasche S, Krautgasser C, Sharova E, Lube T. Fracture toughness testing of small ceramic discs and plates. J. Eur. Ceram. Soc. 34 (2014) 1637–1642.

[91] Jaya BN, Jayaram V. Fracture testing at small-length scales: From plasticity in Si to brittleness in Pt. The Journal of The Minerals, Metals & Materials Society 68 (2016) 94–108.

[92] Wurster S, Motz C, Jenko M, Pippan R. Micrometer-sized specimen preparation based on ion slicing technique. Adv. Eng. Mat. 12 (2010) 61–64.

[93] Wurster S, Motz C, Pippan R. Characterization of the fracture toughness of micro-sized Tungsten single crystal notched specimens. Philos. Mag. 92 (2012) 1803–1825.

[94] Kiener D, Motz C, Rester M, Jenko M, Dehm G. FIB damage of Cu and possible consequences for miniaturized mechanical tests. Mat. Sci. Eng. A 459 (2007) 262–272.

[95] Oliver WC, Pharr GM. An improved technique for determining hardness and elastic modulus using load and displacement sensing indentation experiments. J. Mat. Res. 7 (1992) 1564–1583.

[96] Wang Z, Bei H, George EP, Pharr GM. Influences of surface preparation on nanoindentation pop-in in single-crystal Mo. Scripta Mater. 65 (2011) 469-472.

[97] Franke O, Alcalá J, Dalmau R, Duan ZC, Biener J, Biener M, Hodge AM. Incipient plasticity of single-crystal Tantalum as a function of temperature and orientation. Philos. Mag. 95 (2015) 1866-1877.

[98] Lawn BR. Indentation of ceramics with spheres: A century after Hertz. J. Am. Ceram. Soc. 81 (1998) 1977–1994.

[99] Lee SK, Lawn BR. Role of microstructure in hertzian contact damage in Silicon Nitride: II, strength degradation. J. Am. Ceram. Soc. 81 (1998) 997–1003.

[100] Lawn BR, Wuttiphan S. Model of strength degradation from Hertzian contact damage in tough ceramics. J. Am. Ceram. Soc. 81 (1998) 1509–1520.

[101] Rhee Y-W, Kim H-W, Deng Y, Lawn BR. Brittle fracture versus quasi plasticity in ceramics: A simple predictive index. J. Am. Ceram. Soc. 84 (2001) 561–565.

[102] Morrell R. Fractography of brittle materials. Teddington: National Physical Laboratory, 1999.

[103] Quinn GD. Fractography of glasses and ceramics. Washington: US Government Printing Office, 2007.

[104] Schultz RA, Jensen MC, Bradt RC. Single crystal cleavage of brittle materials. Int. J. Fract. 65 (1994) 291–312.

[105] Wu CCM, McKinney KR, Rice RW. Zig-zag crack propagation in $MgAl_2O_4$ crystals. J. Materi. Sci. Letters 14 (1995) 474–477.

[106] Gumbsch P. Brittle fracture and the brittle-to-ductile transition of Tungsten. J. Nuc. Mater. 323 (2003) 304–312.

[107] Pérez R, Gumbsch P. Directional anisotropy in the cleavage fracture of Silicon. Phsys. Rev. Lett. 84 (2000) 5347.

[108] Ashby MF, Jones DRH. Engineering materials 1. Oxford: Pergamon Press, 1993.

[109] Chae S-H, Zhao J-H, Edwards DR, Ho PS. Effect of backside scratch direction on the Si die strength. Thermal and Thermomechanical Phenomena in Electronic Systems (ITherm), 2010 12th IEEE Intersociety Conference on: IEEE, 2010. p.1-6.

[110] Matoy K, Schönherr H, Detzel T, Dehm G. Micron-sized fracture experiments on amorphous SiO_x films and SiO_x/SiN_x multi-layers. Thin Solid Films 518 (2010) 5796–5801.

[111] Iqbal F, Ast J, Göken M, Durst K. In situ micro-cantilever tests to study fracture properties of NiAl single crystals. Acta Mater. 60 (2012) 1193–1200.

[112] Jaya BN, Kirchlechner C, Dehm G. Can microscale fracture tests provide reliable fracture toughness values? A case study in Silicon. J. Mat. Res. 30 (2015) 686–698.

[113] Iwasa M, Ueno T, Bradt RC. Fracture toughness of Quartz and Sapphire single crystals at room temperature. J. Soc. Mater. Sic. 30 (1981) 1001–1004.

[114] Iwasa M, Bradt RC. Cleavage of natural and synthetic single crystal Quartz. Mater. Res. Bull. 22 (1987) 1241–1248.

[115] John CS. The brittle-to-ductile transition in pre-cleaved Silicon single crystals. The Philosophical Magazine: A Journal of Theoretical Experimental and Applied Physics 32 (1975) 1193-1212.

[116] Nikogosyan DN. Nonlinear optical crystals: A complete survey: Springer Science & Business Media, 2006.

[117] Launey ME, Ritchie RO. On the fracture toughness of advanced materials. Adv. Mater. 21 (2009) 2103–2110.

[118] Lawn BR. Fracture of brittle solids - second edition. Cambridge: Cambridge University Press, 1993.

[119] Renger A. Johnson, kl, contact mechanics. Cambridge etc., cambridge university press 1985. Xii, 452 pp.,£ 17.50 p/b. Isbn 0521347963. Wiley Online Library, 1989.

[120] Vlassak JJ, Nix WD. Indentation modulus of elastically anisotropic half spaces. Philos. Mag. A 67 (1993) 1045–1056.

[121] Vlassak JJ, Nix WD. Measuring the elastic properties of anisotropic materials by means of indentation experiments. J. Mech. Phys. Solids 42 (1994) 1223-1245.

[122] Simmons G, Wang H. Single crystal elastic constants and calculated aggregate properties: A handbook. Cambridge, MA: MIT Press, 1971.

[123] Wereszczak AA, Johanns K, E., Jadaan OM. Hertzian ring crack initiation in hot-pressed Silicon Carbide. J. Am. Ceram. Soc. 92 (2009) 1788–0795.

[124] Lee SK, Wuttiphan S, Lawn BR. Role of microstructure in Hertzian contact damage in Silicon Nitride: I, mechanical characterization. J. Am. Ceram. Soc. 80 (1997) 2367–2381.

[125] Wong KK. Properties of lithium niobate: INSPEC, The Institution of Electrical Engineers, London, United Kingdom, 2002.

[126] Lawn BR, Evans AG, Marshall DB. Elastic/plastic indentation damage in ceramics: The median/radial crack system. J. Am. Ceram. Soc. 63 (1980) 574–581.

[127] Sebastiani M, Johanns KE, Herbert EG, Pharr GM. Measurement of fracture toughness by nanoindentation methods: Recent advances and future challenges. Current Opinion Solid. Stat. Mater. Sci. 19 (2015) 324-333.

[128] Johnson KL. Contact mechanics. Cambridge: Cambridge University Press, 1985.

[129] Brookes C, O'neill J, Redfern B. Anisotropy in the hardness of single crystals. Proc. R. Soc. Lond. A, vol. 322: The Royal Society, 1971. p.73-88.

[130] Bhagavat S, Kao I. Nanoindentation of Lithium Niobate: Hardness anisotropy and pop-in phenomenon. Mat. Sci. Eng. A 393 (2005) 327–331.

[131] Wu JD, Huang CY, Liao CC. Fracture strength characterization and failure analysis of Silicon dies. Microelectronics Reliability 43 (2003) 269–277.

[132] McGuire K, Danyluk S, Baker TL, Ruponw JW, McLaughlin D. The influence of backgrinding on the fracture strength of 100 mm diameter (111) p-type Silicon wafers. J. Mater. Sci. 32 (1997) 1017–1024.

[133] Bermejo R. "Toward seashells under stress": Bioinspired concepts to design tough layered ceramic composites. J. Eur. Ceram. Soc. 37 (2017) 3823-3839.

Publication A

Strength distribution and fracture analyses of $LiNbO_3$ and $LiTaO_3$ single crystals under biaxial loading

M. Gruber, I. Kraleva, P. Supancic, J. Bielen, D. Kiener and R. Bermejo

Abstract:

The strength distribution and fracture behaviour of miniaturized Lithium niobate ($LiNbO_3$) and Lithium tantalate ($LiTaO_3$) single crystals were assessed under biaxial bending. The susceptibility of these materials to environmental assisted cracking (SCCG) was studied by means of constant cross-head displacement rate experiments in air and in water. Two different sample sizes were tested and compared to assess the Weibull volume effect.

Experimental results showed a significant difference in strength, $LiNbO_3$ being weaker than $LiTaO_3$. No apparent SCCG and no volume effect on strength was found. A different distribution to Weibull behaviour was observed in $LiNbO_3$. Fractography showed differences in the fracture patterns, due to the different cutting orientation of the two investigated materials with respect to the loading plane. New cleavage planes were identified as $\{10.1\}$ for $LiNbO_3$ and $\{1\bar{2}.3\}$ for $LiTaO_3$. Fracture surfaces of $LiNbO_3$ revealed surface damage, which may be responsible for the lower strength compared to $LiTaO_3$.

Keywords

Lithium niobate, lithium tantalate, biaxial strength, cleavage planes, fractography.

1. Introduction

Single crystals with non-centrosymmetric lattice structure possess properties such as piezo-electricity, pyro-electricity, or non-linear optical behaviour, making them interesting for electronic devices (e.g. modulators, transducers or detectors). In the smartphone market, for instance, they have found an important application as surface acoustic wave (SAW) filters for Radio Frequency (RF) front ends in mobile phones [1, 2]. In such applications, a piezoelectric substrate is used as a transducer, converting electrical high frequency signals into acoustic waves (and vice versa) using the piezoelectricity (coupling of the electrical and mechanical field) of the material. This specific requirement can be described with the electromechanical coupling factor (k). An important aspect for the functionality of SAW filters is also the temperature stability of the resonance frequency, characterized by the temperature coefficient of frequency (TCF) [3-6]. The choice of a substrate material requires high coupling factor k along with low temperature dependences. Unfortunately, materials with relatively low TCF have, in general, an undesirable lower k. As a consequence of the many demands on the material, compromises have to be made. For instance, for Quartz with a low k, cuts with a TCF close to zero are known and used where accurate frequency generation is needed (e.g. wristwatches) [7]. Due to the anisotropy of these types of crystals, many different cuts under certain angles have been investigated in order to get the required properties for the desired application.

The materials that meet the specifications best for many SAW devices are lithium niobate ($LiNbO_3$) and lithium tantalate ($LiTaO_3$) single crystals. In order to fulfill the above considerations, wafers are cut out of a single crystal grown under specific angles. For $LiNbO_3$ and $LiTaO_3$ two different cuts are usually reported in literature, namely 128° Y-X $LiNbO_3$ and 42° Y-X $LiTaO_3$, respectively [2, 8]. A SAW resonator is then defined by depositing patterned surface metallization (e.g. interdigitated electrodes) on the substrate and the filter component, consisting of several resonators, is soldered to a functional substrate (e.g. ceramic/polymer circuit board), resulting in a combination of materials with different thermo-physical properties (Fig. 1). Differences in thermal expansion coefficients, elastic constants and yield strengths, may lead to high residual internal stresses in the single crystals during the production process. These residual stresses in combination with the applied thermo-mechanical stresses in mandatory qualification tests and/or during service may lead to crack initiation and propagation, which, especially for brittle single crystals, can lead to catastrophic failure of the component and thus loss of functionality of the system. To evaluate the reliability of such electronic devices, knowledge of the strength distribution and fracture behavior of the single crystal components is essential.

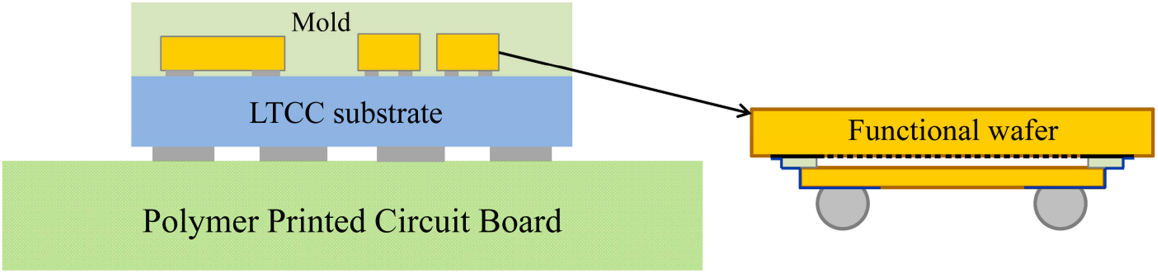

Figure 1: Schematic of a functional system containing a packaged SAW filter with a functional single crystal wafer.

Extensive work has been devoted to understand the fracture of commonly used materials such as single crystal silicon [9-11], including strength measurements under different loading conditions and sample sizes [12-14]. In general, silicon behaves as a brittle material, where fracture is governed by the size of critical defects. In single crystals, intrinsic defects (e.g. vacancies, foreign atoms, dislocations) are very small compared to those in polycrystalline brittle materials, where failure is typically governed by either "volume defects" (e.g. pores, agglomerates or large grains) or "surface defects" (e.g. contact damage/scratches/edge chippings caused by cutting/grinding/polishing). The strength distribution measured in silicon typically follows a Weibull behavior, which is explained by the underlying size distribution of (mainly) surface defects in the material associated with the grinding/polishing process [13, 15]. The characteristic strength values reported under bending can be relatively high (i.e. of the order of several GPa) [13, 16-18], as compared to other brittle materials such as polycrystalline ceramics (i.e. up to 1 GPa) [19]. However, the found strength scatters significantly, yielding very low Weibull moduli, with *m* ranging between 2 and 8 [12]. This is caused by a large scatter of the size of fracture origins. In addition, fracture takes place along "critical" cleavage planes, which may have different fracture energies associated with the high anisotropy in elastic constants of the material [20-23].

Regarding $LiNbO_3$ and $LiTaO_3$, although appropriate functional characterization can be found in the literature [2, 24, 25], only few reported data exist on the mechanical properties of these materials [26-28]. The aim of this work is to evaluate the strength and fracture behavior of $LiNbO_3$ and $LiTaO_3$ single crystals under biaxial bending. Miniaturized rectangular plate specimens with dimensions ~2 × 2 × 0.13 mm^3, similar to the size of SAW components, were tested using the Ball-on-three-Balls (B3B) test in order to investigate the mechanical behavior of the single crystals within the functional system. The B3B method was chosen to induce a biaxial stress field in the specimens and thus assess the mechanical anisotropy of the single crystals. The possible effect of humidity on the strength of the materials, as found in many glasses and ceramics [29], was evaluated by testing various samples at different cross-head displacement rates both in air and in water. In addition, larger samples with dimensions of 12 × 12 × 0.35 mm³ were also tested to analyze the Weibull behavior of the two materials (i.e. volume effect on strength). Selected specimens from the larger sample were employed to perform fractografic analyses and identify the role of the different wafer cuts in $LiNbO_3$ and $LiTaO_3$ with respect to the materials' cleavage planes.

2. Experimental procedure

2.1 Material of study

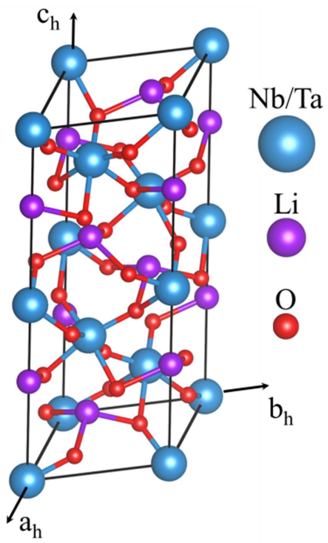

Figure 2: Crystal system of Lithium Tantalate and Lithium Niobate according to [30].

$LiNbO_3$ and $LiTaO_3$ are trigonal crystals belonging (below the Curie temperature) to the 3m point group and the R3c space group (no. 161) [31-33]. Even though they can be described by a rhombohedral lattice with three equivalent vectors, it is more convenient and common to use hexagonal axes ($a = b \neq c$ and $\alpha = \beta = 90°$, $\gamma = 120°$); note that the volume of the hexagonal cell is three times the volume of the trigonal cell, i.e. $V_{hex.} = 3 \times V_{trig.}$. The parameters of the unit cell, which is exemplarily shown in Fig. 2, are $a_h = b_h = 5.148$ Å and $c_h = 13.863$ Å for $LiNbO_3$ and $a_h = b_h = 5.154$ Å and $c_h = 13.783$ Å for $LiTaO_3$, respectively [34]. It is worth indicating that Nb and Ta are in the same group of the periodic table, which implies rather similar chemical properties. Both crystals show a threefold rotation symmetry around the c_h – axis which exhibits the strongest atomic bonds, leading to the highest Young's modulus and lowest coefficient of thermal expansion in this direction [35, 36]. In this work, all directions and planes are described in the hexagonal coordinate system (HK.L), which can be calculated from the rhombohedral one as follows [37]:

$$H = h - k \qquad (1a)$$

$$K = k - l \qquad (1b)$$

$$L = h + k + l \qquad (1c)$$

The hexagonal Bravais-Miller indices can be converted back to rhombohedral Miller indices by: h = 1/3×(2H+K+L); k = 1/3×(–H+K+L); l = 1/3×(–H–2K+L). The angles between two planes ($H_1K_1.L_1$) and ($H_2K_2.L_2$) can be calculated as follows [37]:

$$\cos\phi = \frac{H_1H_2+K_1K_2+\frac{1}{2}\left(H_1K_2+H_2K_1\right)+\frac{3a^2}{4c^2}L_1L_2}{\left(H_1^2+K_1^2+H_1K_1+\frac{3a^2}{4c^2}L_1^2\right)^{\frac{1}{2}}\left(H_2^2+K_2^2+H_2K_2+\frac{3a^2}{4c^2}L_2^2\right)^{\frac{1}{2}}} \qquad (2)$$

2.2 Fabrication of components

The investigated $LiNbO_3$ and $LiTaO_3$ single crystal samples were diced and ground by the company EPCOS OHG, Deutschlandsberg, Austria (a TDK group company). The single crystal wafers were optimized for the application as SAW–bandpass filters and therefore cut under the angles shown in Fig. 3. These special cuts were referred to as 128° Y-X $LiNbO_3$ and 42° Y-X $LiTaO_3$. The “flat” in the disc-shaped wafer, as shown in Fig. 3, is marking the x-axis of the wafer corresponding to the $[2\bar{1}.0]$ crystallographic direction. Plate-like specimens with dimensions of 2 × 2 × 0.13 mm^3 and 12 × 12 × 0.35 mm^3 were prepared from the wafers for the B3B tests. It is worth pointing out that both materials had the same surface finish, i.e. a mirror-like polished surface. Nevertheless, in the case of 12 × 12 mm^2 samples, specimens were taken from 4 different wafers in the case of $LiNbO_3$ materials, and from 8 different wafers for the $LiTaO_3$.

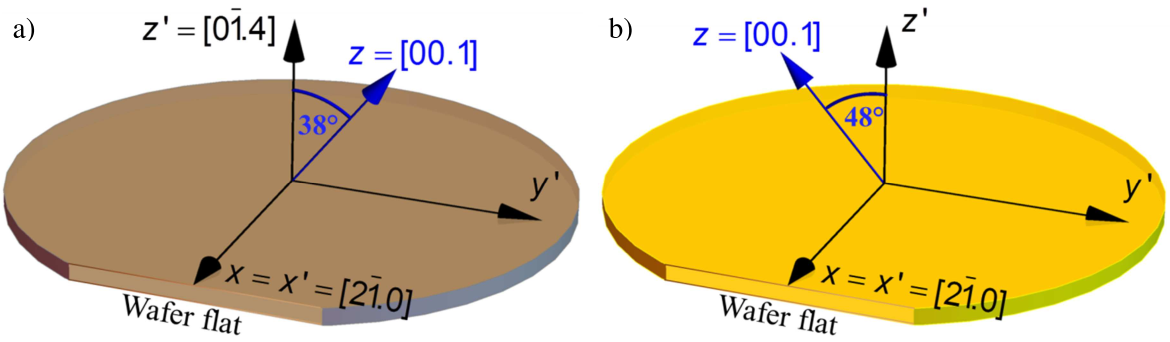

Figure 3: Schematic of the wafers a) 128° Y-X Cut of $LiNbO_3$ and b) 42° Y-X Cut of $LiTaO_3$.

2.3 Strength measurements

The biaxial strength was measured using the B3B method. In the B3B method a small surface (and volume) of the specimen is set under a well-defined biaxial stress field during the test. This may reflect the behaviour of single crystals in real components, which are usually very small and where the stress field maxima are concentrated in small volumes or areas (e.g. at material junctions). The corresponding area under tensile stress contributes to the so-called "effective surface"; the same applies for the volume, referred to as "effective volume". In this testing configuration (see Fig. 4a) a plate or disc is symmetrically supported by three balls and axially loaded via a fourth ball at the centre of the opposite side of the specimen (see more details on the testing methodology in [17, 38-40]). Fig. 4b shows a top view of the B3B-jig with the single crystal specimen under the upper balls. The wafer "flat" is also shown in Fig. 4b to indicate the orientation of the specimen in the test. For testing 2 × 2 mm specimens, the four balls used in the test had a diameter of ~1.19 mm giving a support diameter of ~1.37 mm [38]. For the 12 × 12 mm specimens, the balls had a diameter of 7.5 mm with a resulting support diameter of 8.66 mm. A pre-load of 1 N was applied in all cases. The main advantages of the B3B testing method are the high accuracy, easy testing in different environments, avoidance of edge effects and the ease of testing thin, small specimens. Accordingly, specimens dimensionally close to real components as used in microelectronic applications can be tested (see for instance [18, 41]. Nevertheless, one limitation of the method is associated with the small tested area (or volume). The corresponding stress distribution in the plate during biaxial loading is shown in Fig. 4c. The maximal stress is located in the centre of the three balls. It can be inferred that only the central region, i.e. approx. 1/20 of the support radius, is stressed by more than 90% of the maximal stress. As a consequence, some potential critical defects (lying off the stressed region) might not be activated during the test.

After testing, the failure stress is calculated from the maximum tensile stress σ_{max}, given by:

$$\sigma = f \cdot \frac{P}{t^2} \tag{3}$$

where P is the fracture load, t is the specimen thickness and f is a dimensionless factor depending on geometrical conditions of the testing setup and the specimen's Poisson's ratio, calculated using finite element analysis[∂] [18]. For instance, considering averaged dimensions of $2 \times 2 \times 0.13$ mm^3 and $12 \times 12 \times 0.35$ mm^3 as tested in this study (taken Poisson's ratio as 0.25 [42]), the calculated factor resulted in f~2.0 and f~2.4, respectively.

[∂] For the FE calculation of f, point loads were considered to simulate the contact between balls and specimen.

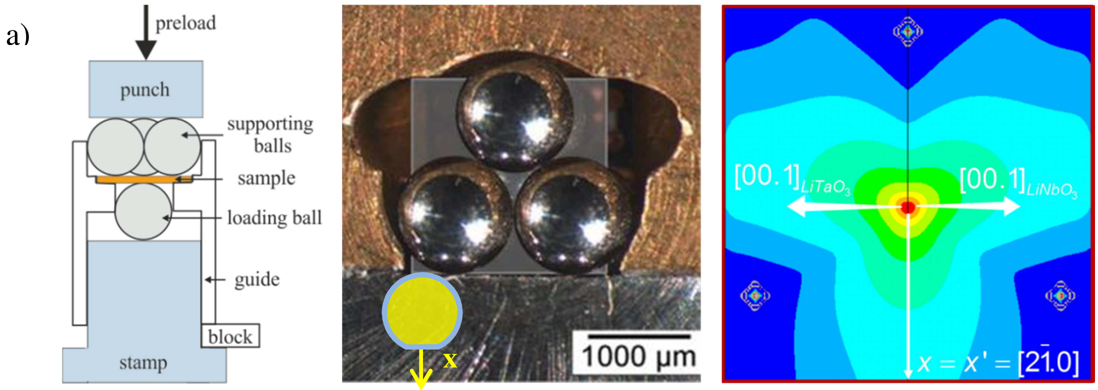

Figure 4: a) side view, b) top view of the B3B testing configuration and c) stress field on the specimen's surface with the corresponding crystallographic directions for 128° Y-X $LiNbO_3$ and 42° Y-X $LiTaO_3$.

All tests were performed in a universal testing machine (Zwick Z010, Zwick/Roell, Ulm, Germany). To assess the effect of humidity on strength, also referred to as sub-critical crack growth (SCCG), tests were conducted both in ambient air and in water with cross-head displacement rates of 0.01, 0.1 and 1 mm/min, respectively, for both materials. For the testing speeds of 0.01 mm/min and 1 mm/min 30 samples, and for 0.1 mm/min 60 samples per material and environment were tested, respectively, in order to ensure statistical significance in the Weibull analyses. All results were interpreted in the framework of Weibull theory according to the EN-843-5 standard [43] under the assumption that the materials exhibit a brittle behaviour. No ferroelectric effects (e.g. contribution of piezoelectric strains) were taken into account in the strength evaluation.

2.4 Fractographic analyses

In order to identify typical fracture patterns in the tested samples, the broken pieces of selected specimens (especially those with relatively low fracture loads) were put together and analyzed with an optical stereo microscope (Olympus SZH10, Olympus Ltd., Tokyo, Japan). Primary and secondary fractures were identified and compared to possible cleavage plane directions for each material. In an attempt to identify the fracture origin, selected broken pieces were tilted and mounted into a holder for analysis using Scanning Electron Microscopy (Jeol JCM-6000Plus Neoscope™, Jeol Ltd., Tokyo, Japan).

3. Results and discussion

3.1. Strength distributions of $LiNbO_3$ and $LiTaO_3$: Effect of environment

Fig. 5 shows the results of B3B tests conducted in ambient air (a, b, c) and ambient water (d, e, f) with different cross-head displacement rates (a, d: 0.01 mm/min; b, e: 0.1 mm/min; c, f: 1 mm/min) for both $LiNbO_3$ and $LiTaO_3$. The biaxial strength distribution for every sample is represented in a Weibull diagram, where the probability of failure, F, is plotted versus the failure stress, σ_f (calculated for every specimen according to Eq. (3)). The Weibull parameters σ_0 (characteristic strength) and m (Weibull modulus) of each sample were calculated according to EN-843-5 standard [43]. The dashed line represents the best fit to the strength data using the maximum likelihood method. The Weibull parameters (σ_0 and m) and their corresponding 90% confidence intervals are listed in Table 1.

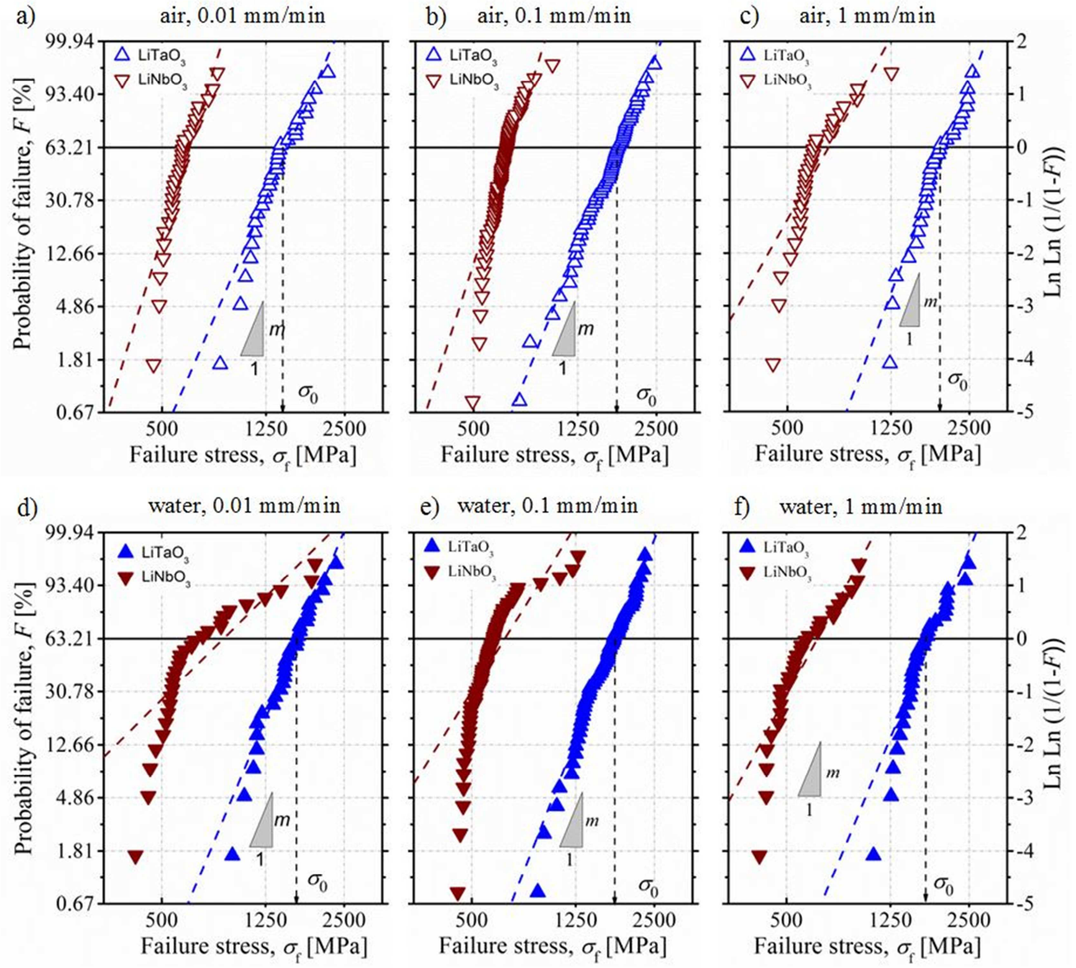

Figure 5: Weibull plot of 2 × 2 mm^2 $LiNbO_3$ and $LiTaO_3$ samples tested in different environments with different cross-head displacement rates: (a) 0.01 mm/min, air; (b) 0.1 mm/min, air; (c) 1 mm/min, air; (d) 0.01 mm/min, water; (e) 0.1 mm/min, water; (f) 1 mm/min, water. The dashed lines refer to the estimated Weibull distribution.

Table 1: Characteristic strength, σ_0, and Weibull modulus, m, of $LiNbO_3$ and $LiTaO_3$ 2 × 2 mm^2 single crystals, tested under biaxial loading both in air and in water with different cross-head displacement rates. The 90 % confidence intervals for σ_0 and m are given in brackets.

		Displacement rate [mm/min]					
		0.01		**0.1**		**1**	
Medium	**Parameter**	**$LiTaO_3$**	**$LiNbO_3$**	**$LiTaO_3$**	**$LiNbO_3$**	**$LiTaO_3$**	**$LiNbO_3$**
Air	**σ_0 [MPa]**	1520 [1421-1629]	638 [608-670]	1789 [1714-1867]	694 [671-718]	2036 [1920-2162]	720 [659-789]
	m	4.9 [3.7-6.0]	6.9 [5.2-8.4]	5.3 [4.4-6.1]	6.7 [5.5-7.3]	5.7 [4.2-6.9]	3.8 [2.8-4.6]
Water	**σ_0 [MPa]**	1680 [1573-1795]	733 [695-773]	1772 [1699-1848]	669 [626-716]	1802 [1688-1925]	657 [604-717]
	m	5.1 [3.8-6.2]	6.3 [4.7-7.6]	5.4 [4.5-6.3]	3.4 [2.8-3.9]	5.1 [3.8-6.2]	3.9 [2.9-4.8]

There is a significant difference in strength between $LiNbO_3$ and $LiTaO_3$ for all testing conditions, the characteristic strength of $LiTaO_3$ being (on average) ~2.5 times higher than that of $LiNbO_3$. It is noticeable that, whereas the strength values of $LiTaO_3$ lie on the fitted Weibull distribution, the strength values of $LiNbO_3$ show in several cases pronounced deviations from the expected Weibull behaviour. On the one hand, especially for lower strength values, the fitted curves do not describe the real strength distribution of the $LiNbO_3$ material. There seems to be a "threshold stress", at *approx.* 450 MPa, below which the material does not fail. On the other hand, in some series (e.g. Fig. 5d, 5e), specimens with extraordinarily high strength values are present. This might be related to specimens with very small surface defects or a consequence of the "inhomogeneous" stress field due to the relatively small surface area of the B3B test. In the latter case, critical defects located outside the region of maximum applied stress during the test may be activated at higher applied loads, thus leading to "apparent" higher strength values. Regarding the scatter of measured strengths, and assuming Weibull behavior, the calculated Weibull moduli is similar for both materials, m ranging between 3 and 7. These values are in the range of those reported for silicon single crystals [12], yet relatively low compared to "polished" polycrystalline ceramics (e.g. alumina, silicon-nitride, glass-ceramic composites, etc.), where m up to 30 or higher have been reported [44].

In order to visualize the effect of environment on strength, the results listed in Table 1 are plotted in Fig. 6 together with their corresponding 90% confidence intervals (CI) for comparative purposes. Due to the overlapping 90% CI it can be concluded that for $LiNbO_3$ neither an influence of the testing speed nor the environment on strength could be found. Only in the case of $LiTaO_3$ tested in water a very slight trend to higher strength with higher cross-head displacement rates could be observed. This leads to the conclusion that both materials are almost not susceptible to environmental assisted cracking. Hence, the mechanical reliability of $LiNbO_3$ and $LiTaO_3$ single crystals is not expected to be compromised when exposed to humid environments.

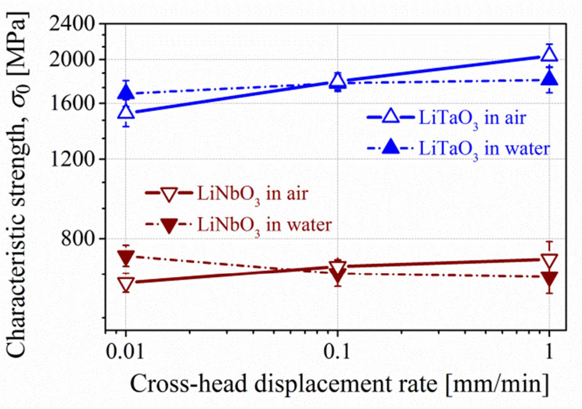

Figure 6: Dependence of characteristic strength of $LiNbO_3$ and $LiTaO_3$ on testing speed and environment.

3.2 Effect of tested volume on the strength

In order to assess the Weibull character of $LiNbO_3$ and $LiTaO_3$, the "volume effect" on strength was investigated by testing larger samples under a particular loading condition. Two series of 60 specimens of dimensions 12 × 12 × 0.35 mm³ were tested at a cross-head displacement rate of 1 mm/min in air for both $LiNbO_3$ and $LiTaO_3$, respectively. Strength results were compared to those from the 2 × 2 × 0.13 mm³ samples. Since no (or very little) environmental effect on strength was found previously, data pooling was performed in the 2 × 2 mm^2 specimens for both $LiNbO_3$ and $LiTaO_3$ in order to gain greatest statistical significance.

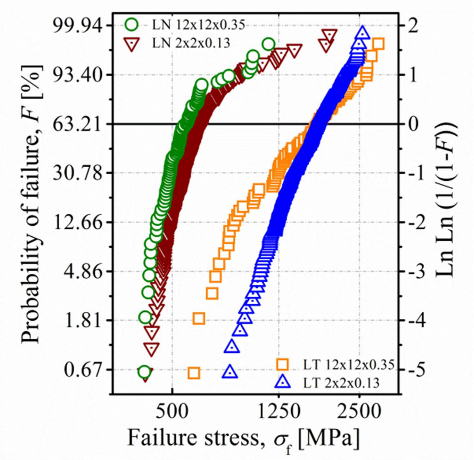

Figure 7: Weibull plot of $LiNbO_3$ and $LiTaO_3$ samples of different sizes (2 × 2 × 0.133 mm³ and 12 × 12 × 0.35 mm³)

Fig. 7 shows the comparison between the strength distribution of small and bigger samples for both $LiNbO_3$ and $LiTaO_3$ materials. It can be observed that the strength values of the bigger $LiNbO_3$ samples are only a few percent lower than those of the small samples. For the case of $LiTaO_3$, both samples exhibit almost the same strengths (although with a slightly higher scatter in the bigger sample)[ξ]. Considering the much larger surface (or volume) of the 12 × 12 × 0.35 mm³ specimens under tensile stresses during the B3B tests, a significant effect on strength should be seen. According to Weibull theory, the following relation holds for two samples having different effective surfaces [45, 46]:

$$\frac{\sigma_{equ,1}}{\sigma_{equ,2}} = \left(\frac{S_{eff,2}}{S_{eff,1}} \right)^{1/m} \qquad (4)$$

where $\sigma_{\mathrm{equ},1}$ and $\sigma_{\mathrm{equ},2}$ are the equivalent stress values for samples 1 and 2, respectively, and $S_{\mathrm{eff},1}$ and $S_{\mathrm{eff},2}$ the corresponding effective surfaces during testing. The parameter m is the Weibull modulus of the material. Scaling using effective surfaces was chosen instead of the more commonly used volume extrapolation, because brittle single crystals usually fail from surface defects [13, 15].

Taking an average Weibull modulus of $m \sim 5$ for both materials (see Table 1), and a calculated ratio between effective surfaces of *approx.* 15 times (the ratio of bending radius squared), a factor difference in strength between the samples of about 1.7 would be expected, according to Eq. (4). However, strength data for both sample sizes result to be very similar (see Fig.7). Based upon these findings, there seems to be no surface (or volume) effect in these materials. A possible explanation may be associated with the used B3B testing method. The maximal loaded surface (or volume) for the B3B test is very small, namely between 0.1% and 1% of the plate surface (or volume). This means that for the 2 × 2 mm^2 samples, a surface as small as 10 × 10 μm^2 may be under maximal load. For the case of 12 × 12 mm^2 samples, this may raise up to 60 × 60 μm^2. As a consequence, the tested surface may not be large enough to sample the real defect distribution in the single crystal materials – for small as well as for bigger specimens – because of the relatively large size of surface defects compared to depth, e.g. for a surface scratch (a detailed analysis is given in section 3.3). Furthermore, it is possible that no surface effect was measured because the damage due to polishing always introduces scratches of the same size - independent of the specimen geometry. However, this should yield higher Weibull moduli, which is not the case obtained experimentally in our studies. In this regard, uniaxial bending tests (e.g. 3 or 4-point-

---

[ξ] We caution the reader that the higher scatter observed in the bigger sample can be associated with the fact that specimens were taken from different wafers (4 wafers for LN and 8 wafers for LT from different suppliers). They may have different finishing.

bending) are planned to sample more “effective surface” during the test and thus be able to assert whether this type of “wafer” material lacks a Weibull character.

3.3 Failure analyses

3.3.1 Indexing of cleavage planes

Figures 8a and 8b show typical fracture patterns found in most of the tested (2 × 2 mm^2) samples for $LiNbO_3$ and $LiTaO_3$, respectively. It is worth highlighting that specimens with relatively low fracture strength were chosen for the analyses because of the fewer fracture pieces. Specimens with high fracture strength broke into tens of pieces due to the high stored elastic energy during the B3B test. The coloured marks on the specimens were intended to facilitate a given orientation of the specimen in the B3B testing jig. The fracture patterns observed in the referred figure revealed different fracture behavior between $LiNbO_3$ and $LiTaO_3$. In almost every tested specimen, cracks parallel to the x-axis (i.e. perpendicular to the wafer flat) could be observed for $LiNbO_3$, while cracks with an angle of ~ 45° were always present for the $LiTaO_3$ material (see Fig. 8). The presence of cleavage planes from the family {01.2} in these type of crystal structures is well documented in literature [28, 32]. These planes can be identified in the fracture patterns shown in Fig. 8, yet having different fracture angles in $LiNbO_3$ and $LiTaO_3$ samples due to the different rotation of the two single crystal materials (different wafer orientation) before cutting. For illustrative purposes, the {01.2} cleavage planes are depicted in Fig. 9 for both $LiNbO_3$ and $LiTaO_3$ samples (after crystal rotation and final cut).

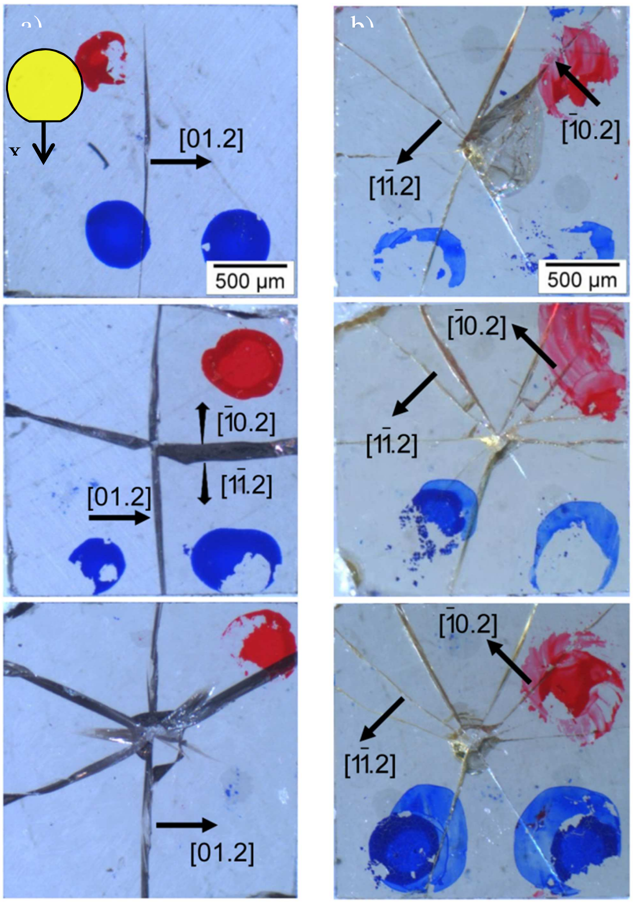

Figure 8: Top view on 2 × 2 × 0.13 mm³ broken specimens from a) $LiNbO_3$ and b) $LiTaO_3$ samples with directions perpendicular to {01.2} cleavage planes. Thickened arrows represent the direction normal to the planes with 47° to the surface (e.g. $(1\bar{1}.2)$ and $(\bar{1}0.2)$). Additional fracture planes are also visible. The coloured marks on the specimens are set for identification purposes.

In Fig. 8 these planes are marked with arrows representing directions perpendicular to them. In $LiTaO_3$ cracks along $(1\bar{1}.2)$ and $(\bar{1}0.2)$, both with an angle of 87° with respect to the surface, were visible in almost every sample. These two planes can also be identified in some $LiNbO_3$ samples where their angle with respect to the surface is 47° for both planes (see Fig. 9a). For illustrative purposes, thickened arrows in Fig. 8a represent the direction normal to these planes. In $LiNbO_3$ cracks along the (01.2) planes, which have an angle of 85° with respect to the surface, are the most common ones. Cleavage occurs due to the presence of a critical tensile stress acting normal to the cleavage plane. The most critical cleavage planes activated during the B3B biaxial test are those which are aligned (close to) 90° with respect to the surface. In our case these planes are: the (01.2) plane with an angle of 85° for $LiNbO_3$ (see Fig. 9a), and the $(\bar{1}0.2)$ and $(1\bar{1}.2)$ planes for $LiTaO_3$, both with an angle of 87° (see Fig. 9b). Whereas for the $LiNbO_3$ cracks can be also observed along the other two {01.2} cleavage planes, i.e. $(1\bar{1}.2)$ and $(\bar{1}0.2)$, both with an angle of 47° with respect to the surface, the (01.2) plane in $LiTaO_3$, with an angle of 9° with respect to the surface, cannot be activated in this testing configuration (see Fig. 4 and Fig. 9).

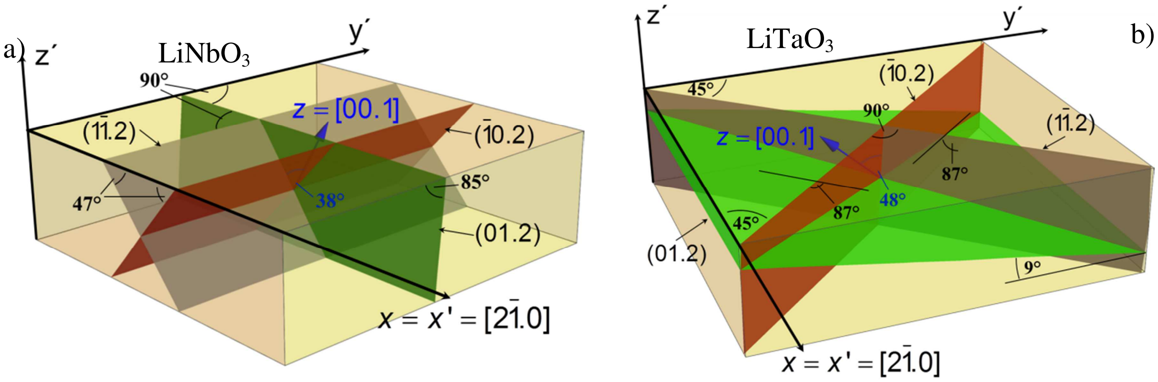

Figure 9: Schematic of cleavage planes for both $LiNbO_3$ and $LiTaO_3$ samples (after crystal rotation and final cut). Note that the three cleavage planes (01.2), $(\bar{1}0.2)$ and $(1\bar{1}.2)$ belong to the same family {01.2}, being equivalent within the C_3-symmetry.

Further observable cracks in Fig. 8, which also belong to crystallographic planes are not documented for $LiNbO_3$ and $LiTaO_3$ in the literature so far, and may also correspond to planes with relatively low fracture energy. In Table 2, the most frequently observed fracture planes activated during B3B tests are indexed for both materials.

Table 2: Indexed fracture planes based upon the fracture patterns observed after the B3B tests in $LiNbO_3$ and $LiTaO_3$ single crystal specimens. The corresponding measured angle at the surface is also given.

Material	Fracture planes / Angle to the surface					
$LiNbO_3$	(01.2) / 85°	$(\bar{1}0.2)$ / 47°	$(1\bar{1}.2)$ / 47°	$(\bar{1}1.1)$ / 87°	(10.1) / 87°	$(0\bar{1}.1)$ / 34°
$LiTaO_3$	(01.2) / 9°	$(\bar{1}0.2)$ / 87°	$(1\bar{1}.2)$ / 87°	$(\bar{1}\bar{1}.3)$ / 76°	$(1\bar{2}.3)$ / 76°	$(\bar{1}2.3)$ / 27°

In order to provide a clearer evidence of the activation of such additional planes, the fracture patterns in the 12 × 12 mm^2 samples were also analysed. The new planes are marked for a 12 × 12 × 0.35 mm^3 128° Y-X $LiNbO_3$ specimen in Fig. 10a. The corresponding Bravais-Miller's indices need to fullfill the equation K–H+L=3k. This mathematical condition comes from the solved system of equations (1). From the crystallographic point of view, this condition needs to be fulfilled because not all Bravais-Miller indices are significant due to the transformation from rhombohedral to hexagonal lattice, where the volume of the unit cell is tripled. Therefore also the number of atoms is tripled making two thirds of the Bravais-Miller indices meaningless [37]. Accordingly (10.1) and $(\bar{1}1.1)$ as well as $(0\bar{1}.1)$ – because of the 120° symmetry of the unit cell – were also identified as cleavage planes in $LiNbO_3$ (and most likely in $LiTaO_3$ too). These {10.1} cleavage planes have been also documented in Sapphire, $CaCO_3$, $MgCO_3$ and $MnCO_3$ [47]. Whereas in 128° Y-X $LiNbO_3$ $(\bar{1}1.1)$ and (10.1) both have an angle of 87°, $(0\bar{1}.1)$ has an angle of 34° with respect to the surface and, therefore, might not be activated in the chosen testing configuration (see Fig. 4 and Fig. 9). Especially for the 12 × 12 × 0.35 mm^3 samples, some of the observed cracks seemed to turn into one of the $\{20.\bar{1}\}$ planes.

Fig. 10b shows new indexed fracture planes for 42° Y-X $LiTaO_3$. Making the same considerations as for $LiNbO_3$, $(\bar{1}\bar{1}.3)$, $(1\bar{2}.3)$ and because of symmetry reasons $(\bar{1}2.3)$ can also be considered to be cleavage planes in the $LiTaO_3$ material (and most likely in $LiNbO_3$ too). Their angles with respect to the surface were 76° for $(\bar{1}\bar{1}.3)$ and $(1\bar{2}.3)$ and 27° for $(\bar{1}2.3)$, respectively. Also cracks along $(2\bar{1}.0)$ were occasionally visible (Fig. 10b).

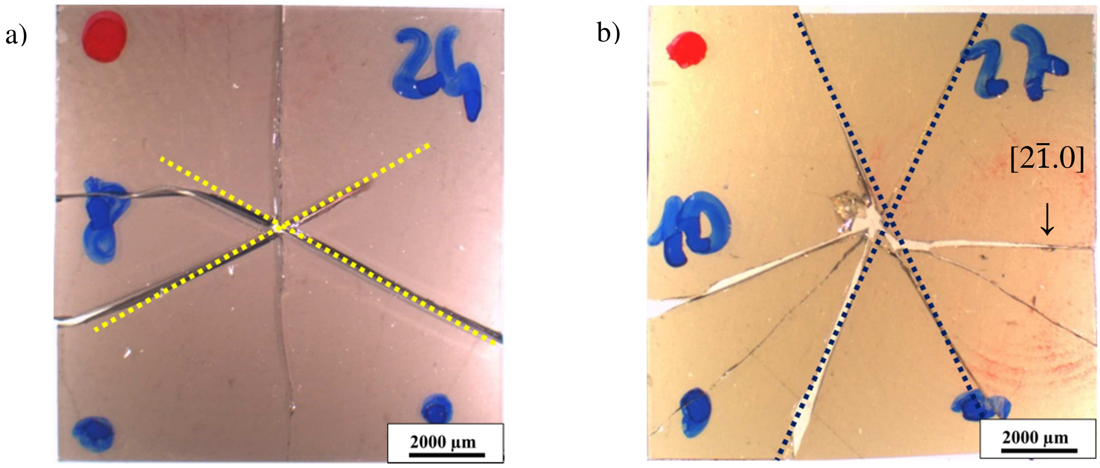

Figure 10: Observed cracks on B3B 12 × 12 mm^2 tested specimens from a) 128° Y-X $LiNbO_3$ and b) 42° Y-X $LiTaO_3$ samples. Additionally to the typical {01.2} cleavage planes, further planes could be identified and indexed as {10.1} for $LiNbO_3$ and $\{1\bar{2}.3\}$ for $LiTaO_3$ (see dashed lines).

3.3.2 Surface characterization

Fracture patterns of biaxial loaded 128° Y-X $LiNbO_3$ and 42° Y-X $LiTaO_3$ single crystal specimens have clearly shown that these materials always fail along certain crystallographic planes of potentially low fracture energy, as expected for brittle single crystals. What remains still unclear is the significant difference in strength between $LiNbO_3$ and $LiTaO_3$ on the one hand and the large scatter in strength for each material on the other hand.

It is well known that brittle single crystals are very sensitive to surface damage [10]. For instance, in silicon single crystals it has been shown in many studies that the surface condition can have a pronounced influence on the measured strength values [13, 16]. In order to address topographic contrast, atomic force microscopy (AFM) was conducted. Fig. 11 provides a closer look onto a representative area of 12 × 12 µm² for both $LiNbO_3$ and $LiTaO_3$ samples.

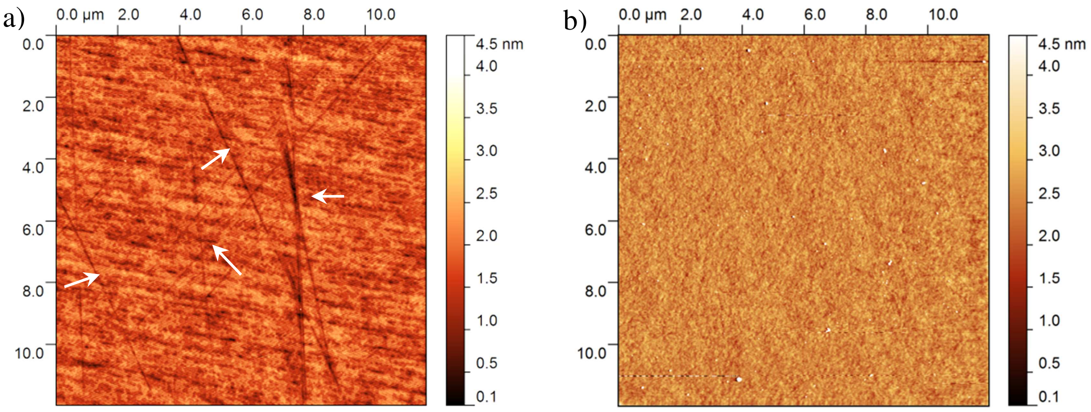

Figure 11: AFM measured topography of a) $LiNbO_3$ and b) $LiTaO_3$ surfaces. Similar roughness on the order of few nanometers are measured in both materials. However, tiny scratches on $LiNbO_3$ can be observed.

For $LiNbO_3$, the topography seems to be a little coarser and also tiny scratches can be observed (see arrows in Fig. 11a). However, these local minima are not located deeper than 4 nm (i.e. approximately the height of only three hexagonal unit cells) compared to the environment and are too small (when considering them as defects) to explain the significant difference in strength between $LiTaO_3$ and $LiNbO_3$ based upon linear elastic fracture mechanics (see more details in the next section). For $LiTaO_3$ no scratches or damage could be measured and peak maxima also do not differ by more than 4 nm from the minima (Fig. 11b). The average roughness was also very similar, resulting in 0.4 ± 0.1 nm for $LiNbO_3$ and 0.3 ± 0.1 nm for $LiTaO_3$. Based upon these measurements, the questions raises whether possible damage below the surface may have been covered during the fine polishing process. In order to identify such possible damage, a detailed analysis of the fracture surfaces of broken specimens was performed using SEM.

3.3.3 Identification of failure origins

Fracture surfaces of two selected $LiNbO_3$ and $LiTaO_3$ specimens from the 12 × 12 × 0.35 mm³ samples that failed at low loads were examined with SEM and are shown in Figs. 12 and 13, respectively. The two $LiNbO_3$ specimens (Fig. 12) failed almost parallel to the most critical (01.2) cleavage plane. The fracture surfaces are very smooth, indicating low fracture energies. Very interestingly, a damaged zone could be identified on the top side (tensile side) of both samples, most probably associated with the polishing process (e.g. scratches), as documented for single crystal silicon [48]. It can be inferred from Fig. 12a that a “pre-damaged” layer (see white full arrows) may have extended upon loading, thus forming a “post-damaged” zone (see white broken arrows), before complete fracture. The “saw-like” feature at the tensile surface on one of the specimens, highlighted in the close-up in Fig. 12a with white arrows, indicates that the pre-damage might have not been perfectly aligned parallel to the cleavage plane and that the propagating crack may have turned into this favoured plane during loading. This surface pre-damaged area extends over more than 100 µm and approximately 1 to 2 µm in depth. This damage was only visible post-mortem, probably due to clogging of these scratches during polishing or forming of an amorphous layer below the surface, as reported elsewhere [49].

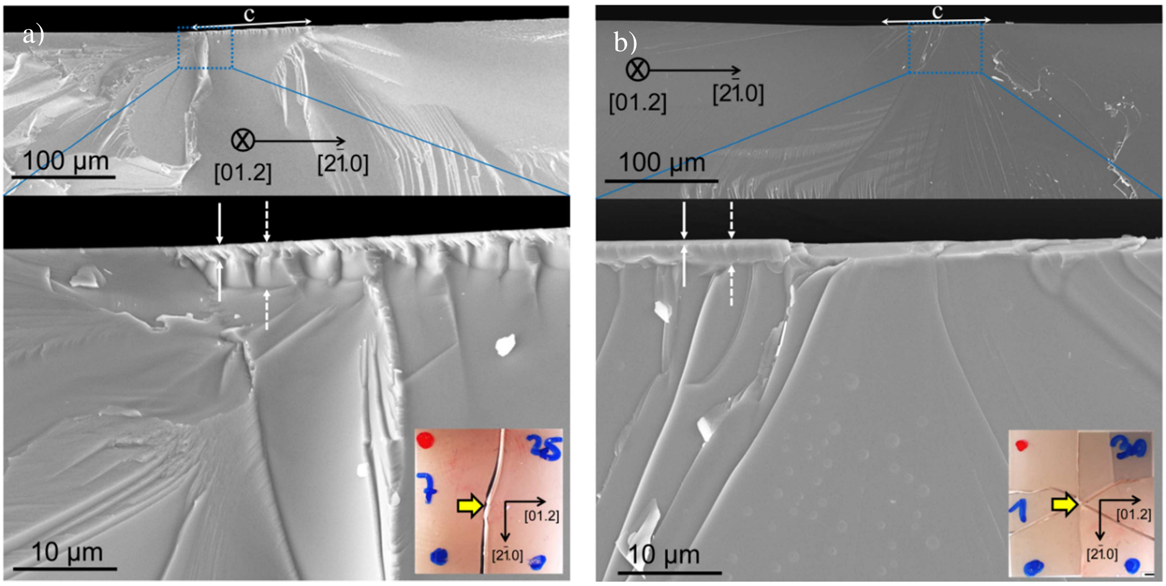

Figure 12: Fracture surfaces of two 12 × 12 × 0.35 mm³ $LiNbO_3$ specimens failed at low loads. White full and broken arrows mark the depth of both the “pre-damaged” and “post-damaged” zone, respectively. The surfaces of the B3B broken specimens are shown as insert for illustrative purposes.

For the $LiTaO_3$ samples the fracture origin could be identified at the tensile surface following back the origin of hackle lines, as illustrated in Figs. 13a) and b). However, in general, clear damage as that evidenced in the $LiNbO_3$ specimens could not be discerned in $LiTaO_3$. Only in some cases, the typical saw-like structure as observed in the $LiNbO_3$ specimens was also identified (see close-up in Fig. 13a), where the orientation of the surface defect might have been misaligned to the cleavage plane. Nevertheless, the initial pre-damage in $LiTaO_3$ seems to be less severe than for $LiNbO_3$.

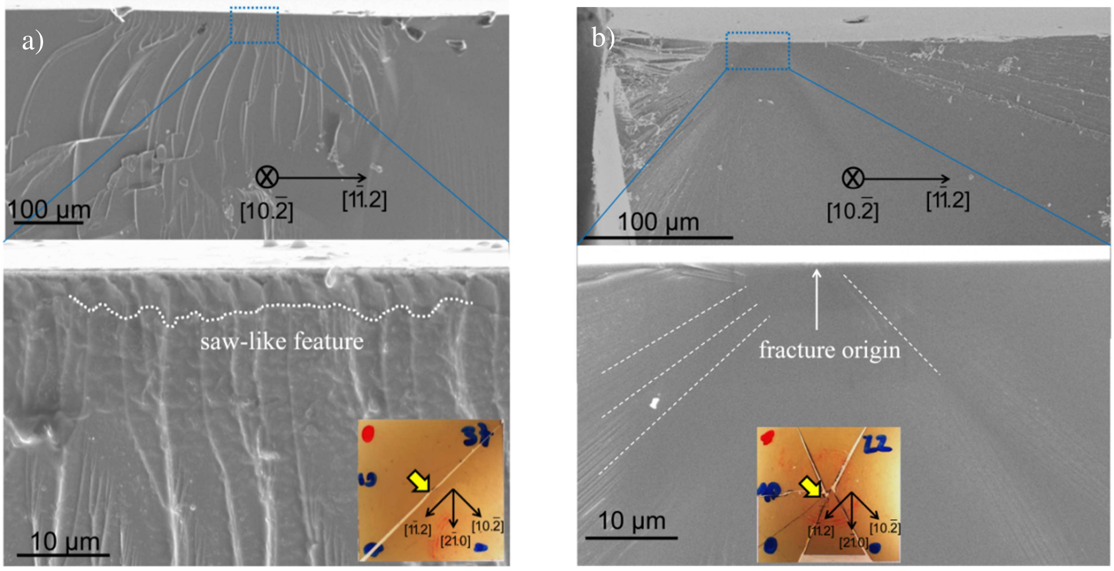

Figure 13: Fracture surfaces of two 12 × 12 × 0.35 mm³ $LiTaO_3$ specimens failed at low loads. A “pre-damaged” area followed by a “post-damage” (saw-like) zone is only found in a). The surfaces of the B3B broken specimens are inserted for illustrative purposes.

In addition, fracture patterns clearly show that not only the depth and extension of the scratch plays a role, but also its alignment with respect to cleavage planes, as reported for other single crystal materials (see Fractography of ceramics and glasses, *Section 8: Single crystals* [48]). A scratch aligned parallel to a cleavage plane will therefore cause significantly lower strength values than for any other orientation because of the low toughness of the cleavage plane and therefore higher sensitivity to defects under applied load (see Ref. [47]). In addition, the toughness of the cleavage planes in both materials may be also different, a fact that would support the strength difference between $LiNbO_3$ and $LiTaO_3$. Based upon fractographic observations in the $LiNbO_3$ material, the fracture resistance was estimated according to the Griffith criterion [50]:

$$K_c = \sigma_f \cdot Y \cdot \sqrt{\pi \cdot a_c} \qquad (5)$$

where K_c is the fracture resistance, σ_f the failure stress of the specimen, a the depth of the crack-like flaw, and Y a dimensionless factor depending on the loading configuration and crack shape. Both $LiNbO_3$ specimens in Fig. 12 showed an extended shallow crack at the surface, c, much longer than the depth of the crack into the material, with a ratio $c/a \approx 50$. Thus, a value of 1.12 (for an infinite surface scratch) was taken for Y [48]. The resulting fracture resistance value for $LiNbO_3$ (for $a \approx 1.5$ µm, $\sigma_f \approx 550$ MPa) in Fig. 12b was approx. 1.3 $MPa{\cdot}m^{1/2}$. The minimum toughness might be a little smaller due to the angle between defect and cleavage plane which probably leads to slightly higher toughness values. For $LiTaO_3$, no clear starting defect could be measured.

It can be concluded that low strength values occurred when scratches orientated parallel to a cleavage plane were aligned in the region of the maximum stress field (see Fig 12 and 13). For the case of the high values in the strength distribution (see Fig 7), these may be explained due to the inhomogeneous stress field during the B3B test. This means that critical defects, which are outside the maximum stress field in the central region of the loading ball, need more applied load to be activated.

To fully answer the question whether different sizes of surface defects are responsible for the different strength between $LiTaO_3$ and $LiNbO_3$ or if scratches in $LiTaO_3$ are simply not visible on the fracture surfaces, further analyses will be required. It is hypothesized that $LiNbO_3$ may be more sensitive to the cutting process, as well as to contact damage during the harsh grinding and polishing process because of its lower hardness compared to $LiTaO_3$. As a result, scratches may simply penetrate deeper during the final polishing. The sensitivity due to contact damage will be evaluated in future work by performing spherical nanoindents and studying the onset of cracks in both materials.

5. Conclusions

Biaxial strength measurements using the B3B test were performed to evaluate the mechanical strength of $LiNbO_3$ and $LiTaO_3$ single crystals. It could be demonstrated that neither materials show significant environmental assisted cracking. The characteristic strengths of $LiTaO_3$ were significantly higher than for $LiNbO_3$. Based upon surface roughness measurements and fractography, the difference in strength between $LiNbO_3$ and $LiTaO_3$ is abscribed to a higher sensitivity of $LiNbO_3$ to surface damaging, because almost no scratches (or not so deep) could be observed in this work for $LiTaO_3$.

Fractographic analyses showed different fracture patterns for both materials due to the different wafer orientations. Both materials tended to fail along the known family {01.2} of cleavage planes. However, further cracks in different directions were observed, which were attributed to cleavage planes with low fracture energies that could be indexed for the first time in this work.

Anomalous Weibull behavior was observed for $LiNbO_3$, with some specimens showing extraordinary high strength values. In addition, strength measurements on larger samples for both materials (i.e. ~15 times larger effective surface than the reference sample) resulted in almost the same strength values, which is also not in agreement with predictions for Weibull materials.

6. Acknowledgements

Financial support by the Austrian Federal Government (in particular from Bundesministerium für Verkehr, Innovation und Technologie and Bundesministerium für Wissenschaft, Forschung und Wirtschaft) represented by Österreichische Forschungsförderungsgesellschaft mbH and the Styrian and the Tyrolean Provincial Government, represented by Steirische Wirtschaftsförderungsgesellschaft mbH and Standortagentur Tirol, within the framework of the COMET Funding Program is gratefully acknowledged. The author M. Gruber would like to acknowledge financial support by the JECS Trust (201363-30).

7. References

[1] K.-Y. Hashimoto, Surface Acoustic Wave Devices in Telecommunications: Modelling and Simulation, Springer-Verlag Berlin Heidelberg GmbH 2000.

[2] D. Morgan, Surface Acoustic Wave Filters, 2nd ed., Academic Press 2007.

[3] A.J. Slobodnik, The Temperature Coefficients of Acoustic Surface Wave Velocity and Delay on Lithium Niobate, Lithium Tantalate, Quartz, and Tellurium Dioxide, Physical Sciences Research Papers 477 (1971).

[4] A.J. Slobodnik, Surface Acoustic Waves and SAW Materials, Proceedings of the IEEE: Special Edition on Surface Acoustic Waves, Institute of Electrical and Electronics Engineers, 1976.

[5] K.-Y. Hashimoto, RF Bulk Acoustic Wave Filters for Communications, ARTECH HOUSE 2009.

[6] C.C.W. Ruppel, T.A. Fjeldly, Advances in Surface Acoustic Wave Technology, Systems and Applications, World Scientific Publishing Group 2000.

[7] M.B. Schulz, B.J. Matsinger, M.G. Holland, Temperature Dependence of Surface Acoustic Wave Velocity on α Quartz, J. Appl. Phys. 41(7) (1970) 2755-2765.

[8] K. Shibayama, K. Yamanouchi, H. Sato, T. Meguro, Optimum Cut for Rotated Y-Cut LiNbO3 Crystal Used as the Substrate of Acoustic-Surface Wave Filters, Proceedings of the IEEE, 1976, pp. 595-597.

[9] T. Yi, L. Li, C.-J. Kim, Microscale material testing of single crystalline silicon: process effects on surface morphology and tensile strength, Sens. Actuators A 83(1-3) (2000) 172-178.

[10] G.D. Quinn, Fractographic analysis of very small theta specimens, Key Eng. Mat. 409 (2009) 201-208.

[11] M.S. Gaither, F.W. DelRio, R.S. Gates, E.R. Fuller, R. Cook, F., Strength distribution of single-crystal silicon theta-like specimens, Scripta Mater. 63 (2010) 422-425.

[12] A.A. Wereszczak, A.S. Barnes, K. Breder, S. Binapal, Probabilistic strength of 1 1 1 n-type silicon, Journal of Materials Science: Materials in Electronics 11(4) (2000) 291-303.

[13] C. Funke, E. Kullig, M. Kuna, H.J. Möller, Biaxial Fracture Test of Silicon Wafers, Adv. Eng. Mat. 6 (2004) 594-598.

[14] B.N. Jaya, V. Jayaram, Fracture Testing at Small-Length Scales: From Plasticity in Si to Brittleness in Pt, The Journal of The Minerals, Metals & Materials Society 68(1) (2016) 94-108.

[15] I. Chasiotis, W.G. Knauss, The mechanical strength of polysilicon films: Part 1. The influence of fabrication governed surface conditions, J. Mech. Phys. Solids 51(8) (2003) 1533-1550.

[16] K.-S. Chen, A. Ayon, S.M. Spearing, Controlling and Testing the Fracture Strength of Silicon on the Mesoscale, J. Am. Ceram. Soc. 83(6) (2000) 1476-1484.

[17] M. Deluca, R. Bermejo, M. Pletz, P. Supancic, R. Danzer, Strength and fracture analysis of silicon-based components for embedding, J. Eur. Ceram. Soc. 31(4) (2011) 549-558.

[18] M. Deluca, R. Bermejo, M. Pletz, M. Weßner, P. Supancic, R. Danzer, Influence of deposited metal structures on the failure mechanisms of silicon-based components, J. Eur. Ceram. Soc. 32(16) (2011) 4371-4380.

[19] R. Danzer, T. Lube, P. Supancic, R. Damani, Fracture of advanced ceramics, Adv. Eng. Mat. 10(4) (2008) 275-298.

[20] J.J. Gilman, Direct Measurements of the Surface Energies of Crystals, J. Appl. Phys. 31(12) (1960) 2208-2218.

[21] M. Iwasa, R.C. Bradt, Cleavage of natural and synthetic single crystal quartz, Materials Research Bulletin 22(9) (1987) 1241-1248.

[22] R. Cook, Strength and sharp contact fracture of silicon, J. Mater. Sci. 41(3) (2006) 841-872.

[23] M. Tanaka, K. Higashida, H. Nakashima, H. Takagi, M. Fujiwara, Orientation dependence of fracture toughness measured by indentation methods and its relation to surface energy in single crystal silicon, Int. J. Fract. 139(3) (2006) 383-394.

[24] Y.S. Kuz'minov, Lithium Niobate Crystals: Physico-chemical Aspects of Technology, Cambridge International Science Publishing 1999.

[25] T. Volk, M. Wöhlecke, Lithium Niobate: Defects, Photorefraction and Ferroelectric Switching, Springer-Verlag Berlin Heidelberg 2008.

[26] N. Miyazaki, A. Hattori, H. Uchida, Thermal shock cracking of lithium niobate single crystal, Journal of Materials Science: Materials in Electronics 8 (1997) 133-138.

[27] N. Miyazaki, N. Koizumi, Analysis of cracking of lithium tantalate ($LiTaO_3$) single crystals due to thermal stress, J. Mater. Sci. 41 (2006) 6313–6321.

[28] W. Hang, L. Zhou, J. Shimizu, J. Yuan, T. Yamamoto, Study on the Mechanical Properties of Lithium Tantalate and the Influence on its Machinability, International Journal of Automation Technology 7(6) (2013).

[29] D. Munz, T. Fett, Ceramics. Mechanical Properties, Failure Behaviour, Materials Selection, Springer, Berlin, 1999.

[30] K. Momma, F. Izumi, VESTA 3 for three-dimensional visualization of crystal, volumetric and morphology data, Journal of Applied Crystallography 44 (2011) 1272-1276.

[31] B.K. Vainshtein, M. Cardona, P. Fulde, H.J. Queisser, Modern crystallography I, symmetry of crystals. methods of structural crystallography, Crystal Research and Technology 17(3) (1982) 352-352.

[32] R.S. Weis, T.K. Gaylord, Lithium niobate: Summary of physical properties and crystal structure, Applied Physics A 37(4) (1985) 191-203.

[33] S.C. Abrahams, J.M. Reddy, J.L. Bernstein, Ferroelectric lithium niobate. 3. Single crystal X-ray diffraction study at 24°C, Journal of Physics and Chemistry of Solids 27(6–7) (1966) 997-1012.

[34] R. Hsu, E.N. Maslen, D. Du Boulay, N. Ishizawa, Synchroton X-ray Studies of LiNbO3 and LiTaO3, Acta Crystallographica Section B 53 (1997) 420 - 428.

[35] R.T. Smith, F.S. Welsh, Temperature Dependence of the Elastic, Piezoelectric, and Dielectric Constants of Lithium Tantalate and Lithium Niobate, AIP Publishing 42(6) (1971) 2219 - 2230.

[36] K. Taki, Y. Shimizu, Material Constants of LiTaO3 Determined from Surface Acoustic Wave Velocities, Japanese Journal of Applied Physics 33 (1994) 2976 - 2978.

[37] K.K. Wong, Properties of Lithium Niobate, INSPEC, The Institution of Electrical Engineers, London, United Kingdom 2002.

[38] A. Börger, P. Supancic, R. Danzer, The ball on three balls test for strength testing of brittle discs: stress distribution in the disc, J. Eur. Ceram. Soc. 22(9-10) (2002) 1425-1436.

[39] A. Börger, P. Supancic, R. Danzer, The ball on three balls test for strength testing of brittle discs: Part II: analysis of possible errors in the strength determination, J. Eur. Ceram. Soc. 24(10-11) (2004) 2917-2928.

[40] R. Danzer, P. Supancic, W. Harrer, Biaxial Tensile Strength Test for Brittle Rectangular Plates, J. Ceram. Soc. Jpn. 114(1335) (2006) 1054 - 1060.

[41] R. Bermejo, P. Supancic, I. Kraleva, R. Morrell, R. Danzer, Strength reliability of 3D low temperature co-fired multilayer ceramics under biaxial loading, J. Eur. Ceram. Soc. 31(5) (2011) 745-753.

[42] G. Simmons, H. Wang, Single Crystal Elastic Constants and Calculated Aggregate Properties: A Handbook, 2nd ed., MIT Press, Cambridge, MA, 1971.

[43] EN 843-5, Advanced Technical Ceramics - Monolithic Ceramics - Mechanical Tests at Room Temperature - Part 5: Statistical Analysis, EN 843-5, 1997, p. 40.

[44] R. Bermejo, P. Supancic, C. Krautgasser, R. Morrell, R. Danzer, Subcritical Crack Growth in Low Temperature Co-fired Ceramics under Biaxial Loading, Eng. Fract. Mech. 100 (2013) 108-121.

[45] W. Weibull, A Statistical Theory of the Strength of Materials, Generalstabens Litografiska Anstalts Förlag, Stockholm, 1939.

[46] R. Danzer, A general strength distribution function for brittle materials, J. Eur. Ceram. Soc. 10 (1992) 461-472.

[47] R.A. Schultz, M.C. Jensen, R.C. Bradt, Single crystal cleavage of brittle materials, Int. J. Fract. 65(4) (1994) 291-312.

[48] G.D. Quinn, Fractography of Glasses and Ceramics, US Government Printing Office, Washington, 2007.

[49] L. Zhang, I. Zarudi, Towards a deeper understanding of plastic deformation in mono-crystalline silicon, International Journal of Mechanical Sciences 43(9) (2001) 1985-1996.

[50] A.A. Griffith, The phenomenon of rupture and flow in solids, Phil. Trans. Roy. Soc. London A221 (1920) 163-198.

Publication B

Understanding the effect of surface flaws on the strength distribution of single crystals

M. Gruber, A. Leitner, I. Kraleva, D. Kiener, P. Supancic and R. Bermejo

Abstract:

The dependence of strength on the surface quality of brittle single crystals is highly relevant in certain microelectronic applications, where a certain roughening of the crystal surface is required to guarantee or enhance the functional properties of the final component. In this work, the effect of surface conditioning on the strength distribution of single crystals is assessed on $LiTaO_3$ and $LiNbO_3$ samples with distinct surfaces (i.e. polished, grinded and scratched). Artificial surface cracks (scratches) were introduced using a Berkovich nanoindenter tip oriented under various angles with respect to the most critical $\{01\bar{1}2\}$ cleavage plane. Biaxial tensile tests were performed using the ball-on-three-balls test. Fractographic analyses were carried out to interpret strength results. A direct correlation between sub-surface damage and strength was observed, associated with the hardness and elastic constants of the material, being strongly dependent on the crystal orientation with respect to the loading axis. The validity of the biaxial tests on scratched specimens for fracture toughness estimation is also discussed.

Keywords: Single crystals, surface modification, nano-scratch, biaxial strength, fracture.

1. Introduction

The constantly growing wireless communication market demands a huge amount of bandpass filters for radio frequencies, lying in a range between 3 kHz and 300 GHz. Especially for frequencies up to 1-2 GHz, surface acoustic wave filters are one of today's leading technologies [1; 2]. A typical device consists of a piezoelectric substrate, with metal finger electrodes on its surface. Some current examples are Die Sized Surface acoustic wave Packages (DSSPs) or Thin Film Acoustic Packages (TFAPs) [3; 4]. When an alternating voltage is applied through the metal electrodes on top of the substrate it causes a periodic displacement on the surface of the single crystals and thereby generates Surface Acoustic Waves (SAWs) at each finger [5]. These waves amplify each other if the wavelength equals two times the electrode's width plus two times the spacing between electrodes, leading to the desired emitted resonance frequency at the input Inter Digital Transducer (IDT). This frequency is a function of the wavelength and velocity of the surface acoustic wave, which depend on the corresponding substrate material and its orientation. For choosing the substrate material various considerations need to be taken into account to ensure functionality, among which a high coupling between electrical and mechanical field together with a low temperature dependence of the emitted resonance frequency, are highly desired [4; 6; 7]. In this regard, $LiTaO_3$ and $LiNbO_3$ turned out to be the most promising candidates, as they exhibit particular low acoustic losses [2; 6; 8].

An additional aspect in the design of these devices concerns the management of the longitudinal and transversal bulk acoustic waves emitted by the finger electrodes, which may lead to undesirable distortion of phase, amplitude and delay of the filter frequency. Figure 1a shows a schematic of a DSSP with the so-called cap chip and the functional chip. Strategies to enhance functionality are: (i) thinning the functional substrate and thus reduce the available volume for bulk acoustic waves (see Fig. 1b), and (ii) roughening the back-side of the functional chip in order to scatter away unwanted bulk waves (see Fig. 1c) [7].

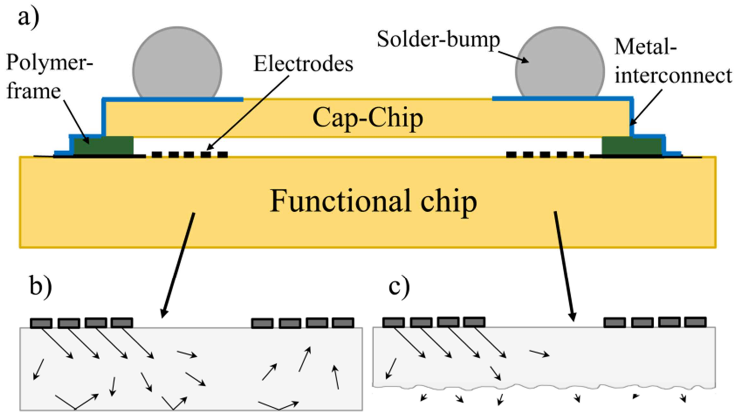

Figure 1. a) Schematic of the different parts of a DSSP. b) and c) Illustration of the effect of thinning and roughening on the propagation and refection of unwanted bulk acoustic waves in the DSSP device.

However, from the structural integrity point of view, thinning would lower the bearable loads. Likewise, roughening of the wafer may significantly reduce the strength of the substrate material, associated with the (relatively larger) introduced surface defects, as described by the Weibull theory [9; 10; 11]. Since significant thermo-mechanical stresses occur during the fabrication, assembly processes and qualification of these microelectronic devices [12; 13], functionality will be lost once the strength of the substrate material is exceeded, leading to cracking and failure.

The effect of roughening on strength has been studied on other brittle single crystals such as silicon [14; 15]. In the case of anisotropic materials as studied in the present work, even the effect of the grinding orientation of the wafer with respect to the applied load can affect the strength distribution of the material [16; 17; 18; 19]. In many cases, a relatively large scatter of the corresponding strength values and thus low Weibull moduli are documented regardless of surface finish (i.e. mirror polished, grinded, etched, or scratched) [12; 14; 18; 19; 20; 21]. The motivation of this work is to clarify the effect of cleavage plane orientation and surface finish on the strength distribution of single crystalline materials. Two highly anisotropic single crystal materials were investigated, namely $LiTaO_3$ and $LiNbO_3$, which exhibit cleavage planes with different orientations to the loading direction. Biaxial tensile testing was performed under identical conditions (controlled temperature and humidity) on samples with different surface conditioning: (i) mirror polished surface ("natural" flaws), (ii) commercially grinded surface (grinding lines), and (iii) mirror polished surface with artificial flaws (scratches) introduced using a Berkovich nano-indenter tip at various angles to the most critical $\{01\bar{1}2\}$ cleavage plane. Fractographic analyses were carried out to assess the possible damage caused by the respective surface conditions and to understand correlations between observed fracture patterns and measured strength values.

2. Experimental

2.1 Material of study and crystallographic orientations

$LiTaO_3$ and $LiNbO_3$ have a trigonal crystal structure. Below Curie temperature they belong to the 3m point group and R3c space group (no. 161) [22; 23; 24]. For the aim of simplicity, they are usually represented using a hexagonal crystal system ($a_h = b_h \neq c_h$ and $\alpha = \beta = 90°$, $\gamma = 120°$), even though the unit cell expands from 10 to 30 atoms, accordingly also its volume is tripled. The corresponding lattice parameters are $a_h = b_h = 5.154$ Å; $c_h = 13.783$ Å for $LiTaO_3$ and $a_h = b_h = 5.148$ Å; $c_h = 13.863$ Å for $LiNbO_3$, respectively [25]. The strong anisotropy of the single crystals can be used to tailor the properties of a respective wafer for its final application by using different wafer orientations. For the application as surface acoustic wave filters two advantageous configurations are provided in Figs. 2a and 2b. For $LiTaO_3$ the [0001] direction is rotated counterclockwise (48°) and for $LiNbO_3$ clockwise (38°) around the $[2\bar{1}\bar{1}0]$ axis, leading to a different alignment of crystallographic planes with respect to the wafer. As experimentally shown in previous work [19], several cleavage planes were prone to be activated during biaxial loading. In particular, $\{01\bar{1}2\}$ planes were identified as critical due to their low fracture energies and alignment (relatively steep angle to the surface) with respect to the loading direction. Figs. 2c and 2d illustrate the cleavage planes of interest in this work.

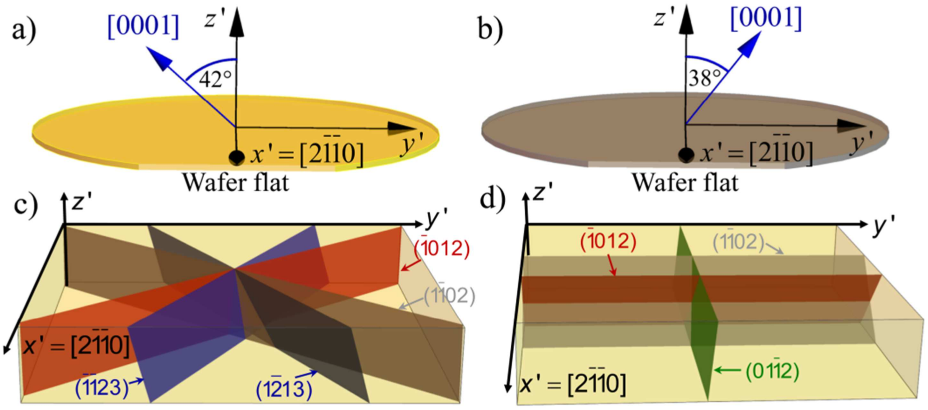

Figure 2. Schematic of a) $LiTaO_3$ and b) $LiNbO_3$ wafers rotated a certain angle around the x-axis. c) and d) orientation of relevant cleavage planes with respect to the wafer surface, for $LiTaO_3$ and $LiNbO_3$ respectively.

The investigated single crystalline samples were provided by EPCOS OHG (a TDK group company), Deutschlandsberg, Austria. Quadratic specimens of 2 x 2 mm^2 size (comparable to real SAW components) were cut from commercial wafers with a thickness of ~130 µm. All wafers were specified to have the same mirror polished quality on one side as well as similar roughened surface on the other side. Every single specimen was marked with colored dots (as depicted in Figs. 3a and 3b) to guarantee correct alignment throughout all performed tests.

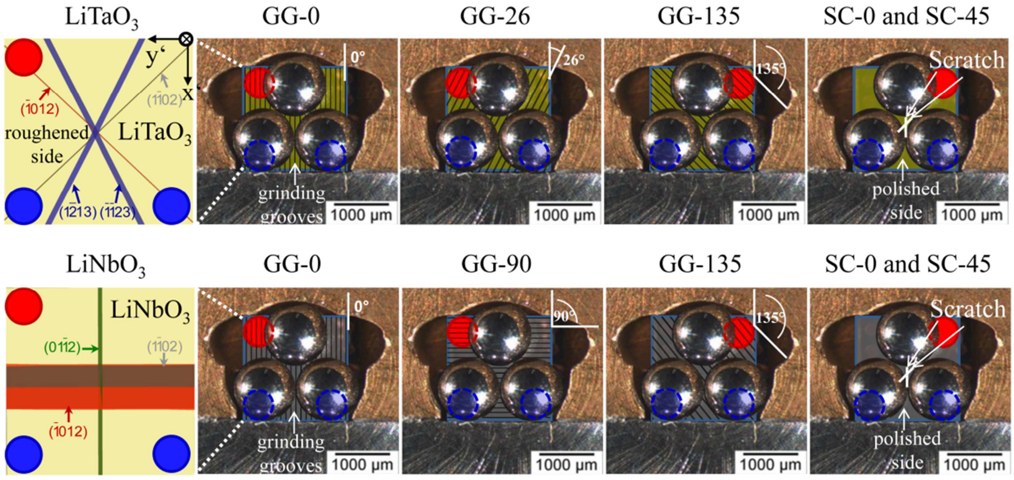

Figure 3. Alignment of critical cleavage planes and orientation of surface features introduced by scratching and grinding for $LiTaO_3$ (first row) and $LiNbO_3$ (second row). Colored dots indicate the testing configuration of the respective samples.

2.2 Surface conditioning

Several samples were prepared for each material, with specimens having different surface conditions: (i) mirror polished surface, (ii) grinded surface, and (iii) mirror polished surface with artificial scratches. The surface finishing of (i) and (ii) was made by the supplier in identical way for both materials.

- In the case of mirror polished specimens (here referred to as MP sample), no scratches could be identified using SEM imaging.
- In the case of the specimens with the grinded (rough) surface, a pattern of parallel grinding grooves (GG) was clearly observed on the surface after optical inspection due to the simultaneous rotation of grinding wheel and wafer. Three sets of samples with grinded surfaces (each containing at least 25 specimens) were prepared for $LiTaO_3$ and for $LiNbO_3$. Samples with grinding orientations of 0°, 26° and 135° for $LiTaO_3$ and 0°, 90° and 135° for $LiNbO_3$ (with respect to the x-axis of specimen in the testing jig) were pre-selected. They are referred to as GG-0, GG-26, GG-90 and GG-135, for the corresponding material as schematically illustrated in Fig. 3.
- For the scratched samples, one set of specimens with scratches parallel to the most critical $\{01\bar{1}2\}$ cleavage plane and one set with scratches as far away as possible (i.e. ~45°) from these crystallographic directions were prepared. These are referred to as SC-0 and SC-45, respectively, for both materials. The controlled surface scratches were introduced in the center of each testing specimen using a G200 nanoindenter (Keysight Technologies, Santa Rosa, California, USA) equipped with a Berkovich indenter tip. The scratch speed was set to 1 µm/s, with an applied load of 10 mN and a total scratch length of 100 µm. The scratch direction was chosen to be along one edge of the Berkovich tip (as schematically shown in Fig. 4). Scratches were exclusively made on mirror polished surfaces.

All experiments were carried out at room temperature and constant humidity (*approx.* 40% RH). Testing set-up and sample orientations are shown in detail in Fig. 3, where the first row belongs to the $LiTaO_3$ and the second row to the $LiNbO_3$ specimens, respectively. A schematic projection of the $\{01\bar{1}2\}$ critical cleavage planes is also depicted in Fig. 3 on the quadratic testing samples, for illustrative purposes. For $LiTaO_3$ also the two most critical out of six $\{11\bar{2}3\}$ planes are shown in Fig. 3.

2.3 Mechanical testing

A biaxial testing method, namely the ball-on-three-balls (B3B), was chosen in order to test the anisotropic fracture behavior of the brittle single crystalline materials. In the B3B method a small region near the surface (small effective surface/volume) is exposed to a well-defined biaxial stress field leading to a similar loading situation as expected for real microelectronic components, where the maximum stresses are usually concentrated in small regions (e.g. at material junctions or edges). Other advantages of the B3B method are the high accuracy and avoidance of edge defects. In the B3B the specimen is supported by three balls on one side and loaded through a fourth ball located in the center of the opposite side. Further information may be found in [26; 27; 28]. The diameter of the four balls employed was ~ 1.19 mm, leading to a supporting diameter of ~ 1.37 mm [26]. A preload of 1 N and cross-head displacement speed of 0.1 mm/min were set on a universal testing machine (Zwick Z010, Zwick/Roell, Ulm, Germany). Failure stress, σ_f, values were calculated according to:

$$\sigma_\mathrm{f} = f \cdot \frac{P}{t^2} \quad , \qquad (1)$$

with P being the maximal load at fracture, t the specimen thickness and f a dimensionless factor[ζ] which can be calculated based on geometry of the test setup and Poisson's ratio of the specimen, which was taken as 0.25 for both materials [29]. Small possible deviations of Poisson's ration due to crystal anisotropy were thereby neglected. For the testing conditions in this work a value of $f \sim 2.0$, as calculated in [12; 30]. Weibull analysis of the obtained failure stresses was performed on each sample according to the EN-843-5 standard [31]. A minimum of 15 specimens per sample (scratched specimens) was selected to guarantee statistical significant results. No contributions of piezo- or ferroelectric effects were taken into account in the strength calculation.

2.4 Fractographic analyses

Surface and cross-sectional sub-surface analyses were performed using a Focused Ion Beam (FIB) work station (Auriga, Zeiss, Oberkochen, Germany; with a gallium FIB system Cobra Z-05, Orsay Physics, Brno, Czech Republic). Roughness was evaluated on 3D surface images employing the software MEX (Alicona, Graz, Austria). For validation and documentation of sub-surface damages cross-sectional FIB cuts were performed with a Ga-beam of 30 kV where the current was systematically reduced from 20 nA down to 100 pA for the final polishing step. To gain more detailed topographic image further analyses were carried out in selected regions using an Atomic Force Microscope (AFM, BRR, Semilab, Budapest, Hungary). Fractographic analyses were performed on an optical microscope (Olympus BX50, Olympus, Tokyo, Japan), for overview images, and on a Scanning Electron Microscope (SEM, Jeol JCM-6000Plus Neoscope™, Jeol Ltd., Tokyo, Japan) for examination of fracture origins of the corresponding surfaces.

[ζ] The calculation of f for disc specimens tested with B3B can be accessed at the ISFK homepage (www.isfk.at).

3 Results and discussion

3.1 Surface and sub-surface morphology

3.1.1 Scratched samples

Figure 4 shows the surface and sub-surface damages caused by scratch experiments for $LiTaO_3$ (a-d) and $LiNbO_3$ (e-h) under the same applied load conditions. Scratch direction and orientation of the Berkovich-tip with respect to the crystallographic orientation (compare with Fig. 2) are schematically illustrated.

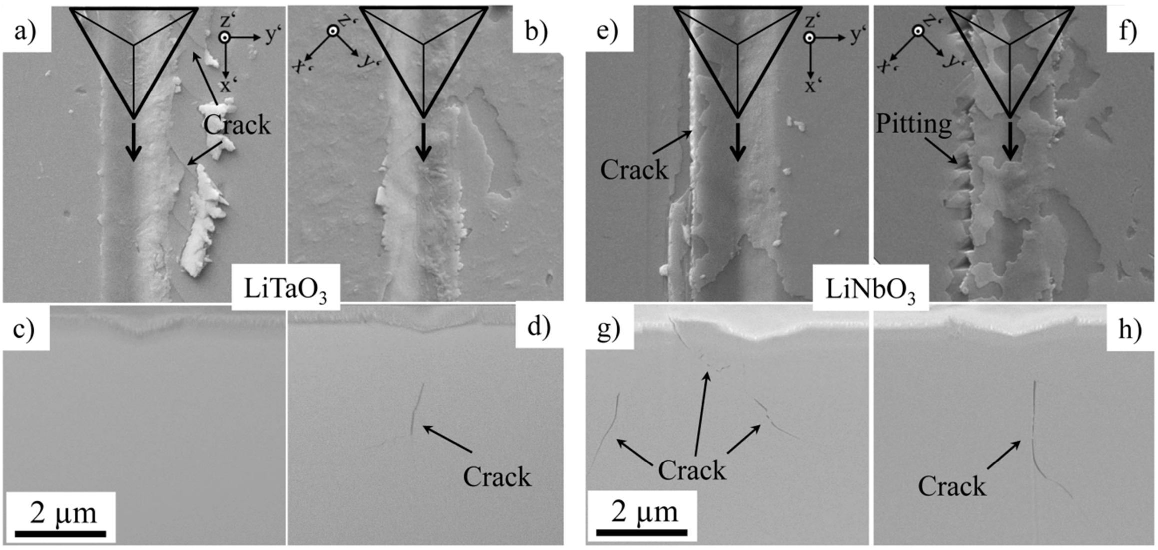

Figure 4. a) Top view on a $LiTaO_3$ specimen scratched in $[2\bar{1}\bar{1}0]$ direction (sample SC-0) with c) corresponding cross-section. b) Top view on a $LiTaO_3$ specimen scratched under 45° to the $[2\bar{1}\bar{1}0]$ direction (sample SC-45) with d) corresponding cross-section. e) Top view on a $LiNbO_3$ specimen scratched in $[2\bar{1}\bar{1}0]$ direction (sample SC-0) with g) corresponding cross-section and f) Top view on a $LiNbO_3$ specimen scratched under 45° to the $[2\bar{1}\bar{1}0]$ direction (sample SC-45) with g) corresponding cross-section. The scale bar in c) applies for all images.

For the $LiTaO_3$ sample with a scratch in $[2\bar{1}\bar{1}0]$ direction (Figs. 4a and 4c) cracks were observed on the surface following either the $(1\bar{1}02)$ plane or the $(1\bar{2}13)$ plane close to the scratch, turning into the $(1\bar{1}02)$ plane at a certain distance to it. Interestingly, no cracks underneath the scratch could be evidenced (Fig. 4c). It is conceivable that the scratches are only present at the very surface and cannot penetrate into the material because of compressive stresses underneath. For the $LiTaO_3$ specimen with the scratch parallel to the $(\bar{1}012)$ plane (see Fig. 4b), i.e. with an angle of 45° to the $[2\bar{1}\bar{1}0]$ direction, a median crack seems to open underneath the surface following the $(\bar{1}012)$ plane (Fig. 4d). In a depth of ~2.5 µm the crack bends into a lateral crack.

For the $LiNbO_3$ sample with the scratch parallel to the most critical $(01\bar{1}2)$ cleavage plane in $[2\bar{1}\bar{1}0]$ direction (Figs. 4e and 4g), a median crack up to the surface was observed. Cross-sectioning revealed a network of median and lateral cracks underneath the damaged region. For specimens with a scratch under 45° to the $(01\bar{1}2)$ plane (Figs. 4f and 4h) a median crack turning into a lateral crack underneath the surface was evidenced. However, no crack up to the surface could be observed. Instead, pitting was found between the damaged and non-deformed region. Interestingly, for both single crystalline materials less pronounced lateral cracks were found compared to scratch testing of soda-lime-silica glass [32], even though for $LiTaO_3$ the weak $(01\bar{1}2)$ cleavage plane is aligned almost parallel to the surface.

The penetration depth was recorded during the scratch tests for $LiTaO_3$ and $LiNbO_3$ specimens. Regardless the scratching direction no significant differences in depth were found. Fig. 5 shows the total penetration depth, h, versus scratch distance, l, in $[2\bar{1}\bar{1}0]$ direction of three representative measurements for each material.

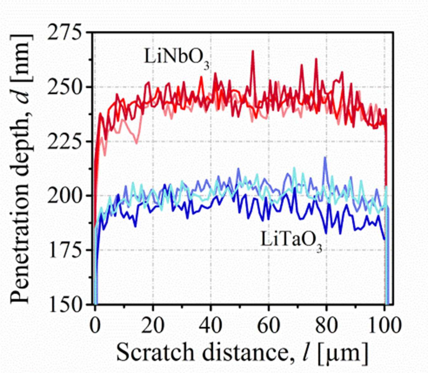

Figure 5. Total penetration depth versus scratch distance for $LiTaO_3$ and $LiNbO_3$ specimens with the orientation shown in Fig. 2 and scratches in $[2\bar{1}\bar{1}0]$ direction under 10 mN load.

It is evident that the residual scratches are deeper in $LiNbO_3$ than in $LiTaO_3$ for the same load of 10 mN, which can be explained by the higher hardness, i.e. 6.6 GPa versus 9.7 GPa respectively [33], and direction dependent stiffness [34; 35] of the latter. Furthermore, based on the observations in Figs. 4c, 4d, 4g, and 4h, it can be concluded that more severe damage occurs in the $LiNbO_3$ than in the $LiTaO_3$ material.

3.1.2 Grinded samples

Figure 6a shows the representative surface topology of a grinded $LiTaO_3$ specimen. An AFM image (close-up in Fig. 6a) is also included, revealing relatively sharp edges along the grinding grooves. The roughness profile along one representative path (red line) is included, showing that roughness minima and maxima differ by up to 200 nm. Similar observations were made for $LiNbO_3$. The average roughness for $LiTaO_3$ and $LiNbO_3$ was 38 ± 2 nm and 49 ± 2 nm, respectively, measured on three different locations on the wafer. In contrast to similar experiments on Si [17], no significant direction dependences could be observed. Figs. 6b and 6c show FIB cross-sections below the surface of $LiTaO_3$ and $LiNbO_3$ specimens, respectively.

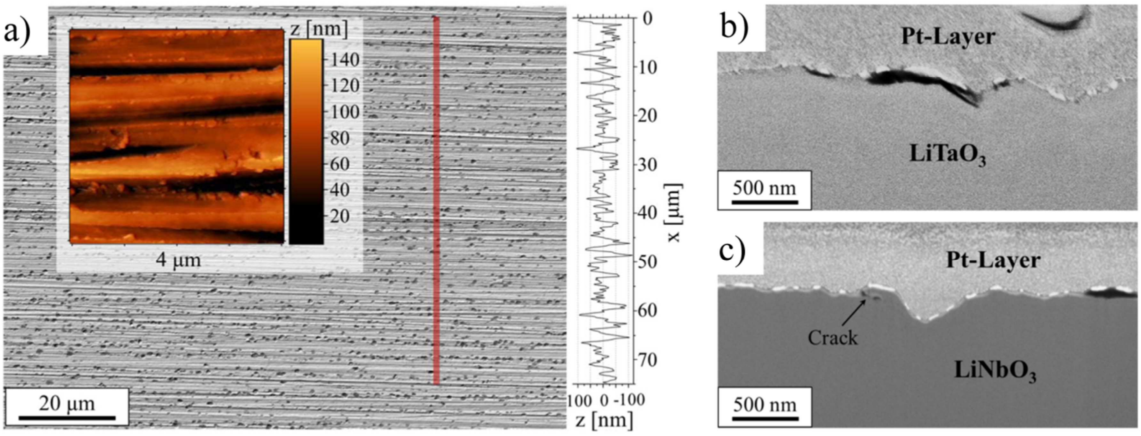

Figure 6. a) SEM image of the grinded side of a $LiTaO_3$ specimen along with the roughness profile along the red path. For a detailed view on the evaluation of scratches a 4 × 4 µm² AFM image is provided; b) and c) FIB cross section of a small region in $LiTaO_3$ and $LiNbO_3$ grinded specimens, substantiating the measured roughness profiles on larger scales in a).

A Pt-layer was deposited on the surface of the specimens before the FIB cut to achieve good image contrast and a sharp surface edge. The roughness profile observed on the cross-sections agrees with the data obtained with the 3D imaging. In the $LiNbO_3$ specimen a small crack close to the surface could be observed. It is worth pointing out that, although the sub-surface damages due to grinding are less severe than those introduced in the scratched specimens (compare Fig. 6 with Fig. 4), the residual depths of the scratches are similar to those of the grinding grooves. For the $LiTaO_3$ specimen with the scratches in $[2\bar{1}\bar{1}0]$ direction no cracks underneath the surface were observed (Fig. 4c). This suggests that the artificially introduced scratches induce well controlled damage as compared to the grinding grooves coming from the industrial surface roughening process.

3.2 Biaxial strength distributions

Figure 7 shows the biaxial strength results from the different samples in a Weibull representation. Figs. 7a and 7b correspond to the $LiTaO_3$ and Figs. 7c and 7d to the $LiNbO_3$ samples respectively, with a) and c) showing scratched samples, and b) and d) grinded samples together with data from mirror polished surfaces measured in previous work [19]. The statistical analyses of the individual strength distributions can be found in Table 1. Characteristic strength values, σ_0, and Weibull moduli, m, are provided along with the corresponding 90% confidence intervals.

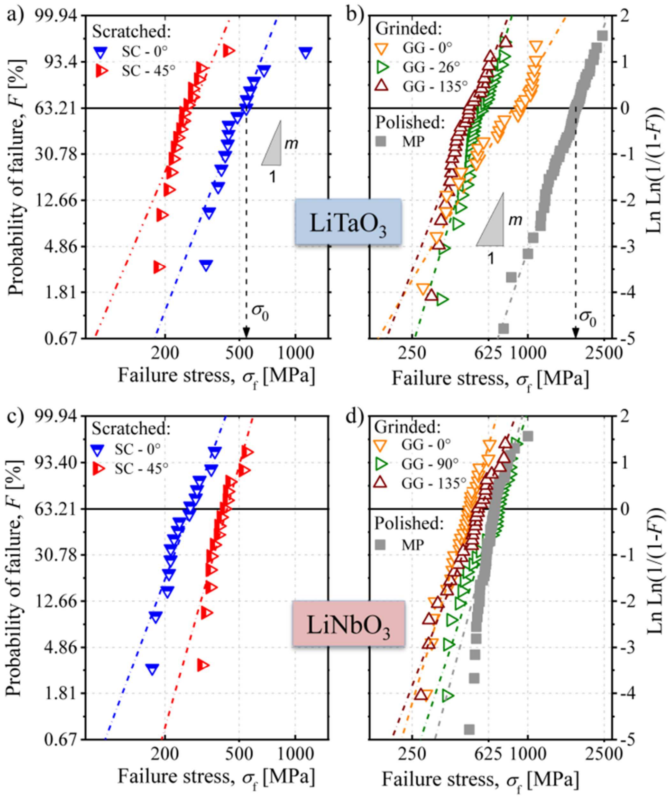

Figure 7. Weibull plots of the biaxial strength distributions for $LiTaO_3$ and $LiNbO_3$ materials with different surface conditions: a) and c) scratched samples, and b) and d) grinded samples together with data from mirror polished surfaces measured in previous work [19], respectively.

Table 1. Characteristic strength σ_0 and Weibull modulus m of the biaxial strength distributions of $LiTaO_3$ and $LiNbO_3$ samples with scratched, grinded and polished surfaces. The 90% confidence intervals for σ_0 and m are given in brackets.

$LiTaO_3$	**Scratch 0° (SC-0)**	**Scratch 45° (SC-45)**	**Grinding grooves 0° (GG-0)**	**Grinding grooves 26° (GG-26)**	**Grinding grooves 135° (GG-135)**	**Mirror Polished (MP)**
σ_0 [MPa]	**521** [467-583]	**279** [248-314]	**835** [740-943]	**593** [561-626]	**523** [487-561]	**1789** [1714-1867]
m	**4.6** [2.9-6.0]	**4.1** [2.7-5.4]	**3.1** [2.2-3.8]	**6.0** [4.5-7.2]	**4.8** [3.6-5.8]	**5.2** [4.4-6.1]
$LiNbO_3$	**Scratch 0° (SC-0)**	**Scratch 45° (SC-45)**	**Grinding grooves 0° (GG-0)**	**Grinding grooves 90° (GG-90)**	**Grinding grooves 135° (GG-135)**	**Mirror Polished (MP)**
σ_0 [MPa]	**277** [250-307]	**430** [397-467]	**499** [472-529]	**685** [644-729]	**566** [526-609]	**694** [671-718]
m	**4.7** [3.1-6.1]	**6.2** [4.0-8.1]	**6.1** [4.5-7.5]	**5.5** [4.1-6.7]	**4.7** [3.5-5.7]	**6.7** [5.5-7.7]

The lowest characteristic strength is obtained for samples with scratches parallel to the most critical $\{01\bar{1}2\}$ cleavage plane, i.e. 45° to the $[2\bar{1}\bar{1}0]$ direction for $LiTaO_3$ (SC-45) and 0° to the $[2\bar{1}\bar{1}0]$ direction for $LiNbO_3$ (SC-0), respectively. Interestingly, the characteristic strength of both materials was similar in those directions (~280 MPa). Orientating the surface scratches as far away as possible to the most critical $\{01\bar{1}2\}$ planes, i.e. 0° for $LiTaO_3$ (SC-0) and 45° for $LiNbO_3$ (SC-45) results in a significant increase in strength of 87% and 55% for $LiTaO_3$ and $LiNbO_3$, respectively. For the case of samples with grinded surfaces, similar conclusions can be drawn. In this case, samples with a grinding groove orientation parallel to the most critical $\{01\bar{1}2\}$ cleavage plane (GG-135 for $LiTaO_3$ and GG-0 for $LiNbO_3$) showed the lowest characteristic strength values, i.e. 523 MPa for $LiTaO_3$ and 499 MPa for $LiNbO_3$ respectively. For $LiTaO_3$ with a grinding direction of 26° to the $[2\bar{1}\bar{1}0]$ direction (GG-26), i.e. parallel to the also relatively weak $(\bar{1}\bar{1}23)$ plane with an inclination angle of 76° to the surface, only slightly higher strength (593 MPa) was measured. Samples with a grinding groove orientation as far away as possible from the most critical cleavage plane (GG-0 for $LiTaO_3$ and GG-90 for $LiNbO_3$) showed the highest characteristic strength values, i.e. 835 MPa for $LiTaO_3$ and 685 MPa for $LiNbO_3$ respectively. To the latter result, it is worth pointing out that the grinding grooves on the $LiNbO_3$ specimens were orientated parallel to the projection of the $(1\bar{1}02)$ and $(\bar{1}012)$ cleavage planes on the surface (see Fig. 1c). Due to the 47°inclination of the planes with respect to the surface, the damage following these directions is not so severe. Since the projected normal stress to the 47° plane is lower than the biaxial applied stress, higher applied load is required to fracture the plane, thus explaining the relatively higher measured strength. Surprisingly, although the strength measured in grinded $LiTaO_3$ sample is still lower by a factor of ~2 than that of the mirror polished side (835 MPa vs. 1789 MPa), no statistically significant difference can be found for the $LiNbO_3$ material (685 MPa vs. 694 MPa). Based on this finding, similar critical defect sizes for the mirror-polished as well as for the ground side should be expected. These defects might only be visible post mortem due to blurring of the scratches during the polishing process. For grinding grooves under an angle of 135° to the $[2\bar{1}\bar{1}0]$ direction on $LiNbO_3$, i.e. in the same direction as the 45° scratch on the opposite side, a moderate strength of 566 MPa was measured.

Regarding the Weibull moduli, all tested samples showed a large scatter in strength leading to a relatively low average m of ~5, comparable to other single crystalline materials [14; 20]. Even in samples with a well-defined scratch and testing conditions [36], no significant increase in m was obtained, although every single specimen fractured from the damage site initiated by the scratch. This finding raises the question whether the induced surface (or sub-surface) damage may be different from specimen to specimen, regardless the very reproducible testing conditions ensured. Fractographic analyses in the next section will help clarifying this issue.

3.3 Fractographic observations

Figure 8 provides post-mortem top-views of representative specimens according to selected testing alignments as shown in Fig. 3, together with the schematic alignment of activated cleavage planes. Figs. 8a to 8e (top row) and Figs. 8f to 8j (bottom row) correspond to $LiTaO_3$ and $LiNbO_3$ specimens, respectively.

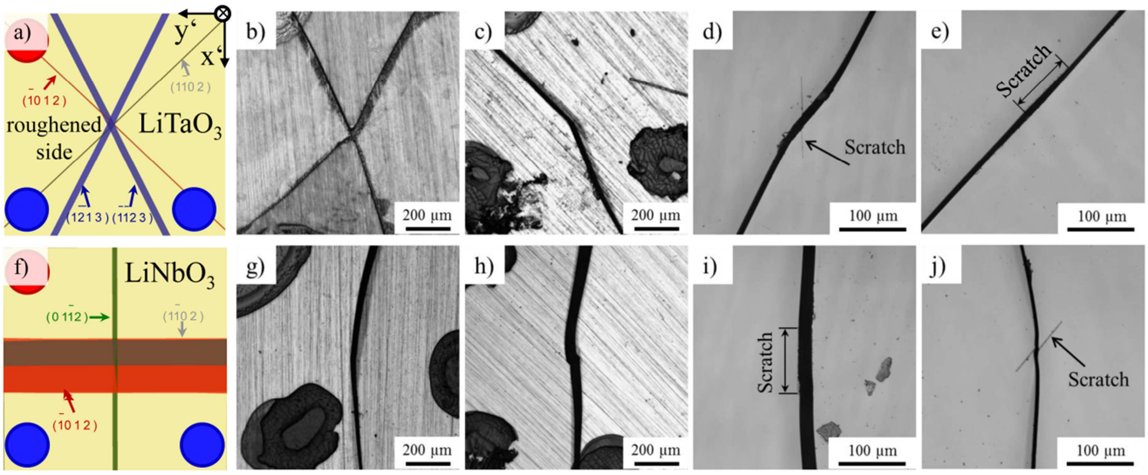

Figure 8. Top view on fractured $LiTaO_3$ (first row) and $LiNbO_3$ (second row) specimens with grinded (b, c, g, h) and scratched (d, e, i, j) surfaces. a) and f) schematically represents expected cleavage planes of low fracture energies. The dots in a) and f) are only help for alignment of specimens on the B3B jig.

For scratches with large inclinations to the most critical cleavage planes, cracks also start in the center of the specimen due to damage introduced by the scratch. However, the crack immediately turns into favored planes of low energy, e.g. belonging to the $\{\bar{1}\bar{1}23\}$ or $\{01\bar{1}2\}$ family of planes for $LiTaO_3$ and $\{01\bar{1}2\}$ for $LiNbO_3$, respectively (compare Figs. 8d and 8j with schematically representation of corresponding planes in a) and b)). The same applies for grinded specimens with a similar orientation of the grinding grooves compared to the scratches (Fig. 8b and 8h). For specimens with scratches parallel to the most critical cleavage plane, cracks follow the scratch and stay in the same plane (see Fig. 8e and 8i). Again, similar conclusion can be drawn from the grinded specimens as shown in Figs. 8c and 8g), where cracks partly follow the grinding direction parallel to the most critical $\{01\bar{1}2\}$ plane. For the $LiTaO_3$ specimen in Figure 8c the crack also turns to the $\{\bar{1}\bar{1}23\}$ plane, confirming the brittle character of this direction as observed in previous work [37].

SEM images in Fig. 9 show fracture surfaces of $LiTaO_3$ and $LiNbO_3$ specimens with scratches (a, c) and grinding grooves (b, d) positioned away from the corresponding most critical $\{01\bar{1}2\}$ plane.

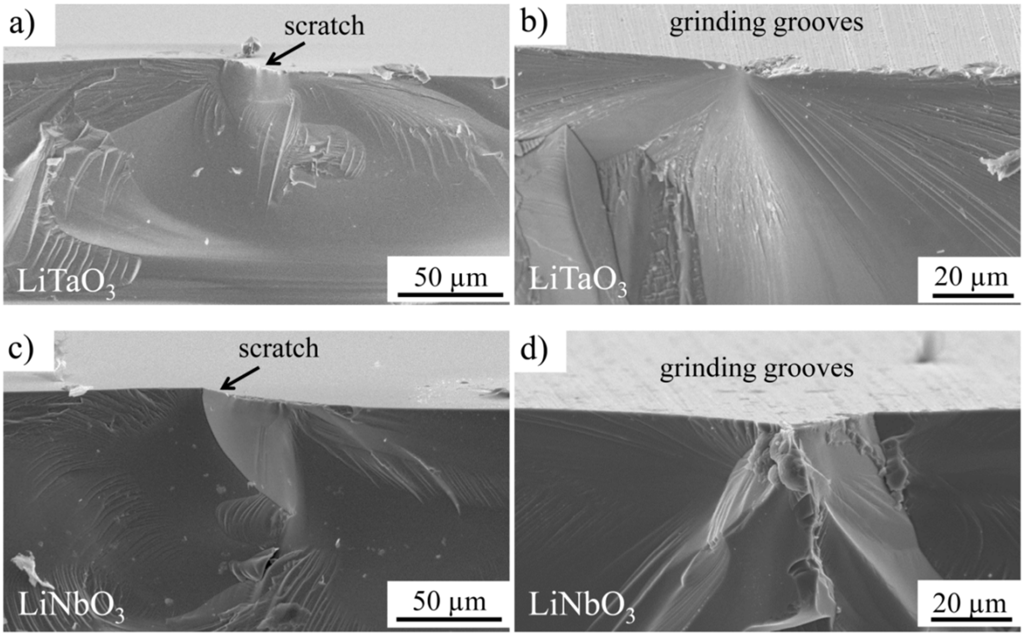

Figure 9. SEM images of fracture surfaces of $LiTaO_3$ and $LiNbO_3$ specimens with scratches (a and c) and grinding grooves (b and d) aligned far away from the respective most critical cleavage planes. The initial crack twists its propagation into weaker planes.

For all specimens it can be seen that failure originates from the introduced surface defect. However, the propagating crack immediately turns into crystallographic planes of lower fracture energy. These observations can explain the relatively high strength values obtained in these samples. First, propagating the initial crack (either a scratch or a groove) along a relatively tough plane requires higher applied stress. Second, twisting of the crack front into the weaker (cleavage) plane also dissipates a certain amount of energy. SEM images in Fig. 10 show fracture surfaces of $LiTaO_3$ and $LiNbO_3$ specimens with scratches (a, c) and grinding grooves (b, d) parallel to the respective most critical $\{01\bar{1}2\}$ plane. Failure initiates from the introduced surface defect (scratch or groove) in all tested specimens in both materials. Due to small misalignments of the introduced flaws, cleavage steps can be observed for all specimens. Also, saw-like defects reaching extraordinarily large depths could be discerned (marked with white arrows in Fig. 10). In these cases, very smooth fracture surfaces can be seen following the most critical $\{01\bar{1}2\}$ cleavage plane, indicating a low fracture energy of the corresponding plane.

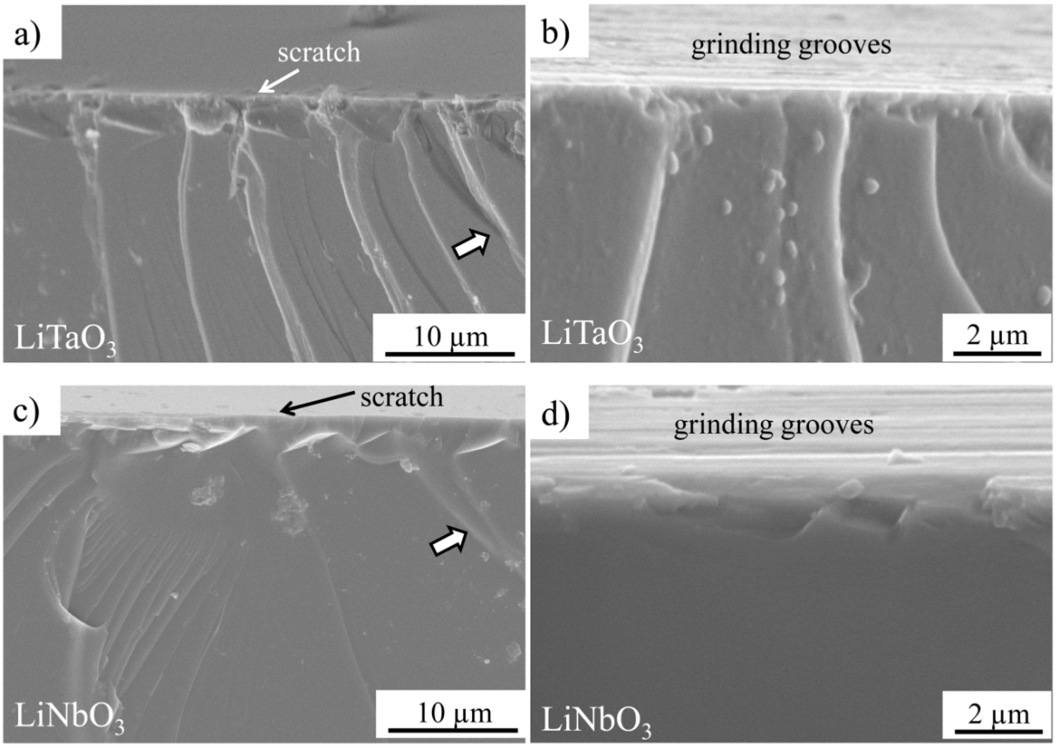

Figure 10. SEM images of the fracture surfaces of $LiTaO_3$ and $LiNbO_3$ specimens either with scratches (a and c) or with grinding grooves (b and d) aligned parallel to the respective most critical cleavage plane. Although small cleavage steps can be observed near the surface, the initial crack propagates straight through the critical cleavage plane.

Based on these fractographic observations a good agreement between strength measurements and sub-surface damage could be found. When a surface defect is orientated parallel to the projection of a highly stressed plane of low fracture energy, cracks initiate at this site and almost perfectly (beside small cleavage steps) follow the corresponding cleavage plane, leading to low bearable loads of the brittle, single crystalline material. Critical flaws oriented with a large inclination angle to the weakest cleavage plane are still responsible for crack initiation. However, higher loads are necessary to deflect the initial crack from a tough into a weak plane, thereby consuming more energy.

3.4 Estimation of fracture toughness of cleavage planes

From the experimental observations of the fracture surfaces on scratched specimens, the size (depth) of the critical defect, a_c, can be estimated. Following Griffith criterion of brittle fracture, along with the corresponding specimen's failure stress, σ_f, from the biaxial tests, a calculation of the critical stress intensity factor, K_c, can be made:

$$K_c = Y \cdot \sigma_f \cdot \sqrt{\pi \cdot a_c} \quad , \qquad (2)$$

where Y is a geometric factor depending on the crack geometry and loading conditions. For the surface cracks considered here of 100 µm length (and a depth of ~2 µm), a geometric factor of $Y = 1.12$ as for through-width cracks can be considered [38]. Assuming a characteristic strength of ~280 MPa (Fig. 7) for both materials for scratched surfaces along the corresponding cleavage planes, and a critical crack size of ~2 ± 1 µm (Fig. 4), a critical stress intensity factor of $K_c \sim 0.8 \pm 0.2$ MPa·m$^{1/2}$ is obtained. On a previous work, fracture toughness of two cleavage planes, i.e. $(\bar{1}012)$ for $LiTaO_3$ and $(01\bar{1}2)$ for $LiNbO_3$ was determined experimentally on notched micro-cantilever specimens, resulting in values of $K_{Ic} \sim 1.7$ MPa·m$^{1/2}$ and $K_{Ic} \sim 1.1$ MPa·m$^{1/2}$, respectively [37]. However, atomistic modelling calculations (using DFT) corresponding to the same planes resulted in $K_{Ic} \sim 0.7$ MPa·m$^{1/2}$ and $K_{Ic} \sim 0.4$ MPa·m$^{1/2}$, respectively [37]. Neglecting small possible influences from the different crack propagation directions [39; 40], the relatively high K_{Ic} values measured using notched micro-cantilevers remain unclear. A possible reason might be the artificial blunt FIB versus naturally sharp crack. Nevertheless, the K_{Ic} values determined from the scratch tests through Eq. (2) seem to agree with the DFT calculations. This suggests the possibility of employing biaxial bending of scratched specimens as an alternative method to estimating the fracture toughness of particular crystallographic directions in brittle solids, and might be extended to polycrystalline ceramics.

4. Conclusion

Biaxial flexural measurements on $LiTaO_3$ and $LiNbO_3$ single crystals revealed a significant effect of surface condition (i.e. mirror-polished, grinded, and nano-scratched) on the strength distribution of the materials. It was demonstrated that not only the surface condition but also the orientation of (sub-)surface damage with respect to the weakest cleavage plane has a significant influence on the strength of brittle single crystalline materials.

The sub-surface analyses of mirror-polished samples with artificial nano-scratched defects in two different directions (i.e. along a weak cleavage plane and 45° to it) explain the higher macroscopic strength of $LiTaO_3$ compared to $LiNbO_3$, the latter showing more pronounced sub-surface cracks for the same applied load. It was shown that the orientation of both nano-scratches and grinding grooves with respect to the weakest cleavage plane controls fracture of the single crystal. In this regard, although the fracture origin is defined by the location of the surface (or sub-surface) defect, initial crack propagation is followed by a deflection of crack path direction into the closest weak plane. This phenomenon requires higher energy if damage and cleavage plane are not parallel and thus yields an apparent higher macroscopic strength for the material.

No significantly higher Weibull modulus was measured in both materials, as compared to other brittle single crystalline materials, even for the case of nano-scratched (well-defined) damaged samples. This shows that due to the combination of flaw type, orientation and depth, along with cleavage plane position (rotation), a high scatter of strength has to be expected in brittle single crystalline materials, thus affecting component's reliability.

The consequence for future design is that not only surface roughening should be controlled by orienting the grinding lines normal to the critical cleavage planes in the single crystal, but also the orientation of (potential) sub-surface damage from mirror-polishing procedures should be taken into account. The existence of brittle and tough crystal planes allows the choice of favourable processing conditions to minimise damage and to enhance performance of single crystalline based components.

5. Acknowledgements

Financial support by the Austrian Federal Government (in particular from Bundesministerium für Verkehr, Innovation und Technologie and Bundesministerium für Wissenschaft, Forschung und Wirtschaft) represented by Österreichische Forschungsförderungsgesellschaft mbH and the Styrian and the Tyrolean Provincial Government, represented by Steirische Wirtschaftsförderungsgesellschaft mbH and Standortagentur Tirol, within the framework of the COMET Funding Programme is gratefully acknowledged. EPCOS OHG (TDK Corporation) is acknowledged for providing the materials for this investigation.

6. References

[1] K.-Y. Hashimoto, "RF Bulk Acoustic Wave Filters for Communications.″ ARTECH HOUSE, (2009).

[2] K.-Y. Hashimoto, "Surface Acoustic Wave Devices in Telecommunications: Modelling and Simulation.″ Springer-Verlag Berlin Heidelberg GmbH, (2000).

[3] T. Heuser, C. Bauer, V. Dragoi, and G. Mittendorfer, "Adhesive wafer bonding applied for fabrication of true-chip-size packages for SAW devices," *ECS Transactions,* **50**[7] 363-70 (2013).

[4] T. Bauer, C. Eggs, K. Wagner, and P. Hagn, "A Bright Outlook for Acoustic Filtering: A New Generation of Very Low-Profile SAW, TC SAW, and BAW Devices for Module Integration," *IEEE Microwave Magazine,* **16**[7] 73-81 (2015).

[5] R. White and F. Voltmer, "Direct piezoelectric coupling to surface elastic waves," *Appl. Phys. Lett.,* **7**[12] 314-16 (1965).

[6] D. Morgan, "Surface Acoustic Wave Filters,″ 2nd ed. Academic Press, (2007).

[7] C. Campbell, "Surface Acoustic Wave Devices and their Signal Processing Applications," pp. 427–58. in**.** Academic Press, 1989.

[8] Y. S. Kuz'minov, "Lithium Niobate Crystals: Physico-chemical Aspects of Technology.″ Cambridge International Science Publishing, (1999).

[9]W. Weibull, "A statistical theory of the strength of materials," pp. 45 **Vol. 151**. Generalstabens Litografiska Anstalts Förlag: Stockholm, (1939).

[10]R. Danzer, "A general strength distribution function for brittle materials," *J. Eur. Ceram. Soc.,* **10** 461–72 (1992).

[11]R. Danzer, "On the relationship between ceramic strength and the requirements for mechanical design," *J. Eur. Ceram. Soc.,* **34** 3435–60 (2014).

[12]M. Deluca, R. Bermejo, M. Pletz, P. Supancic, and R. Danzer, "Strength and fracture analysis of silicon-based components for embedding," *J. Eur. Ceram. Soc.,* **31**[4] 549–58 (2011).

[13]C. H. Hsueh and A. G. Evans, "Residual Stresses and Cracking in Metal/Ceramic Systems for Microelectronics Packaging," *J. Am. Ceram. Soc.,* **68**[3] 120–27 (1985).

[14]A. A. Wereszczak, A. S. Barnes, K. Breder, and S. Binapal, "Probabilistic strength of 1 1 1 n-type silicon," *Journal of Materials Science: Materials in Electronics,* **11**[4] 291–303 (2000).

[15]E. K. C. Funke, M. Kuna, H.J. Möller,, "Biaxial Fracture Test of Silicon Wafers," *Adv. Eng. Mat.,* **6**[7] 594–98 (2004).

[16]J. D. Wu, C. Y. Huang, and C. C. Liao, "Fracture strength characterization and failure analysis of silicon dies," *Microelectronics Reliability,* **43**[2] 269–77 (2003).

[17]K. McGuire, S. Danyluk, T. L. Baker, J. W. Ruponw, and D. McLaughlin, "The influence of backgrinding on the fracture strength of 100 mm diameter (111) p-type silicon wafers," *J. Mater. Sci.,* **32**[4] 1017–24 (1997).

[18]S.-H. Chae, J.-H. Zhao, D. R. Edwards, and P. S. Ho, "Effect of backside scratch direction on the Si die strength," pp. 1-6 in Thermal and Thermomechanical Phenomena in Electronic Systems (ITherm), 2010 12th IEEE Intersociety Conference on.

[19]M. Gruber, I. Kraleva, P. Supancic, J. Bielen, D. Kiener, and R. Bermejo, "Strength distribution and fracture analyses of $LiNbO_3$ and $LiTaO_3$ single crystals under biaxial loading," *J. Eur. Ceram. Soc.,* **37**[14] 4397–406 (2017).

[20]K.-S. Chen, A. Ayon, and S. M. Spearing, "Controlling and Testing the Fracture Strength of Silicon on the Mesoscale," *J. Am. Ceram. Soc.,* **83**[6] 1476–84 (2000).

[21]R. F. Cook, "Fracture mechanics of sharp scratch strength of polycrystalline alumina," *J. Am. Ceram. Soc.,* **100**[3] 1146-60 (2017).

[22]S. C. Abrahams, J. M. Reddy, and J. L. Bernstein, "Ferroelectric lithium niobate. 3. Single crystal X-ray diffraction study at 24°C," *J. Phy. Chem. Solids,* **27**[6–7] 997–1012 (1966).

[23]B. K. Vainshtein, M. Cardona, P. Fulde, and H. J. Queisser, "Modern crystallography I, symmetry of crystals. methods of structural crystallography," *Crystal Research and Technology,* **17**[3] 352-52 (1982).

[24]R. S. Weis and T. K. Gaylord, "Lithium niobate: Summary of physical properties and crystal structure," *Appl. Phys. A,* **37**[4] 191–203 (1985).

[25]R. Hsu, E. N. Maslen, D. Du Boulay, and N. Ishizawa, "Synchroton X-ray Studies of LiNbO3 and LiTaO3," *Acta Crystallographica Section B,* **53** 420 - 28 (1997).

[26]A. Börger and P. Supancic, "Fracture of Brittle Discs under Biaxial Loading," pp. 345–52. in Fracture Mechanics Beyond 2000*,* **Vol. I.** Edited by A. Neimitz, I. V. Rokach, D. Kocanda, andK. Golos. EMAS Publications, Sheffield, 2002.

[27]A. Börger, P. Supancic, and R. Danzer, "The ball on three balls test for strength testing of brittle discs: Part II: analysis of possible errors in the strength determination," *J. Eur. Ceram. Soc.,* **24**[10-11] 2917–28 (2004).

[28]R. Danzer, P. Supancic, and W. Harrer, "Biaxial Tensile Strength Test for Brittle Rectangular Plates," *J. Ceram. Soc. Jpn.,* **114**[11] 1054–60 (2006).

[29]G. Simmons and H. Wang, "Single Crystal Elastic Constants and Calculated Aggregate Properties: A Handbook," pp. 370 2nd ed. MIT Press: Cambridge, MA, (1971).

[30]M. Deluca, R. Bermejo, M. Pletz, M. Wießner, P. Supancic, and R. Danzer, "Influence of deposited metal structures on the failure mechanisms of silicon-based components," *J. Eur. Ceram. Soc.,* **32**[16] 4371–80 (2012).

[31]EN 843-5, "Advanced Technical Ceramics - Monolithic Ceramics - Mechanical Tests at Room Temperature - Part 5: Statistical Analysis," pp. 40. in EN 843-5**.** 1997.

[32]J. Matsuoka, D. Guo, and S. Yoshida, "Cross-section Morphology of the Scratch-Induced Cracks in Soda-Lime-Silica Glass," *Frontiers in Materials,* **4** 8 (2017).

[33]M. Gruber, A. Leitner, D. Kiener, P. Supancic, and R. Bermejo, "Incipient plasticity and surface damage in $LiTaO_3$ and $LiNbO_3$ single crystals," *Materials and Design,* **submitted** (2018).

[34]R. T. Smith and F. S. Welsh, "Temperature Dependence of the Elastic, Piezoelectric, and Dielectric Constants of Lithium Tantalate and Lithium Niobate," *J. Appl. Phys.,* **42**[6] 2219–30 (1971).

[35]K. Taki and Y. Shimizu, "Material Constants of LiTaO3 Determined from Surface Acoustic Wave Velocities," *Jpn. J. Appl. Phys.,* **33** 2976–78 (1994).

[36]R. Bermejo, P. Supancic, and R. Danzer, "Influence of measurement uncertainties on the determination of the Weibull distribution," *J. Eur. Ceram. Soc.,* **32**[2] 251–55 (2012).

[37]M. Gruber, R. Konetschnik, M. Popov, J. Spitaler, P. Supancic, D. Kiener, and R. Bermejo, "Atomistic origins of the differences in anisotropic fracture behaviour of $LiTaO_3$ and $LiNbO_3$ single crystals," *Acta Mater.,* **submitted** (2018).

[38]G. D. Quinn, "Fractography of Glasses and Ceramics." US Government Printing Office: Washington, (2007).

[39]P. Gumbsch, "Brittle fracture and the brittle-to-ductile transition of tungsten," *J. Nuc. Mater.,* **323**[2] 304–12 (2003).

[40]C. C. M. Wu, K. R. McKinney, and R. W. Rice, "Zig-zag crack propagation in MgAl2O4 crystals," *J. Materi. Sci. Letters,* **14**[7] 474–77 (1995).

Publication C

Atomistic origins of the differences in anisotropic fracture behaviour of $LiTaO_3$ and $LiNbO_3$ single crystals

M. Gruber, R. Konetschnik, M. Popov, J. Spitaler, P. Supancic, D. Kiener and R. Bermejo

Abstract

The search of new designs for communication technologies is driven by the required high data transfer rates. Piezoelectric single crystals such as $LiTaO_3$ and $LiNbO_3$ have qualified as materials for efficient and precise frequency filters also considered for the new 5G standards. To ensure optimal high frequency functionality, single crystal wafers are grown and cut in particular directions. However, due to the high anisotropic physical properties of these brittle materials, the structural integrity and reliability of devices are affected by the crystal orientation with respect to the occurring thermo-mechanical stresses. In this work, the anisotropic fracture response of $LiTaO_3$ and $LiNbO_3$ single crystals is investigated through combination of (i) toughness measurements in notched micro-cantilevers along weak cleavage planes and (ii) atomistic modelling of cleavage fracture energies using density functional theory. It is demonstrated that differences in fracture behaviour between $LiTaO_3$ and $LiNbO_3$ can be explained by the stronger chemical bonding in $LiTaO_3$ as compared to $LiNbO_3$ within the loaded crystallographic planes. The knowledge on the alignment of tough as well as weak planes (i.e. cleavage planes) can be used to tailor the design of single crystal based functional components, aiming to exhibit enhanced mechanical reliability without compromising the functionality.

Keywords: single crystals, cleavage, fracture, toughness, DFT.

1. Introduction

Since mobile communication emerged as a substantial aspect of daily life for the general public, approximately every ten years a new generation of mobile networks is introduced. In 1991, data rates started with 64 kilobit per second for the 2G Global System for Mobile (GSM), the first digital mobile communication standard. The next standard, the 3G Universal Mobile Telecommunication System (UMTS), with data rates up to 2 megabit per second (Mbps), was launched in 2001, and more recently superseded by the 4G standard with data rates up to 100 Mbps in 2010. Beyond 2020, the 5G standard should provide data rates of 1-10 gigabit per second [1-3].

Due to the increasing number of frequency bands and request for ever faster down- and upload rates, efficient and precise filtering of frequencies is a key issue for achieving high data rates in mobile devices. In this regard, surface acoustic wave technologies (referred to as SAW) are dominating the smartphone market owing to their efficient production process and applicability for precise frequency filtering as required for high data transfer rates.

A key factor for manufacturing and use of high performance SAW frequency filters is the choice of adequate piezoelectric substrate materials. Many considerations have to be taken into account, for instance low insertion/propagation loss, high electro-mechanical coupling factor, avoidance of beam steering and radiation of bulk acoustic waves, low cost production of large diameter single crystal perovskites, etc. [4, 5] Another crucial issue concerning functionality of the SAW device arises from the permanent exposure to temperature variations during operation. Due to thermal expansion and the temperature dependence of Young's modulus, the filtered frequency, wave velocity and delay may be temperature dependent [6]. In general, only materials with an undesirable low coupling factor show preferable low temperature dependence of frequencies. In this regard, two materials which seem to best satisfy the requirements for SAW filters in mobile applications are $LiTaO_3$ and $LiNbO_3$ single crystals. Here, a relatively low temperature dependence of functional properties can be achieved by growing and cutting the single crystals for the wafer production in special orientations (so-called "functional cuts") [7, 8].

Due to thermo-mechanical loading during fabrication, qualification and/or in-service, the functionality of SAW devices strongly relies on the structural integrity of their single crystalline substrates. Their brittle character and stochastic (Weibullian) mechanical strength imposes a limitation on lifetime of the devices. A certain failure probability exists during such thermo-mechanical loading, becoming extremely critical considering that about a hundred filters are to be integrated into every single next generation smartphone. The substrate strength hereby depends on several factors such as the surface finishing of the wafer, the orientation of the "cut" with respect to the loading direction, as well as the anisotropic fracture resistance of the material cleavage planes along with the direction dependent elastic properties (well known for other single crystal materials) [9-13].

Recent studies on $LiTaO_3$ and $LiNbO_3$ single crystals have revealed fracture behaviour dependent on the crystallographic orientation of the crystal with respect to the mechanical loading. Even though both single crystals have the same crystal structure (Tantalum as well as Niobium belonging to the same group of the periodic table, thus showing a similar electronic structure), macroscopic characteristic strength differences by a factor of ~ 2.5 have been measured in previous work for the same surface finishing [14]. Based upon fracture analyses in previous work, $\{01\bar{1}2\}$ planes were found to be most critical during strength tests in biaxial flexure mode for both materials. This finding suggests that the fracture energy of the distinct cleavage planes in both materials may be significantly different. However, no fracture toughness data are available for these materials. In this regard, small-scale testing is well-established for testing brittle materials such as Si or silicon oxide/nitride, single crystal 6H-SiC, semi-brittle materials like W or NiAl, graphene, and also transition metal nitrides and oxynitrides for coating systems [15-21]. To unveil the local origin of the differences in strength, the anisotropic fracture resistance of $LiTaO_3$ and $LiNbO_3$ single crystals was investigated in this work by in-situ notched micro-cantilever bending tests along $\{01\bar{1}2\}$ planes. Micro-bending samples were prepared with a notch along the plane of study. The notched specimens were subsequently loaded in-situ in a scanning electron microscope (SEM), in order to exclude possible environmental effects such as sub-critical crack growth due to humidity, known from other brittle materials [22, 23]. Experiments were supported by atomistic modelling based upon Density Functional Theory (DFT) to assess the fracture energy of specific “weak” and “strong” cleavage planes in both crystals.

2. Material and methods

2.1 Material of study

The materials of study were $LiTaO_3$ and $LiNbO_3$ single crystals, both exhibiting a crystal structure that can be described with a rhombohedral or a (three times larger) hexagonal unit cell containing 30 atoms [24-27]; the latter representation was chosen in this work, as shown in Figure 1. The single crystalline wafers of study were optimized for use as SAW filters and thus grown under specific “cuts” in order to meet the required specifications (see more details in [4, 28]). As a result, the [0001] direction is rotated 48° counter clockwise for $LiTaO_3$ and 38° clockwise for $LiNbO_3$ around the $[2\bar{1}\bar{1}0]$ axis, respectively, leading to an angle between the wafer surface and the [0001] direction of 42° and 128° for $LiTaO_3$ and $LiNbO_3$, respectively. Consequently for $LiTaO_3$ the surface is close to parallel to the $(01\bar{1}2)$ plane and parallel to the $(0\bar{1}14)$ plane in $LiNbO_3$. From the structural integrity point of view it is noteworthy that for $LiTaO_3$ two of the

{01$\bar{1}$2} cleavage planes are with an angle of 87° almost perpendicular to the surface while for $LiNbO_3$ the (01$\bar{1}$2) plane has an angle of 85° to surface and is expected to be exposed to relatively high thermomechanical tensile stresses in a packaged device.

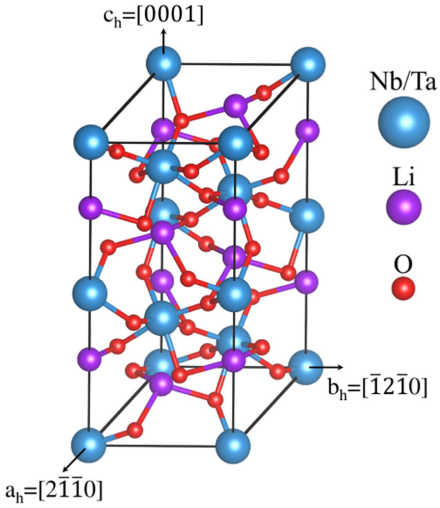

Figure 1: Atomic arrangement in the hexagonal unit cell of $LiTaO_3$ and $LiNbO_3$.

2.2 Experimental details

From a commercial basic raw wafer (Ø 100 mm, thickness 0.13 mm), quadratic specimens were cut and attached to a suitable holder. To lower the amount of material that has to be removed (to reduce accumulated FIB damage [29] and preparation time [30]), thinned free standing lamellas (see Figure 2a) were ion-milled using a low energy ion slicer (IM4000+, Hitachi, Tokyo, Japan), following the procedure described by Wurster et al. [16, 30]. From the obtained lamellas, cantilevers with dimensions of ~4×5×20 µm³ were cut in a FIB working station (Auriga, Zeiss, Oberkochen, Germany; equipped with a gallium FIB system Cobra Z-05, Orsay Physics, Brno, Czech Republic), as exemplarily shown in Figure 2b.

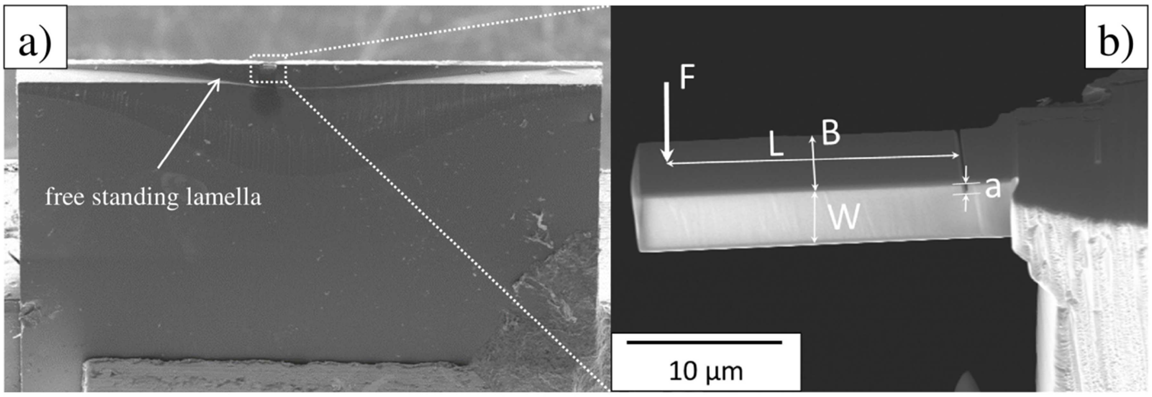

Figure 2: SEM images of (a) an ion-sliced lamella and (b) a free standing FIB-milled micro-cantilever with *B* being the width, *W* the thickness, *a* the notch depth and *L* the lever between the notch and the applied force, *F*.

Coarse cuts were performed with a high current Ga-beam (30 kV, 20 nA), which was systematically reduced down to 100 pA for the final surface polishing step. The notch was milled with an even finer current of 50 pA. The advantage of this miniaturised testing method is twofold: it enables milling specimens to the desired length scale, and it facilitates aligning the $\{01\bar{1}2\}$ planes with respect to the particular orientation of the single crystal wafer. Bending experiments were performed in-situ inside an SEM (Leo 982, Zeiss, Oberkochen, Germany). Load was transferred through a Hysitron PI-85 nanoindenter (Bruker, Eden Prairie, MN, USA) equipped with a conductive wedge shaped diamond (Synton MDP, Nidau, Switzerland), where the load was applied along a line onto the specimen surface. This avoids penetration compared to a point load transferred through an indenter tip. Further, it was ensured that the wedge as well as the beam surface appeared projecting in the SEM to minimise possible torsion. In this context, to further ensure correct alignment also the initial contact was checked by indenting the flat surface next to the beam before conducting the actual experiment. Experiments were performed under displacement control at a rate of 10 nm/s (as shown in Video 1 on a supplementary file). It should be noted that, although the same plane is under maximum tension for both materials, the crack propagation direction is different due to the differences in crystal orientation with respect to the testing set-up (schematically shown in Figure 3), which can influence the obtained toughness values [31, 32].

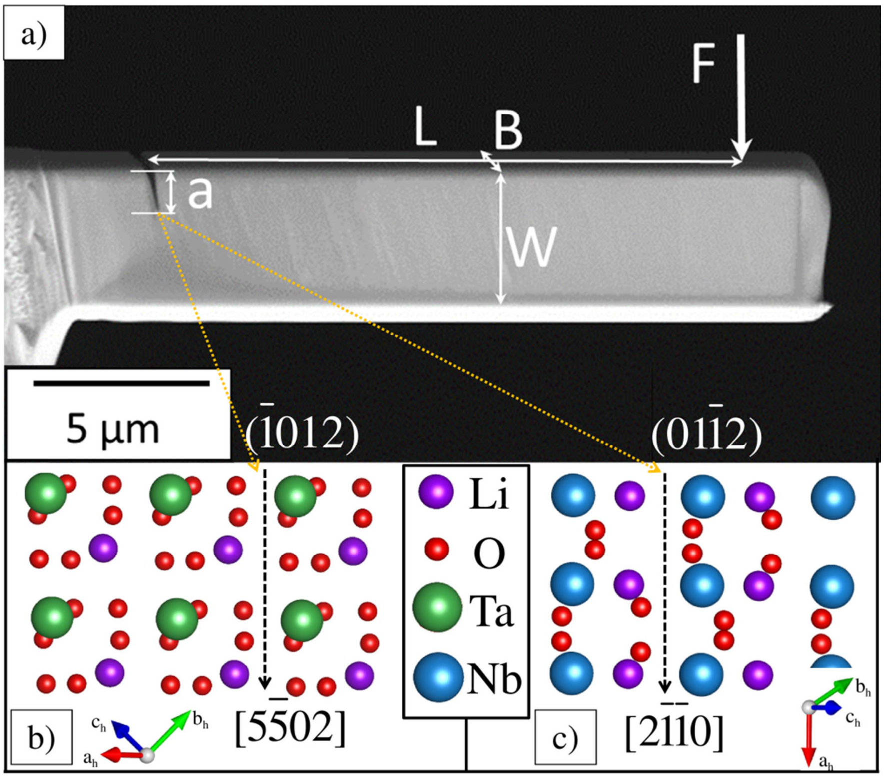

Figure 3: (a) Side view on the experimental testing setup with geometric quantities indicated. (b), (c) Alignment of cleavage plane and crack propagation direction with respect to the atomistic structure for $LiTaO_3$ and $LiNbO_3$, respectively.

The dashed arrow in Figure 3b shows the projection of the most stressed $(\bar{1}012)$ plane (between the atomic layers with weakest bonding forces according to atomistic modelling calculations) along with the prospective crack propagation direction ~$[5\bar{5}02]$ for the $LiTaO_3$ testing set-up. For $LiNbO_3$ the $(01\bar{1}2)$ plane along the $[2\bar{1}\bar{1}0]$ direction was loaded, as indicated by the dashed arrow in Figure 3c. Corresponding stress intensity factors, K_I, were calculated for each specimen based on loading and geometry. Assuming linear elastic fracture behaviour based on the mechanical response and fractography, the critical stress intensity factor (fracture toughness) at the tip of the notch, K_{IC}, was calculated according to [16, 33]:

$$K_{IC} = \frac{F_Q L}{B W^{3/2}} \cdot f(a/W) \tag{1}$$

where

$$f(a/W) = 4 \cdot \frac{3(a/W)^{1/2} \cdot \left(1.23 - (a/W) \cdot (1-(a/W)) \cdot \left(-6.09 + 13.96(a/W) - 14.05(a/W)^2\right)\right)}{\left(2 \cdot (1 + 2 \cdot (a/W)) \cdot (1-(a/W))^{3/2}\right)} \tag{2}$$

with F_Q being the maximum force, L, B, and W the length, width and height of the specimen, respectively, and a the notch depth (as indicated in Figure 2b). Dimensions for all tested specimens are given in Table 1.

Table 1: Detailed information on crack system, dimensions and results of all tested $LiTaO_3$ and $LiNbO_3$ micro-cantilevers including error estimates for the received toughness values. Uncertainties regarding dimensions where taken to be ± 30 nm (based on the resolution of the SEM images), errors from the force measurements were taken to be ± 1 µN (based on the out of contact noise).

	Canti-leverNr.	Crack system	L [µm]	B [µm]	a [µm]	W [µm]	F_Q [µN]	max displ.[nm]	**K_{IC} [MPam$^{1/2}$]**
$LiTaO_3$	1	$(\bar{1}012)$ $[5\bar{5}02]$	15.1	4.80	0.630	3.71	906	521	**1.77 ± 0.13**
	2	$(\bar{1}012)$ $[5\bar{5}02]$	16.1	4.80	0.525	3.76	881	506	**1.56 ± 0.19**
	3	$(\bar{1}012)$ $[5\bar{5}02]$	14.1	4.75	0.700	3.65	820	537	**1.68 ± 0.16**
$LiNbO_3$	1	$(01\bar{1}2)$ $[2\bar{1}\bar{1}0]$	16.7	4.58	0.625	4.20	528	417	**0.90 ± 0.09***
	2	$(01\bar{1}2)$ $[2\bar{1}\bar{1}0]$	16.7	4.58	0.780	4.33	597	489	**1.11 ± 0.09**
	3	$(01\bar{1}2)$ $[2\bar{1}\bar{1}0]$	17.0	4.47	0.630	3.57	454	488	**1.16 ± 0.12**
	4	$(01\bar{1}2)$ $[2\bar{1}\bar{1}0]$	16.9	4.47	0.625	3.64	504	539	**1.22 ± 0.11***
* Crack deviated from notch plane									

2.3 Computational details

The ab initio calculations within the DFT framework were carried out using the Vienna Ab initio Simulation Package (VASP) [34, 35]. The exchange-correlation effects were treated at a level of the generalised gradient approximation [36]. The plane-wave cut-off energy was set to 400 eV. Brillouin zone sampling was performed on 6×2×2 to 6×6×1 meshes (depending on the surface) according to the Monkhorst-Pack method. The electron density for the relaxed structures was re-calculated with the software Wien2k [37] and then contour plots were created using XCrySDen [38]. For calculating the fracture toughness of $LiNbO_3$ and $LiTaO_3$ only the ferroelectric phase (R3c) of these compounds was considered. To deal with the polar surfaces, a dipole correction was applied [39]. Energy corrections due the possible E-field existent inside the slab did not reveal any significant changes in the work of separation, W_{sep}, which was calculated as follows:

$$W_{sep}=\left(U_{slab}\text{-}U_{bulk}\right)/A\ , \tag{3}$$

where U_{slab} is the total energy of a supercell containing a slab of $LiNbO_3$ or $LiTaO_3$ and a thick layer of vacuum, U_{bulk} is the total energy of the bulk, and A is the area of the cleavage plane. The critical stress-intensity factor, K_{IC}, was calculated according to the Griffith-Irwin theory assuming the plane strain situation as occurring in the experiments [40]:

$$K_{IC}=\sqrt{\frac{W_{sep}*E}{1\text{-}\nu^2}}\ , \tag{4}$$

where E is the Young's modulus along the direction normal to the cleavage plane, and ν is the Poisson's ratio. The theoretical values of the elastic constants were derived using the ELATE software [41]. Whereas the spatial dependence of the Young's modulus was fully taken into account, only the average values (Voigt-Reuss-Hill) of the Poisson's ratio were used for the calculation. However, in order to investigate the effect of the spatial variation of the Poisson's ratio on K_{IC} upper and lower bounds were determined based on the maximum and minimum values of ν.

3. Results and Discussion

Figure 4a shows K_I versus displacement for the $LiTaO_3$ and $LiNbO_3$ specimens tested. Two inserts are included, corresponding to a $LiTaO_3$ cantilever during loading and directly after fracture, respectively. Despite minor experimental variations due to geometrical discrepancies, the different slopes observed between the $LiTaO_3$ and $LiNbO_3$ cantilevers indicate the different stiffness of the two materials (for the chosen crystallographic system), with $LiTaO_3$ being stiffer and reaching higher maximum K_I values. Figure 4b shows a representative fracture surface of a $LiTaO_3$ specimen. The very smooth surface indicates precise alignment of the notch with respect to the cleavage plane, as well as low fracture energies for that specific plane. Figures 4c and 4d provide two representative fracture surfaces of the tested $LiNbO_3$ cantilevers. Two out of four specimens exhibited the behaviour in Figure 4c, where a smooth surface with small cleavage steps (indicated by black arrows) is seen. The two remaining cantilevers failed in a manner shown in Figure 4d, where the crack front deviated from the cantilever notch. Details on tested micro-cantilevers together with toughness results are listed in Table 1 along with an estimation of errors based on a total differential approach. It should be noted that the largest contribution to the uncertainties comes from the specimen geometry, associated with the depth of the notch and the thickness of the specimen. In order to minimise this error, post-mortem fractographic analyses were carried out to determine these dimensions, as the through-the-width notch is visible for the fractured specimen (see Figure 4b-d).

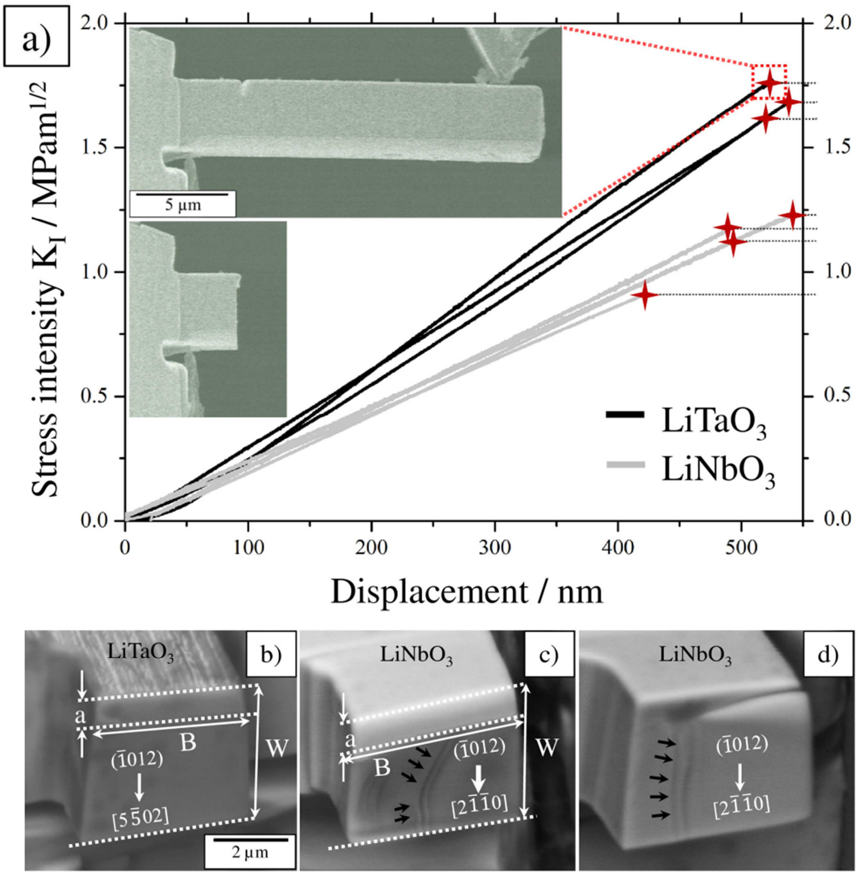

Figure 4: a) Stress intensity factor *K* vs. displacement for all tested $LiTaO_3$ and $LiNbO_3$ cantilevers. The inserted side view shows a representative $LiTaO_3$ cantilever during testing on the eve and directly after fracture. b-d) Fracture surfaces of a $LiTaO_3$ (b) and two $LiNbO_3$ cantilvers (c, d). Observed cleavage steps for the latter ones are highlighted with black arrows.

Averaging the toughness results (i.e. K_I values at the moment of fracture) yields values for K_{IC} of 1.7 ± 0.1 MPam$^{1/2}$ for $LiTaO_3$ and 1.1 ± 0.1 MPam$^{1/2}$ for $LiNbO_3$, respectively, evaluated according to Eqs. (1) and (2), which were developed for this testing configuration [16, 33]. It can be concluded that the toughness of $LiNbO_3$ is significantly lower than that of $LiTaO_3$.

To understand the atomistic origin of this difference in more depth, DFT calculations were performed. The so-called “work-of-separation” (W_{sep}) on the $\{01\bar{1}2\}$ planes was calculated for both materials, which accounts for the energy needed to separate the atoms along a particular plane. In order to compare the calculations with the experimentally determined values, W_{sep} was converted into fracture toughness values, K_{IC}, by taking into account the corresponding elastic properties of the single crystals. Stiffness matrices from DFT calculations at 0 K [42] were taken and compared to experiments at room temperature from Smith et al. [43]. The corresponding twelve non-vanishing coefficients (six are independent) are provided in Table 2. Based on these data, the variation of Young’s modulus in space is plotted in Figure 5 for the experimental as well as the calculated values. Surfaces were obtained by plotting the radius vector r(Φ,ϑ):

$$r(\phi,\theta) = 1/\left(\begin{array}{l} \left(1-\mathrm{Cos}^2(\theta)\right)^2 \cdot S_{11} + \mathrm{Cos}^4(\theta)\cdot S_{33} + \mathrm{Cos}^2(\theta) * \left(1-\mathrm{Cos}^2(\theta)\right)\left(2S_{13}+S_{44}\right) + \\ 2\,\mathrm{Sin}(\theta)\cdot\mathrm{Sin}(\phi)\cdot\mathrm{Cos}(\theta)\cdot\left(3S\,\mathrm{in}\left(\theta\right)\cdot C\,\mathrm{os}^2\left(\phi\right) - (\mathrm{Sin}(\theta)\cdot\mathrm{Sin}(\phi))^2\right)\cdot S_{14} \end{array}\right) \qquad (5)$$

with $0 < \Phi < 2\pi$, $0 < \vartheta < \pi$ and S_{ij} being the values from the compliance matrix, which were calculated by inverting the stiffness matrices in Table 2. *r*(*Φ*,ϑ) represents thereby the response of the material to simple tension, i.e. the ratio of the longitudinal stress to the longitudinal strain for all directions [44].

Table 2: Stiffness matrices in Pa calculated using a DFT approach at 0 K and constant electric field for $LiTaO_3$ (a) and $LiNbO_3$ (b) [40]. Stiffness matrices in Pa coming from experiments at a reference temperature of 298 K and constant electric field for $LiTaO_3$ (c) and $LiNbO_3$ (d) [48], both behaving slightly stiffer compared to the calculations.

a)

$$\begin{array}{l} C^{E}_{LiTaO_3} = \\ 10^{11} \end{array} \begin{bmatrix} 2.23 & 0.51 & 0.78 & -0.06 & 0 & 0 \\ & 2.23 & 0.78 & 0.06 & 0 & 0 \\ & & 2.57 & 0 & 0 & 0 \\ & & & 0.83 & 0 & 0 \\ & & & & 0.83 & -0.06 \\ \mathit{Symm.} & & & & & 0.86 \end{bmatrix}$$

b)

$$\begin{array}{l} C^{E}_{LiNbO_3} = \\ 10^{11} \end{array} \begin{bmatrix} 1.82 & 0.57 & 0.60 & 0.11 & 0 & 0 \\ & 1.82 & 0.60 & -0.11 & 0 & 0 \\ & & 2.08 & 0 & 0 & 0 \\ & & & 0.49 & 0 & 0 \\ & & & & 0.49 & 0.11 \\ \mathit{Symm.} & & & & & 0.62 \end{bmatrix}$$

c)

$$\begin{array}{l} C^{E}_{LiTaO_3} = \\ 10^{11} \end{array} \begin{bmatrix} 2.298 & 0.440 & 0.812 & -0.104 & 0 & 0 \\ & 2.298 & 0.812 & 0.104 & 0 & 0 \\ & & 2.798 & 0 & 0 & 0 \\ & & & 0.968 & 0 & 0 \\ & & & & 0.968 & -0.104 \\ \mathit{Symm.} & & & & & 0.929 \end{bmatrix}$$

d)

$$\begin{array}{l} C^{E}_{LiNbO_3} = \\ 10^{11} \end{array} \begin{bmatrix} 2.03 & 0.573 & 0.752 & 0.085 & 0 & 0 \\ & 2.03 & 0.752 & -0.085 & 0 & 0 \\ & & 2.424 & 0 & 0 & 0 \\ & & & 0.595 & 0 & 0 \\ & & & & 0.595 & 0.085 \\ \mathit{Symm.} & & & & & 0.728 \end{bmatrix}$$

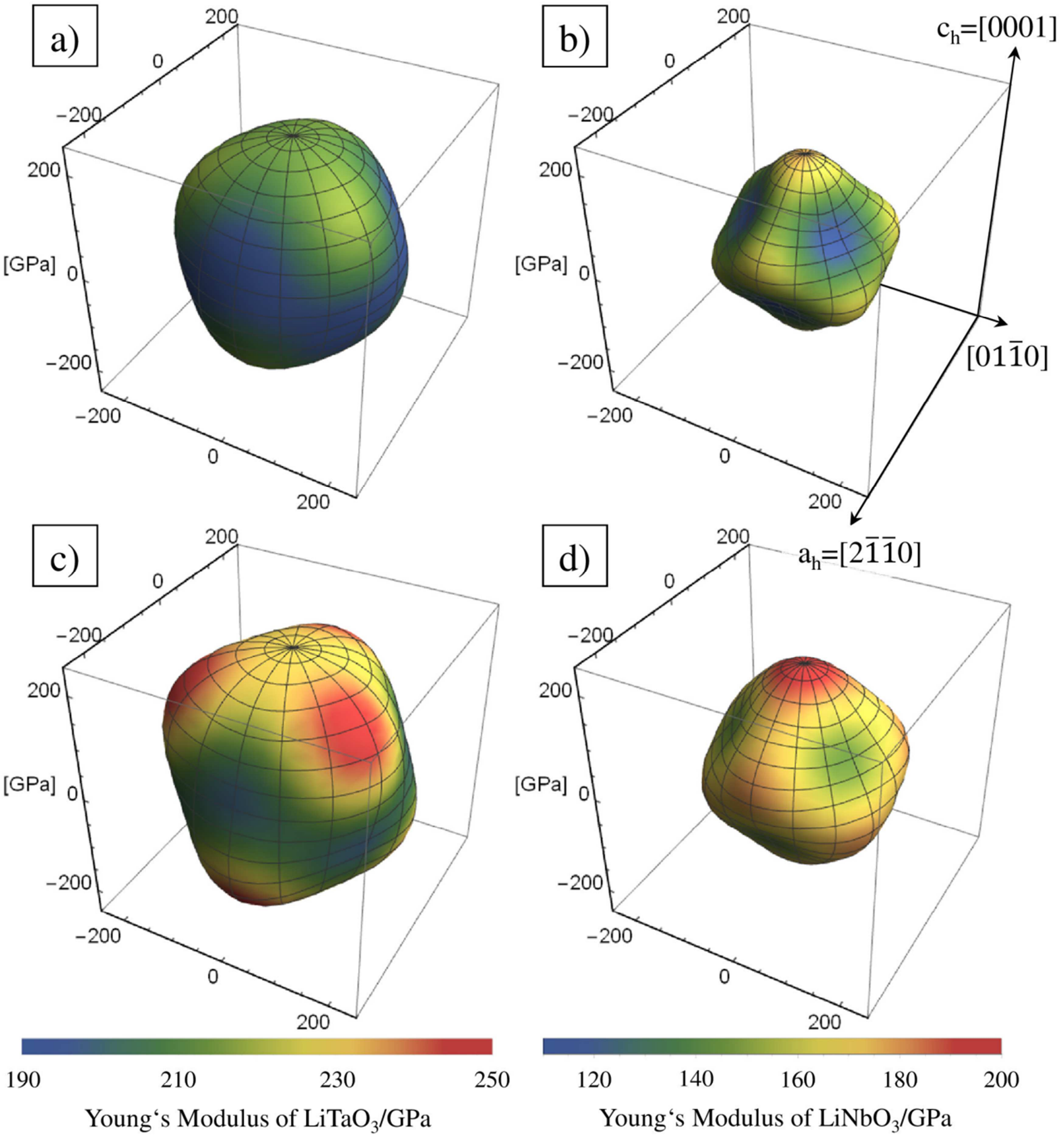

Figure 5: Variation of Young’s modulus at a constant electric field in space according to the stiffness matrices in Table 1. a) $LiTaO_3$ and b) $LiNbO_3$ derived from DFT calculations [42], c) $LiTaO_3$ and d) $LiNbO_3$ from experiments [43].

Even though the experimental values are significantly higher, a similar direction dependent behaviour can be observed, validating the accuracy of DFT calculations. This may not be intuitionally since experimental values derive from measurements at room temperature, where a reduction in modulus compared to calculations at 0 K is expected. Also point defects in a real crystal may further cause a shift to lower measured stiffness. In this context, the exchange-correlation functional used in the DFT calculations could have underestimated bond strengths which would consequently lead to the respective lower values compared to experiments.

Nevertheless it can be concluded that the stiffer character of $LiTaO_3$ compared to $LiNbO_3$ is in good agreement with the different elastic response observed in the experiments (see Figure 4a).

Figures 6a and 6b provide W_{sep} and the corresponding calculated (theoretical) K_{IC} of the crystallographic planes investigated, respectively. The calculations reveal a significant difference in the orientation dependent fracture resistance between $LiTaO_3$ and $LiNbO_3$, confirming the experimental findings. In addition to the experimentally investigated $\{01\bar{1}2\}$ planes, W_{sep} and the associated K_{IC} were calculated for other low-indexed planes using DFT. The results are also presented in Figure 6 for comprehensive purposes. The atomic arrangement corresponding to the planes investigated is shown in Figure 7; the path with the lowest possible W_{sep} is highlighted by a dashed black line. Interestingly, a significantly tougher direction was found for both materials along the $\{0001\}$ plane, which is a relatively stiff direction for $LiTaO_3$ as well as $LiNbO_3$ (see Figure 5).

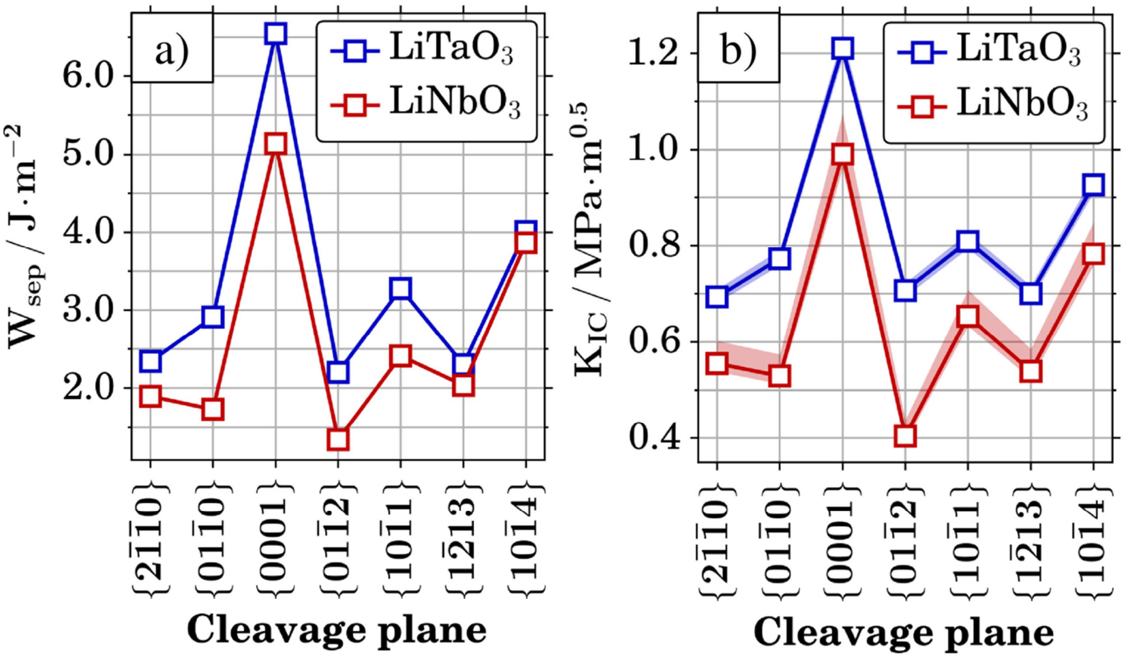

Figure 6: a) Calculated work of separation and b) fracture toughness K_{IC} of $LiTaO_3$ and $LiNbO_3$ for several low-indexed crystallographic planes at 0 K. The solid lines connecting the data points are drawn to guide the eye. Shaded areas indicate the change of K_{IC} when different Poisson's ratio values are considered (see computational details).

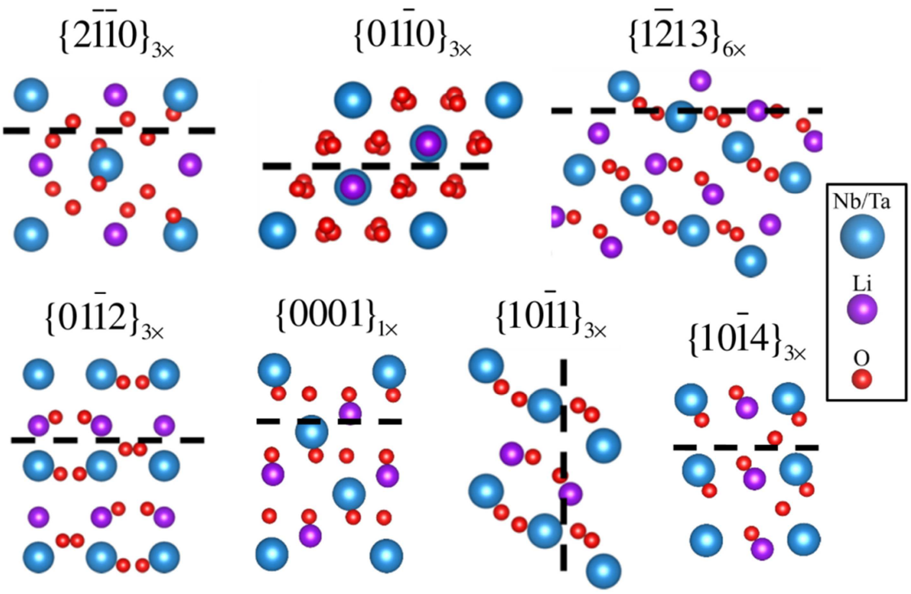

Figure 7: Schematic representation of the critical low-indexed planes for which the work-of-separation and fracture toughness were calculated by DFT. The path with the lowest possible work-of-separation is highlighted by a dashed black line and corresponds to the values shown in Figure 3. Subscripts indicate the number of equivalent planes within the crystal symmetry.

Based upon the experimental findings, the measured toughness values for $LiTaO_3$ and $LiNbO_3$ are similar to other brittle single crystal materials with comparable Young's moduli. In this context, $LiTaO_3$, with a toughness of 1.7 ± 0.1 MPam$^{1/2}$, lies slightly below single crystal sapphire [45], while $LiNbO_3$, with a toughness of 1.1 ± 0.1 MPam$^{1/2}$, is comparable to single crystal quartz [46] or silicon [47]. However, there is a pronounced difference in toughness by a factor of 1.5 between the weakest planes of the two very similar materials. This difference in toughness is in agreement with the atomistic modelling calculations, where toughness values of 0.69 [0.66 – 0.72] MPam$^{1/2}$ for $LiTaO_3$ and 0.40 [0.37 – 0.48] MPam$^{1/2}$ for $LiNbO_3$ were obtained for the same set of $\{01\bar{1}2\}$ cleavage planes. The atomistic origin of this difference is a stronger chemical bonding in $LiTaO_3$ as compared to $LiNbO_3$. More specifically, the six O atoms surrounding either Nb or Ta form two kinds of Nb/Ta-O bonds: i.e. short and long. $LiNbO_3$ exhibits a larger difference between the lengths of these two types of bonds as compared to $LiTaO_3$. This anisotropy is also reflected in different overlap of the electron orbitals taking part in the bonding, as visible in Figure 8. The minimum electron density along the long Ta-O bond is around 0.017 electrons/Å^3, while the corresponding value for the longer Nb-O bond is only 0.011 electrons/Å^3, giving rise to a more rigid and isotropic network of the TaO_6 polyhedra. This is consistent with trends seen for the

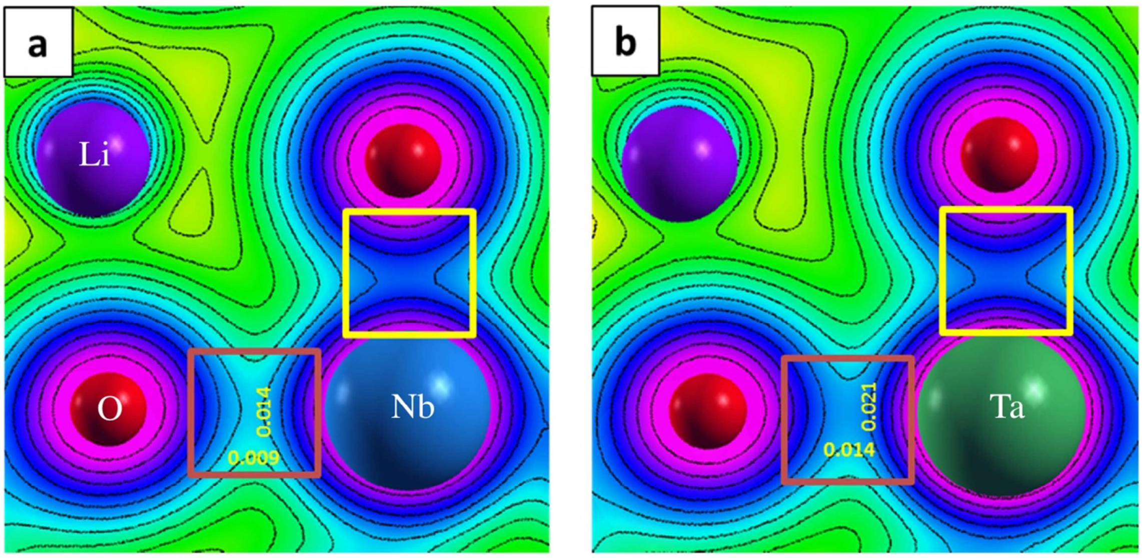

Figure 8: Contour plots of the electron density in the a) O-Nb-O and b) O-Ta-O plane. Orange and yellow boxes indicate the long and the short Nb/Ta-O bonds, respectively. Contour lines range from 0.0004 – 0.1 e/Å^3 with logarithmic spacing.

elastic moduli or cohesion-related properties, e.g. hardness and melting temperature [48]. The calculations also reflect observations of macroscopic fracture experiments from previous work [14]. For specimens failing at low loads, only cracks along one $\{01\bar{1}2\}$ plane were observed, where the lowest toughness values were established for both materials in this work.

It should be noted that, although the results from our experiments are qualitatively in good agreement with the performed atomistic calculations, the absolute values differ significantly. While the exchange-correlation functional used in the DFT calculations could have delivered too low bond strengths and therefore toughness values, the experimental values may be overestimated if plane-strain conditions are not guaranteed during the experiment. In this regard, based upon linear elastic fracture mechanic considerations, testing sample dimensions in terms of notch depth, a, width, B and remaining loading ligament (W - a), as shown in Figure 2b and Figure 3a, need to be sufficiently large compared to the size of the plastic zone according to [33]:

$$a, B, (W-a) \geq 2.5\left(\frac{K_{\mathrm{IC}}}{\sigma_{\mathrm{y}}}\right)^2, \tag{6}$$

with σ_{y} being the yield strength of the material. By taking the maximum of the measured strength values from [14], where the yield strength was still not reached, together with K_{IC} values from this work, the respective specimen dimensions need be larger than ~0.6 µm for $LiTaO_3$ and ~0.5 µm for $LiNbO_3$. Thus Eq. (6) is easily satisfied for each tested cantilever (see Table 1). Another conceivable contribution to the larger experimental values is that in the calculations only the work of separation is taken into account, which considers the propagation of a “sharp crack”. In the experiment however, further dissipation of energy is expected to emerge from other dissipative processes in the material (e.g. plastic displacive deformation, twinning, piezo-elastic domain switching) [49] as well as from the experimental setup itself (no perfectly stiff/elastic testing jig, generation of sound waves, plastic deformation of the material underneath the indenter wedge, etc.) In addition, the notch is not atomically sharp (rather with a radius of ~20 nm). In this regard, a recent work on single crystal 6H-SiC addresses this issue and proposes an alternative method to induce stable crack growth and thus evaluate fracture toughness on specimens with sharp cracks [20]. The results reported fairly agree with those calculated with DFT, although friction during loading may affect the load transfer to the specimen.

In summary, the significant difference in macroscopic strength between $LiTaO_3$ and $LiNbO_3$ single crystals can be explained by the fracture toughness anisotropy of distinct "weak" cleavage planes, which differs among the two materials. The experimental values measured in notched micro-cantilevers showed the same behaviour as atomistic calculations of cleavage fracture energies using DFT, the latter providing a lower bound for the toughness of a cleavage plane.

4. Conclusion

This study demonstrates the atomistic origins of the different fracture behaviour of $LiTaO_3$ and $LiNbO_3$ single crystals with similar crystallographic structure. Density functional theory calculations proved out as a useful strategy to address direction-dependent toughness in both single crystalline materials. The higher toughness of weak cleavage planes in $LiTaO_3$ compared to $LiNbO_3$ agrees with microscopic in-situ testing of notched micro-cantilevers as well as macroscopic strength measurements. The outcomes of this investigation can be used to predict more reliable designs of components as well as tougher orientations along which the single crystals can withstand higher mechanical loading while maintaining functional properties.

5. Acknowledgements

Financial support by the Austrian Federal Government (in particular from Bundesministerium für Verkehr, Innovation und Technologie and Bundesministerium für Wissenschaft, Forschung und Wirtschaft) represented by Österreichische Forschungsförderungsgesellschaft mbH and the Styrian and the Tyrolean Provincial Government, represented by Steirische Wirtschaftsförderungsgesellschaft mbH and Standortagentur Tirol, within the framework of the COMET Funding Programme is gratefully acknowledged. EPCOS OHG (TDK Corporation) is acknowledged for providing the materials for this investigation.

6. References

[1] Osseiran A, Boccardi F, Braun V, Kusume K, Marsch P, Maternia M, Queseth O, Schellmann M, Schotten H, Taoka H, Tullberg H, Uusitalo MA, Timus B, Fallgren M. Scenarios for 5G mobile and wireless communications: the vision of the METIS project. IEEE Communications Magazine 52 (2014) 26–35.

[2] Agarwal A, Misra G, Agarwal K. The 5th Generation Mobile Wireless Networks- Key Concepts, Network Architecture and Challenges. Am. J. Electr. Electron. Eng. 3 (2015) 22–28.

[3] Mitra RN, Agrawal DP. 5G mobile technology: A survey. ICT Express 1 (2015) 132–137.

[4] Morgan D. Surface Acoustic Wave Filters: Academic Press, 2007.

[5] Liu Y, Yang Z, Cui D, Ren X, Sun J, Liu X, Zhang J, Wei Q, Fan H, Yu F, Zhang X, Zhao C, Liu S. Two-Inch-Sized Perovskite CH3NH3PbX3 (X = Cl, Br, I) Crystals: Growth and Characterization. Adv. Mater. 27 (2015) 5176–5183.

[6] Slobodnik AJ. Surface Acoustic Waves and SAW Materials. Proceedings of the IEEE: Special Edition on Surface Acoustic Waves, vol. 64: Institute of Electrical and Electronics Engineers, 1976.

[7] Schulz MB, Matsinger BJ, Holland MG. Temperature Dependence of Surface Acoustic Wave Velocity on α Quartz. J. Appl. Phys. 41 (1970) 2755–2765.

[8] Neurgaonkar RR, Kalisher MH, Lim TC, Staples EJ, Keester KL. Czochralski Single Crystal Growth of Sr. 61Ba39Nb2O6 for Surface Acoustic Wave Applications. Mater. Res. Bull. 15 (1980) 1235–1240.

[9] Reyes-Martinez MA, Ramasubramaniam A, Briseno AL, Crosby AJ. The Intrinsic Mechanical Properties of Rubrene Single Crystals. Adv. Mater. 24 (2012) 5548–5552.

[10] DeLRio FW, Cook RF, Boyce BL. Fracture strength of micro- and nano-scale silicon components. AIP Publishing (2015) 021303.

[11] Cook R. Strength and sharp contact fracture of silicon. J. Mater. Sci. 41 (2006) 841–872.

[12] Jaya BN, Wheeler JM, Wehrs J, Best JP, Soler R, Michler J, Kirchlechner C, Dehm G. Microscale Fracture Behavior of Single Crystal Silicon Beams at Elevated Temperatures. Nano Letters 16 (2016) 7597–7603.

[13] Östlund F, Rzepiejewska-Malyska K, Leifer K, Hale LM, Tang Y, Ballarini R, Gerberich WW, Michler J. Brittle-to-Ductile Transition in Uniaxial Compression of Silicon Pillars at Room Temperature. Adv. Func. Mater. 19 (2009) 2439–2444.

[14] Gruber M, Kraleva I, Supancic P, Bielen J, Kiener D, Bermejo R. Strength distribution and fracture analyses of $LiNbO_3$ and $LiTaO_3$ single crystals under biaxial loading. J. Eur. Ceram. Soc. 37 (2017) 4397–4406.

[15] Matoy K, Schönherr H, Detzel T, Dehm G. Micron-sized fracture experiments on amorphous SiOx films and SiOx/SiNx multi-layers. Thin Solid Films 518 (2010) 5796–5801.

[16] Wurster S, Motz C, Pippan R. Characterization of the fracture toughness of micro-sized tungsten single crystal notched specimens. Philos. Mag. 92 (2012) 1803–1825.

[17] Iqbal F, Ast J, Göken M, Durst K. In situ micro-cantilever tests to study fracture properties of NiAl single crystals. Acta Mater. 60 (2012) 1193–1200.

[18] Zhang P, Ma L, Fan F, Zeng Z, Peng C, Loya PE, Liu Z, Gong Y, Zhang J, Zhang X, Ajayan PM, Zhu T, Lou J. Fracture toughness of graphene: Nature Publishing Group, a division of Macmillan Publishers Limited. All Rights Reserved., 2014.

[19] Jaya BN, Kirchlechner C, Dehm G. Can microscale fracture tests provide reliable fracture toughness values? A case study in silicon. J. Mat. Res. 30 (2015) 686–698.

[20] Sernicola G, Giovannini T, Patel P, Kermode JR, Balint DS, Britton TB, Giuliani F. In situ stable crack growth at the micron scale. Nature Communications 8 (2017) 108.

[21] Gibson JSKL, Rezaei S, Rueß H, Hans M, Music D, Wulfinghoff S, Schneider JM, Reese S, Korte-Kerzel S. From quantum to continuum mechanics: studying the fracture toughness of transition metal nitrides and oxynitrides. Materials Research Letters 6 (2018) 142-151.

[22] Wiederhorn SM. Influence of water vapour on crack propagation in soda-lime glass. J. Am. Ceram. Soc. 50 (1967) 407–414.

[23] Wiederhorn SM. Subcritical Crack Growth in Ceramics. In: Bradt RC, Hasselman DPH, Lange FF (Eds.). Fracture mechanics of ceramics. New York: Plenum, 1974.

[24] Vainshtein BK, Cardona M, Fulde P, Queisser HJ. Modern crystallography I, symmetry of crystals. methods of structural crystallography. Crystal Research and Technology 17 (1982) 352-352.

[25] Weis RS, Gaylord TK. Lithium niobate: Summary of physical properties and crystal structure. Appl. Phys. A 37 (1985) 191–203.

[26] Abrahams SC, Reddy JM, Bernstein JL. Ferroelectric lithium niobate. 3. Single crystal X-ray diffraction study at 24°C. J. Phy. Chem. Solids 27 (1966) 997–1012.

[27] Hsu R, Maslen EN, Du Boulay D, Ishizawa N. Synchroton X-ray Studies of LiNbO3 and LiTaO3. Acta Crystallographica Section B 53 (1997) 420 - 428.

[28] Shibayama K, Yamanouchi K, Sato H, Meguro T. Optimum Cut for Rotated Y-Cut LiNbO3 Crystal Used as the Substrate of Acoustic-Surface Wave Filters. Proceedings of the IEEE, vol. 64, 1976. p.595–597.

[29] Kiener D, Motz C, Rester M, Jenko M, Dehm G. FIB damage of Cu and possible consequences for miniaturized mechanical tests. Mat. Sci. Eng. A 459 (2007) 262–272.

[30] Wurster S, Motz C, Jenko M, Pippan R. Micrometer-Sized Specimen Preparation Based on Ion Slicing Technique. Adv. Eng. Mat. 12 (2010) 61–64.

[31] Wu CCM, McKinney KR, Rice RW. Zig-zag crack propagation in MgAl2O4 crystals. J. Materi. Sci. Letters 14 (1995) 474–477.

[32] Gumbsch P. Brittle fracture and the brittle-to-ductile transition of tungsten. J. Nuc. Mater. 323 (2003) 304–312.

[33] ASTM-E399-09. Standard Test Method for Linear-Elastic Plane-Strain Fracture Toughness K Ic of Metallic Materials. ASTM International, West Conshohocken, PA, (2009).

[34] Kresse G, Furthmüller J. Efficient iterative schemes for ab initio total-energy calculations using a plane-wave basis set. Phys. Rev. B 54 (1996) 11169–11186.

[35] Kresse G, Joubert D. From ultrasoft pseudopotentials to the projector augmented-wave method. Phys. Rev. B 59 (1999) 1758–1775.

[36] Perdew JP, Burke K, Ernzerhof M. Generalized Gradient Approximation Made Simple. Phsys. Rev. Lett. 77 (1996) 3865–3868.

[37] Blaha P, Schwarz K, Madsen G, Kvasnicka D, Luitz J. wien2k. An augmented plane wave+ local orbitals program for calculating crystal properties (2001).

[38] Kokalj A. Computer graphics and graphical user interfaces as tools in simulations of matter at the atomic scale. Comp. Mater. Sci. 28 (2003) 155–168.

[39] Neugebauer J, Scheffler M. Adsorbate-substrate and adsorbate-adsorbate interactions of Na and K adlayers on Al(111). Phys. Rev. B 46 (1992) 16067–16080.

[40] Fischer-Cripps AC. Introduction to contact mechanics: Springer, 2000.

[41] Gaillac R, Pullumbi P, Coudert F-X. ELATE: an open-source online application for analysis and visualization of elastic tensors. J. Phys. Condens. Matter. 28 (2016) 275201.

[42] de Jong M, Chen W, Angsten T, Jain A, Notestine R, Gamst A, Sluiter M, Krishna Ande C, van der Zwaag S, Plata JJ, Toher C, Curtarolo S, Ceder G, Persson KA, Asta M. Charting the complete elastic properties of inorganic crystalline compounds. 2 (Scientific Data 2015) 150009.

[43] Smith RT, Welsh FS. Temperature Dependence of the Elastic, Piezoelectric, and Dielectric Constants of Lithium Tantalate and Lithium Niobate. AIP Publishing 42 (1971) 2219 - 2230.

[44] Nye JF. Physical Properties of Crystals. Oxford: Clarendon Press, 1985.

[45] Iwasa M, Ueno T, Bradt RC. Fracture Toughness of Quartz and Sapphire Single Crystals at Room Temperature. J. Soc. Mater. Sic. 30 (1981) 1001–1004.

[46] Iwasa M, Bradt RC. Cleavage of natural and synthetic single crystal quartz. Mater. Res. Bull. 22 (1987) 1241–1248.

[47] John CS. The brittle-to-ductile transition in pre-cleaved silicon single crystals. The Philosophical Magazine: A Journal of Theoretical Experimental and Applied Physics 32 (1975) 1193-1212.

[48] Nikogosyan DN. Nonlinear optical crystals: a complete survey: Springer Science & Business Media, 2006.

[49] Launey ME, Ritchie RO. On the Fracture Toughness of Advanced Materials. Adv. Mater. 21 (2009) 2103–2110.

Publication D

Incipient plasticity and surface damage in $LiTaO_3$ and $LiNbO_3$ single crystals

M. Gruber, A. Leitner, D. Kiener, P. Supancic and R. Bermejo

Abstract:

The outstanding functional properties of single crystals used in many engineering applications often rely on their surface quality. The associated grinding process in single crystals is known to introduce surface or sub-surface defects (cracks), which may compromise the functionality and/or structural integrity of the final device. The small size of such defects often yields relatively high strength values, but also usually large scatter which implies low reliability. The aim of this work is to analyze the onset of surface contact damage in single crystals with respect to crystal orientation and elastic properties. LiTaO3 and LiNbO3 anisotropic single crystal samples are investigated using nanoindentation techniques and focused ion beam based sub-surface analyses. Experimental findings show that the onset of damage is correlated to weaker cleavage planes. At this stage also traces of plastic deformation on the contact surface due to twinning are observed. Further load increase revealed contact cracks in both materials; their morphology and extension being related to the orientation of the cleavage planes and elastic properties of the crystals. Our results advance the understanding of damage in anisotropic materials such as LiTaO3 and LiNbO3, and can generally be utilized to assess the onset of damage in other brittle materials.

Keywords: nanoindentation; single crystals; anisotropy; Pop-in; twinning; cracking;

1. Introduction

The use of single crystals in engineering applications has been motivated by their outstanding optical, electrical and mechanical properties. A first example is the use of single crystals as gain media for solid state lasers. Particular single crystals also show high dielectric (or piezo-electric) response, which is of prime interest for sensors and actuators. Another example is silicon, which is indispensable in modern semiconductor-based microelectronic components. Special attention has been drawn to single crystal materials for communication technologies; in particular the use of piezoelectric materials as surface acoustic wave frequency filters [1]. Here the piezoelectricity is used for converting electrical frequencies into mechanical, acoustic waves, which are then filtered by destructive/constructive interferences and converted back into electrical output signals, exhibiting the desired bandpass characteristics. Two candidate materials for acoustic filter applications are Lithium Tantalate ($LiTaO_3$) and Lithium Niobate ($LiNbO_3$), as they exhibit particular low acoustic losses [2-4]. Despite their unique properties, brittle single crystals are in general limited in most applications because they lack the structural integrity of (for instance) polycrystalline ceramics. Also for piezoelectronic applications the mechanical properties are topics of recent research [5-7]. Single crystals often show a high anisotropy in their macroscopic physical properties (e.g. coefficient of thermal expansion, elastic modulus), giving rise to significantly different functional properties along individual crystallographic directions. From the application point of view, the mechanical response of single crystals is associated with the orientation of cleavage planes, twinning planes or slip planes with respect to the applied load. The resistance of brittle single crystals to fracture (its fracture toughness) is generally low, on the order of $\sim 1 \cdot \mathrm{MPam}^{1/2}$ [8]. Therefore, the propagation of existing (microstructural) defects upon loading yields brittle fracture, thus compromising the functionality of the component the single crystal material may have been conceived for. The strength limiting factors in brittle single crystals are usually pre-existing flaws coming from the harsh cutting, grinding or polishing processes, as well as sub-surface cracks which are a result of contact loading during assembly procedures [9-12]. For the particular application as surface acoustic wave filters, further damage during pick and place of the microelectronic device may occur due to high contact pressures coming from the small contact area between needle and single crystal material. Depending on the damaged area below the loaded region of a brittle material, gradual or abrupt losses in strength are documented and associated with quasi-plastic damage or cone cracking, respectively [13-16]. The small size of such defects often yields relatively high characteristic strength values, but usually large scatter (low reliability) due to the broad defect size (and orientation) distribution [17, 18]. It is thus mandatory to characterize the mechanical response of single crystals, with special attention to the orientation of the crystal with respect to the loading direction. In this regard, only few works are found in literature concerning the response of $LiTaO_3$ or $LiNbO_3$ to mechanical loading mainly restricted to loading along [0001] or [01$\bar{1}$0] directions [19-23]. However, different orientations are used for engineering devices [4, 24], which can exhibit different mechanical response due to the anisotropic material properties in single crystals and deformation mechanisms acting on a particular high stressed crystal plane. Both, cracks as well as plastic deformation, can influence the functionality (e.g. piezo or damping properties due to different domain structures [25]) of certain materials.

Previous mechanical characterization of these two materials revealed a significant difference in the biaxial strength of wafer samples, with characteristic strengths of ~700 MPa for $LiNbO_3$ versus ~1800 MPa for $LiTaO_3$ [18]. Corresponding fractographic (post-mortem) analyses revealed different sub-surface damage between both materials (i.e. deeper scratches in $LiNbO_3$). However, an understanding of the damage process during loading is still lacking. The aim of this work is to assess the onset of damage in single crystals by combining nanoindentation techniques with focus ion beam (FIB) analyses. The reference materials used for this study are $LiTaO_3$ and $LiNbO_3$, having different orientations with respect to their growth direction. Nanoindents were performed using a Berkovich and a spherical indenter tip at incremental loads to retrieve the elastic properties of the single crystals and capture the onset of plastic deformation and damage. Results are interpreted in the framework of contact mechanics and Weibull statistics, and the conclusions drawn can be extended to other brittle or quasi-brittle materials.

2. Material of study, sample orientation and used methods

$LiNbO_3$ and $LiTaO_3$ are trigonal crystals belonging (below the Curie temperature) to the 3m point group and the R3c space group (no. 161), usually represented using hexagonal axes ($a = b \neq c$ and $\alpha = \beta = 90°$, $\gamma = 120°$) [26, 27]. Both crystals show threefold rotation symmetry around the c_h – axis which exhibits the strongest atomic bonds, leading to the highest Young's modulus and lowest coefficient of thermal expansion in this direction [28, 29]. To enhance the functionality, a particular orientation is usually pursued for each material. As shown in Figure 1, the [0001] direction is rotated 48° counterclockwise for $LiTaO_3$ a) and 38° clockwise for $LiNbO_3$ b) around the [2$\bar{1}\bar{1}$0] axis, marked with the wafer flat. This leads to an angle between the wafer's surface and the [0001] direction of 42° and 128° for $LiTaO_3$ and $LiNbO_3$, respectively. The two materials are therefore referred to as 42° Y-X $LiTaO_3$ and 128° Y-X $LiNbO_3$. The alignment of low indexed planes is provided in the pole figures for $LiTaO_3$ (Figure 1c) and for $LiNbO_3$ (Figure 1d), with dimensions of the unit cells taken from Hsu et al. [30] Relevant planes for the deformation and damage analysis in this work are highlighted with larger colored dots. It is worth pointing out that while for 128° Y-X $LiNbO_3$ the (0$\bar{1}$14) plane is parallel to the surface (in the center of Figure 1d), no low indexed plane corresponds to the wafer surface of the 42° Y-X $LiTaO_3$. The (01$\bar{1}$2) plane is, with an inclination angle of 9°, relatively parallel to the surface (close to the center in Figure 1c).

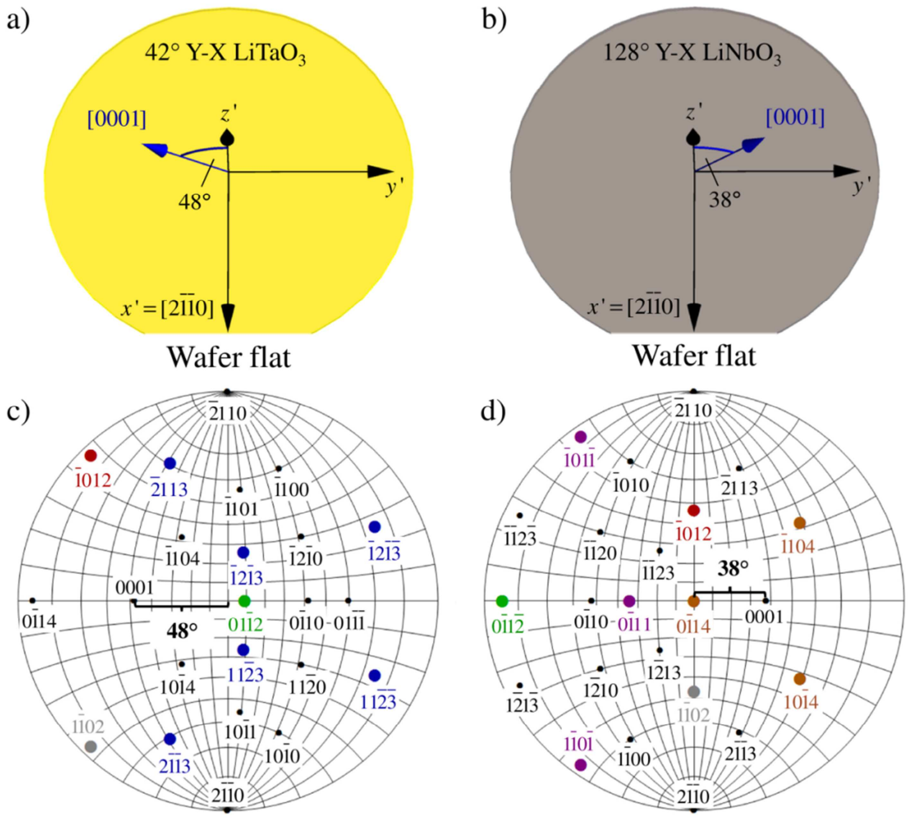

Figure 1: Crystallographic orientation of the used wafers for $LiTaO_3$ (a) and $LiNbO_3$ (b) with corresponding pole figures (grid size of 10 × 10°) containing low indexed crystallographic planes (full symbols). Planes contributing to the observed deformation/damage of the materials are highlighted with larger (colored) dots.

Samples with the respective orientation were diced and ground by the company EPCOS OHG, Deutschlandsberg, Austria (a TDK group company). A mirror-polished surface was provided.

Nanoindentation experiments were performed on these $LiNbO_3$ and $LiTaO_3$ specimens to determine hardness, Young's modulus and onset of damage in both single crystalline materials. Indentation tests were performed at room temperature using a G200 nanoindenter (Keysight-Tec, Santa Rosa, California, USA) equipped with a continuous stiffness measurement (CSM) unit. Two diamond tips with (i) a Berkovich and (ii) a spherical geometry with a radius of 4.5 µm were used and calibrated on fused silica. Displacement controlled experiments were executed with constant strain rates ($\dot{P}/P = 0.05\ s^{-1}$) for Berkovich measurements. The displacement amplitude of the CSM signal was set to 2 nm oscillating at a frequency of 45 Hz to overcome influences of the integrated lock-in amplifier [31]. Thermal drift was measured in a post-test segment and did not exceed 0.3 nm/s for any considered indent. Hardness and Young's modulus were evaluated according to the classical analysis for isotropic samples of Oliver and Pharr [32]. As proposed by

Vlassak and Nix, for anisotropic materials a correction of this value can be employed [33, 34]. Since the anisotropy factor of $LiTaO_3$ as well as $LiNbO_3$ is low (1.3 and 1.4, respectively, calculated using data from [29]), the maximum possible error is expected within 2 % [33, 34]. Thus, this correction is within the measurement uncertainties and was neglected for the sake of simplicity. Details on the tip calibration, in particular for the sphere, can be found in the work of Leitner et al. [35] The required onset of first irreversible damage might slightly depend on the apparent strain-rate as well as the stressed volume [36-38], which in turn correlates with the used tip radius. However, using the same experimental indentation parameters for the two similar materials clearly guarantees an eligible qualitative comparison between $LiNbO_3$ and $LiTaO_3$, even though only one tip radius was employed. All specimens were loaded parallel to the z' direction shown in Figure 1a and 1b.

Surface images were made using a Scanning Electron Microscope (SEM, Zeiss LEO 1525, Oberkochen, Germany) with an acceleration voltage of 10 kV and a beam-current of 200 nA. Focused Ion Beam (FIB) cross-sections of the indented material were prepared using a FIB working station (Auriga, Zeiss, Oberkochen, Germany) equipped with a gallium FIB system (Cobra Z-05, Orsay Physics, Brno, Czech Republic). Operated at 30 kV coarse cuts were performed with a high current Ga-beam of 20 nA and systematically reduced down to 100 pA for the final surface polishing step.

3. Results and discussion

3.1. Material response to Berkovich nanoindentation tests

Figure 2 shows the load (P) versus displacement (h) curves of both $LiTaO_3$ and $LiNbO_3$ single crystalline samples using a Berkovich tip. The curves with steeper slopes belong to the harder and stiffer material, i.e. $LiTaO_3$. The detailed view in Figure 2 represents the initial contact regions of the curves at low loads and low displacements. They show pop-in events in both materials (exemplarily marked by arrows), indicating first deviations from purely elastic contact. These discontinuities occurred at loads between 0.18 and 0.26 mN, at a penetration depth ranging between 20 and 25 nm and were considered as the point where irreversible deformation of the material (e.g. movement of dislocations, twinning, etc.) takes place [39-43].

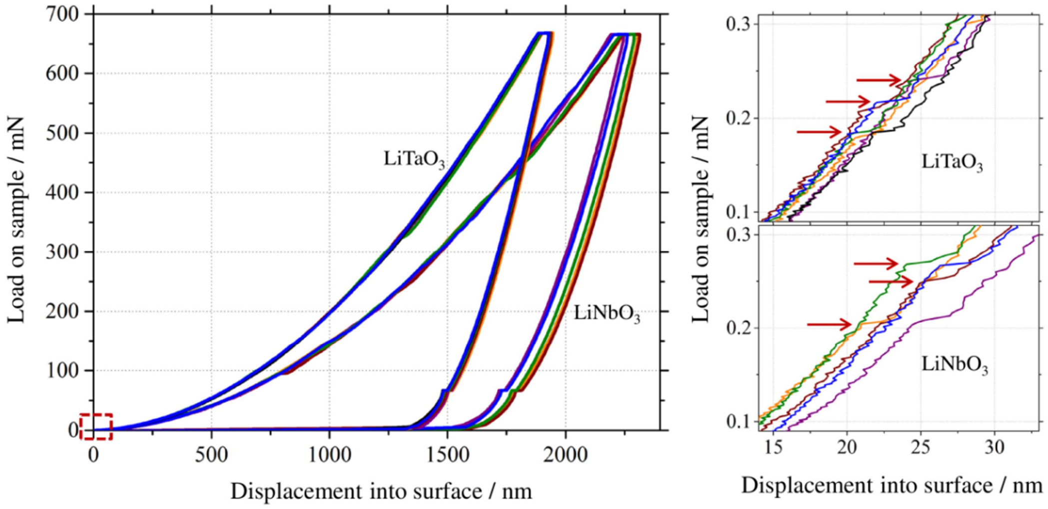

Figure 2: Load-displacement curves for Berkovich indents into $LiTaO_3$ and $LiNbO_3$ with a detailed view of the first pop-ins (exemplarily highlighted by arrows).

Table 1 shows the averaged hardness and Young's moduli values of six Berkovich indents performed for each material. It can be seen that the hardness of the tested $LiTaO_3$ – with the surface close to $(01\bar{1}2)$ – is almost 50% higher than of the indented $(0\bar{1}14)$ $LiNbO_3$ plane, which is known to be relatively soft [44]. Also the Young's modulus of $LiTaO_3$ is significantly higher compared to $LiNbO_3$, which was expected comparing the stiffness matrices of both materials [28, 29].

Table 1. Young's modulus and hardness of $LiTaO_3$ and $LiNbO_3$

	$LiTaO_3$	**$LiNbO_3$**
Young's Modulus [GPa]	248 ± 2	195 ± 1
Hardness [GPa]	9.7 ± 0.1	6.6 ± 0.2

During unloading, in particular for brittle materials, cracks may occur due to residual tensile stresses induced from plastic deformation [39, 45]. Constant load levels in the unloading curves result from the thermal drift determination at 10% of the maximum load and must not misleadingly be ascribed to any pop-out effects related, for instance, to phase transformations.

It should be noted that these indents were performed using a Berkovich tip, which is associated with an anisotropic stress and strain field. This may influence the mechanical response, as it will promote plastic deformation in certain preferred directions of the anisotropic single crystal. For a general statement on deformation and cracking behaviour, several different orientations of the indenter's edges with respect to the crystallographic directions would have to be investigated. Furthermore, the pop-in events occur at relatively low loads (see Figure 2). This makes it difficult to identify the small residual imprints at this onset of irreversible deformation, and the corresponding analyses of surface and sub-surface damage. To overcome these challenges, spherical nanoindentation tests were performed in order to to retrieve more reliable results on the incipient irreversible deformation mechanisms taking place in these materials.

3.2. Material response to spherical nanoindentation tests

Spherical nanoindentation tests were employed using a tip radius of R = 4.5 µm. During spherical indentation a symmetrical multiaxial stress field around the indent is introduced, which facilitates the evaluation of damage in the anisotropic materials concerned. The corresponding P–h curves for indentation depths up to ~2 µm are shown in Figure 3a for $LiTaO_3$ and in Figure 3b for $LiNbO_3$, respectively. The inserts in Figure 3 show the detailed pop-in events. It should be noticed that the mean load necessary to induce the pop-ins is slightly higher for $LiNbO_3$ (~ 75 mN) than for $LiTaO_3$ (~ 60 mN) and a few orders of magnitude higher than for the Berkovich indentation tests, where higher stress concentrations occur at the sharp tip, in a smaller loaded volume. Furthermore, significant differences in the maximum displacement were measured for each material (see Figure 3). This can be ascribed to discrete stochastic events occurring in the holding regime at the maximum load, such as the nucleation, propagation and arrest of cracks. However, fractographic results in the next sections could not reveal significant differences in damage morphology associated with such distinct displacement bursts.

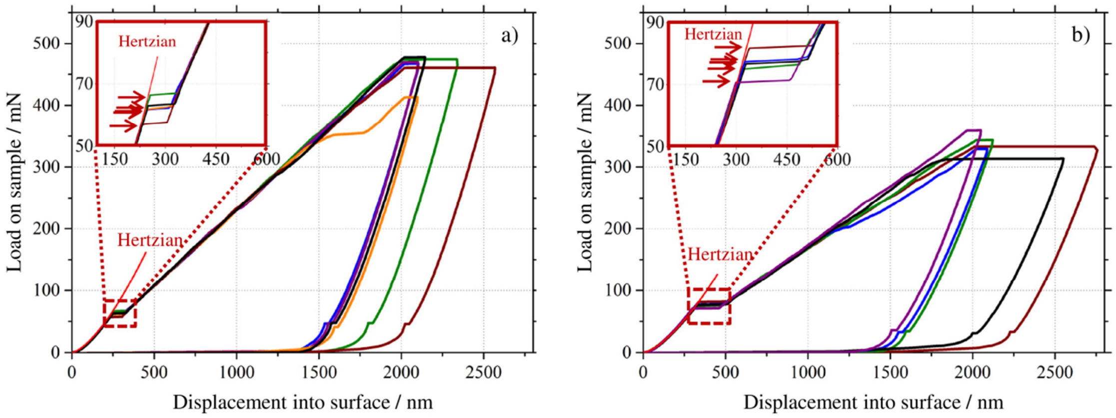

Figure 3: Load-displacement curves for spherical indents (R =4.5 µm) into a) $LiTaO_3$ and b) $LiNbO_3$. Pop-ins are clearly visible and marked with arrows in the magnified inserts.

Purely elastic Hertzian contact is represented in the figures according to the following equation [46]:

$$P = \frac{4}{3} E^{*} h^{\frac{3}{2}} \sqrt{R} \qquad (1)$$

where P is the load, h is the displacement into the surface, R is the radius of the indenter and E^* is the reduced modulus, which (for isotropic materials) is calculated according to [47]:

$$\frac{1}{E^*} = \frac{1-\nu_s^2}{E_s} + \frac{1-\nu_i^2}{E_i} \tag{2}$$

with E and ν being the Young's modulus and Poisson's ratio of an isotropic sample (s) and the indenter (i), respectively. For anisotropic materials the theoretical value E^* may also be determined by:

$$\frac{1}{E^*} = \frac{1}{E_{eff}} + \frac{1-\nu_i^2}{E_i} \tag{3}$$

where E_{eff} is the effective indentation modulus that can be calculated based on the elastic constants [33, 48, 49]. In this work the Hertzian contact P–h relation, as given in Equation (1), was calculated using E^* from Equation (2) with $R = 4.5$ µm, $E_{\mathrm{i}} = 1141$ GPa, $\nu_{\mathrm{i}} = 0.07$ and $\nu_{\mathrm{s}} = 0.25$ [50]. The elastic constants for both materials, as derived from the P-h curves from the spherical indenter were: $E_{\mathrm{LiTaO3}} = 254$ GPa and $E_{\mathrm{LiNbO3}} = 195$ GPa, respectively. Both results are in good agreement with the Berkovich indentation results in Table 1.

3.3. Surface damage after spherical indentation

Figure 4 shows representative surfaces after spherical indents onto $LiTaO_3$ (Figure 4a, b) and $LiNbO_3$ (Figure 4d, e) specimens, respectively. Severe damage was observed for all specimens, with cracks always following distinct preferential crystallographic directions. For the $LiTaO_3$ material, cracks were visible along all three $\{01\bar{1}2\}$ planes and also four out of the six $\{11\bar{2}3\}$ planes. The corresponding planes are schematically shown in Figure 4c (as represented in the corresponding pole figure in Figure 1c). Whereas the activated $(\bar{1}012)$ and $(1\bar{1}02)$ planes both have an angle of 87° with respect to the surface, the $(01\bar{1}2)$ plane is almost parallel (9°) to the surface and is most likely responsible for the chipping of some parts of the material close to the indent. Further cracks, belonging to the $\{11\bar{2}3\}$ set of planes, often occurred along the $(\bar{2}113)$ and $(2\bar{1}\bar{1}3)$ plane, both with an angle of 71° with respect to the surface. Cracks along $(1\bar{2}13)$ and $(\bar{1}\bar{1}23)$ planes, both with an angle of 76° to the surface, were also visible in some specimens. For the two remaining planes belonging to the same family, i.e. $(\bar{1}2\bar{1}3)$ and $(11\bar{2}3)$ with an angle of 27° with respect to the surface, no cracks were observed in any experiment.

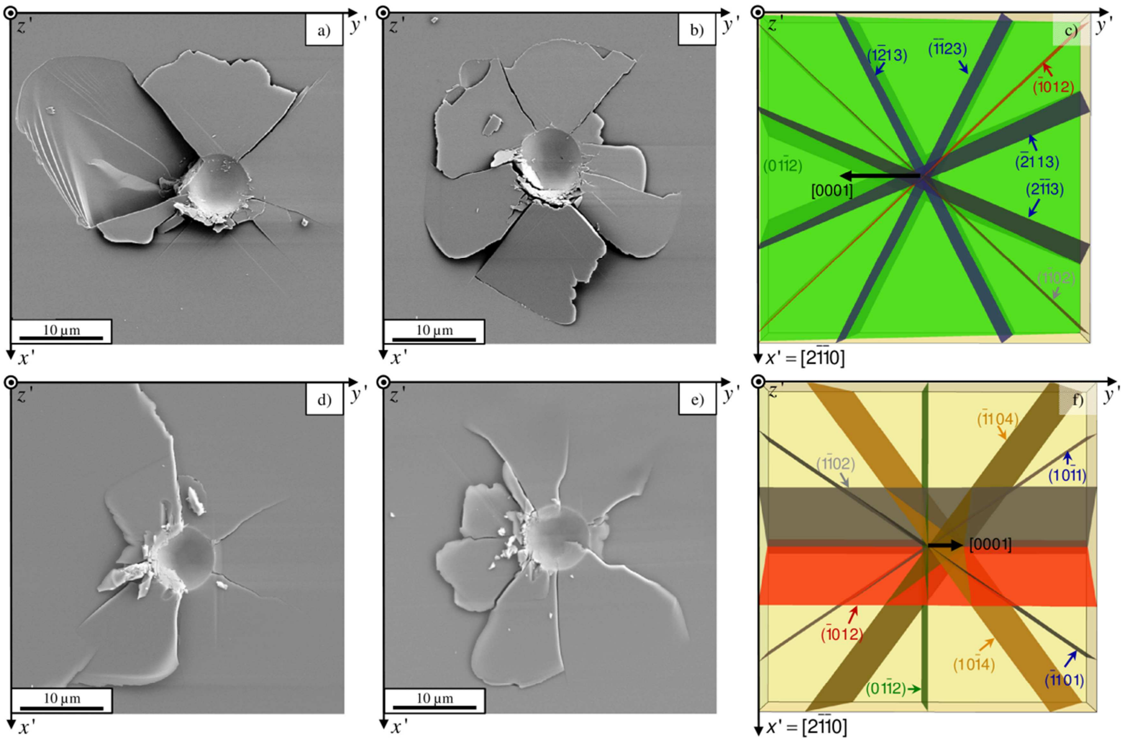

Figure 4: Representative SEM images after spherical indentation (R = 4.5 µm) with a depth of ~2 µm in $LiTaO_3$ (a,b) and $LiNbO_3$ (d,e). Schematics of frequently activated low indexed planes for $LiTaO_3$ (c) and $LiNbO_3$ (f).

Also for the $LiNbO_3$ single crystal, severe damage dominated by cracks following preferred crystallographic directions, as those represented in Figure 4f, was generated in the surface region. Similar to $LiTaO_3$, cracks along the $\{01\bar{1}2\}$ cleavage plane family were always observed. The most pronounced ones were those along the $(01\bar{1}2)$ plane, with an angle of 85° with respect to the surface. Further, slightly smaller cracks along $(\bar{1}101)$ and $(10\bar{1}1)$, both with an inclination angle of 87°, were also visible (see Figure 4d, e). For some specimens additional cracks along $(1\bar{1}04)$ and $(10\bar{1}4)$, both with an angle of 64° to the surface, could be discerned (compare Figure 4e, 4f). Generally, the fracture patterns are similar to those observed for biaxial strength measurements, where also cracks along $\{01\bar{1}2\}$ and $\{11\bar{2}3\}$ for $LiTaO_3$ as well as $\{01\bar{1}2\}$ and $\{10\bar{1}1\}$ for $LiNbO_3$ were documented [18]. Especially the $\{01\bar{1}2\}$ planes are often reported as preferred cleavage planes for this kind of materials [18, 26, 51]. Cracks along $\{10\bar{1}4\}$ in $LiNbO_3$ have only been reported in this work for the first time.

3.4. Evolution of sub-surface damage

Figure 5a shows the load-displacement curves of spherical indents with a depth of ~125 nm performed into $LiTaO_3$. Up to this load no pop-ins occurred and, as expected, no plastic deformation was observable on the surface of the specimens after unloading. Further measurements were performed just to the load where the first pop-ins occurred (see Figure 5b) to examine the surface and sub-surface damages, by setting the displacement limit at a value which is within the expected displacement excursion. The first pop-in events were detected at loads of ~50-55 mN.

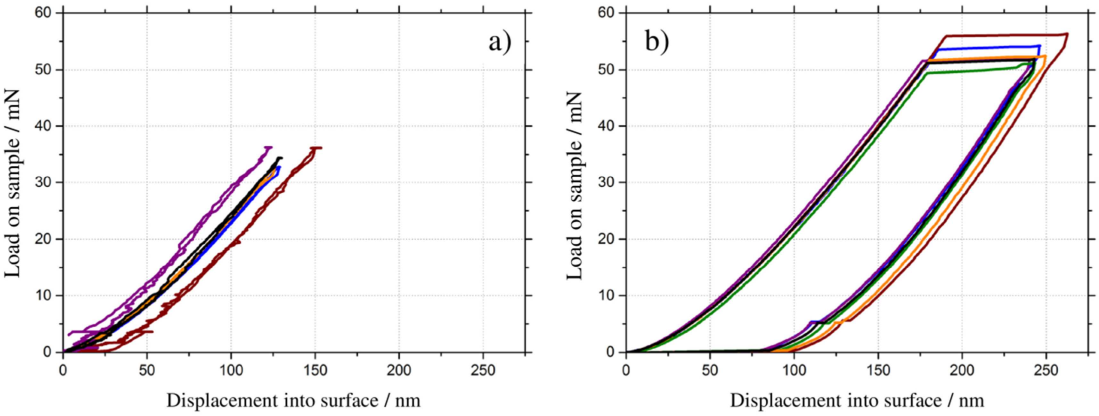

Figure 5: Load-displacement curves for spherical indents (R = 4.5 µm) in LiTaO3 up to a depth of a) ~125 nm, where no pop-ins were observed and b) where loading was stopped after the first pop-in.

Figure 6a shows a representative surface of a $LiTaO_3$ specimen after this very first contact damage corresponding to one of the load-displacement curves in Figure 5b. Traces of plastic deformation along the $(\bar{1}012)$ and $(1\bar{1}02)$ planes (shown schematically in Figure 4c) are visible. In addition to the first plastic response of the $LiTaO_3$ material, the first cracks can be seen along the same planes. It should be noted that direct observation of the crack onset was not feasible during indentation. All examinations were performed after unloading of the sample. Thus, crack formation might have occurred during the unloading process.

The sub-surface damage was assessed through successive cross-sectioning of the site of interest (see black arrows in Figure 6a) by using FIB milling. Figure 6b shows the corresponding section perpendicular to the $(1\bar{1}02)$ plane, as represented in Figure 6a by a white, dashed line and dashed arrows. The insert in Figure 6b shows schematically the alignment of these activated planes according to the FIB cut to facilitate the correlation between the crystal orientation and the observed sub-surface crack pattern. It can be seen that a main crack almost perpendicular to the surface initiated upon contact loading. This crack followed the $(1\bar{1}02)$ plane, which lies 87° to the surface. Interestingly, also cracks along the plane $(01\bar{1}2)$ could be observed, which extended almost parallel (i.e. 9°) to the surface. These are responsible for causing “lateral chipping”, as observed in Figure 4. From all traces of plastic deformation visible on the specimen’s surface (see Figure 6a: positions of the “steps” are marked with black arrows) only the most pronounced one turned into a crack. This observation demonstrates that the onset of cracking in these materials is located in regions which were plastically deformed (steps in Figure 6a), and then proceeds along the cleavage plane $(01\bar{1}2)$ or $(1\bar{1}02)$. Cracks following the $(2\bar{1}\bar{1}3)$ and $(\bar{2}113)$ planes (compare

Figure 6a and Figure 4c) were significantly longer than those along the $\{01\bar{1}2\}$ planes for every single performed indent indicating a low toughness. Even though the remaining spherical impression had a depth of only ~100 nm (Figure 5b), cracks down to a depth of ~6 µm could be evidenced (Figure 6b), thus manifesting the brittle character of the material.

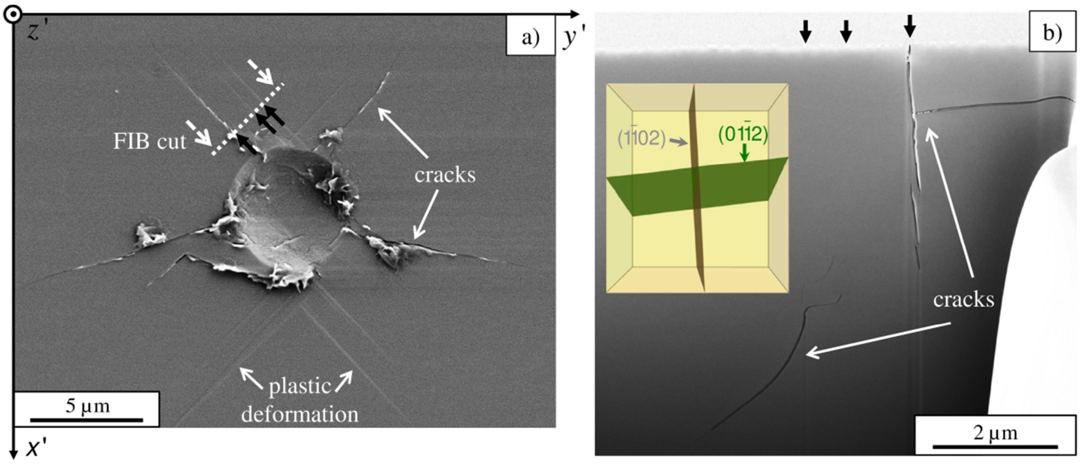

Figure 6: SEM-image of the surface of a $LiTaO_3$ specimen after spherical indentation (R = 4.5 µm) up to the first pop-in load (a) and FIB cross-section according to the dashed white line in (a) with inserted alignment of the activated $\{01\bar{1}2\}$ cleavage planes (b). Positions of traces of plastic deformation are highlighted with black arrows in both images.

Following the same procedure as for $LiTaO_3$, spherical indentations were performed in the $LiNbO_3$ material. Figure 7a shows the load-displacement curves up to a maximal load of ca. 60 mN, with a penetration depth of ~250 nm. All specimens (including the one with a slight deviation from linear elastic behaviour at 63 mN) were examined in the SEM after the test, showing no visible damage on the surface. The first pop-in events were detected at higher loads between 60 and 80 mN (see Figure 7b), i.e. at higher loads compared to the $LiTaO_3$ specimens (see Figure 5b). Moreover, the pop-ins occurred over a larger load range.

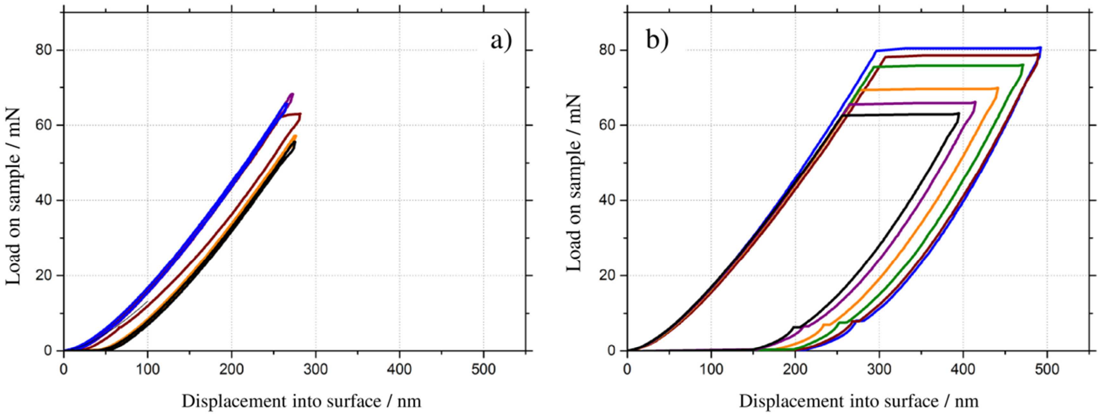

Figure 7: Load-displacement curves for spherical indents (R = 4.5 µm) in LiNbO3 a) up to a maximal load of ca. 60 mN (with a penetration depth of ~250 nm), where no pop-ins were observed and b) up to 80 mN, where loading was stopped after the first pop-in.

Figure 8a shows a representative surface of a LiNbO$_3$ specimen after loading up to the first pop-in shown in Figure 7b. Analogue to LiTaO$_3$, traces of plastic deformation along the $\{01\bar{1}2\}$ set of planes, which are schematically shown in Figure 4c, are visible. Already after this very first irreversible deformation of LiNbO$_3$, the first cracks are visible along the $(01\bar{1}2)$ plane, with an angle of 85° with respect to the surface. The FIB cut perpendicular to the $(2\bar{1}\bar{1}0)$ plane provided in Figure 8b (projection of the cut plane and view direction indicated by white, dashed line and arrows) shows that the sub-surface crack initially follows the $(01\bar{1}2)$ plane (see insert in Figure 8b). However, the penetrating crack also bends into other directions, which cannot be clearly assigned to low-indexed crystallographic planes. Traces of plastic deformation on the specimen's surface were again not possible to be discerned in the cross-sections. The depth of the crack exposed with FIB (Figure 8b) was about 2 µm, i.e. not as deep as the crack observed in LiTaO$_3$, being in agreement with the shorter cracks visible on the LiNbO$_3$ surfaces. This may be related to the higher elastic modulus of LiTaO$_3$; as the deformation upon loading induces higher stresses under the same applied strain.

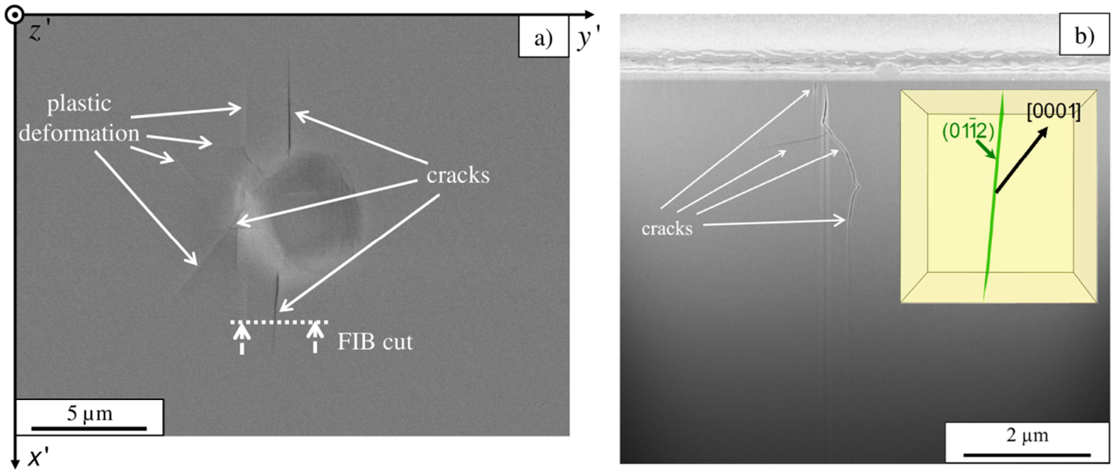

Figure 8: a) SEM image of the surface of a LiNbO$_3$ specimen after spherical indentation (R = 4.5 µm) up to the first pop-in load and b) FIB cross-section according to the white, dashed line in a) with inserted alignment of the activated $(01\bar{1}2)$ cleavage plane.

3.5. Twinning and cracking

Based upon the experimental observations using spherical indents there seems to be a relation between plastic deformation and cracking in both LiTaO$_3$ and LiNbO$_3$. In this regard, twinning of the $\{01\bar{1}2\}$ planes has been reported for LiTaO$_3$ [22] as well as for LiNbO$_3$ [21, 23]. Even at elevated temperatures twinning of the $\{01\bar{1}2\}$ set of planes is still preferred over dislocation glide in LiTaO$_3$ [52] as well as for LiNbO$_3$ [19], providing an explanation for the origin of the observed plastic deformation of LiTaO$_3$ for loading along the c-axis [52]. In our investigation, the traces on the surface of LiTaO$_3$ (Figure 6a) and on LiNbO$_3$ (Figure 8a) are aligned along this set of planes (compare with 4c and 4f). Therefore, it can be concluded that for the loading conditions investigated in this work, twinning of the $\{01\bar{1}2\}$ planes is observed. The regarded twinning system with $K_1=(01\bar{1}2)$, $\eta_1=[0\bar{1}11]$, $K_2=(0\bar{1}14)$ and $\eta_2=[02\bar{2}1]$, as summarized in [53], is shown in Figure 9 for a cut perpendicular to $[2\bar{1}\bar{1}0]$, analogue to the SEM image in Figure 8b. The small burgers vector of the required partial dislocation of $1/21[01\bar{1}\bar{1}]$ would make this deformation favorable over nucleation of a full dislocation, where the corresponding burgers vector is $1/3[01\bar{1}\bar{1}]$. The head to head and tail to tail configuration of the polar c-axis caused by twinning would lead to charges on this planes. This could cause repulsive forces acting on the $\{01\bar{1}2\}$ planes.

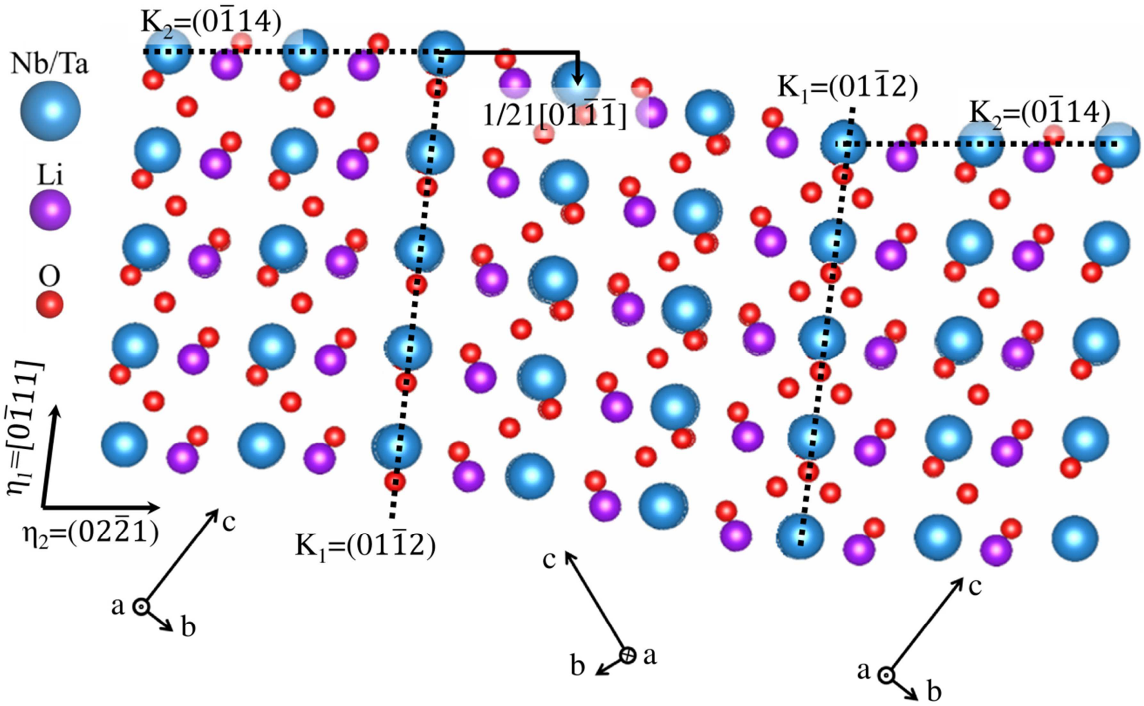

Figure 9: Schematic representation of a twin domain mirrored onto the $(01\bar{1}2)$ plane as observed in $LiNbO_3$ single crystals after spherical indentation.

For the movement of an already existing dislocation, a shear stress of below 3 GPa for $LiTaO_3$ and below 2 GPa for $LiNbO_3$ is estimated by taking half of the hardness as yield strength and a Taylor factor of $3^{-1/2}$ for a averaging over possible slip systems to convert normal into shear stresses, as commonly done [54]. Since these values are significantly lower than the stress values observed in this work (see 3.6), glide of existing dislocations can be excluded as predominant deformation mechanism. However, the twin shown in Figure 9 for $LiNbO_3$ would not explain the surface mark of the indenter after the pop-in, since no shortening in z' direction is caused by this deformation (only shear strain). Twinning along the $(\bar{1}012)$ and $(1\bar{1}02)$ would shift the longer c-axis of the crystal almost parallel to the surface and could therefore cause an elongation in plane and consequently a shortening in z' direction, providing the space for the residual spherical imprint. For $LiTaO_3$ no such favorable twinning system could be evidenced, thus requiring plastic shear by dislocations underneath the imprint to realize the prescribed geometry. This might be responsible for the smaller residual depth after the pop-in (compare Figure 5b and 7b) and the correlated higher hardness.

Also twinning of the $\{0\bar{1}14\}$ planes has previously been reported for $LiTaO_3$ [55], and could be confirmed for $LiNbO_3$ in this work (Figure 8a). Park et al. [56] documented for $LiNbO_3$ twins as well as cracks along the $\{01\bar{1}2\}$ set of planes and assumed that cracks nucleate at the crossing points of twins. Also in the present work cracks seem to nucleate and propagate at the same planes where twins occurred. Thus it is assumed that these cracks develop due to tensile stresses emerging during unloading and follow the twinned planes, promoted by the repulsive electrostatic forces due to the mirrored alignment of the polar axis. Since this kind of defect is exactly located at documented cleavage planes [18], a significant loss in mechanical strength is expected after the very first pop-in. According to linear elastic fracture mechanics, this effect is expected to be even more severe for $LiTaO_3$, because the cracks penetrate deeper into the material (compare Figure 6b and 8b). In addition, for larger indents, a gradual increase in damage and thus decrease in mechanical strength may be expected.

3.6. Statistical evaluation of pop-in stresses

In order to rationalize the stresses leading to pop-in events (and eventually cracking) in both materials, a statistical analysis of the pop-in stresses is required. Since the pop-in behavior depends on the activated volume, statistical evaluation of pop-in stresses was performed within the framework of Weibull theory [57]. Weibull parameters were determined by the Maximum-Likelihood method [58] and represented in Weibull plots, where the probability of a pop-in (here considered as a fracture event) is plotted over the maximum shear stress. The maximum occurring shear stresses were evaluated because they might be responsible for the first plastic deformation underneath the indenter. They are significantly higher than those in locations where twin-patterns on the specimen surface were observed. Thus, twinning would be expected as easy deformation mechanism.

Since already the very first pop-in would lower the strength of the investigated single crystal materials due to cracks and twins on the surface, the exact point of this event needs to be evaluated. In total 35 spherical indents were performed for each materials to get significant statistics for the measured pop-in stresses [58]. These stresses were calculated according to Hertzian elastic contact theory, where the maximum shear stress $\tau_{\max}$ is evaluated by [47]:

$$\tau_{\max} = 0.31 \times \left(\frac{6 P_{pop-in} E^{*2}}{\pi^3 R^2} \right)^{1/3} \qquad (4)$$

with $P_{\text{pop-in}}$ being the pop-in load, R the indenter radius and E^* as described in section 3.2.

In order to prove the suitability of this equation for the anisotropic materials investigated and gain more insight on the stress distribution prior to the pop-in event, a finite element simulation was performed using the commercial software ANSYS 18.2. The anisotropic material properties for $LiTaO_3$ and $LiNbO_3$ (as given in [29] at 25°C) and the elastic constants for the spherical diamond indenter [50] were introduced in the model. A contact load corresponding to the average pop-in load (see Table 2) was applied. For illustrative purposes, only the numerical results for $LiNbO_3$ are presented in Figure 10.

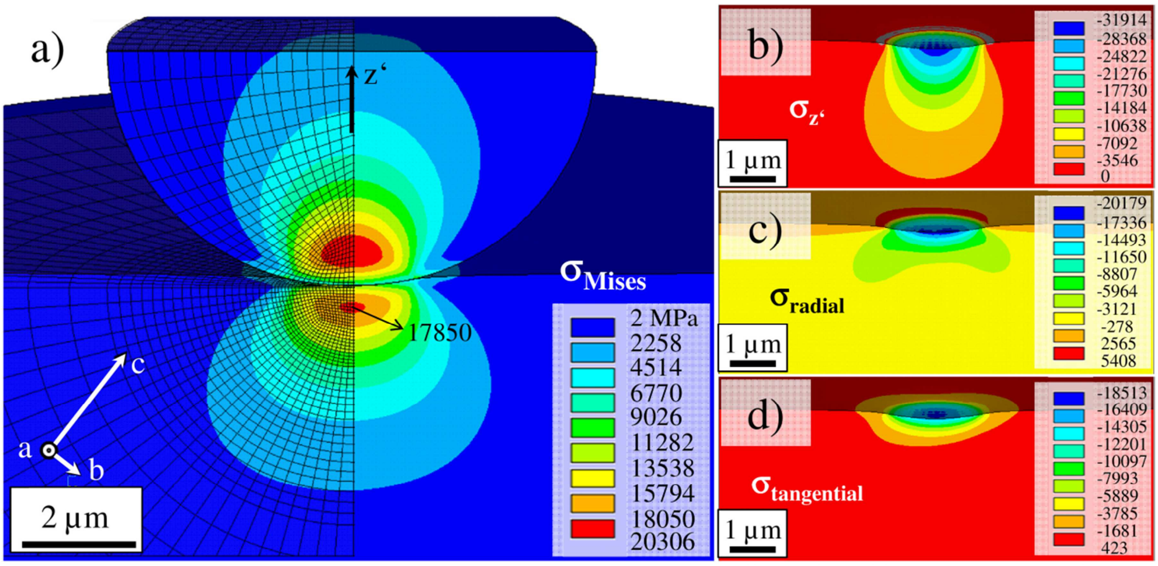

Figure 10: Contour plots from the elastic contact analysis showing a) σ_{Mises}, b) $\sigma_{z'}$, c) σ_{radial} and d) $\sigma_{\text{tangential}}$ for 128° Y-X $LiNbO_3$ calculated using the commercial finite element software ANSYS 18.2. The stresses are not symmetrical with respect to the z'-axis as a consequence of the anisotropic elastic constants of the material.

The referred figure shows a) σ_{Mises}, b) $\sigma_{z'}$, c) σ_{radial}, d) $\sigma_{\text{tangential}}$, in $LiNbO_3$, neglecting piezoelectric effects. It is worth pointing out that the stresses are not symmetrical with respect to the z'-axis, which is a consequence of the anisotropic elastic constants of the material. The maximum shear stress of 8925 MPa (half of the maximum of σ_{Mises}) is in good agreement with the experimental shear stress value of 9065 MPa as derived from Equation (4). For 42° Y-X $LiTaO_3$ the numerical contact analysis delivered a maximum shear stress of 9743 MPa; a value slightly above the experimental result of 9346 MPa (as calculated from Equation (4)). The resulting stress profiles were similar to those in $LiNbO_3$. However, all stress components (i.e. σ_{Mises}, $\sigma_{z'}$, σ_{radial}, $\sigma_{\text{tangential}}$) were slightly higher in $LiTaO_3$ than in $LiNbO_3$, due to the stiffer behavior of the former material. We caution the reader that the incorporation of piezoelectric constants in the model revealed no significant differences concerning Mises stresses, but larger differences for the radial and especially tangential components, which may be related to the selected electrical boundary conditions. However, this is out of the scope of this work. After reliable flow properties of the materials are evaluated, another subject for prospective work, will be the assessment of tensile residual stresses suspected to cause cracks during unloading, once irreversible plastic deformation has occurred.

Figure 11 shows a Weibull plot, where the probability of a pop-in event is plotted vs. the corresponding maximum shear stress, calculated using Equation (4). For both materials very similar characteristic pop-in stresses were measured.

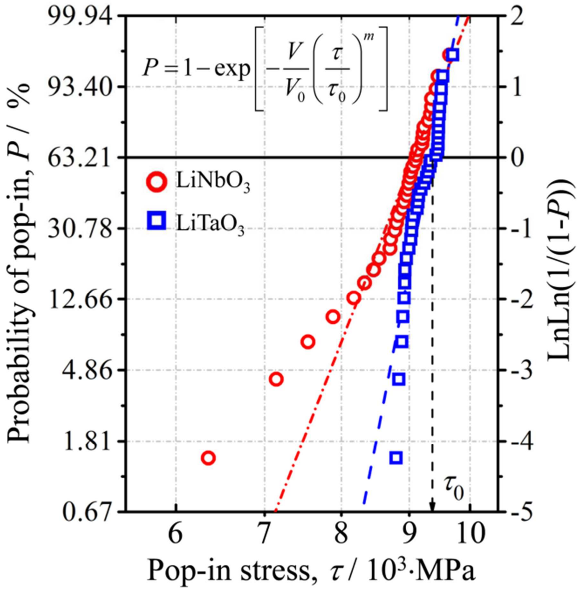

Figure 11: Weibull diagram showing the probability of pop-in event versus the measured (pop-in) shear stresses for spherical indents (R = 4.5 μm) in $LiTaO_3$ and $LiNbO_3$.

The average as well as the "characteristic" shear stress, τ_0 and the corresponding Weibull modulus, m (slope in the Weibull diagram) are listed in Table 2 along with their 90 % confidence intervals. For both materials a characteristic shear stress of ~9 GPa was determined, which equates ~E/27 for $LiTaO_3$ and ~E/22 for $LiNbO_3$, with E being the modulus determined from the spherical indents. These values are already close to the region of the theoretical strength of ~E/15 for brittle materials like ceramics or glasses [59].The pop-in stress values measured for $LiTaO_3$ are slightly higher and within a narrower range, leading to a two times higher Weibull modulus compared to $LiNbO_3$ (see Table 2).

Table. 2: Average pop-in loads, $P_{pop\text{-}in}$, average shear stresses, τ, characteristic shear stresses, τ_0, and Weibull modulus, m, together with 90% confidence intervals for $LiTaO_3$ and $LiNbO_3$ single crystals obtained after spherical nanoindentation measurements.

	$P_{\text{pop-in}}$ [mN]	**τ [MPa]**	**τ_0 [MPa]**	***m***
$LiTaO_3$	57 ± 5	9226 ± 252	9346 [9278 - 9415]	42 [32 – 51]
$LiNbO_3$	79 ± 16	8807 ± 686	9065 [8933 – 9200]	21 [16 – 25]

The statistical evaluation of the data reveals that the characteristic pop-in stresses in both materials are indeed slightly different within the 90% confidence intervals. It is conspicuous that, although the higher stress values for both materials are almost identical, in $LiNbO_3$ several pop-ins at relatively low loads are present causing the lower Weibull modulus. Nevertheless, the bearable load before pop-in for the same indenter radius is higher for the $LiNbO_3$ due to the lower reduced modulus (see Equation 4). Also the contact radius is larger for this material leading to a larger stressed volume which increases the chance of activating a second defect population. This would lead to the pop-ins at relatively low loads (Figure 11) which also yield a different Weibull modulus. Nevertheless, the origins of defects leading to the observed pop-ins could not be discerned in this work.

3.7. Understanding crack extension in $LiTaO_3$ and $LiNbO_3$

There seems to be a sort of paradox between the onset of damage and macroscopic mechanical failure in these two materials. On the one hand $LiTaO_3$ is approx. 50% harder than $LiNbO_3$. A direct implication of this higher hardness might be a higher resistance to deformation, indentation or penetration (e.g. due to grinding, impact or wear). As a consequence, smaller defects (e.g. micro-cracks) are expected to be encountered at or below the surface of $LiTaO_3$ samples. The biaxial strength measured in previous work agrees with this hypothesis, where the strength of $LiTaO_3$ was found to be ~2.5 times higher than that of $LiNbO_3$. On the other hand, cross-sectional FIB analysis of the $LiTaO_3$ and $LiNbO_3$ samples after nanoindentation showed longer extension of the sub-surface cracks in the $LiTaO_3$ samples. The explanation for this may be related to the stored elastic energy during the loading process, which may be different in both materials, and that can trigger the propagation of the originated cracks. According to Ashby [59], the stored elastic energy up to the crack formation can be described as $U_e=\sigma_y^2/2E$ (per volume unit), with σ_y being the yield strength and E the Young's modulus. Approximating the yield strength for both materials to 1/3 of their hardness values [59], and introducing the corresponding Young's moduli, the stored energy in $LiTaO_3$ is approx. 1.8 times higher than that stored in $LiNbO_3$. This excess of energy may foster further crack propagation or activation of other cracks in neighboring planes.

Based upon these findings, the mechanical behavior of single crystals is not only related to the orientation of cleavage planes with respect to the loading direction, but very importantly depends on the type of loading and elastic properties of the material. A competition between hardness, crystal orientation and elastic properties seems to apply. Last but not least, the resistance of the material to the propagation of an existing crack can also play an important role in the macroscopic mechanical behavior of the single crystal. Therefore, fracture toughness measurement in specific cleavage planes is ongoing work.

4. Conclusion

The onset of contact damage in single crystal brittle materials has been investigated on $LiTaO_3$ and $LiNbO_3$ samples combining Berkovich and spherical nanoindentation with FIB sub-surface analyses in the corresponding damaged regions. The materials of study exhibited different contact responses (i.e. crack orientation and length) associated with their distinct intrinsic elastic properties and orientation of brittle cleavage planes with respect to the loading. The onset of contact damage occurs under similar maximum shear stresses in both materials, and is preceded by traces of plastic deformation (twinning) on the contact surface, developed along distinct cleavage planes. These initial locations of plasticity are subsequent sites for crack initiation along those planes. The more pronounced damage in terms of crack length encountered in the $LiTaO_3$ material is ascribed to its higher elastic modulus, and less capability of accommodating plastic deformation. It can be concluded that in anisotropic brittle single crystals the fracture response is determined by a competition between hardness, crystal orientation and elastic properties, and thus must be adequately considered for the design of reliable functional components.

5. Acknowledgements

Financial support by the Austrian Federal Government (in particular from Bundesministerium für Verkehr, Innovation und Technologie and Bundesministerium für Wissenschaft, Forschung und Wirtschaft) represented by Österreichische Forschungsförderungsgesellschaft mbH and the Styrian and the Tyrolean Provincial Government, represented by Steirische Wirtschaftsförderungsgesellschaft mbH and Standortagentur Tirol, within the framework of the COMET Funding Programme is gratefully acknowledged.

6. References

[1] Campbell C. Surface Acoustic Wave Devices and their Signal Processing Applications. Academic Press; 1989. p. 427–58.

[2] Kuz'minov YS. Lithium Niobate Crystals: Physico-chemical Aspects of Technology: Cambridge International Science Publishing; 1999.

[3] Hashimoto K-Y. Surface Acoustic Wave Devices in Telecommunications: Modelling and Simulation: Springer-Verlag Berlin Heidelberg GmbH; 2000.

[4] Morgan D. Surface Acoustic Wave Filters. 2nd ed: Academic Press; 2007.

[5] Chen Y, Miao C, Xie S, Xu L, Wang Q, Zhu J, et al. Microstructural evolutions, elastic properties and mechanical behaviors of W/Cr Co-doped Bi 4 Ti 3 O 12 ceramics. Materials & Design. 2016;90:628-34.

[6] Jo S, Hong CH, Kim DS, Kang HW, Ahn CW, Lee HG, et al. Phase transition behavior and mechanical properties of (1-x)(Bi1/2Na1/2)TiO3-xSrTiO3 lead-free piezoelectric ceramics. Sensors and Actuators, A: Physical. 2017;258:201-7.

[7] Choi M, Murillo G, Hwang S, Kim JW, Jung JH, Chen CY, et al. Mechanical and electrical characterization of PVDF-ZnO hybrid structure for application to nanogenerator. Nano Energy. 2017;33:462-8.

[8] Schultz RA, Jensen MC, Bradt RC. Single crystal cleavage of brittle materials. Int J Fract. 1994;65:291–312.

[9] Tsai YL, Mecholsky Jr JJ. Fracture mechanics description of fracture mirror formation in single crystals. Int J Fract. 1992;57:167–82.

[10] Chen K-S, Ayon A, Spearing SM. Controlling and Testing the Fracture Strength of Silicon on the Mesoscale. J Am Ceram Soc. 2000;83:1476–84.

[11] Wereszczak AA, Barnes AS, Breder K, Binapal S. Probabilistic strength of {1 1 1} n-type silicon. J Mater Sci. 2000;11:291–303.

[12] C. Funke EK, M. Kuna, H.J. Möller,. Biaxial Fracture Test of Silicon Wafers. Adv Eng Mat. 2004;6:594–8.

[13] Lawn BR. Indentation of Ceramics with Spheres: A Century after Hertz. J Am Ceram Soc. 1998;81:1977–94.

[14] Lee SK, Lawn BR. Role of Microstructure in Hertzian Contact Damage in Silicon Nitride: II, Strength Degradation. J Am Ceram Soc. 1998;81:997–1003.

[15] Lawn BR, Wuttiphan S. Model of Strength Degradation from Hertzian Contact Damage in Tough Ceramics. J Am Ceram Soc. 1998;81:1509–20.

[16] Rhee Y-W, Kim H-W, Deng Y, Lawn BR. Brittle Fracture versus Quasi Plasticity in Ceramics: A Simple Predictive Index. J Am Ceram Soc. 2001;84:561–5.

[17] Deluca M, Bermejo R, Pletz M, Supancic P, Danzer R. Strength and fracture analysis of silicon-based components for embedding. J Eur Ceram Soc. 2011;31:549–58.

[18] Gruber M, Kraleva I, Supancic P, Bielen J, Kiener D, Bermejo R. Strength distribution and fracture analyses of $LiNbO_3$ and $LiTaO_3$ single crystals under biaxial loading. J Eur Ceram Soc. 2017;37:4397–406.

[19] Vere AW. Mechanical twinning and crack nucleation in lithium niobate. J Mater Sci. 1968;3:617–21.

[20] Subhadra KG, Kishan Rao K, Sirdeshmukh DB. Systematic hardness studies on lithium niobate crystals. Bull Mater Sci. 2000;23:147–50.

[21] Basu S, Zhou A, Barsoum M. Reversible dislocation motion under contact loading in LiNbO3 single crystal. J Mat Res. 2008;23:1334–8.

[22] Anasori B, Sickafus KE, Usov IO, Barsoum MW. Spherical nanoindentation study of the deformation micromechanisms of LiTaO3 single crystals. J Appl Phys. 2011;110:023516.

[23] Zhang Z, Yang S, Xu C, Wang B, Duan N. Deformation and stress at pop-in of lithium niobate induced by nanoindentation. Scripta Mater. 2014;77:56–9.

[24] Shibayama K, Yamanouchi K, Sato H, Meguro T. Optimum Cut for Rotated Y-Cut LiNbO3 Crystal Used as the Substrate of Acoustic-Surface Wave Filters. Proceedings of the IEEE1976. p. 595–7.

[25] Weng W, Wang H, Ma N, Wu Y, Li J. Effect of domain structure on the damping properties of LiNbO3/Al composites. Materials and Design. 2010;31:4116-21.

[26] Weis RS, Gaylord TK. Lithium niobate: Summary of physical properties and crystal structure. Appl Phys A. 1985;37:191–203.

[27] Abrahams SC, Reddy JM, Bernstein JL. Ferroelectric lithium niobate. 3. Single crystal X-ray diffraction study at 24°C. J Phy Chem Solids. 1966;27:997–1012.

[28] Taki K, Shimizu Y. Material Constants of LiTaO3 Determined from Surface Acoustic Wave Velocities. Jpn J Appl Phys. 1994;33:2976–8.

[29] Smith RT, Welsh FS. Temperature Dependence of the Elastic, Piezoelectric, and Dielectric Constants of Lithium Tantalate and Lithium Niobate. J Appl Phys. 1971;42:2219–30.

[30] Hsu R, Maslen EN, Du Boulay D, Ishizawa N. Synchroton X-ray Studies of LiNbO3 and LiTaO3. Acta Crystallographica Section B. 1997;53:420 - 8.

[31] Merle B, Maier-Kiener V, Pharr GM. Influence of modulus-to-hardness ratio and harmonic parameters on continuous stiffness measurement during nanoindentation. Acta Mater. 2017;134:167–76.

[32] Oliver WC, Pharr GM. An improved technique for determining hardness and elastic modulus using load and displacement sensing indentation experiments. J Mat Res. 1992;7:1564–83.

[33] Vlassak JJ, Nix WD. Indentation modulus of elastically anisotropic half spaces. Philos Mag A. 1993;67:1045–56.

[34] Vlassak JJ, Nix WD. Measuring the elastic properties of anisotropic materials by means of indentation experiments. J Mech Phys Solids. 1994;42:1223-45.

[35] Leitner A, Maier-Kiener V, Kiener D. Essential refinements of spherical nanoindentation protocols for the reliable determination of mechanical flow curves. Acta Mater. 2017;submitted.

[36] Zhu T, Li J, Samanta A, Leach A, Gall K. Temperature and Strain-Rate Dependence of Surface Dislocation Nucleation. Phsys Rev Lett. 2008;100:025502.

[37] Shim S, Bei H, George EP, Pharr GM. A different type of indentation size effect. Scripta Mater. 2008;59:1095–8.

[38] Gao Y, Bei H. Strength statistics of single crystals and metallic glasses under small stressed volumes. Prog Mater Sci. 2016;82:118–50.

[39] Lawn BR, Evans AG, Marshall DB. Elastic/Plastic Indentation Damage in Ceramics: The Median/Radial Crack System. J Am Ceram Soc. 1980;63:574–81.

[40] Schuh CA, Mason JK, Lund AC. Quantitative insight into dislocation nucleation from high-temperature nanoindentation experiments. Nat Mater. 2005;4:617–21.

[41] Gaillard Y, Macías AH, Muñoz-Saldaña J, Anglada M, Trápaga G. Nanoindentation of BaTiO3: dislocation nucleation and mechanical twinning. J Phys D. 2009;42:085502.

[42] Gerberich WW, Venkataraman SK, Huang H, Harvey SE, Kohlstedt DL. The injection of plasticity by millinewton contacts. Acta Metall Mater. 1995;43:1569–76.

[43] Asaro RJ, Suresh S. Mechanistic models for the activation volume and rate sensitivity in metals with nanocrystalline grains and nano-scale twins. Acta Mater. 2005;53:3369–82.

[44] Bhagavat S, Kao I. Nanoindentation of lithium niobate: hardness anisotropy and pop-in phenomenon. Mat Sci Eng A. 2005;393:327–31.

[45] Sebastiani M, Johanns KE, Herbert EG, Pharr GM. Measurement of fracture toughness by nanoindentation methods: Recent advances and future challenges. Current Opinion Solid Stat Mater Sci. 2015;19:324–33.

[46] Lawn BR. Fracture of Brittle Solids - Second Edition. Cambridge: Cambridge University Press; 1993.

[47] Johnson KL. Contact Mechanics. Cambridge: Cambridge University Press; 1985.

[48] Willis JR. Hertzian contact of anisotropic bodies. J Mech Phys Solids. 1966;14:163–76.

[49] Swadener JG, Pharr GM. Indentation of elastically anisotropic half-spaces by cones and parabolae of revolution. Philos Mag A. 2001;81:447−66.

[50] Simmons G, Wang H. Single Crystal Elastic Constants and Calculated Aggregate Properties: A Handbook. 2nd ed. Cambridge, MA: MIT Press; 1971.

[51] Hang W, Zhou L, Shimizu J, Yuan J, Yamamoto T. Study on the Mechanical Properties of Lithium Tantalate and the Influence on its Machinability. Fuji Technology Press LTD. 2013;7:644–53.

[52] Doukhan JC, Cordier P, Doukhan N, Fragneau M, Aubry JP. Lattice defects in lithium tantalate. 43rd Annual Symposium on Frequency Control1989.

[53] Wong KK. Properties of Lithium Niobate: INSPEC, The Institution of Electrical Engineers, London, United Kingdom; 2002.

[54] Nix WD, Gao H. Indentation size effects in crystalline materials: A law for strain gradient plasticity. J Mech Phys Solids. 1998;46:411–25.

[55] Bursill LA, Lin PJ. Chemical twinning and ferroelectric domains in $LiTaO_3$. Philos Mag A. 1982;46:1−24.

[56] Park BM, Kitamura K, Furukawa Y, Ji Y. Relation between Mechanical Twinning and Cracking in Stoichiometric Lithium Niobate Single Crystals. J Am Ceram Soc. 1997;80:2689–92.

[57] Weibull W. A statistical distribution function of wide applicability. J Appl Mech. 1951;18:293−7.

[58] EN 843-5. Advanced Technical Ceramics - Monolithic Ceramics - Mechanical Tests at Room Temperature - Part 5: Statistical Analysis. EN 843-51997. p. 40.

[59] Ashby MF, Jones DRH. Engineering Materials 1. Oxford: Pergamon Press; 1993.

Publication E

Effect of metallization on the strength and fracture behaviour of functional co-fired multilayer ceramics

M. Gruber, P. Supancic, F. Aldrian and R. Bermejo

Abstract.

Functional components are commonly fabricated combining a ceramic substrate with external and/or internal metallization. Different layers are printed and fired onto the ceramic part to provide the component with a functionality. As a result of the combination of materials with different coefficients of thermal expansion, internal stresses during the fabrication steps may lead to cracks and/or reduce the strength. In this work, several architectures combining metal and glass layers on the surface of ZnO substrates were analyzed to identify critical fabrication steps in functional co-fired multilayer ceramics. Three-point bending tests were performed on samples taken after different process steps. Experimental results showed a strong effect of the layered architecture on the strength distributions: details of geometrical designs can have a dramatic impact on the strength. Fractographic analyses and *ex-situ* Focused Ion Beam experiments in pre-loaded samples were the key to assess the location of failure and predict critical configurations.

Keywords. Functional ceramic components miniaturized mechanical testing, strength distribution, damage, fractography.

1. Introduction

In many applications for microelectronics it is necessary to combine different materials (ceramic, metals and polymers) that can bring new functionality to components, creating so-called hybrid planar systems. Functional components such as multilayer varistors (MLV), piezoelectric actuators (MPA), multilayer ceramic capacitors (MLCC), Low Temperature Co-fired Ceramics (LTCC) and semiconductors, among others, are examples of combination of a ceramic-based (or silicon based) substrate with internal electrodes as well as surface features (e.g. metallization, contacting pads, cylindrical vias, etc.) However, it entails a number of multidisciplinary challenges which have to be solved (e.g. geometrical tolerances, fabrication of internal structures, co-sintering of different materials, development of internal stresses, etc.) In this regard, tape casting technology has enabled the fabrication of such hybrid devices based on a "multilayer architectural design", with high degree of dimensional accuracy [1, 2]. Some examples of such advanced engineering systems are (i) planar Solid Oxide Fuel Cells (SOFC), (ii) stacked piezo-actuators and sensor devices, and (iii) conducting plates for wireless communications. Typical components are based on low temperature co-fired ceramics substrates (e.g. alumina-glass composites, ZnO), which enable the co-sintering of (low melting point) glass ceramics with high electrical conductivity materials (e.g. silver, gold, galvanized nickel) [3]. In the co-sintering process, different layers are printed and/or sintered (e.g. up to 900°C) onto the ceramic substrate according to the component design. In any case, the fabrication of components having two or more different materials can be a challenge from the structural viewpoint. The different thermal expansion coefficients and elastic properties of the combined materials can generate significant "residual stresses" in some of the parts (e.g. in the ceramic layers), which may induce cracks that truncate the electrical performance of the component [4, 5]. While compressive residual stresses can be beneficial in strengthening the material (e.g. ion exchange process as used in Gorilla® glass [6, 7]), tensile residual stresses may lead to the initiation and/or propagation of cracks (e.g. surface cracks) from starting defects, even before service loading conditions [8]. In addition, although some of these tensile residual stresses may relax due to plastic deformation of metallic materials, stress concentrations generated in material junctions or terminations (imposed by geometrical constrains) may lead to failure during fabrication or in service.

In a previous work the fracture behavior of a co-fired multilayer structure based on ZnO ceramic substrate was investigated [9]. Two architectures were analyzed, holding a slightly different combination of metal and glass layers onto the substrate material. In one case, a significant different strength distribution was found, as compared to bulk ZnO material. A FE analysis simulating the residual stress distribution during the fabrication process showed relatively high stress concentration in the junction between metal and glass layers [9]. Such location was found to be the fracture origin in both configurations (i.e. crack initiation). A fracture mechanics analysis showed a preferred angle of crack propagation, being closed to the metal-glass interface. Nevertheless, based on those results, the difference in strength between both configurations remained unclear. This previous work demonstrated that the different steps during the fabrication of the multilayer architecture may have played a role on the final behavior of the structure.

In this work the effect of metallization steps and layered architecture on the fracture behaviour of ceramic-based functional multilayer components has been experimentally assessed. Different configurations of metal and glass layers attached onto the surface step by step were analyzed. Mechanical testing using three-point bending was performed on samples taken after different process steps and compared to the strength distribution of the bulk substrate material. Strength results were interpreted according to Weibull statistics. In order to identify the failure origin in the different architectures, fractographic analyses were performed on broken samples. In addition, Focused-Ion-Beam (FIB) analyses were carried out on preloaded (pre-damage) samples to understand the onset and propagation of cracks during mechanical loading.

2. Experimental

2.1 Materials and architectures

Figure 1 schematically shows the typical build-up of the functional multilayer architecture (thereafter referred to as FMA) of study. The fabrication process is described in detail in Ref. [9]. It consists of a ZnO ceramic substrate (green), two silver metallization layers (light blue), a glass layer in between (blue) and a nickel (Ni) galvanic coating (orange).

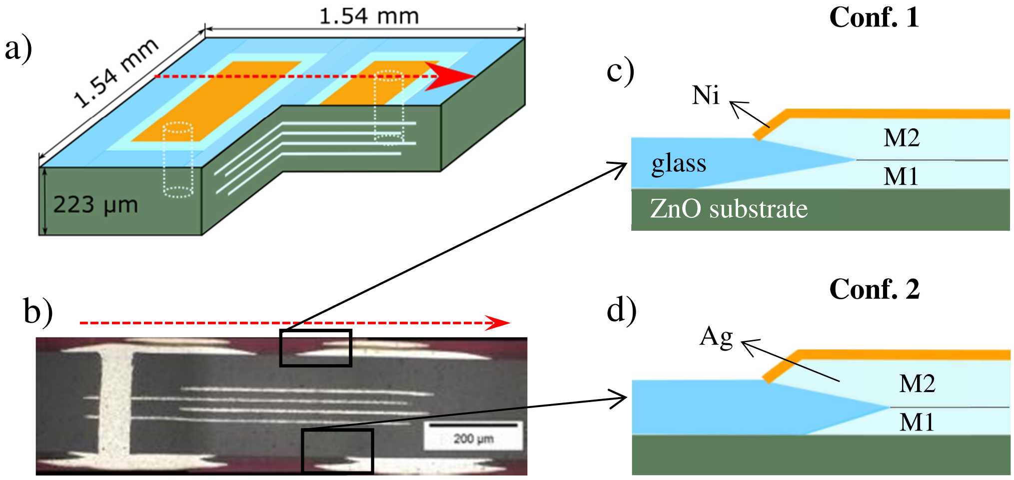

Figure 1: (a) 3D schematic of the FMA component, (b) Cross-section showing the top and bottom architecture of the FMA (c) Metallization configuration 1 (Conf. 1), (d) Metallization configuration 2 (Conf. 2).

The typical dimensions of such FMA components are given in Fig. 1a. A detail of the cross-section of the component is shown in Fig. 1b. It is worth pointing out that the overlapping of the two metallization layers (i.e. M1 and M2) can be done following two distinct configurations. In configuration 1 (referred to as Conf. 1) the area covered by the metallization 1 (M1) is larger than that of metallization 2 (M2), see Fig. 1c. In configuration 2 (named as Conf. 2) the area metallization 2 (M2) is the one covering a larger area, see Fig. 1d. For both configurations, after the co-firing of the ZnO substrate with internal electrodes and vias, the FMA is produced following these process steps: (i) first metallization of silver (M1) onto the ZnO substrate, (ii) printing of a glass layer, (iii) second metallization of silver (M2) onto the top of M1 and the glass layer, and (iv) galvanization of the electroless nickel (~ 4 µm layer) on the metallization M2 followed by a very thin gold layer (~ 60 nm), see top (orange) layer in Fig. 1.

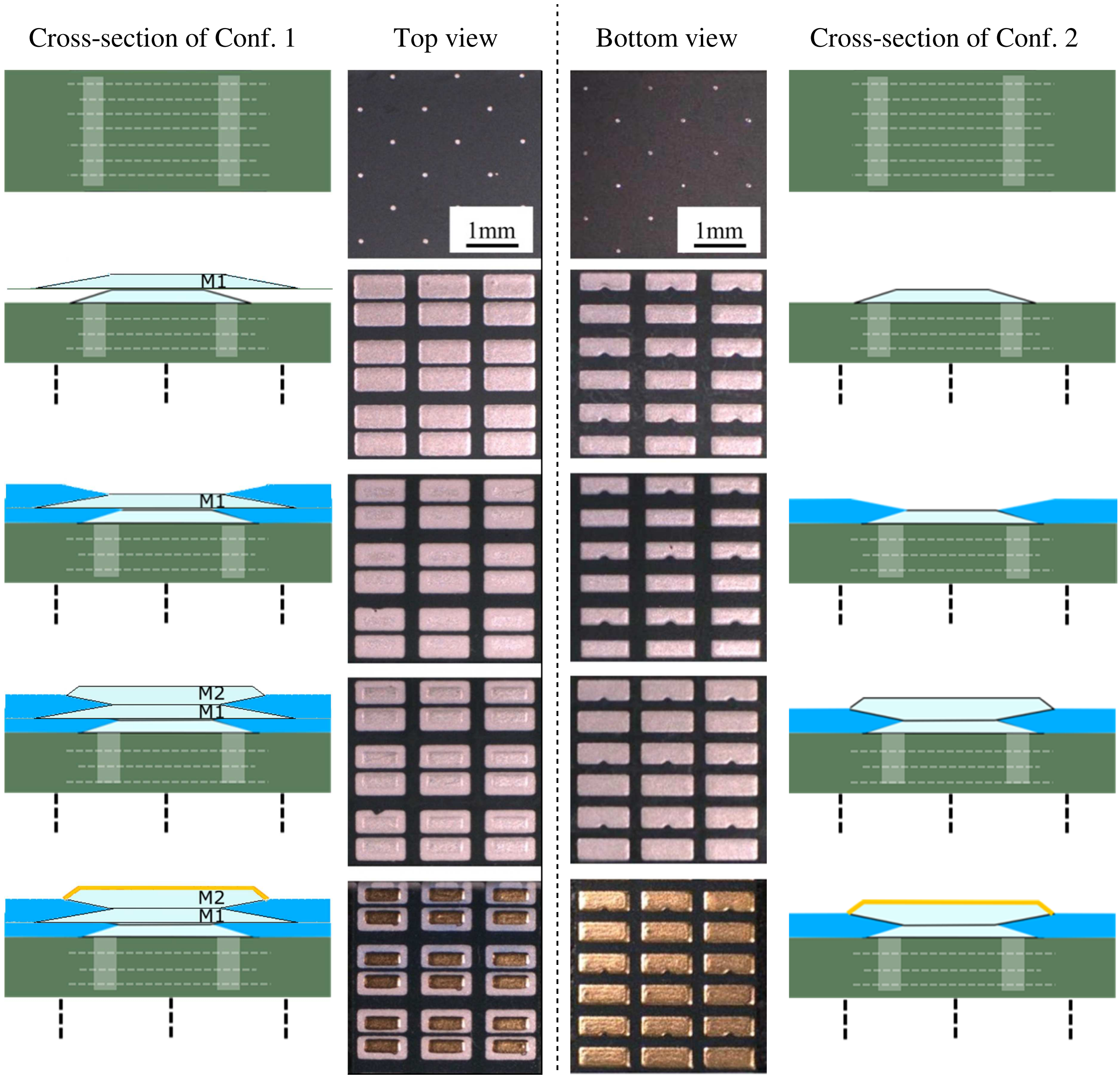
Cross-section of Conf. 1

Top view

Bottom view

Cross-section of Conf. 2

Figure 2: Schematic of the different process steps in the FMA for (left) configuration 1 and (right) configuration 2.

For illustrative purposes, a schematic of the different steps for both configurations along with a top view of the structures are represented in Fig. 2. It should be noticed that both configurations were manufactured the same way. The only difference between these two configurations is the size ratio between metallization M1 and M2, with M1/M2 > 1 for Conf. 1 and M1/M2 < 1 for Conf. 2. No other influences of the processing are to be expected. The cross-section in Fig. 2b provides a closer look into the structure and shows the differences in geometry of the metal layers from the side view.

3. Mechanical characterization

3.1 Testing samples

Bending bars were fabricated for the mechanical testing, containing equally spaced distributed FMA components corresponding to Conf. 1 and Conf. 2, see Figs. 3a and 3b, respectively. For comparison, bulk bending bars were also tested (Fig. 3c). Typical dimensions were (l x b x t) 25 mm x 3.8 mm x ~0.25 mm, with l, b and t being the length, width and thickness of the specimen, respectively. Details on specimens preparation can be found in [9].

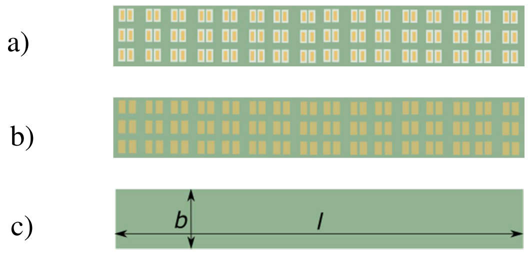

Figure 3: Rectangular bending bars containing (a) FMA Conf. 1, (b) FMA Conf. 2, and (c) bulk ZnO.

3.2 Strength evaluation

The bending tests were performed according to the ASTM C1161 standard [10] using a three-point bend (3PB) fixture, with an outer span S_0 of 20 mm. Tests were conducted in ambient conditions (25 °C, 15 % relative humidity) under displacement control with a load cell of 200 N at a rate of 5 mm/min using a universal testing machine (Zwick Z010, Zwick/Roell, Ulm, Germany). The maximum stress in the specimen during the bending test (failure stress), σ_f, was calculated for each bar following the expression [10]:

$$\sigma_\mathrm{f} = \frac{3}{2}\frac{PS_0}{bt^2} \tag{1}$$

where P is the fracture load. The thickness t was considered to be the substrate thickness (t_s) for the bulk samples, and the thickness of substrate plus glass layer for the FMA samples.

3.3 Fractographic analyses

The light microscope images (LIMI) were made on an optical microscope (BX50, Olympus, Tokyo, Japan). The scanning electron microscope (SEM) images, focused ion beam (FIB) cuts and energy dispersive X-Ray (EDX) analysis were performed in a SEM (Auriga, Zeiss, Germany) equipped with an EDX detector (Apollo, EDAX, Mahwah, NJ, USA) and a FIB system (Cobra Z-05, Orsay Physics, Brno, Czech Republic) with a Gallium ion source.

4. Results and Discussion

4.1 Strength distributions after different process steps

The failure stress values obtained for the three samples were analyzed according to Weibull theory [11]. The resulting strength distributions for every sample were represented in a Weibull diagram (Fig. 4), where the probability of failure, *F*, is plotted versus the failure stress, σ_f (calculated for every specimen according to Eq. (1)) [9].

For the sake of simplicity, only bulk material and Conf. 1 and Conf. 2 after galvanization process are shown in Fig. 4. The dashed lines represent the best fit to the failure stress data using the maximum likelihood method. The Weibull parameters σ_0 (characteristic failure stress) and *m* (Weibull modulus) of all different samples (after the different process steps) were calculated according to EN-843-5 [12], and are given in Table 1, along with the 90% confidence intervals. For illustrative purposes, the characteristic strengths of all samples after the different process steps are represented in Fig. 5 for Conf. 1 and Conf. 2. It can be seen that ZnO with inner metallization layers and vias is weaker than ZnO bulk material. M1 seems to increase the strength almost up to the value of ZnO bulk material for both configurations. Whereas almost no changes up to the last process step were found for Conf. 1, Conf. 2 shows a significant decrease in strength after the last step where the thin galvanic Ni and negligible Au layer are attached onto M2. In order to identify the reason for the big differences and the critical process step, where the significant decrease in strength for Conf. 2 appears, fractographic analyses were performed.

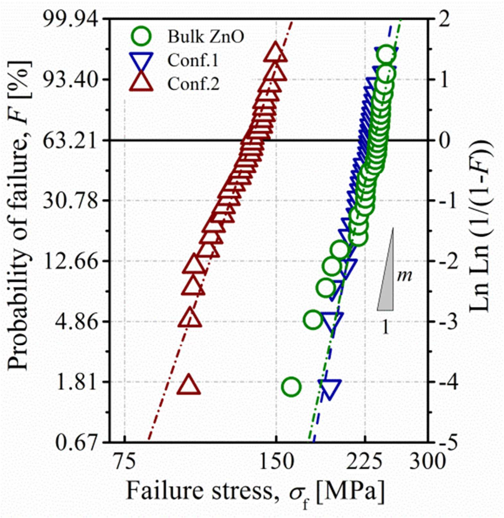

Figure 4: Weibull diagram showing probability of failure vs. failure stress of FMAs with different configurations, as compared to ZnO bulk material [9].

Table 1: Characteristic strength σ_0 and Weibull modulus m with corresponding 90 % confidence intervals for ZnO-based co-fired FMAs after different process steps. The Weibull parameters for ZnO bulk are $\sigma_0 = 235$ [230 – 240] MPa and $m = 17$ [12 – 20], for comparative purposes (see Ref. [9]).

Configuration		**Step 1** (Susbtrate with Vias)	**Step 2** (M1 layer)	**Step 3** (Glass layer)	**Step 4** (M2 layer)	**Step 5** (Galvanization)
Conf. 1	**σ_0 [MPa]**	161 [154-169]	220 [215-226]	215 [212-219]	217 [213-222]	230 [226 – 234]
	m	10 [7-12]	17 [12-22]	25 [17-32]	20 [14-26]	20 [15 – 24]
Conf. 2	**σ_0 [MPa]**	160 [156-165]	226 [222-230]	206 [202-210]	236 [229-242]	134 [130-138]
	m	14 [10-18]	23 [16-29]	22 [15-28]	15 [11-20]	11 [8-13]

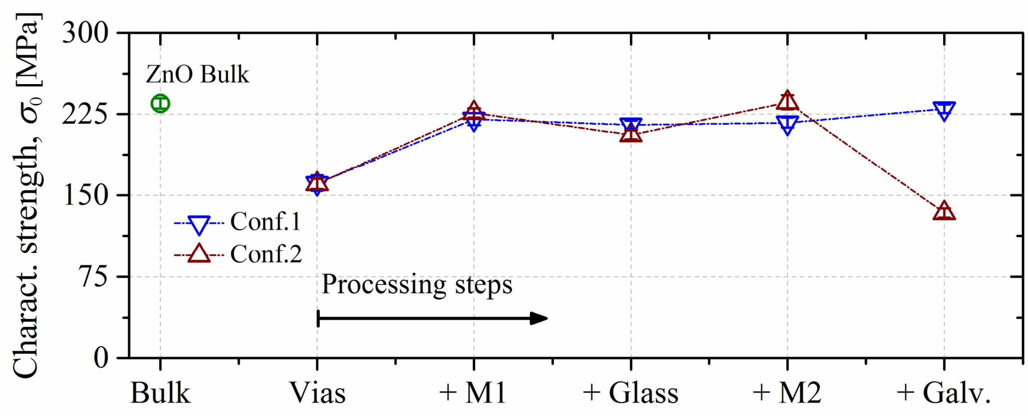

Figure 5: Comparison of characteristic strength for ZnO-bulk material and FMAs after different process steps. The error bars represent the 90 % confidence intervals.

4.2 Fracture analyses

Fractographic analyses using LIMI, REM and FIB were performed in order to identify the origins of failure, the crack path and consequentially the reason for the significant difference in strength between the two investigated configurations after the different process steps. Figure 6 shows SEM images of fracture surfaces of representative specimens of the different samples: a) ZnO bulk, b) ZnO with inner metallization and vias, c) after M1, d) after attachment of glass, e) after M2, f) Conf. 1 after galvanization and e) Conf. 2 after galvanization. Red dashed ellipses mark traces of vias and red arrows mark possible fracture origins. In all cases, intergranular fracture occurs through the ZnO ceramic.

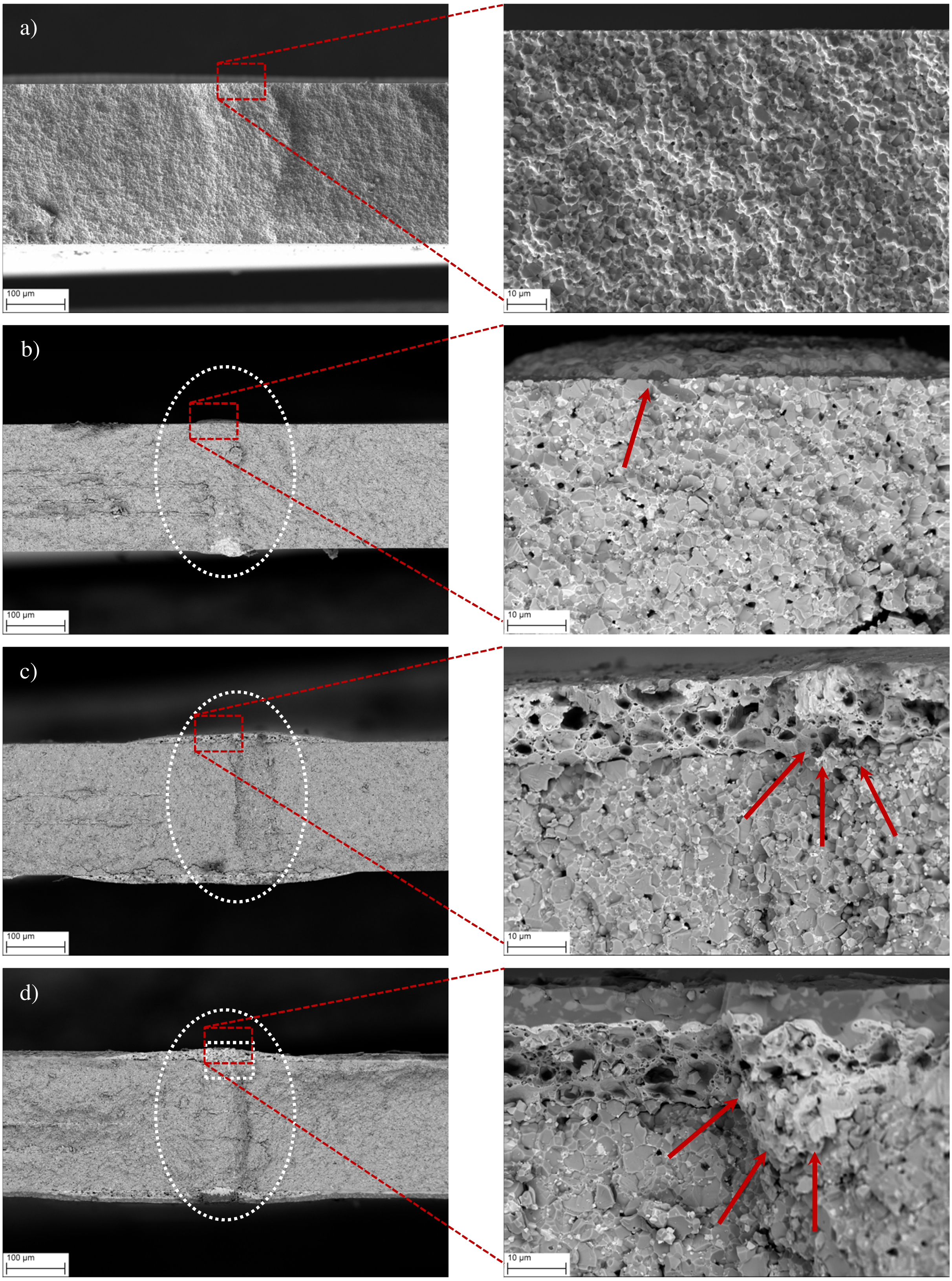
a)
100 µm
10 µm
b)
100 µm
10 µm
c)
100 µm
10 µm
d)
100 µm
10 µm

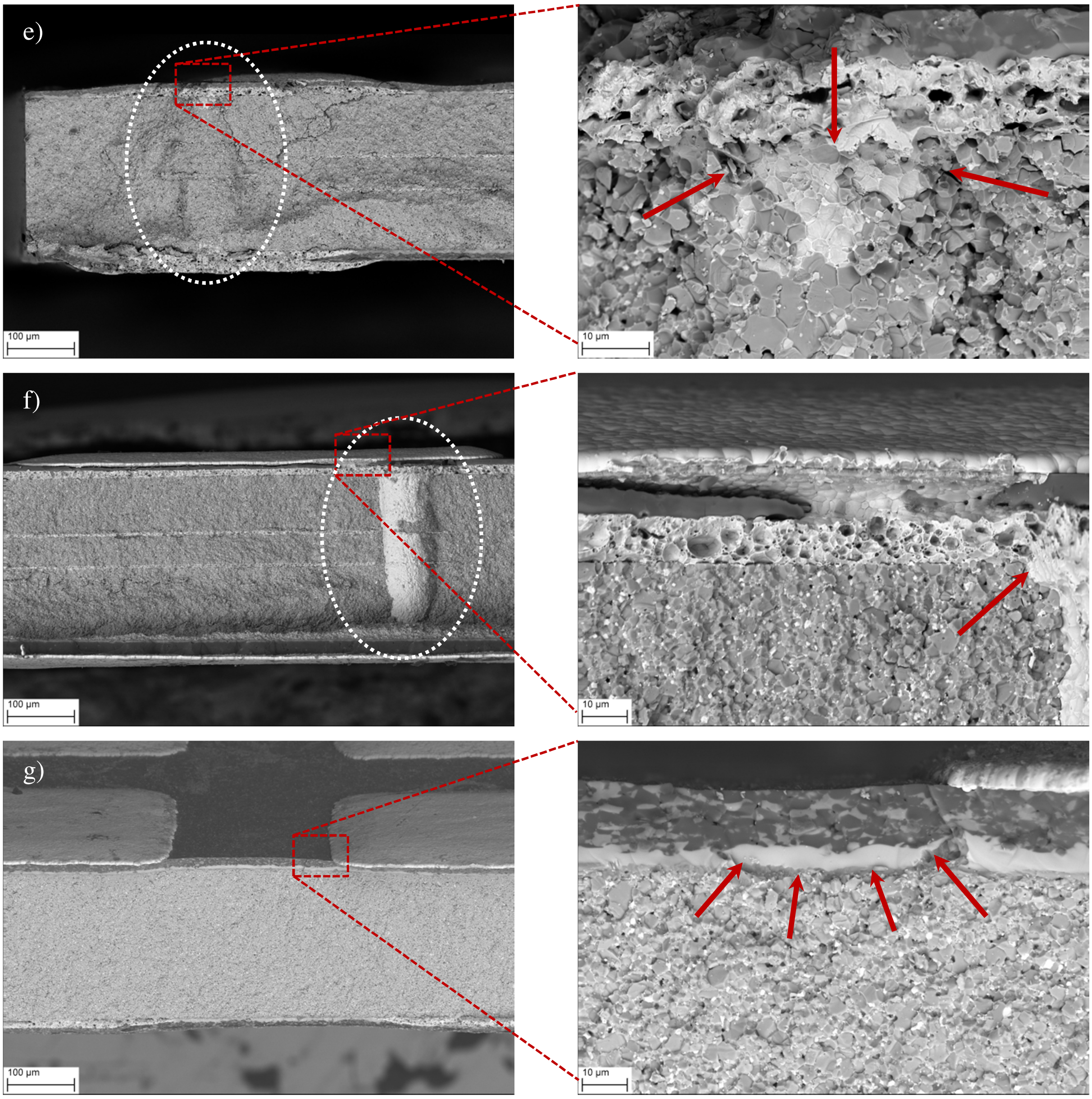

Figure 6: SEM images of fracture surfaces of representative specimens after different process steps: a) ZnO bulk, b) ZnO with inner metallization and vias, c) after M1, d) after attachment of glass, e) after M2, f) Conf. 1 after galvanization and e) Conf. 2 after galvanization. White dashed ellipses mark traces of vias and red arrows mark possible fracture origins.

In order to estimate the size of critical defects, a_c, causing the failure, the bulk sample was analysed according to linear elastic fracture mechanics [13]:

$$a_c = \frac{1}{\pi}\left(\frac{K_{Ic}}{Y\sigma_f}\right)^2 \qquad (2)$$

where K_{Ic} is the fracture toughness, σ_f is the failure stress and Y is the geometric factor depending on the shape and location of the defect. Taking the characteristic strength for the bulk sample, i.e. $\sigma_0 = 235$ MPa, and assuming a $K_{Ic} = 1.3 \pm 0.1$ MPa·m$^{1/2}$ (internal measurements on bulk ZnO substrate using SEVNB [14]) and a $Y = 0.7$ (for small semi-elliptical surface flaw [15, 16]), a defect size in the range of $a_c \sim 20 \pm 3$ µm can be estimated. However, a critical defect of this size could not be found on any fracture surface leaving the reason for failure of ZnO bulk material unclear.

Specimens of both configurations after further process steps tended to fail along the vias, which is exemplarily shown in Figs. 6b to 6e. Possible fracture origins are marked with red arrows and show, that the weakest points of this three-dimensional structures are almost always at least close to the via/ZnO interface. This observation agrees well with the strength measurements, where ZnO with inner metallization and vias has a significant lower strength than ZnO bulk material (see Table 1). M1 may “neutralize” this weak point and therefore lead to the measured increase in strength almost up to the value of ZnO bulk material. The next process steps (i.e. +Glass, +M2) show no significant effect on the strength, compared to M1 in both configurations (see Table 1). However, after the galvanization process, a different characteristic strength is observed between Conf. 1 and Conf. 2. For Conf.1 the strength distribution is similar as for bulk ZnO, as well as after steps M1, Glass and M2. The failure mode observed is also the same (i.e. through the vias), see Fig. 6f. For Conf. 2 the characteristic strength measured is approx. 40% lower than that of Conf. 1. The fracture mode observed is also completely different (see Fig. 6g); the crack path following the edge of the two metallizations (M1 and M2). Based upon these findings, it can be concluded that an even weaker point than the Ag/ZnO interface is introduced due to the galvanization process.

4.3 Understanding the onset of damage after galvanization

FIB-cuts on semi-finished (after M2) and finished FMAs (after galvanization) were performed in order to assess why the galvanization step has such a high effect on Conf. 2 compared to Conf. 1 (see Ref. [9] for more details on the FIB sample preparation). The position of interest was determined at the edge of M2 for both configurations. Fig. 7a shows that before galvanization, M2 is well attached to the glass surface. However, after galvanization a delamination crack between M2 and glass can be observed (Figs. 7b, 7c) for both configurations. It is thus hypothesized that the Ni layer deposited during the galvanization process may introduce residual stresses, which can cause bending and corresponding “de-attachment” from the M2 layer. Comparing the position of these delamination cracks with the crack paths seen on the fracture surfaces (Figs. 6f, 6g) leads to the conclusion that, during bending, fracture may be triggered by these initial (delamination) cracks. Nevertheless, although the delamination cracks are very similar for Conf. 1 and Conf. 2, the strength values after galvanization differ significantly (see Table 1).

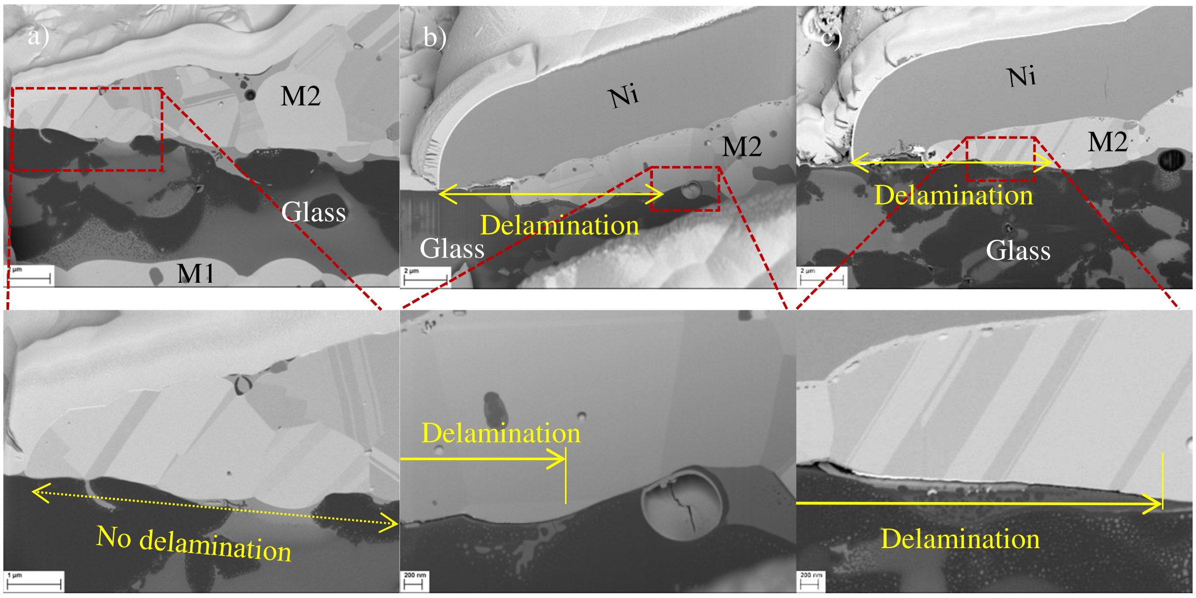

Figure 7: FIB-cuts at the edge of M2 in a) Conf. 1 before galvanization, b) Conf. 1 after galvanization and c) Conf. 2 after galvanization.

In order to understand the further fracture process, *ex-situ* pre-loaded samples were examined using FIB for Conf. 1. It is hypothesized that cracks starting at the tip of the delamination area in Conf. 1 propagate through the glass layer, might arrest in the M1 layer, following a similar process observed in layered ceramics designed with compressive stresses (see for instance [17, 18]) as well as in silicon-based components ([19, 20]). However, for Conf. 2, no crack arrest may take place due to the lack of M1, and thus the propagation of the crack through the glass is followed by unstable fracture.

To proof this hypothesis, a selected Conf. 1 sample was pre-loaded with an applied force corresponding to the characteristic strength of Conf. 2, where 63.21 % of the Conf. 2 samples would have already failed. Fig. 8 shows a FIB-cut performed on this sample where already a small crack into the glass, perpendicular to the delamination crack, can be observed. Stopping of the crack in the glass indicates compressive stresses inside the glass which may be induced by the higher CTE of the surrounding metal compared to glass (see Ref. [9] for more details).

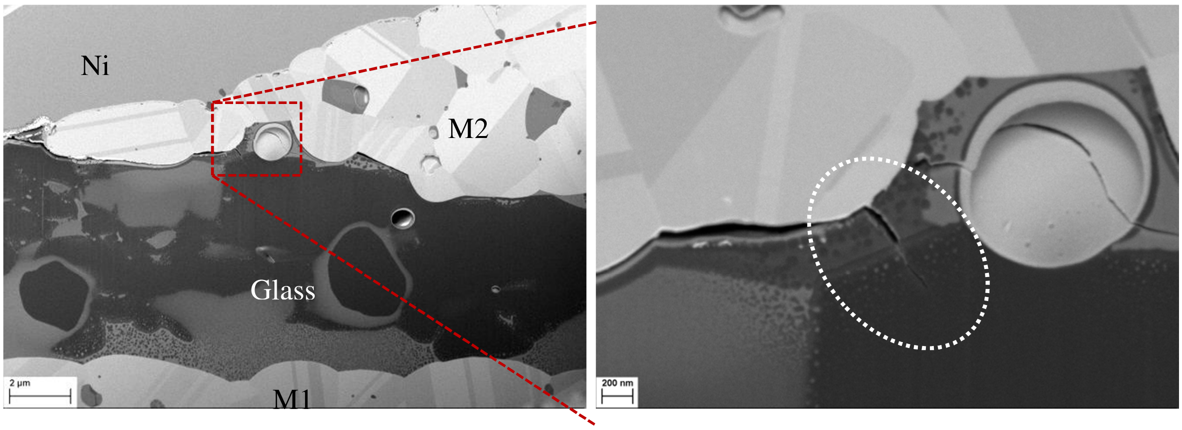

Figure 8: FIB-cut in preloaded samples with an applied equivalent stress of ~60 % of $\sigma_{0,\mathrm{Conf.1}}$.

Additionally, a second Conf. 1 sample was loaded up to 80% of the characteristic strength of Conf. 1 (i.e. ~80 % of $\sigma_{0,\mathrm{Conf.1}}$), where all Conf. 2 samples would have failed. Figure 9 shows the FIB-cut performed on the referred sample where a crack propagating through the glass layer can be observed. As hypothesized, the crack arrests at the M1 layer, which prevents its unstable propagation though the ZnO substrate. This experimental findings clearly show the different behaviour of cracks in Conf. 1 and Conf. 2., thus explaining the higher strength values obtained during the bending tests of Conf. 1 samples.

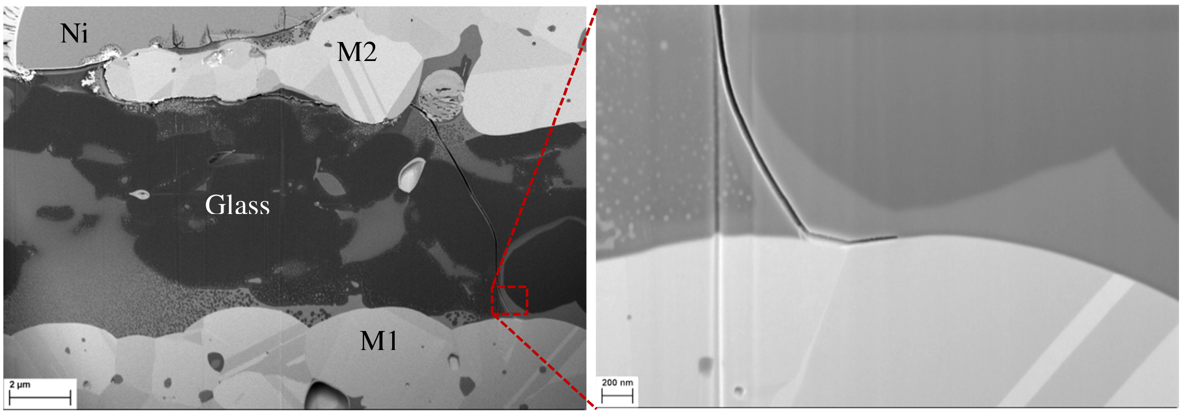

Figure 9: FIB-cut in preloaded sample with an applied equivalent stress of ~80 % of $\sigma_{0,\mathrm{Conf.1}}$.

5. Conclusions

The effect of metallization on the strength and fracture behaviour of ZnO ceramic-based multilayer components was investigated under bending after several fabrication steps. Experimental results showed a strong effect of the layered architecture on the component strength distribution. Two architectures were analysed (Conf. 1 and Conf. 2), holding a slightly different disposition of the (inner most) top metallization. Vias were identified in both cases as key factor to reduce the strength of the component compared to bulk substrate. However, the further metallization over the vias yielded an apparent increase of strength, with values similar to those of bulk.

The galvanization process resulted to be the most significant step, yielding a strong difference in strength between Conf. 1 and Conf. 2. These results in combination with fractographic analyses and *ex-situ* Focused Ion Beam experiments in pre-loaded samples were used to assess the location of failure and predict critical configurations. The higher strength measured in Conf. 1 was ascribed to the capability of the (inner most) top metallization in arresting the propagation of delamination cracks.

This case study showed that, for a given ceramic substrate, details of geometrical design can have a significant impact on the strength of structural components.

6. Acknowledgements

Financial support by the Austrian Federal Government (in particular from Bundesministerium für Verkehr, Innovation und Technologie and Bundesministerium für Wissenschaft, Forschung und Wirtschaft) represented by Österreichische Forschungsförderungsgesellschaft mbH and the Styrian and the Tyrolean Provincial Government, represented by Steirische Wirtschaftsförderungsgesellschaft mbH and Standortagentur Tirol, within the framework of the COMET Funding Program is gratefully acknowledged.

7. References

[1] A. Roosen, Tape casting of ceramic green tapes for multilayer device processing, in: H.J. Jean, T.K. Gupta, K.M. Nair, K. Niwa (Eds.), Ceramic Transactions, The American Ceramics Society, Columbus, Ohio, 1999.

[2] A. Roosen, New lamination technique to join ceramic green tapes for the manufacturing of multilayer devices, J. Eur. Ceram. Soc. 21(10-11) (2001) 1993-1996.

[3] R. Bermejo, P. Supancic, I. Kraleva, R. Morrell, R. Danzer, Strength reliability of 3D low temperature co-fired multilayer ceramics under biaxial loading, J. Eur. Ceram. Soc. 31(5) (2011) 745-753.

[4] A.G. Evans, D.R. Biswas, R.M. Fulrath, Some Effects of Cavities on the Fracture of Ceramics: I, Cylindrical Cavities, J. Am. Ceram. Soc. 62(1-2) (1979) 95-100.

[5] C.H. Hsueh, A.G. Evans, Residual Stresses and Cracking in Metal/Ceramic Systems for Microelectronics Packaging, J. Am. Ceram. Soc. 68(3) (1985) 120-127.

[6] M.E. Nordberg, E.L. Mochel, H.M. Garfinkel, J.S. Olcott, Strengthening by Ion Exchange, J. Am. Ceram. Soc. 47(5) (1964) 215-219.

[7] S.P. Fillery, F.F. Lange, Ion-Exchanged Glass Laminates that Exhibit a Threshold Strength, 2007, pp. 2502-2509.

[8] R. Bermejo, A.J. Sanchez-Herencia, C. Baudin, L. Llanes, Residual stresses in Al_2O_3-ZrO_2 multilayered ceramics: nature, evaluation and influence on the structural integrity, Bol. Soc. Esp. Ceram. V. 45(5) (2006) 352-357.

[9] K. Macurova, M. Gruber, M. Pletz, P. Supancic, R. Danzer, F. Aldrian, R. Bermejo, Mechanical testing and fracture analyses of miniaturized ZnO-based multilayer components, International Symposium on Microelectronics 2015(1) (2015) 000163-000168.

[10] ASTM C 1161-02c, Standard Test Methods for Flexural Strength of Advanced Ceramics at Ambient Temperature, American Society for Testing and Materials, 2002.

[11] W. Weibull, A statistical distribution function of wide applicability, J. Appl. Mech. 18 (1951) 253.

[12] EN 843-5, Advanced Technical Ceramics - Monolithic Ceramics - Mechanical Tests at Room Temperature - Part 5: Statistical Analysis, EN 843-5, 1997, p. 40.

[13] D. Munz, T. Fett, Ceramics. Mechanical Properties, Failure Behaviour, Materials Selection, Springer, Berlin, 1999.

[14] ISO 23146, Fine ceramics (advanced ceramics, advanced technical ceramics) -- Test methods for fracture toughness of monolithic ceramics -- Single-edge V-notch beam (SEVNB) method, 2008.

[15] G.D. Quinn, Fractography of Glasses and Ceramics, US Government Printing Office, Washington, 2007.

[16] R. Danzer, On the relationship between ceramic strength and the requirements for mechanical design, J. Eur. Ceram. Soc. 34 (2014) 3435-3460.

[17] R. Bermejo, Y. Torres, C. Baudin, A.J. Sanchez-Herencia, J. Pascual, M. Anglada, L. Llanes, Threshold strength evaluation on an Al_2O_3-ZrO_2 multilayered system, J. Eur. Ceram. Soc. 27 (2007) 1443-1448.

[18] Y. Chang, R. Bermejo, O. Ševeček, G.L. Messing, Design of alumina-zirconia composites with spatially tailored strength and toughness, J. Eur. Ceram. Soc. 35(2) (2015) 631-640.

[19] M. Deluca, R. Bermejo, M. Pletz, P. Supancic, R. Danzer, Strength and fracture analysis of silicon-based components for embedding, J. Eur. Ceram. Soc. 31(4) (2011) 549-558.

[20] M. Deluca, R. Bermejo, M. Pletz, M. Wießner, P. Supancic, R. Danzer, Influence of deposited metal structures on the failure mechanisms of silicon-based components, J. Eur. Ceram. Soc. 32(16) (2012) 4371-4380.